Study of Gas-Phase Reactions in TiO_2 Production and Functionalised Thin Films

EngD Thesis

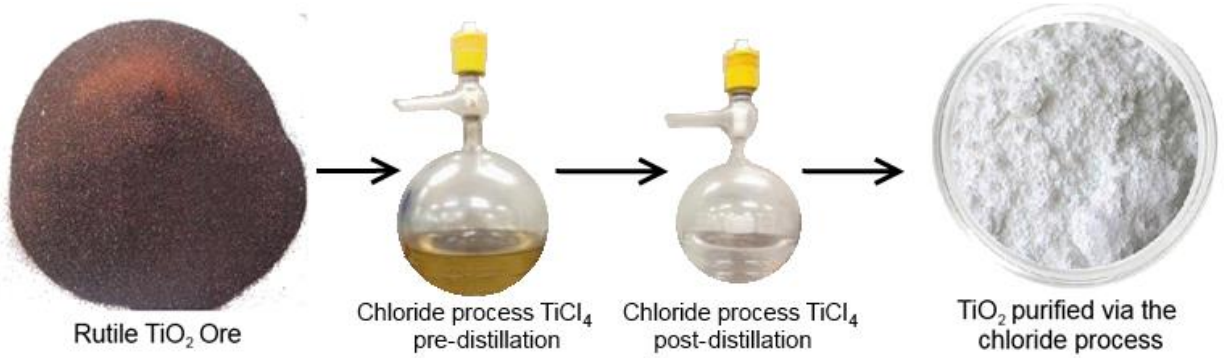

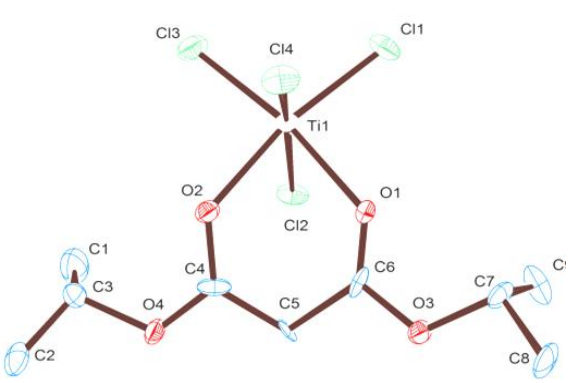

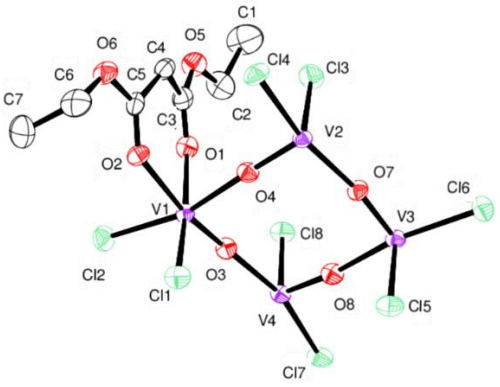

Ben Blackburn

Supervisors

Prof. Ivan Parkin
Prof. Claire Carmalt

Disclaimer

I Ben Blackburn confirm that the work presented in this thesis is my own. Where information has been derived from other sources, I confirm that this has been indicated in the thesis.

Signed: .....

Acknowledgements

This project was funded by contributions from Huntsman Pigments, the EPSRC as well as the UCL EngDoc Center.

I would like to thank Professors Ivan Parkin and Claire Carmalt for their guidance and support throughout this project, as well as Dr. Stephen Sutcliffe and Andrew Brown at Huntsman Pigments and Additives for providing and industrial insight to the work done.

In addition thanks are owed to Dr. Jared Crane for his assistance in handling and analysis of $TiCl_4$ samples and inorganic synthesis. Dr. Caroline Knapp, Dr. Peter Marchand, Dr. David Pugh for assistance in determining molecular structures using X-ray crystallography, Dr. Kristopher Page for assistance in procuring reagents, Dr. Steve Firth for instruction in Raman Spectrosocopy, Dr. Andreas Kafizas for assistance with X-ray diffraction analysis, Dr. Michael Parkes and Dr. Kirsty Karu for assistance mass spectroscopy, Dr. Michael Powell, Dr. Carlos Sotelo-Vazquez, Dr. Raul Quesada-Cabrera for their instruction in testing the thermochromic nature of thin films determining solar modulation and Dean Brett, Charalampos Drosos for their contributions to the deposition of thin films.

This thesis is dedicated to Amy, whose love, friendship and patience has made the last four years easier in every possible way.

Abstract

Titanium dioxide (TiO_2) is a pigment used in the whitening of millions of products from paint to foodstuffs. Produced *via* purification of ores using the Chloride Process, the mined TiO_2 ore is chlorinated along with all of the impurities. The resulting $TiCl_4$ is a liquid at room temperature and can be separated from its impurities using distillation. V_2O_5, an impurity present in this ore is converted to vanadium oxytrichloride ($VOCl_3$) which is too similar in boiling point to $TiCl_4$ to separate *via* distillation and instead is removed *via* addition of an oil, which preferably binds to $VOCl_3$.

This work, sponsored by Huntsman Pigments and Additives, seeks to better understand this reaction, as well as other aspects of the Chloride Process. This is achieved by analysing industrial samples as well as producing lab scale models for the process and investigating inorganic synthesis of analogous compounds $[TiCl_4\{CH_2(CO_2CH(CH_3)_2\}_2]$ [**1a**], $[(\mu\text{-}O)(TiCl_3\{CH_2(CO_2CH(CH_3)_2\}_2)]$ [**1b**], $[TiCl_4\{CH_2(CO_2CH(C_6H_5)\}_2]$ [**2**], $[TiCl_4\{C_2H_4(CO_2CH_3)\}_2]$ [**3**], $VOCl_3$+glycerol tribenzoate [**4**], $[VOCl_2(acac)]$ [**5**], $[\{VOCl_2(CH_2(CO_2Et)_2\}_4]$ [**6**] and $[VOCl_2\{C_2H_4(CO_2Et)_2\}]_n$ [**7**] that were characterised *via* single crystal X-ray diffraction analysis (with the exception of 4)

Alongside this study, multiple side projects were undertaken that sought to use some of the novel materials produced in materials synthesis, due to the useful nature of both TiO_2 and VO_2 in window coating applications, the abundance of oxygen in the products making them good contenders for metal oxide precursors. This included the deposition of TiO_2 /SiO_2 thin films for photocatalytic self cleaning applications, VO_2 thin films for energy saving windows and VC/VN particles for mechanical hardening applications.

In addition, a new system for the *in-situ* study of high temperature gas phase inorganic reactions *via* mass spectroscopy was developed and used to study the reactivity of gaseous $TiCl_4$ and $VOCl_3$, as well as several other species including vanadium chloride, titanium isopropoxide and butyltin trichloride considered to be of greater interest to the field of thin film deposition.

Contents

List of Figures

List of Tables

List of Schemes

List of Abbreviations

AACVD	aerosol assisted chemical vapour deposition
Acac	acetyl acetonate (2-4, pentadione)
ALD	atomic layer deposition
APCVD	atmospheric pressure chemical vapour deposition
aq	aqueous
CVD	chemical vapour deposition
EDX	energy dispersive x-ray spectroscopy
FEG	free electron gun
FT-IR	Fourier transform infrared spectroscopy
GADDS	general area detector diffraction system
MS	mass spectroscopy
NMR	nuclear magnetic resonance spectroscopy
PECVD	plasma enhanced chemical vapour deposition
SEM	scanning electron microscopy
TEM	transmission electron microscopy
TTIP	titanium isopropoxide
UV	ultra-violet
UV/Vis	ultraviolet/ visible spectroscopy
XPS	X-ray photoelectron spectroscopy
XRD	X-ray diffraction

Chapter 1

Introduction

1.1. Project Overview

This project was funded by Huntsman Pigments and Additives, branch of Huntsman Chemicals that produces titanium dioxide, a pigment used in the production of paints. TiO_2 is produced on an industrial scale by The Chloride Process, a series of steps in which TiO_2 ore is converted to $TiCl_4$ and the impurities removed *via* distillation. One impurity in particular, $VOCl_3$, is removed *via* the injection of oil, which is found to react exclusively with the gaseous $VOCl_3$, leaving the $TiCl_4$ to distil into the next part of the process. This technique is widely used, but little is known as to why the $TiCl_4$ does not react with the oil.

This project seeks to further the understanding of the Chloride Process. The reactions of $TiCl_4$ and $VOCl_3$ with oils have been studied using a number of methods. Initially industrial samples of $TiCl_4$ taken from the Chloride Process were analysed using nuclear magnetic resonance (NMR) spectroscopy. Following this various β-diketo esters and triesters were used as analogues for the triglyceride backbone of the oil and reacted with both species. The products of these reactions were crystallised, and the products used to explain the oils preferred reactivity in the Chloride Process.

The gas phase interactions of $TiCl_4$ and $VOCl_3$ were then studied by building a laboratory scale replica of the distillation phase of the Chloride Process, and the samples produced were analysed. Following this a system for studying the contents of a high temperature vapour

deposition reactor was designed and built, and used to study the reactivity of $TiCl_4$ and $VOCl_3$ in the gas phase directly, as well as several other molecules frequently used in the vapour deposition of thin films.

In addition to data on The Chloride Process, several new single source precursors for the chemical vapour deposition (CVD) of VO_2 and composited TiO_2-SiO_2 thin films were produced as an indirect result of this project. The precursors were characterised and the resulting films grown and were analysed.

1.2. Titanium Dioxide

Titanium Dioxide (TiO_2) is a heavily studied material that has a variety of uses, with over 4.5 million tonnes produced annually.[1] Titanium dioxide is mostly obtained through mining and purification of the ore, which is carried out by one of two main processes (*vida infra)*. In recent years a synthetic alternative to production has been developed using titanium slag from metallurgical processes.[2]

1.2.1. Structure and Phases

Titanium dioxide has three common mineral phases: Rutile, Brookite and Anatase (Figure 1). All of these phases consist of distorted octahedra with titanium surrounded by six oxygen atoms. The orientation of these octahedral alters depending on the phase present. The most thermodynamically stable phase is Rutile TiO_2. Anatase and Brookite convert to this phase when heated to 915 ˚C and 730 ˚C, respectively. [3]

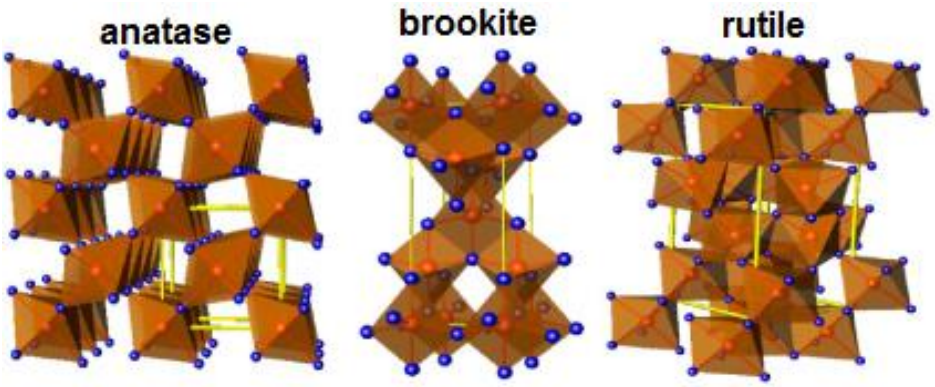

Figure 1: Crystal structures of the three polymorphs of TiO_2.[4]

Rutile TiO_2 has a primitive tetragonal geometry with space group *4/m 2/m 2/m*. The Rutile unit cell consists of two TiO_6 octahedra each coordinated to 6 oxygen atoms which are in turn shared by 3 titanium atoms. The resulting greater structure appears as an array of corner sharing octahedra.

Anatase TiO_2 also has tetragonal geometry and shares its space group with rutile TiO_2; however the structures differ in that the TiO_6 octahedra are linked at two corners (edge sharing). This makes the Anatase phase less dense and hard than the Rutile (Anatase has a Moh hardness of 5.5 vs. 6.5 For Rutile).[5] Despite this, Anatase frequently finds mechanical uses due to its lower abrasiveness compared to that of Rutile.[3] Brookite TiO_2 has a crystal structure with Orthorhombic geometry and space group *2/m 2/m 2/m*. Unlike the other two polymorphs it is brown in colour.

1.2.2. Uses of TiO_2

Titanium dioxide's primary uses derive from its extremely high refractive index of 2.73 for Rutile and 2.55 for Anatase.[6] This makes it the 'whitest white pigment' available, zinc oxide

having a refractive index of 2. This has led to titanium dioxide being used in whitening of a large number of products, with a market worth $15.17 billion in 2014. [7]

Figure 2 gives a breakdown of the uses of TiO_2 pigments. By far the largest portion of the TiO_2 pigments market is taken up by coatings (paint), however it is also heavily used in plastics, where it is added to the resin in order to whiten the product,[8] as well as the food, makeup and clothing industries.[9] As Figure 2 shows, over the last 15 years these uses, as well as the demand for energy and antimicrobial applications, have seen a huge increase in demand for TiO_2, with 'other' now responsible for over half of the annual consumption of TiO_2

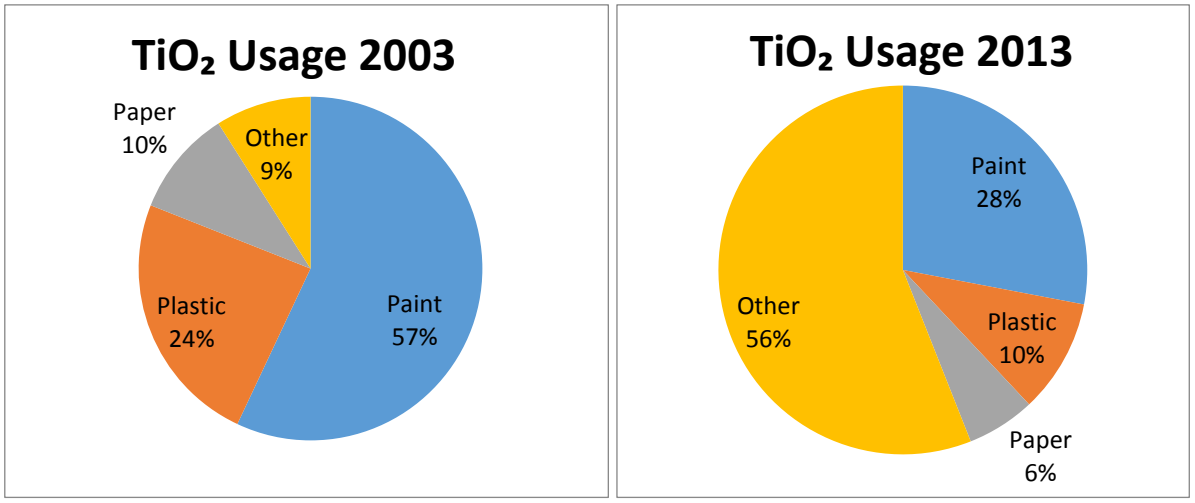

Figure 2: Breakdown of TiO_2 use in 2003[1] compared with 2013.[10]

The refractive index of titania is found to relate to the particle size, as well as the polymorph present. For instance when TiO_2 is encased in a polymer resin with a refractive index of 1.5, then the refractive index is found to increase with particle size up to 0.19 µm, at which point there is a drop off.[11] This is important in the later stages of TiO_2 production. In addition to pigmentation, TiO_2 has found use in a wide variety of applications, as described below.

Self-Cleaning Coatings. Titanium Dioxide's self-cleaning capabilities are well studied. The material exhibits super-hydrophilicity as well as photocatalysing the breakdown of dirt.[12] This

process occurs as a result of photoexcitation. TiO_2 has a band gap of 3.2 eV for the Anatase phase,[13] putting it in the UV region of the Electromagnetic spectrum. When the material comes into contact with UV light, electrons are excited to the conductance band, leaving positive holes. Some of these charge carriers migrate to the surface of the material, where the holes reduce the organic material on the surface and the electrons combine with atmospheric oxygen to form superoxide radicals, which aggressively break down organic materials.[14]

Antibacterial Coatings: The light induced generation of the superoxide radicals is also responsible titanium dioxide's effectiveness in killing bacteria. This is believed to be due to a mechanism known as lipid peroxidation,[15] in which TiO_2 catalyses the formation of radicals, which go on to remove a proton from an unsaturated fatty acid chain. The organic radical then reacts with dioxygen, forming a peroxide radical that removes another proton, propagating a chain reaction. This chain of reactions is believed to prevent the cell membrane from functioning, leading to cell death. Nanostructured TiO_2 films have been shown to kill 99.9% of bacteria in light conditions typical of hospitals.[16]

Photovoltaic Devices: Titanium dioxide is frequently utilised in the field of solar power generation, most prominently in the field of dye sensitized solar cells. First developed by Gratzel and Oregan in 1991,[17] these are electric circuits with wide band gap semiconductor anodes, that have been sensitized by dye molecules that are excited by visible light, allowing them to conduct in the visible region. TiO_2 has a wide band gap of 3.2 eV and is commonly used as an anode material.

1.3. Titanium Dioxide Production

Industrial titanium dioxide production consists of two main possible processes for purifying titanium dioxide ore, the Chloride Process and the Sulfate Process. There are multiple different types of TiO_2 ore available, with each process using different ores. The three most commonly used types in the Chloride Process are rutile, anatase and ilmenite. Rutile and anatase are mainly used in the Chloride Process, with rutile considered the best option due to its higher purity.[18] At the beginning of this project the price of these ores had increased greatly year-on-year for some time, with Rutile TiO_2 ore priced at $3000/tonne in 2012. Ilmenite ($FeTiO_3$) mainly used in the Sulfate Process but also sporadically in the Chloride Process and is considerably cheaper at $285/tonne,[19]. In the intervening years, however, the cost of titanium containing mineral has fallen dramatically (Figure 3).

There are also 'slags' available for each of the processes,[20] which are mineral ores with greater percentages of Fe_2O_3. These are cheaper but harder to work with due to the high volume of solid iron compounds damaging waste disposal relative to rutile.[21]

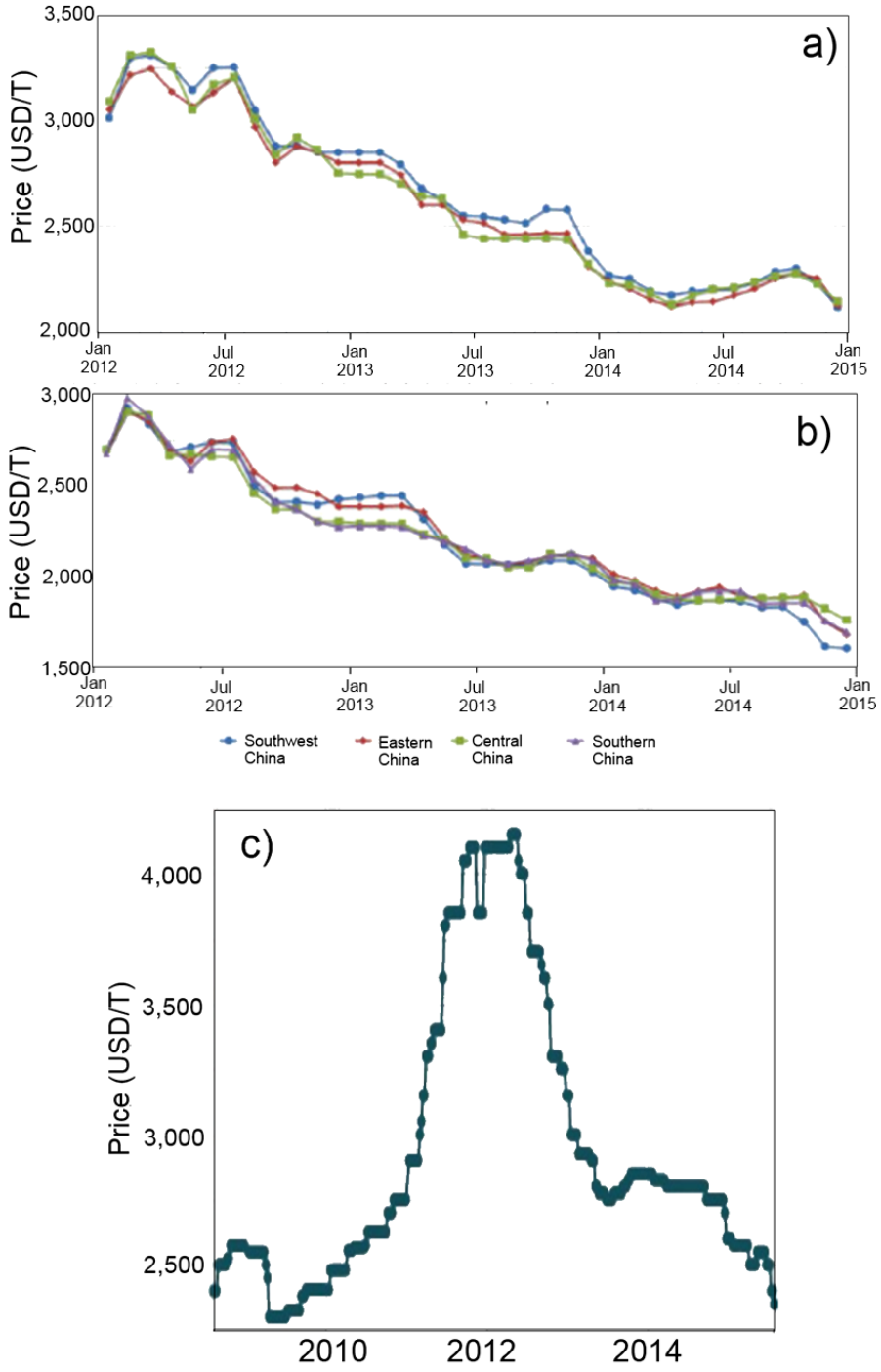

Figure 3: Price of rutile ore a) and anatase ore b) from 2012 to 2015 and retail price of TiO_2 from 2010 to 2015 (c),[22]

1.3.1. The Sulfate Process

The Sulfate Process was the first major method for producing TiO_2 from its ores on a large scale (Figure 4A).[23] The dried, ground ilmenite ore is 'digested' using sulfuric acid to separate

the $FeTiO_3$ into separate sulfates. This results in a solid 'cake' which is leached using dilute sulfuric acid to produce a viscous liquid, which contains predominantly $TiOSO_4$ and $FeSO_4$.[24] The liquid is cooled, allowing some $FeSO_4$ to be removed by precipitation of iron sulfate heptahydrate. With the solid particulates removed, the $TiOSO_4$ is hydrolysed to $TiO(OH)_2$ by heating with dilute sulfuric acid. The material is then filtered and redissolved in water repeatedly and a bleaching agent, such as aluminium is added.[25] At the hydrolysis stages of the Sulfate Process it is usual to add seed solution, consisting of a suspension of TiO_2 particles that can alter the size and shape of the titanium dioxide particles that are produced.[26] Dopants can also be added during the process to affect the size of the particles formed (usually aluminium oxide or zinc oxide).[27] In the final stage of the Sulfate Process the $TiO(OH)_2$ is calcinated at 1000 ˚C in a rotary kiln, to produce TiO_2 of the correct particle size and distribution.

The Sulfate Process is technically the simpler of the two, and has a far cheaper feedstock, however it has several drawbacks. The sulfuric acid must be recycled which is difficult, or neutralized, which is costly.[25] Also there is the environmental issue of disposing of large amounts of highly acidic waste product. Since the innovation of the Chloride Process, the Sulfate process has been in a state of decline.[3]

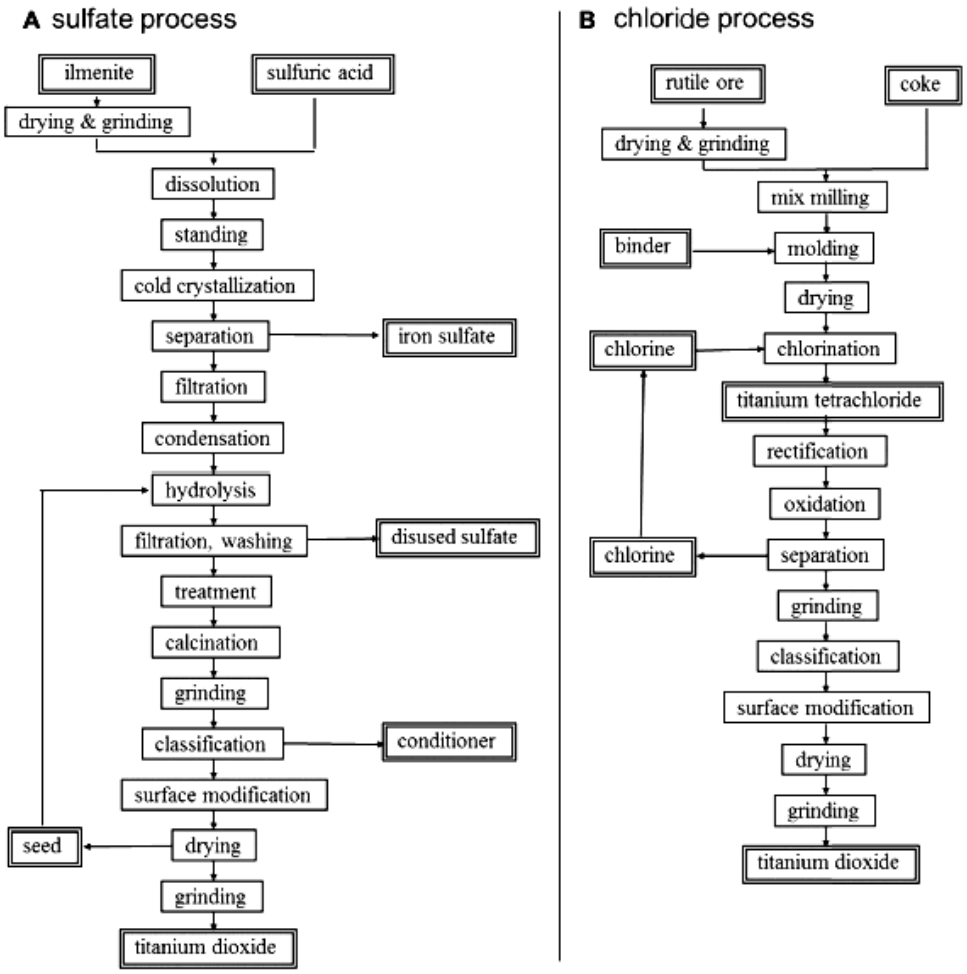

Figure 4: Simplified schematic representations of the Sulfate and Chloride Processes.[28] In the Chloride Process, all of the chemical purification takes place between the 'chlorination' and 'oxidation' steps.

1.3.2. The Chloride Process

The Chloride Process was first developed in the 1950s by Dupont as an alternative to the Sulfate process (Figure 4B). It involves taking impure TiO_2 ore and converting it to titanium tetrachloride. Impurities are then removed *via* condensation and distillation, following which the titanium tetrachloride is reverted back to TiO_2 (Figure 5). This is the process employed by Tioxide and is thus investigated in this project. The process itself can be separated into 6 stages as described below and is shown in Figure 6.[29]

i) *Chlorination:* The ore is fed into the chlorinator with chlorine gas and coke. The chlorinator acts as a pressure vessel, with the reactants heated to 900 - 1100 ˚C. This leads to the following chlorination reaction:

$$TiO_{2(s)} + 3/2\ C_{(s)} + 2\ Cl_{2(g)} \rightarrow TiCl_{4(g)} + CO_{(g)} + ½\ CO_{2(g)}$$

The coke is added in order to facilitate the chlorination of the metal by acting as a reducing agent, forming CO, which extracts oxygen from the TiO_2, increasing the rate of the chlorination.[3] This stage also leads to the chlorination of all of the metal oxide impurities in the ore, most prominently:

$$2\ VO_{2(s)} + 3\ Cl_{2(g)} \rightarrow 2\ VOCl_{3(g)} + O_2$$

$$2\ Fe_2O_{3(s)} + 6\ Cl_{2(g)} \rightarrow 4\ FeCl_{3(g)} + 3\ O_2$$

$$2\ Al_2O_{3(s)} + 3\ Cl_{2(g)} \rightarrow 2\ AlCl_{3(g)} + 3\ O_2$$

$$SiO_{2(s)} + 2\ Cl_{2(g)} \rightarrow SiCl_{4(g)} + 2\ O_2$$

Although not shown in the above equations, the coke functions a reducing agent in all of the above reactions in addition to the chlorination of TiO_2. These are all carried through to the quench tower with the $TiCl_4$ and the carbon dioxide.

ii) *Removal of Solid Impurities*: when the gaseous chlorides exit the chlorinator they are met with a stream of liquid $TiCl_4$ from further along the process which cools the gas from 1000 ˚C to below 230 ˚C. The lower temperature causes many of the chloride impurities, most importantly $FeCl_2$ to condense out of the gas stream as solids. The stream of metal chloride gaseous material is pushed with nitrogen through a dirt cyclone (a cooled pipe with sloped

walls that forces the gas into a cyclone that pushed the solid into the walls *via* centrifugal force). The tangential angle causes the solid to fall along the walls into a 'dirt handling' tank where the waste is neutralized, whilst the lower boiling chlorides including $TiCl_4$ exit through the top of the cyclone, still in their gaseous form.

iii) Gas Cleaning: At this point, the only remaining chlorides in the $TiCl_4$ gas stream should be $SiCl_4$, $VOCl_3$ and $AlCl_3$. These are problematic to remove due to their having similar boiling points to $TiCl_4$. The gas cleaning tower enables the removal of the $VOCl_3$ by injection of a small amount of mineral or vegetable oil, which complexes to the $VOCl_3$.[30] This leads to an increase in the boiling point of $VOCl_3$ enabling it to be removed *via* distillation.[31] The gas cleaning tower also injects a small amount of water and sometimes sodium chloride into the gaseous $TiCl_4$ flow. This is thought to to remove the $AlCl_3$ by converting it to AlOCl which is insoluble in $TiCl_4$.[32] The reaction is believed to take place in two stages, with a titanium oxychloride intermediate that facilitates the oxidation of the aluminium, as shown below.[33] The small amount of water added leads to partial oxidation of the $TiCl_4$ to $TiOCl_2$, which exists as a highly unstable coordination complex that rapidly reacts with the $AlCl_3$ due to the entropically favourable products. [34]

$$TiCl_{4(g)(excess)} + H_2O_{(g)} \rightarrow TiOCl_2.2HCl_{(l)}$$

$$TiOCl_2.2HCl_{(l)} + AlCl_{3(l)} \rightarrow TiCl_{4(g)} + AlOCl_{(s)} + HCl_{(g)}$$

The injection of water takes place in the gaseous phase. The high temperature in the tower (230 ˚C) leads to corrosion by the hot acid produced. Furthermore, to ensure complete $AlCl_3$ removal an excess of water to $AlCl_3$ is required, meaning that some $TiOCl_2$ remains after this stage, however it is recycled and converted back into $TiCl_4$ minimising loss.

iv) Condensation: The condensation of the $TiCl_4$ takes place in two columns. The primary column cools the gas flow with a stream of liquid $TiCl_4$, pumped through the system and cooled with a spiral heat exchanger. The majority of the $TiCl_4$ is condensed in this column (around 95%). Any uncondensed gas moves through to a second condenser, which refrigerates the stream to -12 ˚C causing the remaining $TiCl_4$ to condense and impurities that are less soluble in the $TiCl_4$ to crash out as solid.

v) Distillation: This stage is a simple distillation of the liquid $TiCl_4$ to remove remaining impurities, mostly the oil added during the gas cleaning phase, combined with the vanadium containing impurities. The liquid is fed through to a tank that is heated using a calandria. A calandria is a thermosiphon boiler that heats a flow of liquid *via* thermal transfer from a series of tubes heated with high pressure steam.[35] The $TiCl_4$ exits that calandria as a mixture of boiling liquid and vapour. It is then circulated back into the distillation column where the gaseous $TiCl_4$ rises to the top of the column. The 'pure' $TiCl_4$ gas stream is then condensed and either moved into storage tanks or straight to the furnace for oxidation.

vi) Oxidation: The final stage of purification is the oxidation of the $TiCl_4$ back to its original form. The resulting TiO_2 pigment is rutile. The liquid $TiCl_4$ is heated using a furnace to 350 ˚C becoming a vapour. The vapour is fed into a reactor and mixed with a flow of oxygen. The oxygen is typically heated to a far higher temperature than the $TiCl_4$, usually 900-1000 ˚C.[36] This ensures that the reaction initiates and goes to completion as it cools. The resulting powder is ground to a specific particle size and coated in order to produce a specific pigment type, Further treatment allows specific products such as the Deltio® Freeflow TiO_2 pigment which is treated in order to make it flow more easily, leading to a higher throughput, minimising dust.[37]

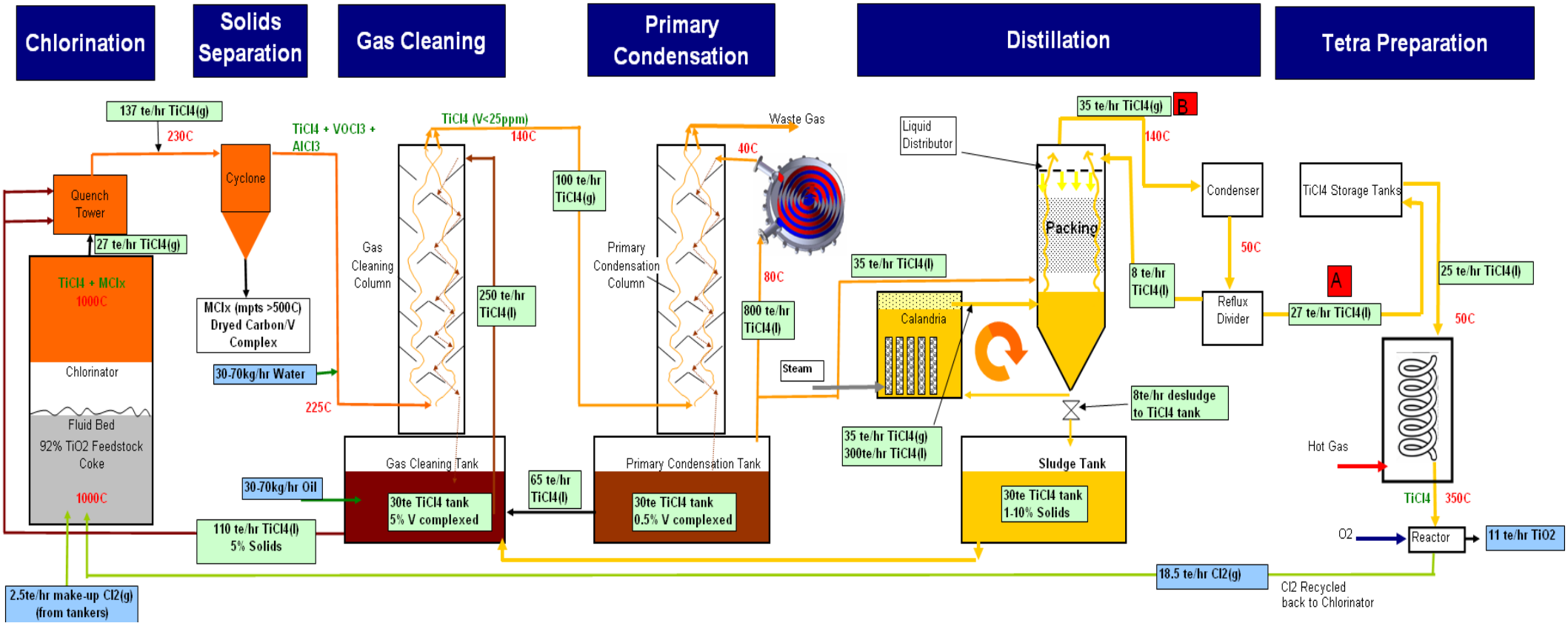

Figure 5: Schematic Diagram of the Chloride process, as used in the Tioxide facility in Greatham[33]

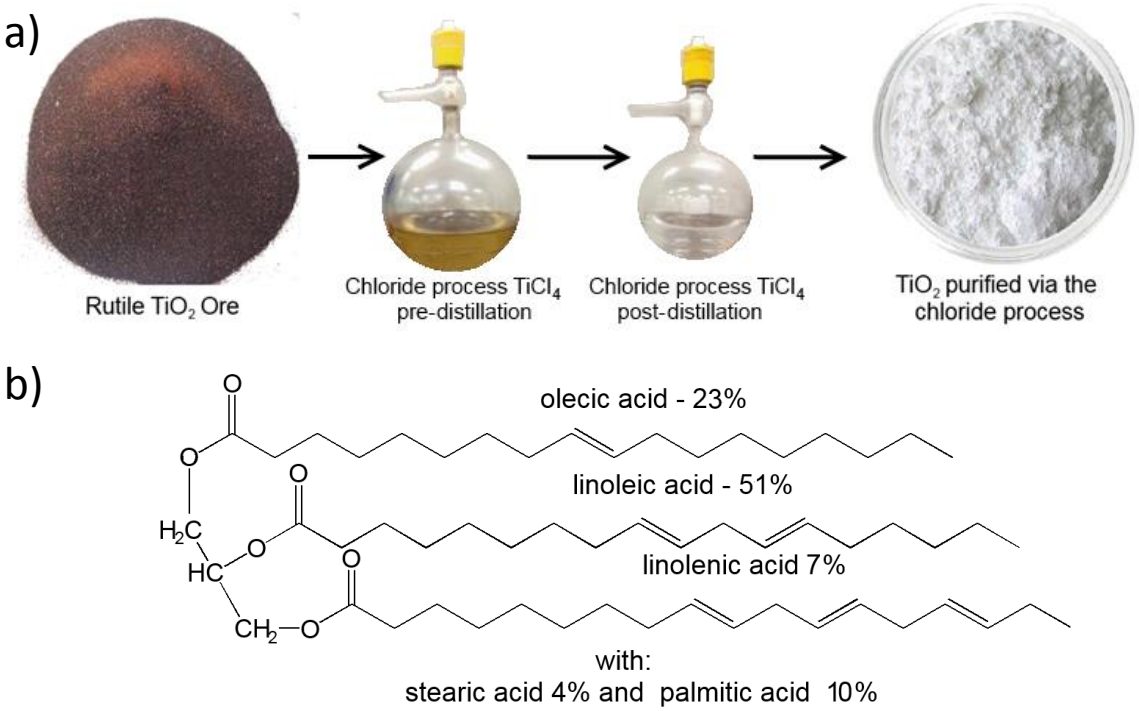

Figure 6: a)Rutile TiO_2 ore before[38] and after[39] the purification *via* the Chloride Process, as well as the intermediate $TiCl_4$ samples before and after purification. b) The structure of the vegetable oil,[40] used to separate the vanadium oxychloride that gives the intermediate $TiCl_4$ its yellow colouring.

1.3.3. Issues with the Chloride Process

Although the Chloride Process is considered less problematic than the Sulfate Process in terms of environmental damage, the lengthier process, as well as the aggressive nature of the chlorides formed, can lead to several issues with production[41] These problems can lead to plant down time, at a cost of approximately £300,000 per day

i) Vanadium Carryover: When not enough oil is injected into the system, the vanadium oxytrichloride is not fully removed from the $TiCl_4$ before oxidation to TiO_2. This causes the resulting pigment to appear yellow. This product cannot be sold and is disposed of into landfill at high cost. $TiCl_4$ appears yellow at $VOCl_3$ concentrations greater than 5 ppm, although most processes aim for closer to 1-2 ppm. Addition of too much oil, however, can lead to fouling of

components further along the process. Much of the research relating to the Chloride Process involves researching the oils used and how vanadium can be removed more effectively.

Figure 7: Collected black residue in the furnace, following cleaning.

ii) Fouling of Plant Components: Many of the components in the process have their life cycles cut very short due to the build up of material on their surfaces, which damages their effectiveness (Figure 7). The three main areas where fouling is an issue are the spiral heat exchangers in the gas cleaning section, the calandria in the distillation tower and the furnace in which The $TiCl_4$ is heated before oxidation. The coating appears to be black, however due to the air sensitive nature of $TiCl_4$ and the enclosed nature of the components, the only way to make it safe to collect a sample is to completely hydrolyse it, which would in turn greatly diminish the value of any compositional data collected.

iii) Tetra Sample Aging: Throughout the process, samples of the liquid $TiCl_4$ known as 'tetra' can be tapped off, from the gas cleaning, primary condensate and post distillation points. This is an excellent way of determining where exactly a problem might be if the TiO_2 produced were to look 'dirtier' than it otherwise should. It can also be a useful selling point for the process, to observe the quality of the product. Generally speaking the tetra should be

as clear and colourless as possible, becoming more so, the further along the process, as more of the impurities are removed. It has been observed that over time the samples taken from the process at all points seem to 'age'. This is seen in a gradual discolouration of the liquid, going from colourless to yellow. This is observed in many samples of $TiCl_4$, including those bought commercially from firms such as Sigma Aldrich. The samples from Huntsmanare also observed to precipitate a black solid over a period of weeks.

iv) Packing of the Distillation Column: When $TiCl_4$ is industrially distilled, it is common to pack the column with glass. This is thought to increase the surface area of the passage that the gaseous $TiCl_4$ has to navigate and 'catch' some of the lower boiling impurities that would otherwise make it through the column. The packing has to be replaced at least once a year, resulting in costly downtime and there has been some debate as to how much a role in the separation of the impurities the column packing actually plays. One of the distillation studies carried out in this work was repeated with and without a vertical column packed with glass beads in order to determine how much a difference their presence makes.

1.4. Titanium(IV) Tetrachloride

For the vast majority of the Chloride Process the titanium is present in the form of titanium(IV) tetrachloride. This is a wellstudied compound due to its unusual properties and high reactivity. $TiCl_4$ is one of only three transition metal halides that is a liquid at room temperature (the others are VCl_4 and $SnCl_4$). This is because whilst most metal halides form polymeric octahedral species such as the edge sharing octahedral structure of $ZrCl_4$,[42] titanium tetrachloride is a tetrahedral monomeric species due to the relatively high enthalpy of the Ti-Cl bond (494 $kJmol^{-1}$)[43] and lewis acidic nature of the compound making it more

stable than the equivalent edge sharing lattice Infrared spectroscopy shows the Ti-Cl bond to have a length of 2.185 Å,[44] which has been verified computationally.[45]

Titanium(IV) tetrachloride's strong Lewis acid character is responsible for the majority of its uses. It is the starting point for the synthesis of a number of titanium complexes in inorganic synthesis and has been used in the formation of novel CVD precursors, such as titanium(IV) arsenide complexes.[46,47] $TiCl_4$ itself is also frequently used in chemical vapour deposition, usually in the deposition of TiO_2 nanostructures,[48] however it has also been used in combinatorial CVD in the formation of titanium oxynitrides.[49]

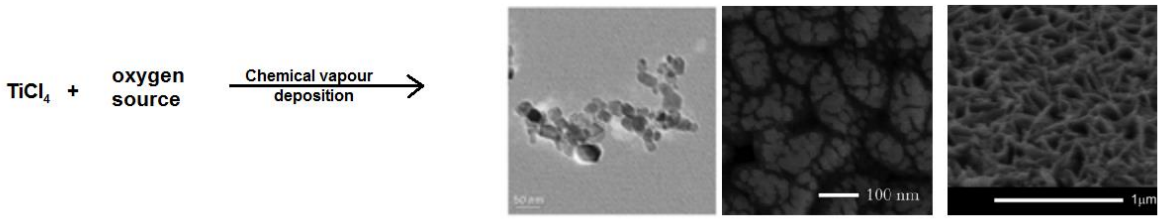

Figure 8: Different morphologies of TiO_2/composites that have been deposited from $TiCl_4$ using CVD

In organic chemistry it is frequently used in coupling reactions, such as the condensation reaction of alcohols and aromatics and aldol coupling reactions, for instance the Mukaiyama aldol coupling which traps the enolate by forming a silyl enol ether.[50]

By far the most well known use of titanium tetrachloride is that of Ziegler Natta catalysis, a specific class of heterogeneous catalysts that are used in the polymerization of alkenes. They typically involve a transition metal halide, usually $TiCl_4$ with an alkyl metal co-catalyst ($AlEt_3$). The resulting polymers are noted for their high linearity and taticity.[51] [52] Zeigler And Natta both separately proposed a mechanism for the polymerization involving the propagation of free radicals, however this does not explain the high level of steroselectivity.[53,54,55]

. Difficulty arises when investigating titanium tetrachloride due to the highly Lewis acidic nature of the $TiCl_4$ centre. The moisture sensitive nature of $TiCl_4$ results in a hydrolysis reaction.[56]

$$TiCl_4(l) + 2H_2O(g) \rightarrow TiO_2(s) + 4HCl(g)$$

This makes analysis of samples of $TiCl_4$ and its use in synthesis challenging and requires a moisture free atmosphere, necessitating the use of Schlenk techniques. This was a challenge that had to be overcome in the first part of this project, which required characterizing a large number of samples of $TiCl_4$ taken directly from the industrial process in order to identify the impurities that were carried through the different stages of the Chloride Process.

Chapter 2

Analysis of Samples from Industrial TiO_2 Production

This section details work done in relation to improving the understanding of the Chloride Process, by analysing various samples sent from the Greatham TiO_2 production facility in order to identify potential impurities within the samples that could lead to downtime or discolouration of the product further down the production process. These samples consisted of liquid $TiCl_4$ samples which were analysed using NMR spectroscopy and black solid precipitates that forms within these samples over time, which was separated from the $TiCl_4$, oxidised and identified using various analytical techniques.

2.1. NMR study of Industrial $TiCl_4$ Samples

Initial experiments largely consisted of developing a means of reliably creating NMR samples of $TiCl_4$ samples and then investigating the products present in different fractions from the distillation of those samples.

2.1.1. Experimental

2.1.1.1. Making an NMR sample

NMR spectra were obtained for a number of $TiCl_4$ samples collected from the Chloride process at different points and different times. The highly air sensitive nature of the samples meant that they had to be made up under an atmosphere of nitrogen using Schlenk techniques. This was achieved using the apparatus displayed in Figure 9.

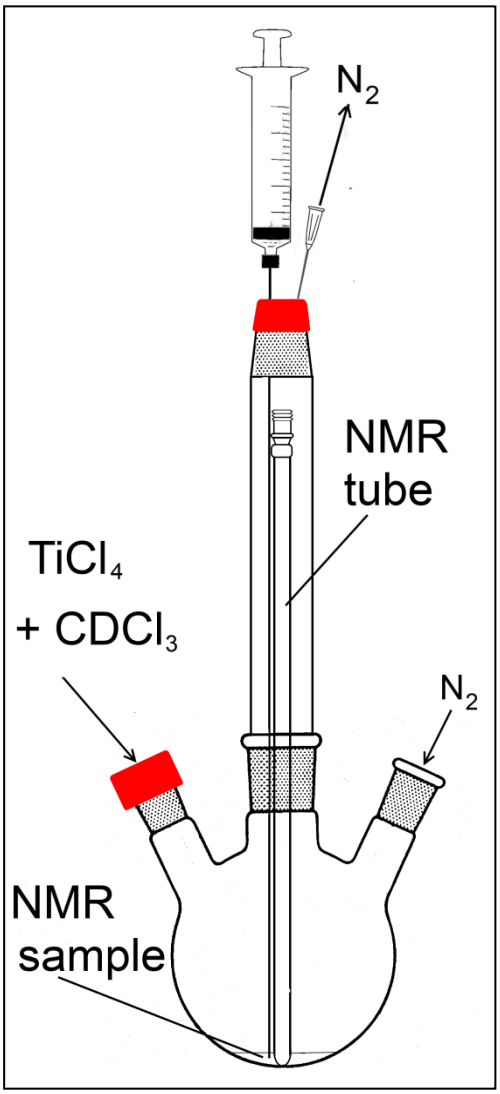

Figure 9: apparatus used to collect NMR samples of $TiCl_4$

Experiment	Sample	Point in Process	Year
Initial Study	1	Primary condensate	2012
	2	Plant distilled	2012
	3	Primary condensate (lab distilled)	2012
Sample Aging	4	Primary condensate	2013 (new)
	5	Primary condensate	2011 (2 yrs old)
	6	Plant distilled	2013 (new)
	7	Plant distilled	2011 (2 yrs old)
Fractional Distillation of Primary Condensate	8	Primary condensate 1st 20 ml (packed)	2013 (new)
	9	Primary condensate 2nd 60 ml (packed)	2013 (new)
	10	Primary condensate 3rd 20 ml (packed)	2013 (new)
	11	Primary condensate 1st 20 ml (packed)	2013 (new)
	12	Primary condensate 2nd 60 ml (packed)	2013 (new)
	13	Primary condensate 3rd 20 ml (packed)	2013 (new)

Table 1: Complete list of industrial $TiCl_4$ samples analysed

The sample was made by using a canula to move 3 drops of the $TiCl_4$ into a three necked round bottom flask, under a flow of nitrogen. The flask was equipped with an elongated neck piece, capped with a subaseal and a release needle, with a screw-top NMR tube inside.

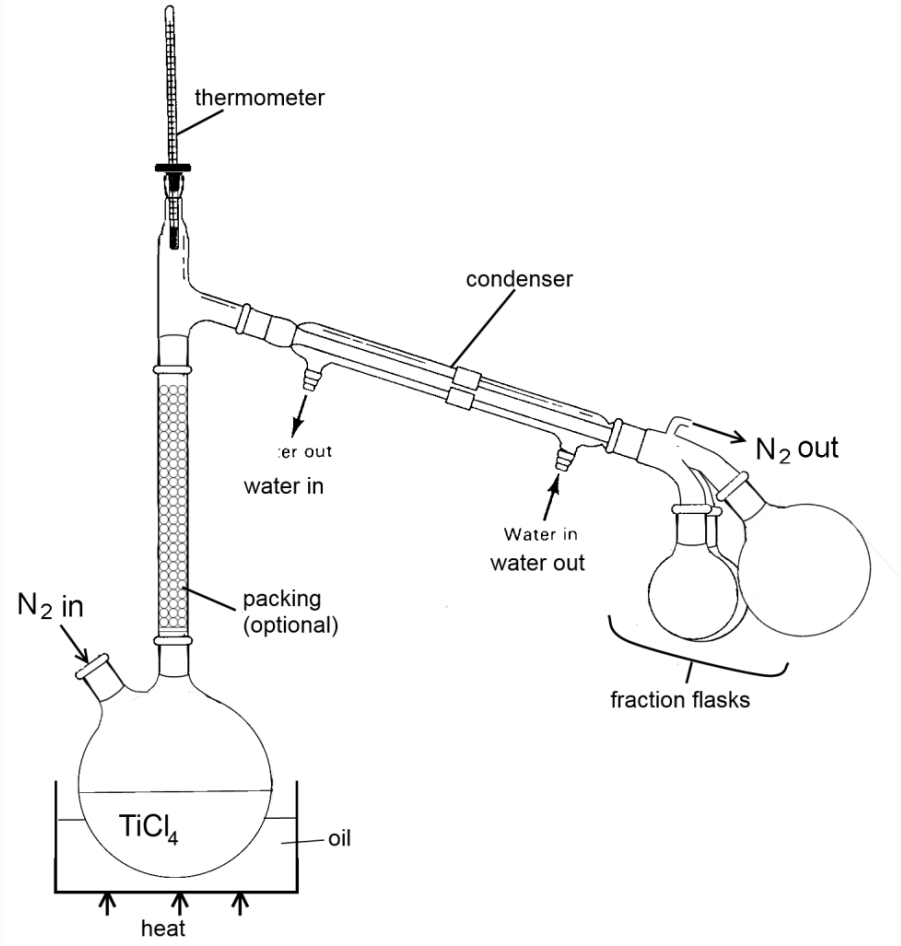

Figure 10: Schematic of $TiCl_4$ distillation with packed column

To the $TiCl_4$, 2 ml of $CDCl_3$ (Sigma Aldrich, 99.8 atom% D, anhydrous, dried over activated molecular sieves) was injected into the flask through a side arm using a plastic syringe and deposable needle. The solution was then taken into a second syringe *via* a needle through the top subaseal, before being injected directly into the NMR tube. The tube was then screwed shut under a flow of nitrogen and removed. Samples were collected in this manner for primary condensate, plant distilled and laboratory distilled $TiCl_4$, as well as the distilled fractions of plant distilled and non-distilled $TiCl_4$.

2.1.1.2. Distilling Titanium Chloride Samples

Two distillations were carried out following the collection of the initial NMR data: one for the $TiCl_4$ that had passed through the distillation column at the site in Greatham and one that had

not. In each case an air sensitive distillation was carried out by heating a 110 ml sample of $TiCl_4$ in a two necked round bottom flask to 120 ˚C using an isomantle, under a flow of nitrogen (Figure 10). The gaseous $TiCl_4$ and volatile impurities passed up a 10 cm column into a cold water condenser.

At the bottom of the condenser was a three pronged distillation receiver, with two 25 ml flasks and one 100 ml flask. These are marked at the 20 ml and 60 ml levels respectively. Upon filling the first flask to 20 ml the join was turned allowing the second to fill to 60 ml and finally the third to 20 ml. The flasks were then stoppered and NMR samples immediately made up (*vide infra)*.

2.1.2. Results and Discussion

2.1.2.1. Initial Study

NMRs taken were from the primary condensate and the distilled portion of the plant (Figure 9). Another sample was made by distilling the primary condensate in the lab under nitrogen. The samples used were all over one year old and were highly discoloured with black precipitate in all except for the lab distilled primary condensate.

The spectra showed several collections of peaks that can be divided into three categories according to how their relative intensity and therefore the concentration of the source molecule can be reduced by distilling the sample: (a) those removable by plant or lab distillation (b), those removable by lab distillation only and (c) those not removable by either plant or lab distillation.

a) The peaks removed by plant distillation have chemical shifts between 0.8 and 1.5 ppm. Although these peaks were dramatically reduced by distillation, they appear

in all three spectra. They are likely the result of the oil breaking down into alkyl species that boil lower than $TiCl_4$

b) The peaks that can be removed by laboratory distillation fall between 0.4 and 0.6 ppm. These are likely caused by silane compounds present in the material. These occur as a result of SiCl4 reacting with the oil species.

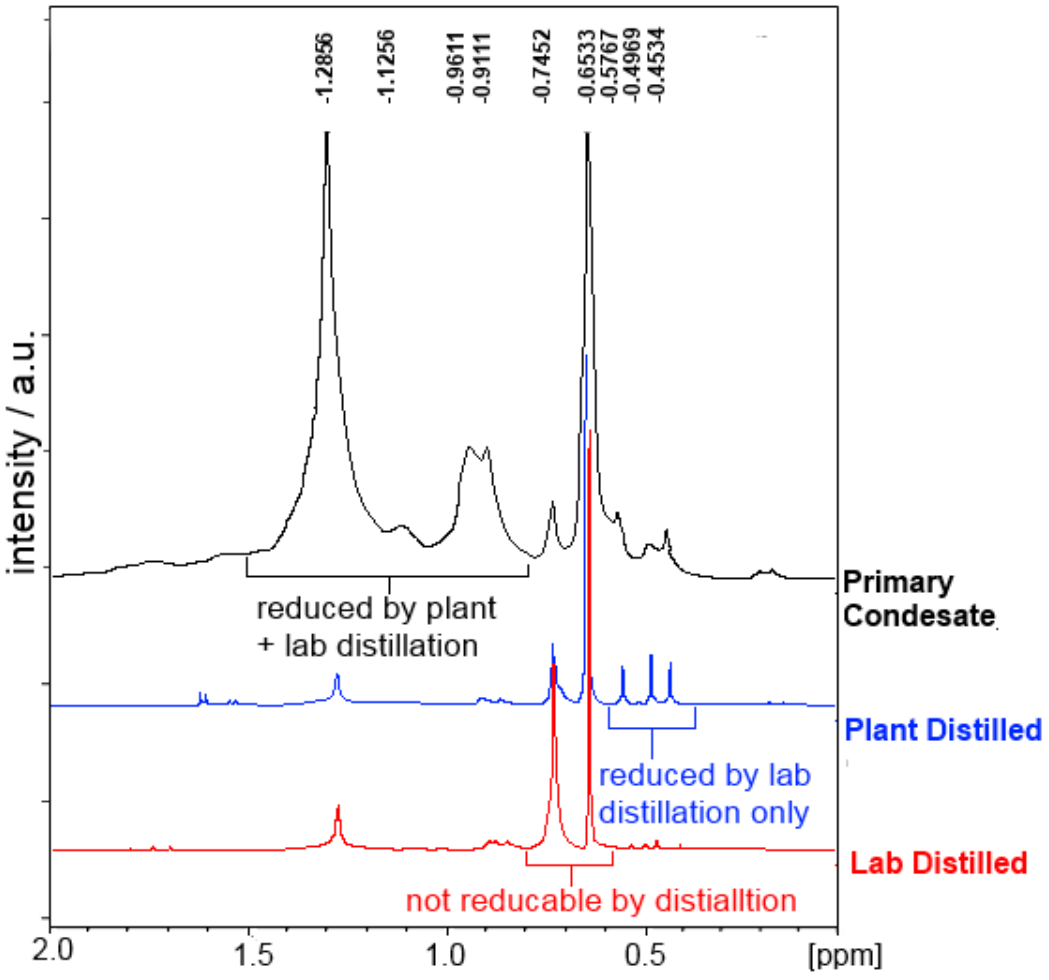

Figure 11: Comparison of the ^{1}H NMR spectra of primary $TiCl_4$ undistilled (black), plant distilled at Greatham (blue) and laboratory distilled (red)

c) The relative intensity of peaks at 0.65 ppm and 0.75 ppm were increased by the distillation process, indicating that they were not affected by distillation as removal of other impurities would lead to an increase in their relative concentration.

Due to the large number of species present it would be impossible to reliably define the peak integrals and very difficult to ascertain exact structures of the species present. Interestingly, none of the unbroadened peaks in the spectra display any coupling, suggesting a number of methyl species. On the other hand, some of the peaks appeared rather broad in some instances, which may mask coupling

2.1.2.2. Comparison of Recent and Older $TiCl_4$ Samples

Following the initial testing, 'fresh' $TiCl_4$ samples were obtained from Huntsman. Samples were once again taken from the primary condensation, and post-distillation parts of the process. NMR spectra were taken of each sample and compared with the equivalent 15 month old samples (Figures 12 + 13).

All samples saw a dramatic increase in the number and relative intensity of the 'silane peaks' between 0.0 ppm and 0.7 ppm in the newer samples over the equivalent older one. The only exception to this was the two peaks at 0.64 ppm and 0.73 ppm, both of which were far more prominent in the older samples. There are a number of possible reasons for this occurrence. It is probable that the silane species react slowly over time within the $TiCl_4$ samples, resulting in the observed difference in peak patterns. This study cannot confirm this however as the samples were taken from the plant at different points in time meaning that the different patterns could be due to a change in the manufacturing process or the starting material. The firm were unable to confirm this. To confirm that there is a slow reaction within the $TiCl_4$ samples, NMR spectra were collected of several samples two months after they arrived. The spectra collected show changes in the peak patterns.

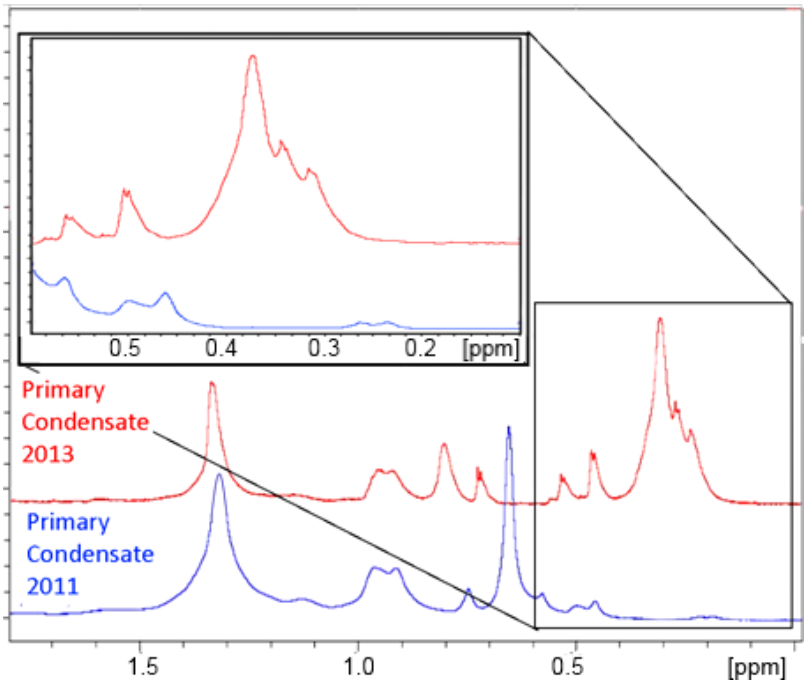

Figure 12: ^{1}H NMR spectra of Primary $TiCl_4$ samples produced approximately 15 months apart, with the shifts between 0.6 and 0.0 ppm enhanced (inset).

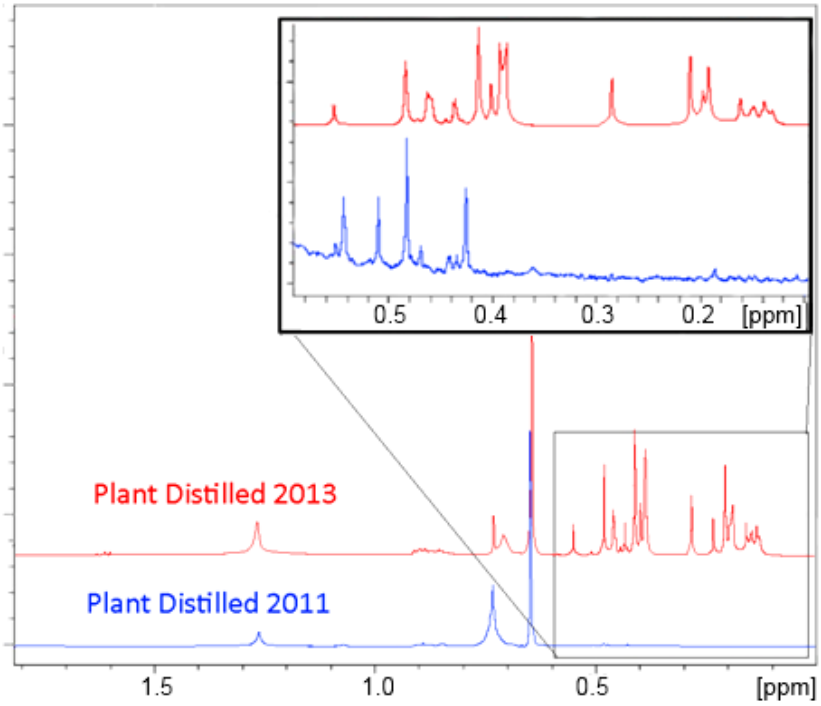

Figure 13: ^{1}H NMR spectra of Plant distilled $TiCl_4$ samples produced approximately 15 months apart, with the shifts between 0.6 and 0.0 ppm enhanced (inset), with the 2011 sample enhanced in order to see much less abundant peaks that are near the baseline.

2.1.2.3. Lab-distilled Primary Titanium Tetrachloride Samples

With the study of samples taken directly from the plant complete, the next step was to simulate the distillation part of the column in the laboratory setting. 110 ml samples of primary tetra were distilled at 140 ˚C, with three samples collected from each: a) The first 20 ml to distil over, b) The following 60 ml of distillate, c) The final 20 ml. NMR spectra were obtained from all three fractions (Figure 14) . The experiment was repeated, with the column packed with 6 mm diameter glass beads, to emulate the packing in one of the distillation columns at the Greatham plant (Figure 15).

2.1.2.3a. The First 20 ml of Distillate

The first fraction showed a large amount of peak broadening not seen in the other two. This implies that some paramagnetic species with low boiling points were brought over early in the distillation, mostly likely a vanadyl species vanadium (IV) (although it should be noted that both samples were colourless when tested, so the concentration of vanadyl species would be below 5 ppm). The majority of peaks seen were downfield from 0.7 ppm, which is indicative of methylsilyl species. The packed column's distillate was observed to give a less broadened spectrum, implying that the packing may be able to retard distillation of $VOCl_3$.

2.1.2.3b. The Second 60 ml of Distillate

The spectra appeared similar to the first 20 ml although far less broadened. This suggests that all of the paramagnetic species have already distilled over and are therefore all lower boiling than the $TiCl_4$ itself. The vanadium is likely causing a broadening through weak, labile coordinating to some of the molecules of the alkyl species distilling over.

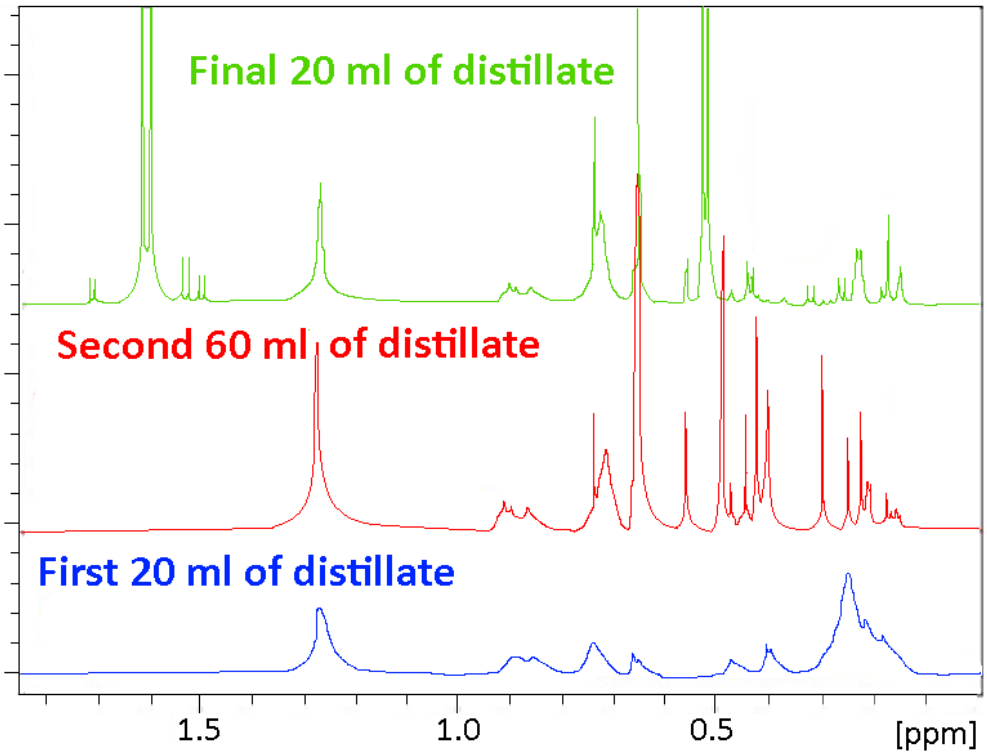

Figure 14: ^{1}H NMR spectra of all three fractions of Distilled Primary $TiCl_4$ using an unpacked column

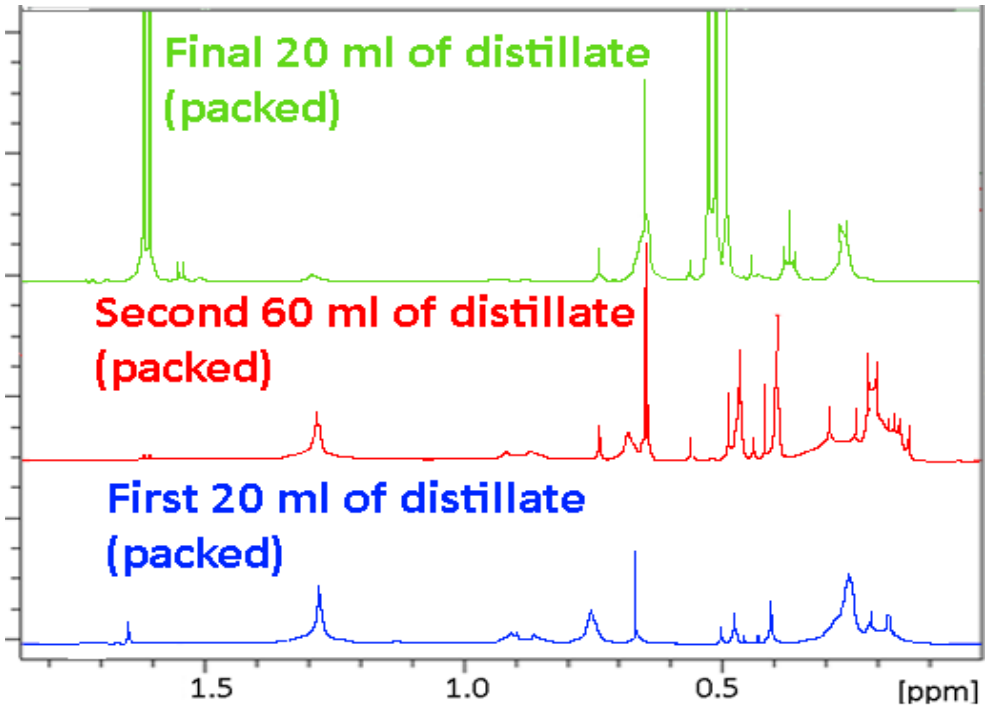

Figure 15: ^{1}H NMR spectra of all three fractions of Distilled Primary $TiCl_4$ using a packed column

There were no discernible differences between the two peak patterns for the packed and unpacked column however there are differences in the relative intensities of some of these peaks. A set of peaks between 0.38 ppm and 0.49 ppm, appears to consist of two related pairs of peaks, at 0.42 and 0.49 ppm and 0.39 and 0.47 ppm (Figure 16).

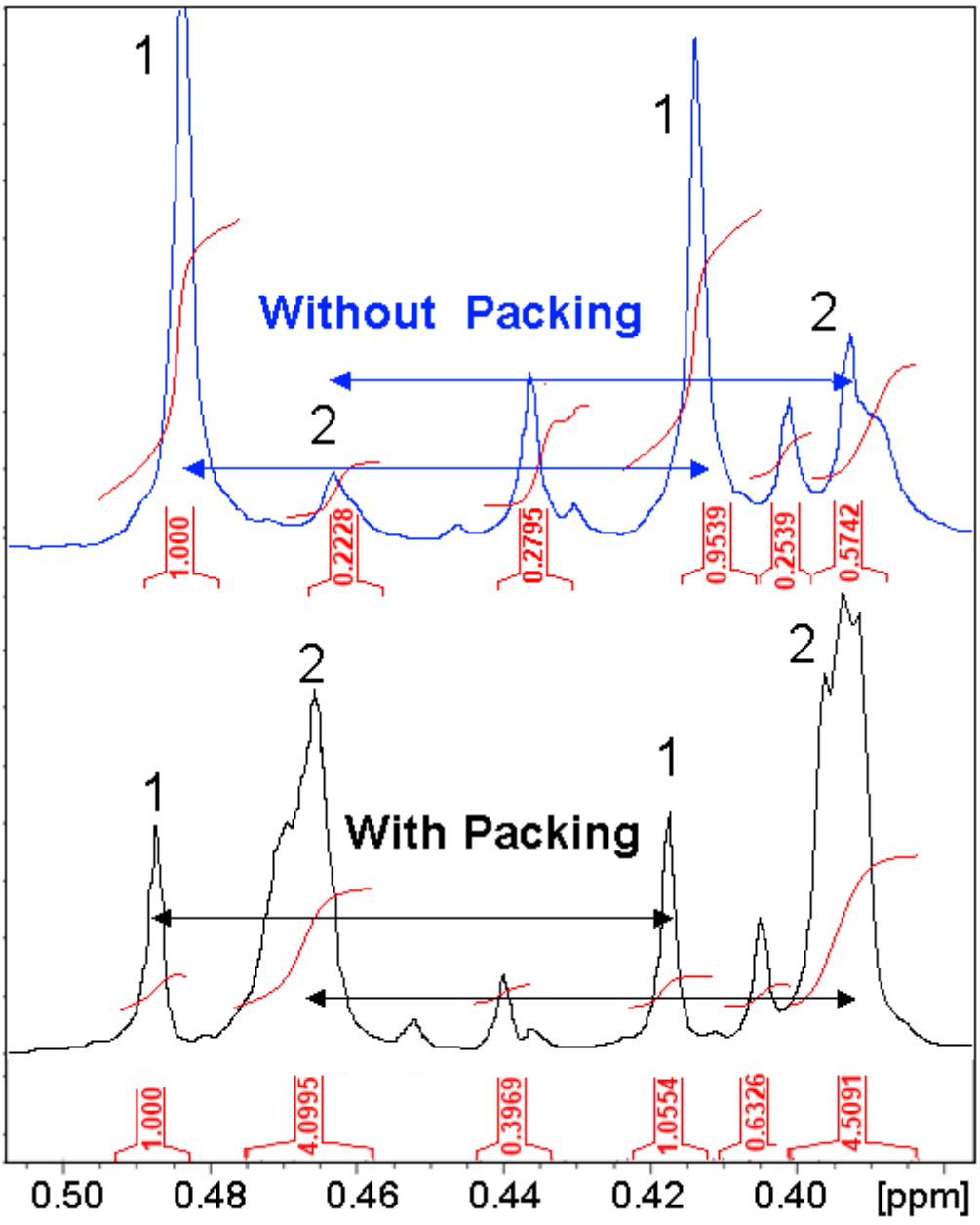

Figure 16: Comparison of ^{1}H NMR peak pattern thought to relate to siloxane rings, distilled primary (second fraction) in packed and unpacked distillation columns

It is possible that the peaks relate to the same group in the axial and equatorial positions on a siloxane ring. A study by Pelletier et al. showed similar patterns with methyl and hydrogen substituted cyclosiloxanes.[57]

The intensities of these peaks in relation to each other remain roughly the same over the two spectra, increasing and diminishing by the same amount. Pair 1 is two singlets, whereas the other pair appears as two multiplets, with a small coupling constant. The difference in the shifts between these two 'pairs' peaks is too great to be down to J-coupling.

2.1.2.3c. The Third 20 ml of Distillate

Rather than the multitude of singlets seen in the earlier samples, the majority of the peak patterns in the final distillate showed splitting, especially the more upfield peaks. This is expected as these patterns likely relate to larger alkyl groups, whereas before they related to smaller methyl species. These groups would be heavier and therefore would distil over after the methyl species. Further downfield there are two shifts: a doublet at 1.60 ppm and a septet at 5.15 ppm, with an integral ratio of 6:1. This pattern resembles the well known pattern of isopropyl alcohol.[58] Figure 17 is an enhanced image of these two environments. The septet for the central carbon's proton is shifted further downfield, indicating the presence of an ester or acyl-chloride group. This pattern is by far the most prominent in the spectra and is likely a product of the breakdown of the soya oil at high temperatures. Samples of plant distilled $TiCl_4$ do not feature this pattern at all. Therefore it can be inferred that the final fraction is likely to bear the least resemblance to the actual distilled product of the three studied.

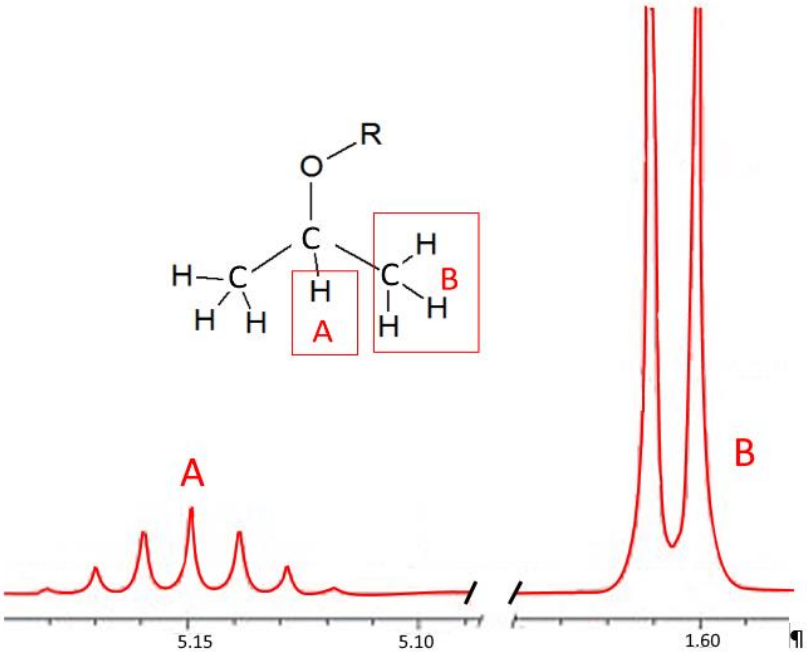

Figure 17: Shifts present in the ^{1}H NMR spectra of the final fractions of Distilled Primary $TiCl_4$ indicating the present of an Isopropyl group, attached to an electron withdrawing group

2.1.2.4. Investigation of Aging in Distilled Fractions

Inspection of the fractionated products two months after the initial study was carried out revealed a surprising result. The first and third fractions in both cases turned from colourless to dark yellow as expected, however the middle fractions remained relatively colourless. All samples were stored in the same type of container so this difference is not environmental. The implication of this is that there are multiple species within the distilled tetra that lead to the discolouration/precipitation. Retaking the ^{1}H NMR spectra of the first and second fractions from the packed column indicated that this could be a result of reactions of the silane compounds. The broad hump in the ^{1}H NMR of the first fraction is no longer present, and the intensities peaks from 0.4 - 0.5ppm have altered relative to each other. The spectra are compared in Figure 18. The emergence of doublets with a shift of 1.5 - 1.7 ppm is also observed, however it is possible that this is due to the breakdown of the

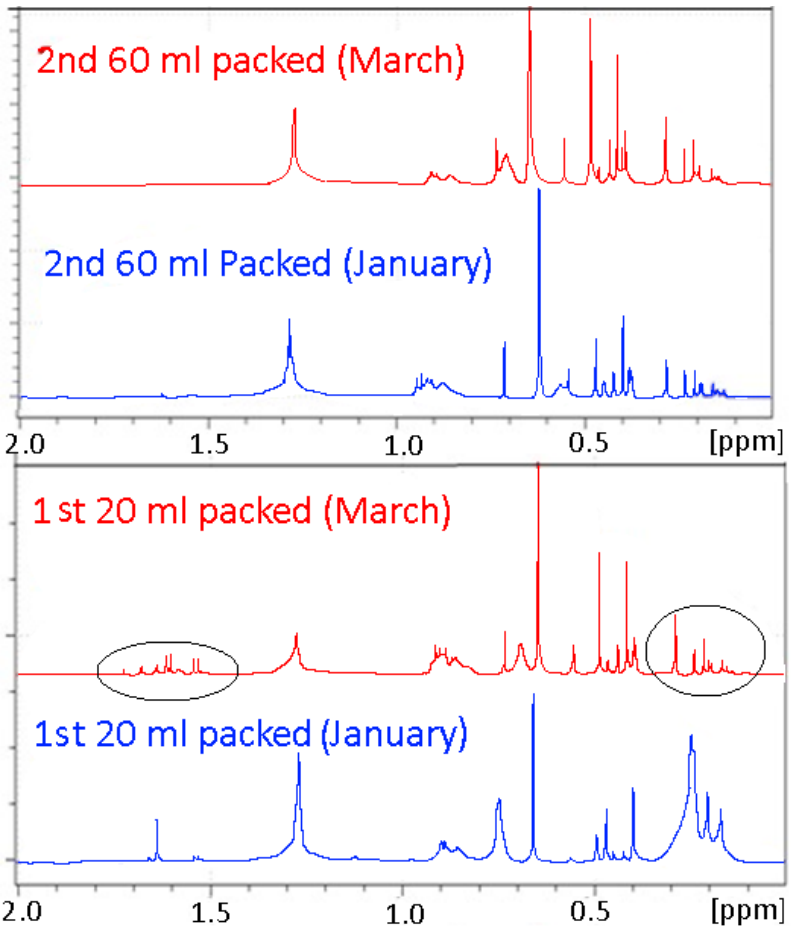

Figure 18: ^{1}H NMR spectra of the first and second fractions of distillate collected from distilling 110 ml of $TiCl_4$, using a packed column, collected two months apart

syringe used to make up the ^{1}H NMR sample. Conversely, the ^{1}H NMR spectra of the second fraction, which had remained colourless, were almost identical, with both peak patterns and integrals unchanged. It should be noted that for the sake of completeness, ^{13}C NMR were recorded for allsamples, however the higher concentrations of materials required to obtain a signal and the numerous low concentration species present, meant that they possesses very little useful information about the species.

2.1.3. Conclusion

This study of industrial samples of $TiCl_4$ suggests strongly that there are a large number of silicon based impurities within the samples, due to the multitude of peaks in the 0.7 ppm - 0.0 ppm region, which is usually too upfield for alkyl protons without the upfield directing shielding character of the silane coordinated to the carbon. These peaks were largely absent in the oldest samples, which comparatively had relatively simple NMR patterns. There are several possible explanations for this. The silyl compounds with the very downfield shifts could be intermediates that over a long period will react to form a smaller group of more energetically favourable species. Another option is that they gradually form insoluble molecules that are part of the precipitate observed, no longer appearing in the NMR. Finally they could be caused by the use of different starting material, or a change in the process. Components such as the distillation calandria foul quickly and must be replaced or cleaned, so it is possible that the different stages of fouling could affect the contaminants in the $TiCl_4$ samples that are removed.

Whilst the number of shifts present in the NMR makes characterising individual contaminant species impossible, general structures representing groups of silanes can be inferred. The silanes must have a boiling point close to that of $TiCl_4$ itself or it would not make it through distillation. If the species were too high boiling it would be recycled to the sludge tank, too low and it would exit as waste gas. The lack of splitting in the samples suggests relatively small alkyls. This information allows for a few general impurity structures to be proposed.

Methylcyclosiloxanes: This group consists of ring systems of alternating silicon and oxygen, with methyl groups or chlorine bound to the silicon. Hexamethyl cyclosiloxane (Figure 19) has an identical boiling point to $TiCl_4$[59] and a mass spectroscopy study commissioned by

Tioxide found cyclosiloxanes present in samples of the material that fouls the calandria, however the samples used to generate them were completely hydrolysed so it was not possible to say for sure that they were present in the $TiCl_4$ during the process. The peak patterns between 0.3 and 0.5 ppm resemble those of chlorosiloxanes,[60] with the peaks with matching integrals representing different structural isomers of the same ring system. The singlets may represent the hexamethyl material and the triplets the ethyl equivalents which would present themselves as peaks in the 1.0- 1.5 region, as seen in the first 20 ml of the more aged sample.

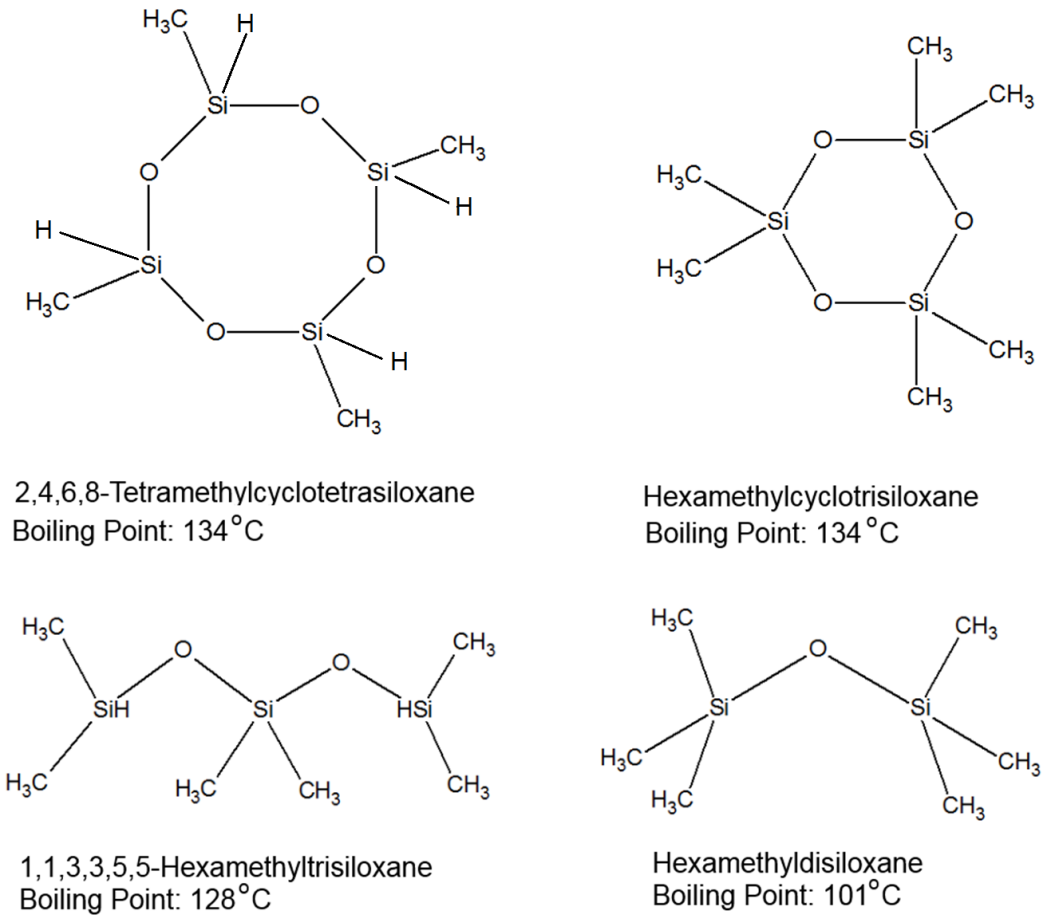

Figure 19: Structures of four potential siloxane species forming within the $TiCl_4$ samples, all with boiling points between 100 and 134 ˚C, and all with ^1H NMR spectra that would only give highly upfield peaks.[61–64]

Methylchlorosilanes: A far wider range of compounds, usually involving a single silicon atom or two silicon atoms bound directly or with a methyl bridge, with methyl/chlorine substituents. These are the most probable source of the very downfield peaks between 0.0 and 0.3 ppm. Many molecules in this group have boiling points similar to that of $TiCl_4$, such as 1-Chloro pentamethyldisilane and dichlorosilyltrimethylsilane, both of which boil at 136˚C.[65,66]

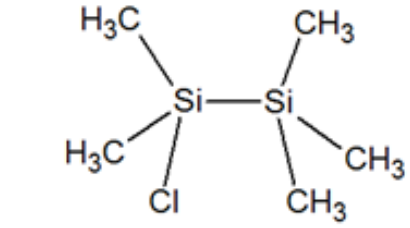

Chloropentamethyl-disilane
Boiling point: 136 °C

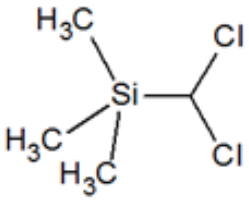

Dichloromethyltrimethylsilane
Boiling Point: 136 °C

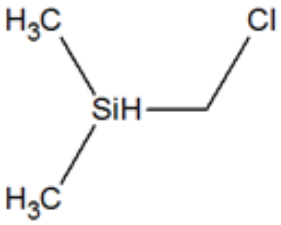

Chloromethyl(dimethyl)silane
Boiling Point: 88 °C

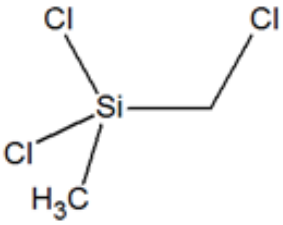

Dichloro(chloromethyl)methylsilane
Boiling Point: 121 °C

Figure 20: Structures of four potential chlorinated methyl silane species forming within the $TiCl_4$ samples, all with boiling points between 80 and 134 ˚C,[65–68] and all with NMR spectra that would only give highly upfield peaks.

In addition to those species, a great number of similar species exist with boiling points lower than 136 ˚C that would likely be found in the first few ml of distillate. These usually resemble a chlorinated version of tetramethylsilane such at Chloromethyl(dimethyl)silane and dichloro(chloromethyl)methylsilane, both shown in Figure 20, which have boiling points of 88 and 121 ˚C respectively.

2.2 Analysis of the Black Precipitate in the Tetra Samples

Each of the samples of $TiCl_4$ was found to precipitate out a black solid over a period of time. This occurred in both industrial samples and the samples bought from chemical suppliers The analysis of the black precipitate found in the stored samples of $TiCl_4$ was carried out primarily in order to discover what it consists of and how it forms. With this information, the aim was to confirm whether or not its formation was related to the discolouration of $TiCl_4$ samples and if it could be analogous to the solids that foul the process components.

The black solid in three samples of $TiCl_4$ were isolated. The samples analyzed were from the primary condensation tank, the distillation step and the third fraction from the lab distillation (with packing). These samples were chosen due to the high volume of black solid present, as well as being representative of some of the problem areas of the plant, for instance the primary tetra would be analogous to what runs through the calandria and the distilled tetra would be similar in content to that which causes fouling of the furnace in the production process. The primary and distilled samples were both eighteen months old at the time of testing and the lab distilled three months old.

2.2.1. Experimental

The tetra samples were stored under air in glass jars. The $TiCl_4$ was removed from the jars as fully as possible, leaving the black solid in the jar. This was done by flushing the jar with nitrogen before removing the majority of the $TiCl_4$ with a filter canula with a separate flask. The remaining solid was then washed by adding 20 ml of hexane, forming a suspension with the precipitate. This was then stirred for one hour whilst heating to 40 ˚C before the hexane was removed into a separate flask *via* a filter canula. This was repeated twice more, with all three of the washings entering into the same flask. Following the washing, each sample was left under vacuum for 6 hours in order to remove any remaining hexane and $TiCl_4$. When the drying process was completed, the jars that had held the distilled and primary tetra held roughly 0.25 g of grey solid and the lab distillation fraction jar held roughly 0.1 g. The samples were then stored under air in the jars they came in.

The samples were analyzed using ^{1}H NMR spectroscopy was carried out using a 600 Hz Bruker Avance 600 Cryo III spectrometer, and X-ray Photoelectron spectroscopy (XPS) carried out using a Thermo Scientific™ K-alpha™ spectrometer, with monochromated Al Kα radiation, a dual beam charge compensation system and constant pass energy of 50 eV. Survey scans were collected in the energy range of 0 – 1200 eV.

Mass Spectra were obtained using chemical ionization with a methane reagent gas with the Finnigan Thermo MAT900xp spectrometer. XPS measurements were carried out on a VG ESCALAB 220i XL instrument using focused (400 lm spot) monochromatic Al Ka radiation at a pass energy of 20 eV. Scans were acquired with steps of 100 meV. EDX analysis was carried out on carbon coated samples on a Philips XL30 ESEM instrument. FT-I*R* spectra were obtained using an FT-IR Shimadzu 8700 spectrometer over a range of 400-3500 cm^{-1}.

2.2.2. Results and Discussion

2.2.2.1. NMR spectroscopy

The black solid was largely insoluble in most NMR solvents. Samples were made by NMR spectra of the black precipitate were obtained by placing a spatula tip full of solid into a small sample tube and shaking with 5 ml of $CDCl_3$ for 30 minutes. Although some solid remained, some appeared to have dissolved. The spectra for all three solid species were extremely similar. The most prominent peak in all three spectra appears at 1.45 ppm. This is similar to the position of the diminished peak in the filtered $TiCl_4$, further implying that the black solid consists at least partially of an alkyl species.

2.2.2.2 Toluene Washings

The samples were washed repeatedly using hexane, however initially it was planned that toluene would be used. In an initial test with an older sample of gas cleaning tetra $TiCl_4$ removal was carried out in the way described above and the material washed three times with dry toluene. It was observed that the solid became much lighter in colour following the washings. Conversely the toluene took on a faint purple grey colour. This suggests that the supposedly black solid impurities are in fact coated in a substance that gives them the black/grey appearance, with a lighter core. As the samples were stored under air rather than nitrogen due to the nature of their containers, it is a reasonable assumption that this could be solid TiO_2 with an organic coating.

2.2.2.3. Mass Spectroscopy

Mass spectrum were obtained for the three solid samples. Appendix 5 shows the mass spectra of the plant distilled solid sample. The spectra all share two notable characteristics. Firstly, the prominent peaks that appear in all three spectra: 391, 338, 279, 167, 149 and 113 *m/z* can all be attributed to the molecule bis 2-ethylhexyl phthalate (Figure 21).[69]

This molecule is a common mass spec impurity due to its use as a plasticizer for materials such as PVC. Plastics can contain between 1 and 40%, bis 2-ethylhexyl phthalate depending on their purpose.[70] The mass spectrum peaks can be assigned to fragments of the molecule. The only exception to this is the peak at 338 *m/z*. This peak is most likely attributable to euracamide,[71] a very common slip agent, added to plastics in order to reduce surface friction and improve slip. It is also a well-known mass spec contaminant. The other important trait to emerge from the mass spectra of the solid is the pattern of peaks every 14 *m/z* up to around 800 *m/z*. Intervals of 14 *m/z* are a strong indicator of long alkyl chains, such as polymers. This is fitting with the broad peak present in the proton NMR, which is similar in position and shape to that of a polyethylene backbone of a polymeric species.[72]

Both of the distilled samples showed this pattern, despite the fact that the distillation process would remove any high molecular weight polymeric species. This implies that they are entering the sample at another point in the process.

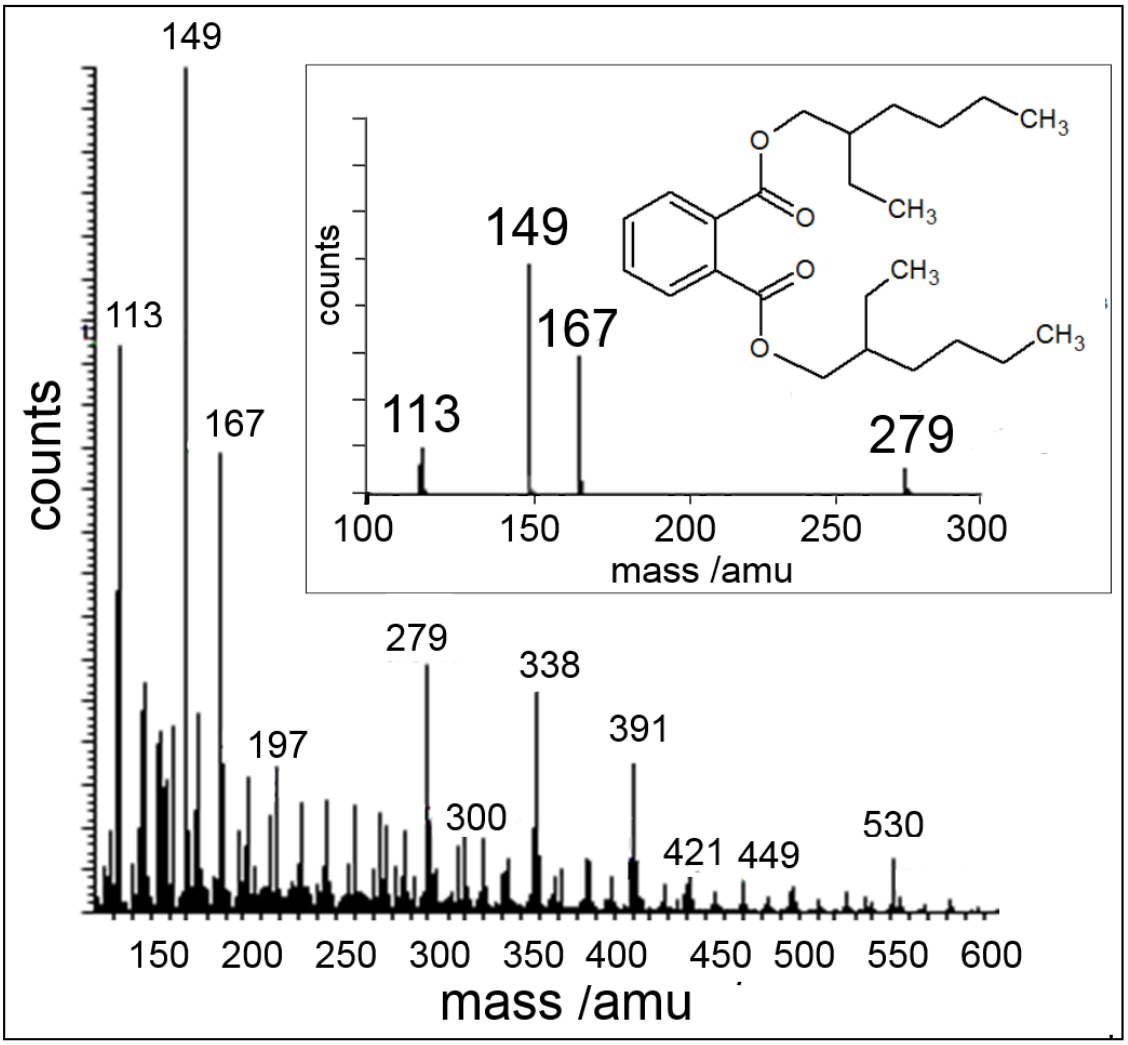

Figure 21: Mass spectrum of a sample of DCM that has been shaken with the black solid. Structure and simulated spectrum of plasticizer molecule bis 2-ethylhexylphthalate inset.

2.2.2.4. Infrared Spectroscopy

IR spectra were taken of all three solid samples (Figure 22). They were prepared by grinding a spatula tip of the solid with 0.2 g of KBr and then pressing into a disc using a dye. The spectra of all three materials were very similar. The most noticeable feature of all three spectra is the presence of a large broad peak between 3000 cm^{-1} and 3500 cm^{-1}, which suggests the presence of water. This confirms that the material in question is hygroscopic.

The spectra also has several peaks that could be due to the presence of the plasticizer that was picked up in the mass spectroscopy experiments, namely the peak at 2932 cm^{-1} which represent the stretching vibrations of ethylene C-H bonds. The peak at 1641 cm^{-1} is in the correct position for the aromatic C=C bond, however the broadened shape and high relative intensity suggest that it is not the only bond vibrating at that frequency. This could be due to the ester group in the phthalate, although this shift appears at a lower wavenumber than normally expected for a phthalate C=O asymmetric stretching, which usually occurs at just above 1700 cm^{-1}.

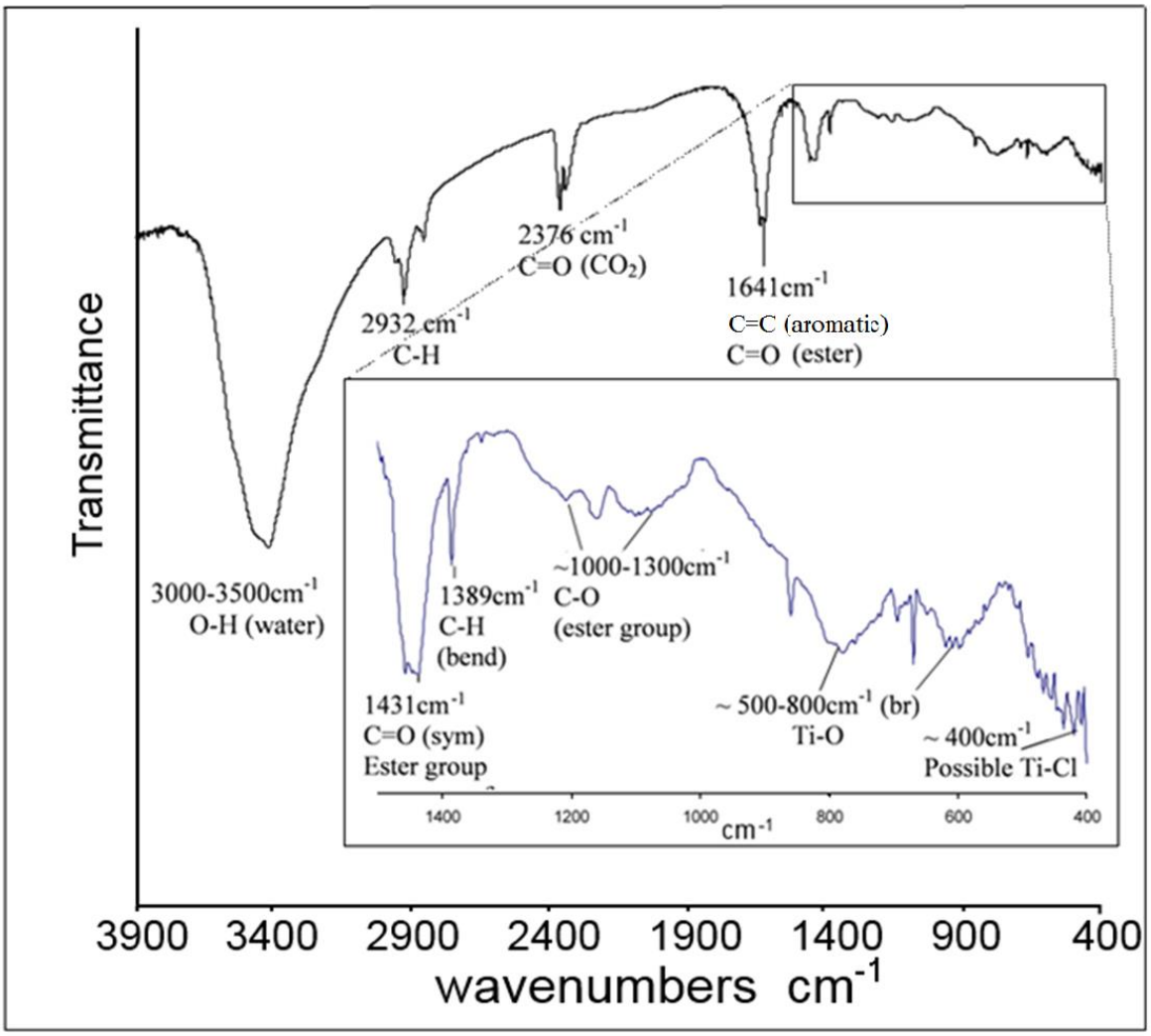

Figure 22: Infrared Spectrum of the black solid, as prepared using a pressed KBr disc.

This could be explained by the carbonyl groups co-coordinating to a metal species, which would remove electron density from the bond, lowering its vibrational frequency. This could explain how the phthalate is part of the precipitate and not seen in the solution NMR. Further relevant peaks were found in the fingerprint region. The large peak at 1431cm^{-1} is characteristic of the symmetric stretching of the C=O bond in the ester group. As with the asymmetry stretch it is shifted from its expected position (1400 cm^{-1}) in a way that suggests that the group is coordinated to a transition metal species. The two broad bands between 1000 and 1300 cm^{-1} are characteristic of the C-O stretch in an ester group. The spectra also feature two distinct broad humps at the low frequency end of the spectrum, between 500 and 800 cm^{-1}. These represent the vibrational frequency of the Ti-O bonds in a lattice. The broad hump at 400 cm^{-1} could also be representative of $TiCl_4$ however due to the large amount of interference and the fact that only half of the peak is visible this is not certain.

2.2.2.5. Energy Dispersive X-ray Spectroscopy (EDX)

The elemental composition of the three samples was studied using EDX and is shown in Table 2. The values shown in Table 2 are compositions of area scans of dimensions approximately 30 x 30 µm. The major components of each sample were carbon which makes up 40-55% of the species present, and oxygen which makes up 25-40% of the material present in the precipitate samples of primary condensate, plant distilled and lab distilled (3rd fraction) tetra.

Table 2: Atomic percentages of the elements present in the black solid as determined by EDS

	Atomic%		
Element	Primary Condensate	Plant Distilled	Lab Distilled 3rd Fraction
C K	46.16	55.19	39.66
O K	31.99	26.01	40.46
Cl K	11.24	8.85	7.24
Ti K	10.29	9.07	12.1

Each sample also has a significant amount of chlorine and titanium. The chlorine is likely in the form of residual Ti-Cl bonds exiting within the solid, most likely as partially oxidized $TiOCl_2.2(H_2O)$ within the solid. However this cannot be the only source of titanium as the chlorine would only account for around 10 - 20% of the atomic titanium present. The rest can be assumed to be in the oxidized form. This implies that some of the oxygen is present in the form of TiO_2. Once again however this does not cover all of the atomic species present. The remaining titanium in each sample only accounts for 25 -50% of the oxygen. The remaining oxygen could be present in the form of the bis 2-ethylhexyl phthalate plasticizer picked up in the mass spectroscopy experiments.

The plasticizer bis 2-ethylhexyl phthalate is 17% oxygen. Assuming that all the carbon comes from the plasticizer, which it almost certainly does not, this still only accounts for two

combined only account for around 35% oxygen content in the older samples and 60% and the lab distilled. The actual value is likely to be lower as mass spectroscopy suggests the presence of a polymeric species in the material as well. The remaining oxygen most likely comes from the water present in the solid as observed by the NMR and IR spectroscopy.

2.2.2.6. X-ray Photoelectron Spectroscopy

X-ray photoelectron spectroscopy was carried out on the solid from the primary condensate $TiCl_4$. The resulting spectra (Figure 23) showed the expected strong environments for the carbon and oxygen, measuring the atomic percentages at 46.8% and 28.93% respectively. This combined total is higher than the EDX, with substantially lower proportion of the oxygen. The atom% of titanium is lower than that predicted by EDX at only 6.3%. The binding energies of the Ti $2p_{3/2}$ and $2p_{1/2}$ peaks at 458.78 eV and 464.61 eV respectively indicate the presence of Ti4+ exclusively,[57, 58] as expected for the $TiCl_4$ and TiO_2 present. The atom% of Si is also lower at 4.13%

The ratio of Ti : Cl is roughly the same in XPS and EDAX, which indicates that they are present together at the same point in the solid, lending credence to the theory that the chlorine exists as a small amount of unreacted $TiCl_4$. The reason for the lower overall percentages of the Titanium and chlorine could be the result of the XPS sampling the surface of the material. The XPS penetrates less deeply into the material and therefore pick up more of the organic surface coating. This also explains why the atom% of oxygen is lower as less TiO_2 is being sampled at the expense of the surface organics. The oxygen peak at 531.99 eV is seen to be a compound of four different oxygen environments which account for the organic oxygen, the oxygen in the water and the TiO_2 present.[59, 60]

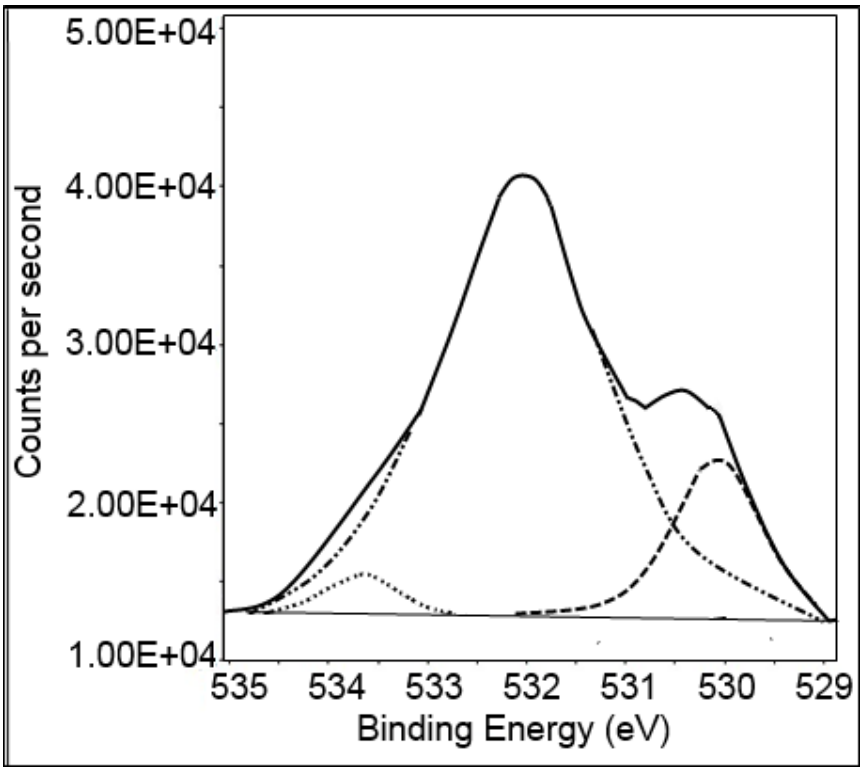

Figure 23: Compound peak in the O1s environment form the XPS spectrum of the black solid, showing organic oxygen (dotted + dashed), H_2O (dotted) and TiO_2 (dashed).

2.2.3. Conclusion

Analysis of the solid confirms the presence of the bis 2-ethylhexyl phthalate plasticizer molecule. This almost certainly came from the lid of the jars in which the $TiCl_4$ is stored. The process is gradual which explains why EDX analysis showed a greater carbon content for the older samples when compared to the new ones. Infrared spectroscopy showed a peak pattern that matches that expected from bis 2-ethylhexyl phthalate; however the peak that is thought to represent the carbonyl group is shifted to a lower frequency than expected. This can be explained by the carbonyl coordinating to a metal centre, co-ordination chemistry of phthalates has been shown to cause this carbonyl peak shift.[61]

A schematic shown in Figure 24 shows a simplified, proposed mechanism for the formation of the black solid. Exposure to the air in the jar (these samples are collected in open air from valves on the side of the process), causes the reaction of $TiCl_4$ with small amounts of H_2O trapped inside the jar, leading to the formation of the solid TiO_2. The corrosion of the lid, possibly due to the release of the HCl, leads to the leaching of bis 2-ethylhexyl phthalate into the solution, which then binds to the surface of the TiO_2 particles.

Phthalates have been shown in the literature to co-ordinate to the surface of titania[62] and have been used in the surface characterization of TiO_2 nanoparticles.[63] The mass spectra confirms the presence of the phthalate, however it is not seen in any of the NMR spectra of the liquid $TiCl_4$ samples. This could be due to the breakdown of the phthalate in solution by the TiO_2, a common UV catalyzed reaction.

To simulate the conditions for the formation of the black precipitate in different samples of $TiCl_4$, shavings of one of the sample caps were placed in to $TiCl_4$ (Aldrich 99.9%) under N_2 and left in a cupboard. After one week the shavings had discolored but there was no colour change or precipitate growth in the $TiCl_4$. The flask was filled with air, sealed and left in darkness. After one week, a black precipitate was observed in the bottom of the flask. When this was repeated without the plastic in the sample, a small amount of much lighter solid formed.

The mass spec also strongly suggests the presence of long chain alkyl species as seen by the repeating peak pattern every 14 *m/z* up to 600 *m/z*. There are a number of explanations for this occurrence. The corrosion of the lid could also leach polymer chains into the solution; however the lid is predominantly PVC, which would give a different mass pattern. Alkyls of

that molecular weight would not be able to move through either the lab or plant distillation columns so they cannot be carried over from the oil added in the process.

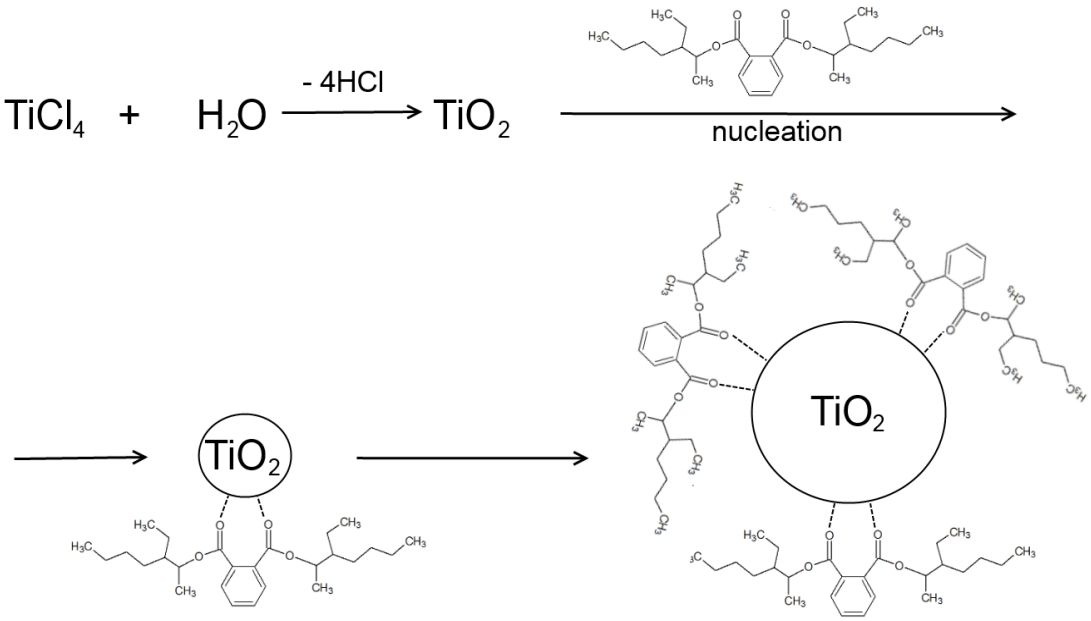

Figure 24: Proposed stepwise process for the formation of the precipitate, consisting of TiO_2 particles with bis 2-ethylhexyl phthalate molecules coordinating to the surface.

A possible explanation is the formation of a Zeigler Natta type polymerization system in the liquid $TiCl_4$. Small alkyl molecules from the breakdown of the oil could make it through the distillation column, or from the UV catalyzed breakdown of the phthalate molecules. Traditional Ziegler Natta catalysis uses a heterogeneous system such as the TiO_2 particles. $TiCl_4$ at the surface of these particles could act as a source for the polymerization of the polymeric species in solution. Furthermore, phthalates are widely used as electron donors in Zeigler Natta catalysis, encouraging polymerization, as well as controlling the nature of the polymer produced.[64] The $TiCl_4$ would be activated by Lewis basic materials, possibly the silanes and chlorosilanes present, which have been shown to interact with the alkylaluminium co-catalysts in a way that affect the polymerization of alkyls.

Chapter 3

Reaction of Titanium Chloride and Vanadium Oxytrichloride with Diester and Triester Molecules as Analogues for Oil

3.1. Introduction

During the Chloride Process, titanium dioxide ore is commonly purified using a fluid bed reactor which is heated to over 1000 ˚C whilst a stream of concentrated chlorine gas is passed over the ore. This converts the all solid TiO_2 present into gaseous $TiCl_4$.[73] The ores used are heavily contaminated with various other metal oxide species. These contaminants, most notably Fe_2O_3, V_2O_5, Al_2O_3 and SiO_2 are chlorinated along with the TiO_2, forming gaseous chlorinated species that rise out of the fluid bed reactor along with the $TiCl_4$. Purification of the $TiCl_4$ is carried out using a series of temperature changes and distillations, described in detail in the introductory chapter of this thesis, before being oxidised back to TiO_2.[74]

Vanadium oxytrichloride ($VOCl_3$) represents the most challenging impurity to remove (with the exception of $SiCl_4$ which is not removed due to its lower concentration in the ore and lower boiling point along with the relative inertness and whiteness of SiO_2 meaning that its presence is not detrimental to the final product). The p

resence of over 5 ppm of $VOCl_3$ in the $TiCl_4$ distillate can be extremely damaging to the final product due to the intense yellow colour of vanadium oxide, due to the presence of Vanadium (V) centres, ruining the white titania pigment. $VOCl_3$ has a similar boiling

point to $TiCl_4$, (126 ˚C and 136 ˚C respectively) and is therefore extremely challenging to separate effectively using a large scale industrial distilling column without somehow increasing the boiling point of the $VOCl_3$.[75] This is traditionally achieved *via* addition of mineral oils, the active component of which are triglyceride backbones and unsaturated carbon chains of lengths C15-18 (Figure 25).[76] Although this process has been used for decades, little is understood about why the oil preferentially reacts with the $VOCl_3$ rather than the $TiCl_4$.[77]

In order to improve the understanding of the Chloride Process on a molecular level, substituted esters were reacted with titanium chloride and vanadium oxytrichloride. The esters used were diethyl malonate, diethyl succinate, dibenzyl malonate, bis-isopropyl malonate and glycerol tribenzoate. Each molecule used was a diester, featuring two carbonyl groups, with the exception of glycerol tribenzoate which features three carbonyl groups. Glycerol tribenzoate was considered by far the most similar to the triglyceride backbone of the oil. The diester ligands were used to study the effects of the length of the hydrocarbon backbone separating the carbonyl groups, as well as the size of the side groups of the products formed.

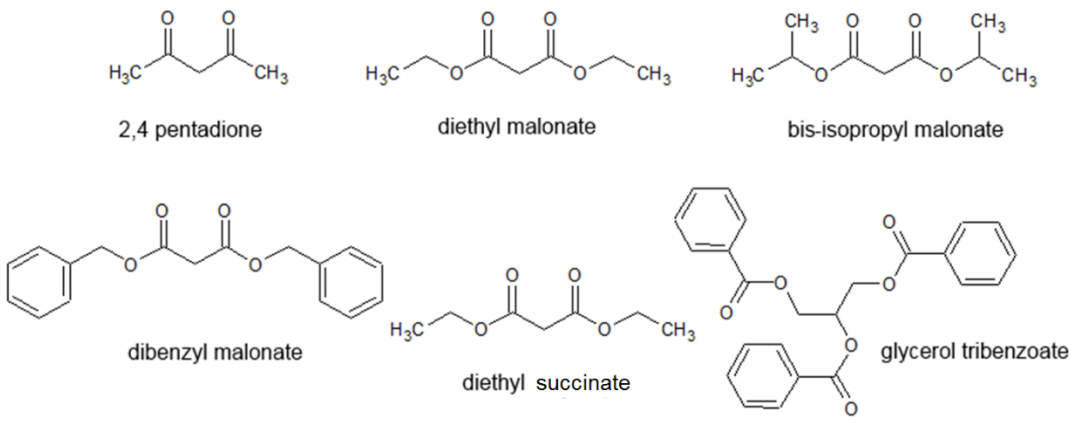

Figure 25: Ester species used as analogues for the triglyceride backbone of oil in the reaction with $TiCl_4$ and $VOCl_3$

The simple structures of the diester species were also beneficial in producing single crystals of the reaction products. Due to $TiCl_4$ having a prominent role in Zeigler Natta catalysis and the use of diesters as electron donor species,[78] several studies have been carried out on the reactivity of $TiCl_4$ with bidentate carbonyl ligands. Maier *et al*. found that co-ordination of 3,3-dimethyl 2,4-pentadione to $TiCl_4$, resulted in a six coordinate octahedral complex, with both carbonyl oxygen atoms coordinating to the metal centre without the displacement of the chloride ligands.[79]

Conversely a similar study found that unsubstituted 2,4-pentadione (acacH) displaces a chloride atom, giving the dimeric $[TiCl_2(acac)\mu\text{-}Cl]_2$ as a product. The monomeric equivalent was prepared by carrying out the reaction in tetrahydrofuran (THF) as opposed to CH_2Cl_2, with the THF acting as an Lewis base stabilising the monomeric species.[80]

Complexes of $TiCl_4$ with diesters have been studied previously using diethyl malonate.[81] Like with acac, diethyl malonate acts as a bidentate ligand with the titanium coordinating to both carbonyl oxygen atoms. However, unlike acac, all of the chloride ligands were retained. The crystal structure showed that the ligand molecule was unchanged and the complexes adopted a distorted octahedral geometry (Figure 26).

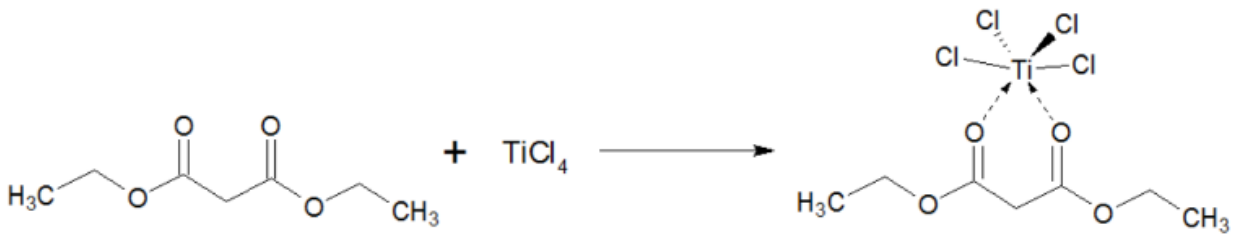

Figure 26: Reaction of diethyl malonate and titanium(IV) chloride, observed by both Sobota *et al*. and Kakkonen *et al*.[81,82]

3.2. Experimental

All reactions were carried out under argon obtained from BOC using standard Schlenk techniques. All Solvents were dried over activated alumina by the Grubbs method using anhydrous engineering equipment, such that the water concentration was 5 – 10 ppm.[83] Anhydrous $TiCl_4$ and malonate starting materials were purchased from Sigma Aldrich; all were used without further purification. ^1H and $^{13}C\{^1H\}$ NMR spectra were obtained on a Bruker AV-600 Mz spectrometer, operating at 295 K and 600.13 MHz (^1H). Signals are reported relative to $SiMe_4$ (δ = 0.00 ppm) and the following abbreviations are used s (singlet), d (doublet), t (triplet), q (quartet), m (multiplet), b (broad). $CDCl_3$ was obtained from GOSS Scientific and was dried and degassed twice over activated 3 Å molecular sieves.

3.2.1. Synthesis of tetrachloro(diisopropyl malonate)-titanium(IV) [1a]

Diisopropyl malonate (0.5 cm^3, 3.3 mmol) was added dropwise to $TiCl_4$ (1.0 cm^3, 9.1 mmol) in 50 cm^3 of hexane and stirred under argon for 2 h. A yellow precipitate was immediately formed but the mixture was stirred for a further 2 h to ensure no further reaction. The solvent and excess $TiCl_4$ were removed *via* filtration and the precipitate was filtered and washed three times with 20 cm^3 hexane before drying *in vacuo* to afford complex **1a** in good yield (0.8 g, 63%). Some of the product was re-dissolved in 5 cm^3 of dichloromethane and layered with 15 cm^3 of hexane. After 48 hours small crystals formed. The molecular structure of **1a** was determined by X-ray crystallography. ^1H NMR ($CDCl_3$): δ 5.46 (b, 2H, -CH), 3.95 (b, 2H, $-CH_2$), 1.47 (d, 12H, $-CH_3$, J = 6.20Hz). $^{13}C\{^1H\}$ NMR ($CDCl_3$): δ 21.7 ($-CH_3$), 38.0 ($-CH_2$), 54.8 ($-OCH_2$), 172

(C=O). Elemental analysis calculated for $TiCl_4C_9O_4H_{16}$: C, 28.60; H, 4.27. Found: C, 26.03; H, 3.45.

When **1a** was crystallised, two types of crystals were observed, block type and plate type. Carrying out single crystal XRD on both types revealed that a second product had formed (**1b**), a dimeric species consisting of two titanium centres linked by a bridging oxygen, each titanium centre coordinated to one malonate ligand. The additional oxygen that entered the system is likely responsible for the discrepancy between calculated atomic percentage and that found through elemental analysis.

3.2.2. Synthesis of tetrachloro(dibenzyl malonate)-titanium(IV) [2]

Dibenzyl malonate (1.0 cm^3, 3.5 mmol) was added dropwise to $TiCl_4$ (1.0 cm^3, 9.1 mmol) in 50 cm^3 of hexane. A yellow precipitate was observed immediately and the reaction was stirred under argon for 2 h. The solvent and excess $TiCl_4$ were removed *via* filtration and the precipitate was filtered and washed three times with 20 cm^3 hexane before drying *in vacuo* to afford **2**. A good yield was recovered (1.2 g, 77%). Yellow crystals were again formed from a solution in CH_2Cl_2 layered with hexane. The molecular structure of **2** was determined by X-ray crystallography. ^{1}H NMR ($CDCl_3$): δ 7.3 – 7.5 (m, 10H, Ph), 5.5 (b, 4H, -CH_2), 4.0 (b, 2H, -CH_2). ^{13}C {^{1}H} NMR ($CDCl_3$): δ 38.0 (-CH_2), 73.0 (-OCH_2), 129-130 (m, C6, -Ph). Elemental analysis calculated for $TiCl_4C_{15}O_4H_{12}$: C, 43.08; H, 3.40. Found: C, 43.24; H, 3.40.

3.2.3. Synthesis of tetrachloro(diethyl succinate)-titanium(IV) [3]

Diethyl succinate (0.5 cm^3, 3.3 mmol) was added dropwise to $TiCl_4$ (2.0 cm^3, 18.2 mmol) in 50 cm^3 of hexane and stirred under argon for 2 h. A yellow precipitate formed immediately, the reaction was stirred for 2 h to ensure completion. The yellow precipitate was filtered off and washed three times with 10 cm^3 hexane and dried *in*

vacuo, to afford complex **3** in good yield (0.9 g, 75%). The product was re-dissolved in 5 cm^3 dichloromethane and layered with 10 cm^3 hexane. Small crystals formed overnight allowing the molecular structure of **3** to be determined by X-ray crystallography. ^1H NMR ($CDCl_3$): δ 4.61 (q, 4H, $-CH_2$, J = 14.3 Hz), 3.08 (s, 4H, $-CH_2$), 1.46 (t, 6H, $-CH_3$, J = 14 Hz). ^{13}C {^1H} NMR ($CDCl_3$): δ 14.1 ($-CH_3$), 29.2 ($-CH_2CH_2$), 66.2 ($-OCH_2$), 179 (C=O). Elemental analysis calculated for $TiCl_4C_8O_4H_{14}$: C, 26.4; H, 3.88. Found: C, 26.41; H, 4.02

3.2.4. Synthesis of complex of titanium(IV) chloride with glycerol tribenzoate [4]

Glycerol tribenzoate (0.5 g, 1.2 mmol) was added gradually to $TiCl_4$ (2.0 cm^3, 18.2 mmol) in 50 cm^3 of hexane and stirred under argon for 2 h. An excess of $TiCl_4$ was used as its removal after reaction completion is facile. Gradual precipitation of a yellow product was observed. The solvent and excess $TiCl_4$ were removed *via* filtration and the precipitate was filtered and washed three times with 20 cm^3 hexane before drying *in vacuo* to afford **4** in good yield (1.6 g 75%). Crystals suitable for X-ray diffraction were obtained by dissolving the yellow product in a minimum amount of dichloromethane, cooling to -10 ˚C, and leaving for one month. ^1H NMR ($CDCl_3$): δ 8.27 (d, 2H, *o*-CH, J = 7.7 Hz), 8.17 (d, 4H, *o*-CH, J = 7.7 Hz), 7.69 (t, 2H,$-CH_2$, J = 4.8 Hz, 12.3 Hz). 2H, *p*-CH J = 7.7 Hz), 7.65 (t, 1H, *p*-CH, J = 7.7 Hz), 7.53 (t, 2H, m-CH, J = 7.7 Hz), 7.50 (t, ^1H, m-CH, J = 7.7 Hz), 5.82 (quin, 1H, -OCH, J = 5.1 Hz), 4.98 (dd, 2H, $-CH_2$, J = 4.8 Hz, 12.3 Hz), 4.75 (dd, 4H, $^{13}C\{^1H\}$ NMR ($CDCl_3$): δ 63.5 (CH_2), 72.2 (CH), 129 (*o*-CH), 131 (*p*-CH), 135 (*m*-CH), 168 (C=O). Elemental analysis calculated for $Ti_4Cl_{16}C_{48}O_{12}H_{46}$: C, 36.64; H, 2.95. Found: C, 37.6; H, 2.98.

3.2.5. Synthesis of Dichloro(oxo)(2, 4-Pentanedione) vanadium(V) [5]

2,4-pentadione (acacH) (0.5 cm^3, 4.87 mmol) was added dropwise to $VOCl_3$ (2 cm^3, 21.1 mmol) in 30 cm^3 of hexane and stirred under nitrogen for 2 h. A dark precipitate formed immediately, giving a thick suspension that appeared black. The precipitate was filtered and washed with hexane and dried *in vacuo*. This afforded the dark red complex 5 in good yield (1.1 g, 75%). ^1H and ^{13}C NMR were carried out on this product under nitrogen. Crystals suitable for single crystal X-ray diffraction were grown by layering a saturated solution of **5** in dichloromethane with hexane. Large green crystals formed over the course of 2 days and were analysed. ^1H NMR ($CDCl_3$): δ 2.39 (s, 6H, CH_3), 6.13 (s, 1H, CH). ^{13}C {^1H} NMR ($CDCl_3$): δ 26.4 (CH_3), 105 (CH), 193 (C=O). Elemental analysis calculated for $VO_3Cl_2C_5H_7$: C, 25.34; H, 2.98. Found: C, 25.80; H, 3.02.

3.2.6. Synthesis of Dichloro(oxo)(diethyl malonate) vanadium(V) [6]

Diethyl malonate (0.5 cm^3, 3.3 mmol) was added dropwise to $VOCl_3$ (2 cm^3, 21.1 mmol) in 50 cm^3 of hexane and stirred under nitrogen for 2 h. An excess of $VOCl_3$ was used to ensure completion as unreacted $VOCl_3$ is facile to remove from the reaction. A very dark precipitate was formed in a dark red solution. The precipitate was filtered and washed three times with 20 cm^3 hexane and dried *in vacuo* to afford **6** in good yield (0.9 g, 78%). ^1H and ^{13}C NMR were carried out on this product under nitrogen. Some of the product was re-dissolved in 5 cm^3 dichloromethane and layered with 15 cm^3 hexane. Small crystals formed over approximately a week. ^1H NMR ($CDCl_3$): δ 1.34 (t, 6H, -CH_3, *J* = 7.25 Hz, 3.35 (s, 2H, -CH_2), 4.18 (q, 4H, -CH_2, *J* = 7.25 Hz). $^{13}C\{^1H\}$ NMR ($CDCl_3$): δ 14.2 (CH_3), 55.9 (CH_2), 63.6 (CH_2CH_3), 163 (C=O). NMR peaks were highly

broadened due to presence of paramagnetic vanadium species. Elemental analysis calculated for $V_4Cl_8C_{28}O_{20}H_{48}$: C, 28.21; H, 4.06. Found: C, 26.38; H, 3.78.

3.2.7. Synthesis of $VOCl_3$ Bis-isopropyl malonate Complex [*7*]

Bis-isopropyl malonate (0.5 cm3, 2.7 mmol) was added dropwise to $VOCl_3$ (2 cm^3, 21.1 mmol) in 30 cm^3 of hexane and stirred under nitrogen for 2 h. A dark red precipitate **[7]** was formed in a dark solution, the precipitate was filtered and washed 3 times with 20 cm^3 hexane. The final washing was coloured red suggesting the product is partially soluble in hexane. The sample was dried *in vacuo*. ^1H NMR ($CDCl_3$): δ 5.14 (b, 1H, -CH), 3.37 (b, 2H, -C**H**$(CH_3)_2$), 1.30 (b,12H, $-CH_3$) ^{13}C {^1H} NMR ($CDCl_3$): δ 21.5 (CH_3), 54 (CH_2), 73 (CH_2), 129 (C = 0).

3.2.8. Synthesis of Dichloro(oxo)(diethyl succinate) vanadium(V) [8]

Di-ethyl succinate (0.5 cm^3, 3.3 mmol) was added dropwise to $VOCl_3$ (2 cm^3, 21.1 mmol) in 40 cm^3 of hexane and stirred under nitrogen for 2 h. A dark red solution formed immediately but no precipitate was observed. The product was dried *in vacuo* leading to the removal of the solvent and $VOCl_3$, leaving a viscous red liquid product (0.8 g, 90%). ^1H and ^{13}C NMR were carried out on this product under nitrogen. The flask containing the liquid product was left on its side for two weeks. Small green crystals were observed in the flask. ^1H NMR ($CDCl_3$): δ 1.21 (b, 6H, $-CH_3$), 2.59 (b, 4H, $-CH_2CH_2$), 4.12 (b, 4H, $-CH_2CH_3$). ^{13}C {^1H} NMR ($CDCl_3$): δ 14.3 (CH_3), 29.2 (CH_2CH_2), 60.9 (CH_2CH_3), 173 (C = 0).

3.2.9. Synthesis Of Glycerol tribenzoate $VOCl_3$ [*9*]

2 cm^3 of $VOCl_3$ (21.1 mmol) in 10 cm^3 of toluene, was added dropwise to a rapidly stirred suspension of glycerol tribenzoate (0.5 g, 1.2 mmol) in toluene (30 cm^3)using a canula. The mixture was refluxed under nitrogen for 15 h. A red-brown solution was removed by filtration to yield and a brown precipitate. This precipitate was washed and dried *in vacuo* and ^1H and

^{13}C NMR were obtained. The compound was dissolved in CH_2Cl_2 and layered with hexane in an attempt to grow crystals, however none formed after multiple attempts. NMR ($CDCl_3$): δ 8.05 (b, 9H, (*o*-CH)), 7.5 (b, 16H, *p*-CH and *m*-CH) 5.7 (b, 1H, -OCH), 4.8 (b, 4H, -CH_2), 4.12 (broad, 2H, (O-CH_3). ^{13}C {^1H} NMR ($CDCl_3$): 63.30 (CH_2), 71.32 (CH), 128 (*o*-CH), 130 (*p*-CH), 134 ($_m$-CH), 166 (C=O). Elemental analysis calculated for $VCl_2C_8O_5H_{14}$: C, 30.79; H, 4.52. Found: C, 29.83; H, 4.49.

It should be noted that although elemental analysis results for carbon and hydrogen were in come cases, outside of the 0.4% tolerance, this was expected due to the exteremly air sensitive nature of these compounds,

3.2.10. Crystallography

Suitable crystals were selected and mounted on a nylon loop, datasets of **1a** and **1b** were collected on a *Rigaku AFC12* goniometer equipped with an enhanced sensitivity (HG) *Saturn724+* detector mounted at the window of an *FR-E+ SuperBright* molybdenum rotating anode generator (λ_1 = 0.71073 Å) with VHF *Varimax* optics (100 µm focus). Crystals of compound **1b** were of poor quality and did not diffract well, leading to a low-quality dataset. Although the atomic connectivity is unambiguous, the high R factors (R_1 = 0.1153, wR_2 = 0.3054) and low precision on C–C bond lengths preclude accurate comparison of bond lengths and angles. The diffraction pattern for **3** was obtained using a *Rigaku R-Axis Spider diffractmeter* including curved Fujifilm image plate and a graphite monochromated sealed tube Mo generator (λ_1 = 0.71073 Å). The datasets of **2**, **4**, **5**, **6**, and **8** were collected on a *SuperNova, Dual*, *Cu*, *Atlas* diffractometer. The crystal was kept at 150 K during data collection. **1a, 1b,** and **3** were solved using cell determination, data collection, data reduction, cell refinement

and absorption correction were carried out using CrystalClear-SM Expert 3.1 b18.[84] Structure solution and refinement were carried out using WinGX and software packages.[85] H atoms attached to C atoms were placed in geometrically assigned positions, with C-H distances of 0.95 Å (CH), 0.98 Å (CH_3) or 0.99 Å (CH_2) and refined using a riding model, with U_{iso}(H) = 1.2U_{eq}(C) (CH, CH_2) or 1.5U_{eq}(C) (CH_3). enCIFer was used to sprepare CIFs for publication.[86] Compounds **2**, **4**, **5**, **6**, and **8** were solved using Olex2,[87] the structure was solved with the olex2.solve[88] structure solution program using Charge Flipping and refined with the ShelXL[89] refinement package using Least Squares minimisation. The crystal structures were solved by Dr. David Pugh and Dr. Peter Marchand in the case of **1a, 1b** and **3** and Dr. Caroline Knapp in the case of **2, 4, 5, 6**, and **8.**

3.3. Results and Discussion

The diesters bis-isopropyl malonate, dibenzyl malonate, diethyl succinate and the triester glycerol benzoate were all added to solutions of $TiCl_4$ in hexane. In each case a bright yellow precipitate was observed to form immediately. After the solution was stirred for two hours the precipitate was separated *via* filtration and washed with moisture free hexane three times. All of the reactions gave yields above 60%. The products were analysed using NMR spectroscopy and elemental analysis. Single crystals for X-ray diffraction analysis were obtained by layering saturated solutions of products in CH_2Cl_2 with hexane in the case of **1-3** and cooling a saturated solution in CH_2Cl_2 in the case of **4**.

All four complexes adopt a pseudo octahedral geometry with two carbonyl oxygen atoms coordinating to the titanium centre without the displacement of the chlorine

atoms. The octahedral geometry of the complex is distorted, largely due to the chelating nature of the ligands, which forces the O(1)-Ti(1)-O(2) bond to narrow to 80.23(4) ° as the carbon carbon bonds are generally longer than the titanium oxygen bonds. Although chelation is the dominant force in the narrowing of the angle, the effect is exacerbated due to the electronegative nature and greater atomic radii of the chlorine, compared with the carbonyl oxygen. Chlorine has a Van der Waals radius of 1.75 Å whereas the Van der Waals radius of oxygen is 1.52 Å,[90] leading to the bond angles between the chlorine ligands to be wider than those between the oxygens. Forcing the less electronegative carbonyl oxygen atoms closer together.

3.3.1. Interaction of $TiCl_4$ with Diester Ligands

In addition to the triester species, the interactions of the dieter molecules (diisopropyl malonate, dibenzyl malonate and diethyl succinate) with $TiCl_4$ were also studied. Whilst less indicative of the active species in the oils used for vanadium removal, these molecules still provide information regarding the potential reactivity of $TiCl_4$ with ester functionality. These species were advantageous in that their simplicity allowed for single crystals to be obtained easily. The resulting NMR spectra were far less complex and easy to rationalize. As only two ester groups are present the species behave in the same way as the glycerol tribenzoate species without the third carbonyl species facilitating dimerisation. This may be of relevance as it is likely that the long alkyl chains of the oil could sterically hinder dimerisation observed in **4,** making it less favourable.

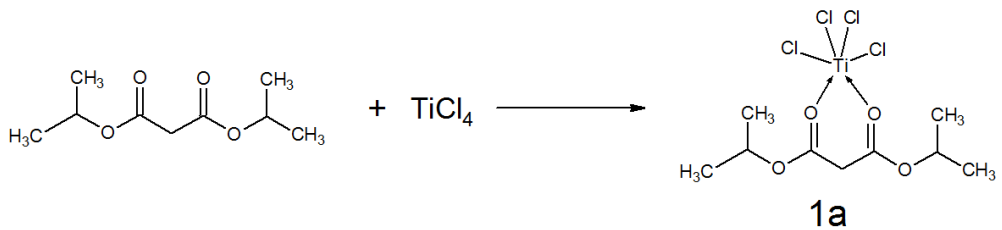

1a

Scheme 1: Reaction of $TiCl_4$ with bis-isopropyl malonate to give tetrachloro(bis-isopropylmalonate)-titanium(IV) [**1a**]

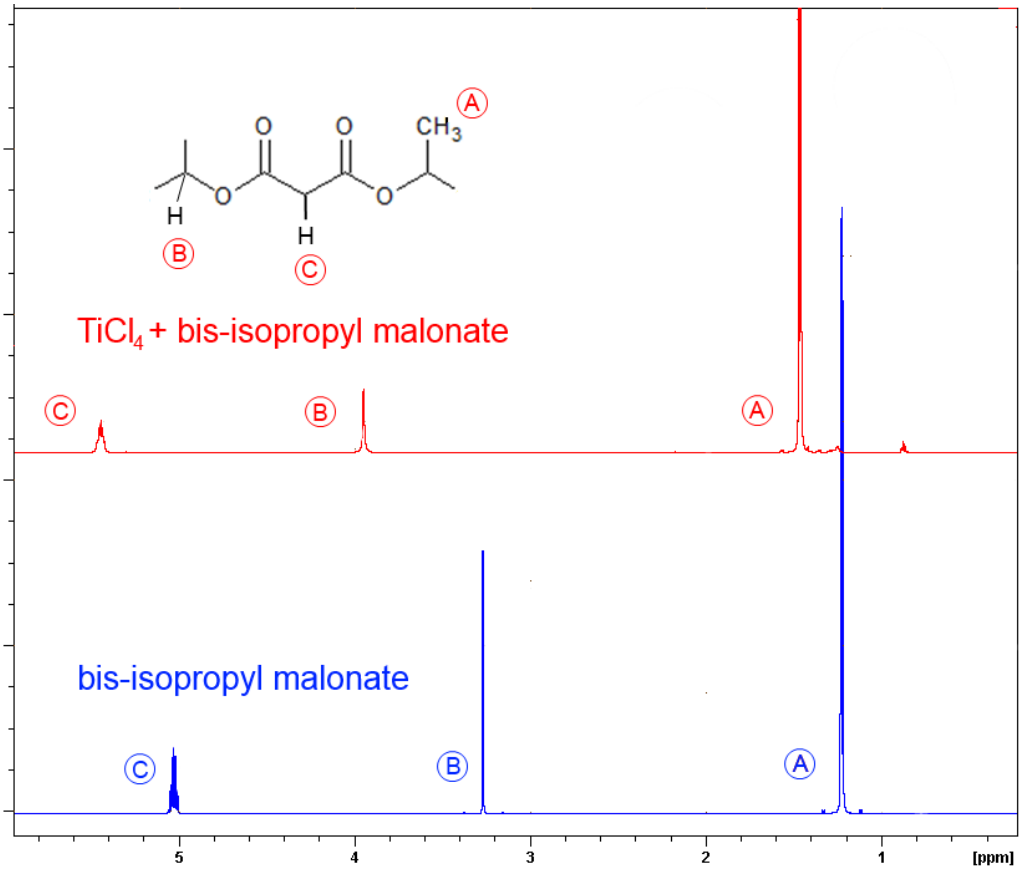

Figure 27: ^1H NMR spectra of bis-isopropyl malonate and the product of its reaction with $TiCl_4$ **[1a]**, all peaks exhibiting a downfield shift indicating coordination to the titanium metal centre

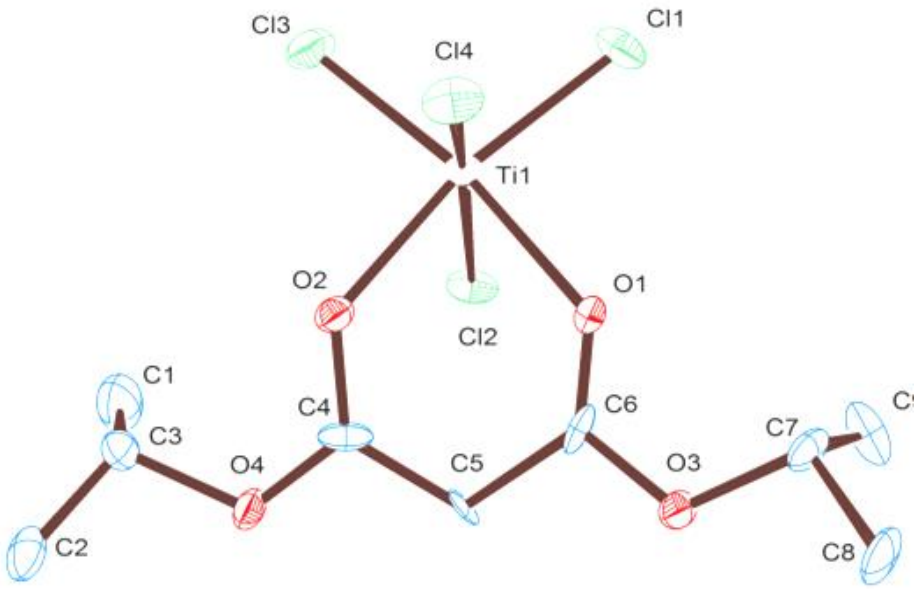

Figure 28: ORTEP representation of the crystal structure of tetrachloro(diisopropyl malonate)-titanium(IV) **[1a]**, with thermal ellipsoids at the 50% probability level. Hydrogen omitted for clarity.

Table 3: Crystallographic Data and Selected bond lengths angles for the crystal structur**e** of **1a** the product of reaction $TiCl_4$ and bis isopropyl malonate

Structural Data	
crystal system	Monoclinic
space group	P21/c
A	6.6655(14) Å
B	12.954(3) Å
C	18.983(5) Å
A	90.000°
B	90.032(4)°
Γ	90.000°
R_1	0.023
wR_2	0.0569

Selected Bond Angles °	
C(4)-O(2)-Ti(1)	129.89(9)
C(6)-O(1)-Ti(1)	131.45(9)
O(1)-Ti(1)-O(2)	80.23(4)
O(1)-Ti(1)-Cl(3)	170.85(3)
O(1)-Ti(1)-Cl(4)	84.68(3)
Cl(1)-Ti(1)-Cl(4)	97.21(2)
O(1)-Ti(1)-Cl(1)	90.40(3)
Cl(1)-Ti(1)-Cl(3)	98.44(2)
O(1)-Ti(1)-Cl(2)	83.26(3)
Cl(3)-Ti(1)-Cl(2)	93.86(2)

Selected Bond Lengths Å	
Cl(3)-Ti(1)	2.2312(6)
Cl(4)-Ti(1)	2.2519(5)
O(2)-Ti(1)	2.1032(10)
O(1)-Ti(1)	2.1120(10)
C(4)-O(2)	1.2340(15)
Cl(1)-Ti(1)	2.2322(5)
Cl(2)-Ti(1)	2.3414(5)
C(6)-O(1)	1.2294(16)
C(4)-C(5)	1.506(2)
C(7)-C(8)	1.4996(18)

3.3.1.1. Tetrachloro(diisopropyl malonate)-titanium(IV) [1a]

Diisopropyl malonate was reacted with an excess of titanium(IV) chloride (Scheme 1) at room temperature, yeilding yellow crystals after layering in CH_2Cl_2 with hexane.

NMR spectroscopy indicates a simple 1:1 coordination complex of the ligand and $TiCl_4$ (Figure 27). The ^1H NMR signal of the two protons of the central carbon atom between the two ester groups has shifted by 0.66 ppm downfield in comparison to the free ligand. Likewise the signal of the isopropyl CH group had shifted by 0.42 ppm and the signal of the four isopropyl methyl groups have shifted by 0.25 ppm when compared to the uncoordinated ligand. The NMR confirms there is no loss of a proton from the central carbon, as is customary with the similar ligand acac, implying that the ester groups are able to mitigate the formation of a charged complex, instead the product

remains covalent. This is confirmed by the crystal structure which shows no shortening of the C(4)-C(5) bond compared with other C-C bonds (table 3).

The structure of **1a** was confirmed by single crystal XRD (Figure 28). The malonate ligand forms a six membered ring structure with the titanium centre, datively bound to the two carbonyls, linked in turn by a carbon chain. The C(4)-O(2)-Ti(1) angle of the six membered ring species is considerably wider (129.89(9)°) than that expected for a flat hexagon (120°).

Comparatively the O-Ti-O bond angle observed for this complex is 80.23(4)°, narrower than 90° due to the electronegativity of the chlorine atoms forcing the carbonyls closer together. This, combined with the differing length of the Ti-O bonds (~ 2.1Å) and C-O bonds (~ 1.2Å) leads to considerable ring puckering. Sobota *et al*. observed similar angles when carrying out the related reaction with $TiCl_4$ and diethyl malonate.[16] The length of the bond between the titanium and the carbonyl oxygen on the diisopropyl malonate is 2.123(3) Å. This is far closer to the dative Ti-O bond length of $[TiCl_4(THF)_2]$ [91,92] than that of a covalent Ti-O bond[27] and is due to the coordination of the bis-isopropyl malonate being dative, *via* a lone pair on each the carbonyl oxygen atoms.

3.3.1.2. Bis-trichloro-μ-oxo-(diisopropyl malonate)-titanium(IV) [1b]

This dimeric species was produced during the same synthesis as **1a** described above. The reaction produced yellow crystals, after workup. Two noticeably different types of crystal were observed, both of which were characterized by single crystal X-ray diffraction. While all of the other compounds described in this thesis form as a result of simple addition of the ligand to the tetrahedral $TiCl_4$ with no displacement of chlorine, **1b** contains titanium centres linked by an oxygen atom, facilitated by loss of chlorine (Figure 29).

This was likely a result of a small amount of air entering the vessel, which lead to reaction of the product with water in which the addition of oxygen was facilitated by the formation of HCl gas. This effect has been reported with similar titanium chloride complexes, leading to oxo bridged dimers and tetramers (Scheme 2). [93] The bond distances between the bridging oxygen and the titanium centres was 1.741(7) and 1.863(7) Å, showing the bonding to be covalent in nature.[28]

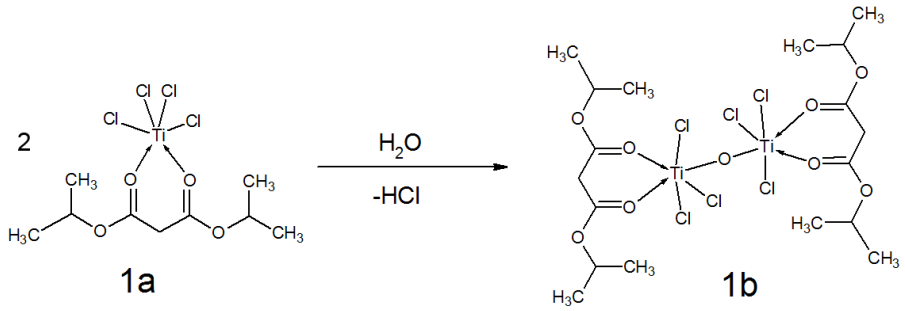

Scheme 2: Reaction of **1a** with atmospheric water to give bis-trichloro-μ-oxo-(diisopropyl malonate)-titanium(IV) **[1b]**, facilitated by the elimination of HCl.

The bridging oxygen stabilised the system and similar bridging compounds have been reported before as easier to crystallise. [94] This is likely a result of the system forming multiple π-bonding interactions between the filled p orbitals of the bridging oxygen and the empty d orbitals of the two titanium centres, interactions which are stronger than two Ti-Cl bonds that are replaced. The species is likely the result of there being a limited oxygen supply, with further oxidation occurring over time should the flask have been opened fully.

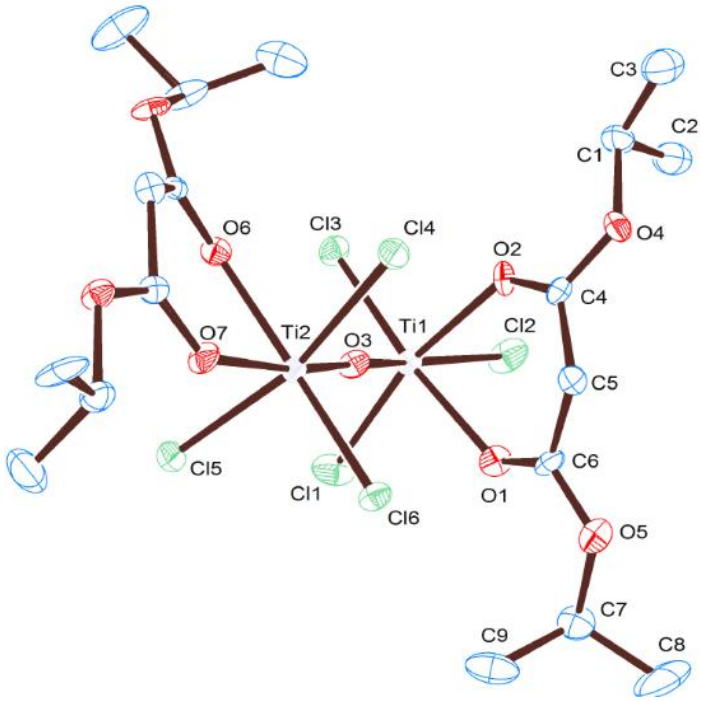

Figure 29. ORTEP representation of **1b** with thermal ellipsoids at the 50% probability level. Hydrogen atoms omitted for clarity

Table 4: Crystallographic Data and Selected bond lengths angles for the crystal structure of 1b the product of reaction $TiCl_4$ and bis isopropyl malonate and subsequent air exposure

Structural Data	
crystal system	triclinic
space group	P21/c
a	18.335(16) Å
b	12.436(12) Å
c	13.683(11) Å
α	90.000°
β	102.474(14) °
γ	90.000°
R_1	0.1153
wR_2	0.3054

Selected Bond Angles °	
C(4)-O(2)-Ti(1)	133.0(7)
C(6)-O(1)-Ti(1)	131.2(8)
O(1)-Ti(1)-O(2)	80.0(3)
O(1)-Ti(1)-Cl(3)	167.3(3)
O(1)-Ti(1)-Cl(1)	92.3(2)
Cl(1)-Ti(1)-Cl(3)	100.31(14)
O(1)-Ti(1)-Cl(2)	81.7(2)
Cl(3)-Ti(1)-Cl(2)	96.22(16)
O(6)-Ti(2)-Cl(6)	168.9(2)
Ti(2)-O(1)-Ti(1)	177.2(5)

Selected Bond Lengths Å	
Cl(3)-Ti(1)	2.230(4)
O(2)-Ti(1)	2.136(8)
O(1)-Ti(1)	2.129(8)
C(4)-O(2)	1.225(14)
Cl(1)-Ti(1)	2.222(4)
Cl(2)-Ti(1)	2.306(4)
C(6)-O(1)	1.233(14)
Ti(2)-Cl(5)	2.373(3)
O(3)-Ti(2)	1.741(7)
O(3)-Ti(1)	1.863(7)

The bond angles and distances in the two bridged titanium centres of **1b** are similar to those reported previously. The bridging Ti-O-Ti bond angle being 177.3(5)°, which is similar to other oxo-bridged titanium chloride dimers with alkoxide ligands that are less sterically hindering.[94,95] In the presence of bulkier ligands, more acute oxo bridge

angles have been reported.[93] The formation of the dimer demonstrates how air/moisture sensitive this system is and how oxygen can stabilise the product.

3.3.1.3. Tetrachloro(dibenzyl malonate)-titanium(IV) [2]

Dibenzyl malonate was reacted with an excess of titanium(IV) chloride at room temperature (Scheme 3), which yielded yellow crystals after layering in dichloromethane with hexane. NMR spectroscopy revealed that the ligand coordinated to the metal centre, in a manner similar to compound **1a.** The ^{1}H NMR spectra of the product shows the signal of the two central protons to shift 0.50 ppm downfield from the signal of the free ligand. Signals from the two CH_2 groups adjacent to the ester oxygen shifted by 0.32 ppm (Figure 30).

Finally the benzyl proton signal, a single broad peak in the spectrum of the uncoordinated ligand is shifted to reveal two of the overlapping phenyl group proton signals. The *ortho* protons shifted downfield by 0.9 ppm, the meta and para by only 0.5 ppm. As described for the diisopropyl malonate, the complex features a puckered six membered ring (Figure 31).

Like compound **1a**, the chelating nature of the ligand as well as the repulsion of the four chlorine ligands resulted in the subsequent compression of the O-Ti-O bond angle to 79.33(19)°. As with the diisopropyl malonate complex, the Ti-O bond length of 2.122(5) Å suggests that the bond between the titanium and the carbonyl is dative in nature (Figure 31).

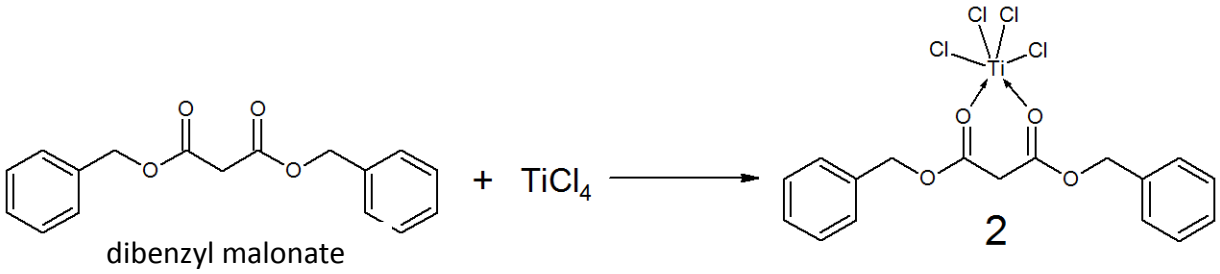

Scheme 3: reaction of $TiCl_4$ with Glycerol tribenzoate give tetrachloro(dibenzyl malonate)-titanium(IV) [2].

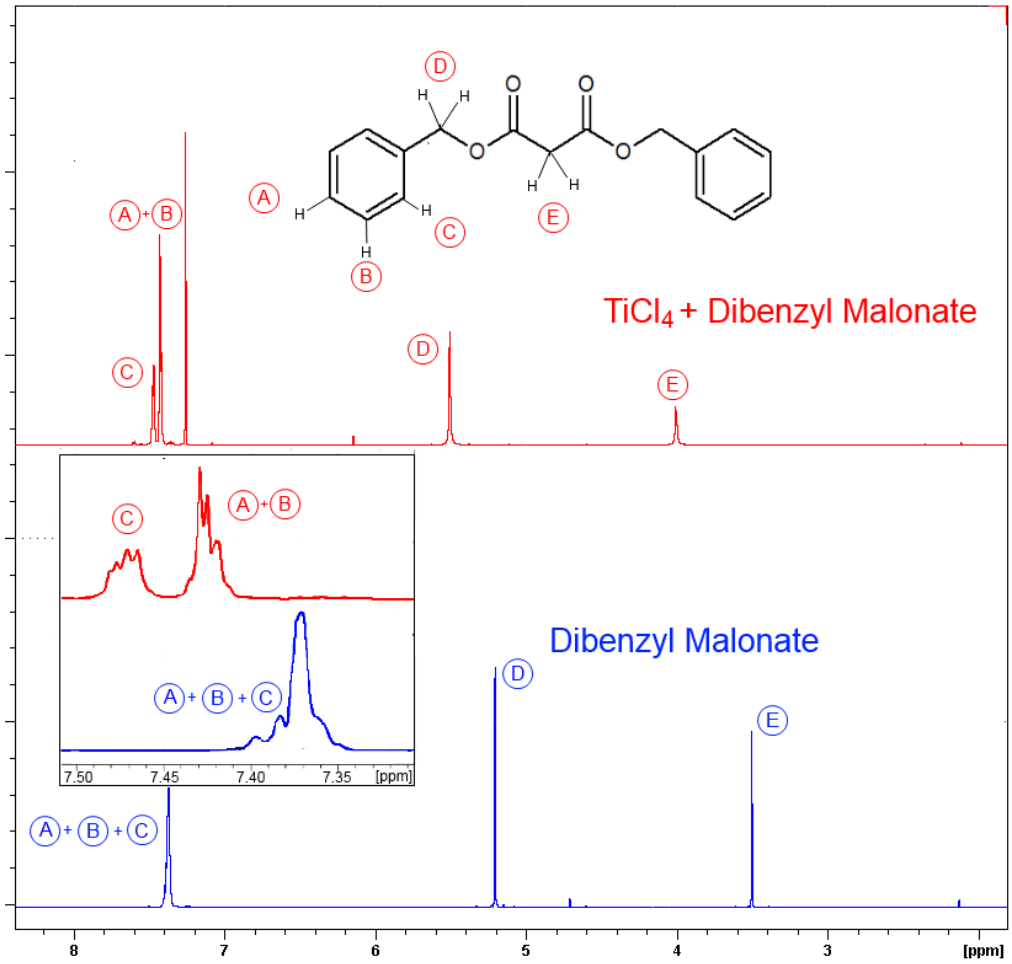

Figure 30: ^1H NMR spectra of dibenzyl malonate and the product of its reaction with $TiCl_4$ **[2],** all peaks exhibiting a downfield shift indicating coordination to the titanium metal centre.

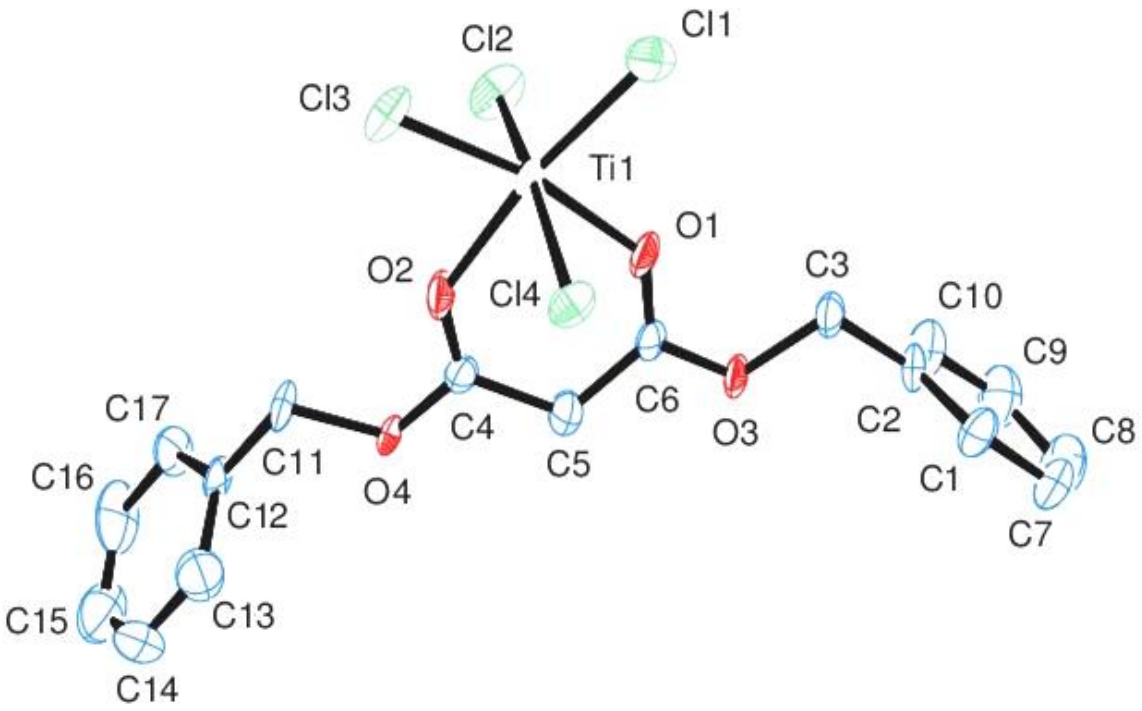

Figure 31 : ORTEP representation of tetrachloro (dibenzyl malonate)-titanium(IV) [**2**] with thermal ellipsoids at the 50% probability level. Hydrogen atoms omitted for clarity.

Table 5: Crystallographic Data and Selected bond lengths angles for the crystal structure of **2** the product of reaction $TiCl_4$ dibenzyl malonate

Structural Data	
crystal system	monoclinic
space group	P21
a	16.3215(4) Å
b	9.5645(2) Å
c	19.7379(4) Å
α	90.000°
β	90.069(2) °
γ	90.000°
R_1	0.0849
wR_2	0.2263

Selected Bond Angles °	
C(4)-O(2)-Ti(1)	134.6(5)
C(6)-O(1)-Ti(1)	134.4(4)
O(1)-Ti(1)-O(2)	79.33(19)
O(1)-Ti(1)-Cl(3)	169.39(16)
O(1)-Ti(1)-Cl(4)	82.63(16)
Cl(1)-Ti(1)-Cl(4)	95.47(8)
O(1)-Ti(1)-Cl(1)	90.59(15)
Cl(1)-Ti(1)-Cl(3)	99.96(9)
O(1)-Ti(1)-Cl(2)	84.78(16)
Cl(3)-Ti(1)-Cl(2)	95.28(8)

Selected Bond Lengths Å	
Cl(3)-Ti(1)	2.224(4)
Cl(4)-Ti(1)	2.303(2)
O(2)-Ti(1)	2.115(5)
O(1)-Ti(1)	2.122(5)
C(4)-O(2)	1.221(8)
Cl(1)-Ti(1)	2.213(2)
Cl(2)-Ti(1)	2.292(2)
C(6)-O(1)	1.224(8)
C(4)-C(5)	1.489(12)
C(3)-C(2)	1.482(13)

3.3.1.4. Tetrachloro(diethyl succinate) titanium(IV) [3]

Diethyl succinate was reacted with an excess of titanium(IV) chloride in hexane at room temperature, which yielded yellow crystals after dichloromethane/hexane layering. ^{1}H NMR once again revealed that the ligand had coordinated to the metal centre unchanged, forming a simple 1:1 adduct (Figure 32). This was confirmed by single crystal X-ray diffraction.

Like other complexes synthesised in this work, this structure contains a ring system formed by the bidentate coordination of the ligand to the metal centre. In this case however the ring is seven membered. As with the compounds **1a** and **2** the ring is puckered, taking on the boat chair conformer, and distorted by the presence of the chloride ligands to give an acute Ti-O-Ti bond angle of 86.26(6)° (Figure 33, Table 6). This is wider than that of the malonate complex 80.23(4)° , due to the extra C-C bond making a less restrictive chelating complex.

This is to my knowledge the first time that a succinate ligand has been coordinated to titanium chloride. Due to the increased rigidity and shorter C-C bond length resulting from the double bond, the malonate structure is more strained, with a Ti-O-Ti bond angle of 81.2°.

As with the structure reported here for compound **2a**, due to the dative nature of the coordination between the malonate ligand and the Ti centre the metal oxygen distance is longer (2.1101(10) Å) than for other compounds of this type.

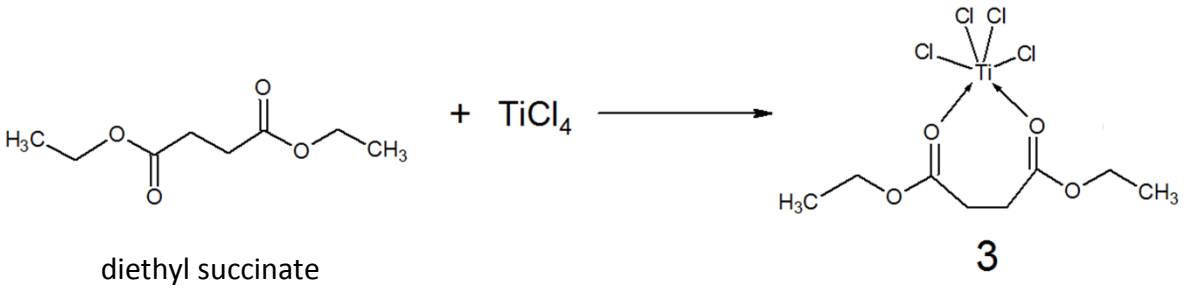

Scheme 4: reaction of $TiCl_4$ with diethyl succinate to give tetrachloro(diethyl succinate)-titanium(IV) [**3**].

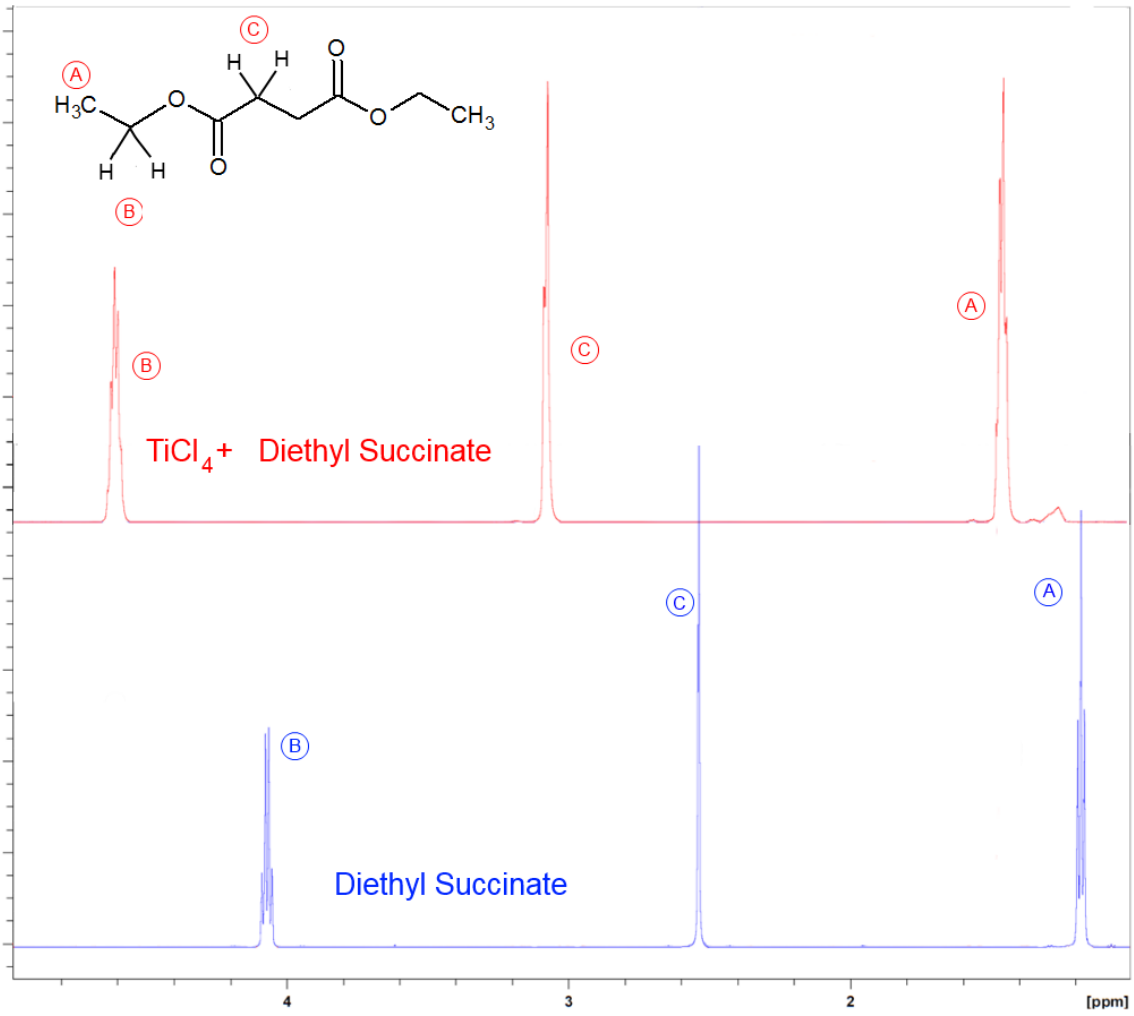

Figure 32: ^1H NMR spectra of diethyl succinate and the product of its reaction with $TiCl_4$ **[3]**, all peaks exhibiting a downfield shift indicating coordination to the titanium metal centre.

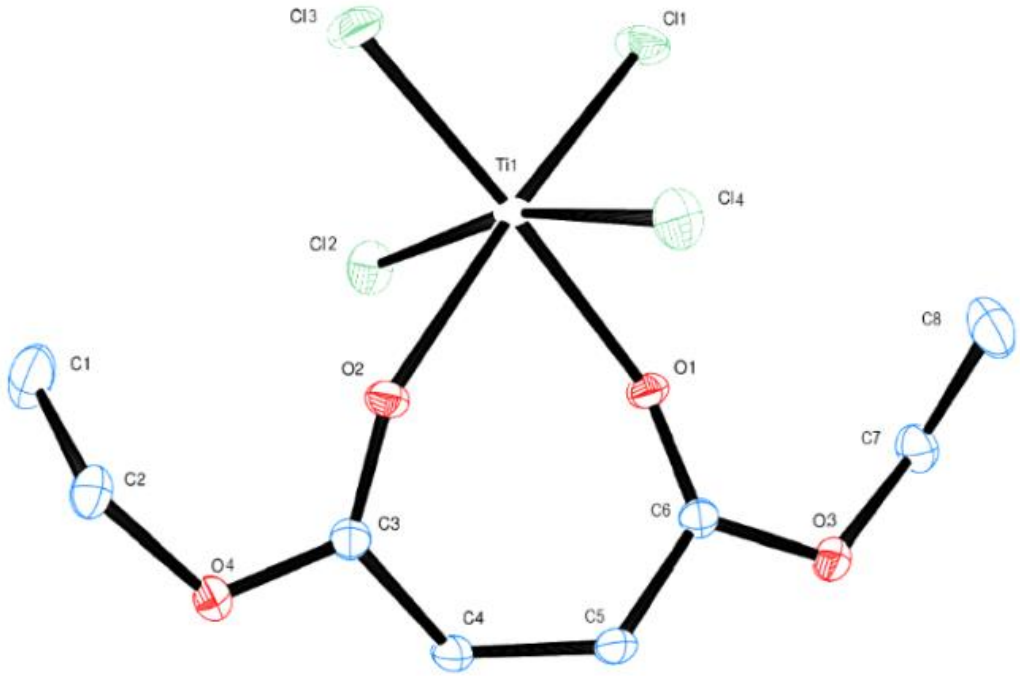

Figure 33: ORTEP representation of the crystal structure of tetrachloro (diethyl succinate)-titanium(IV) **[3]** with thermal ellipsoids at the 50% probability level. Hydrogen atoms omitted for clarity.

Table 6: Crystallographic Data and Selected bond lengths angles for the crystal structure of **3** the product of reaction $TiCl_4$ diethyl succinate

Structural Data	
crystal system	monoclinic
space group	C 2/c
a	16.6592(11) Å
b	8.5418(5) Å
c	10.3708(7) Å
α	90.000(5) °
β	98.836(3)°
γ	90.000(5)°
R_1	0.0244
wR_2	0.0669

Selected Bond Angles °	
C(4)-O(2)-Ti(1)	136.55(10)
C(6)-O(1)-Ti(1)	136.55(10)
O(1)-Ti(1)-O(2)	86.26(6)
O(1)-Ti(1)-Cl(3)	173.87(3)
O(1)-Ti(1)-Cl(4)	83.57(3)
Cl(1)-Ti(1)-Cl(4)	95.985(15)
O(1)-Ti(1)-Cl(1)	88.39(3)
Cl(1)-Ti(1)-Cl(3)	97.10(2)
O(1)-Ti(1)-Cl(2)	86.39(3)
Cl(3)-Ti(1)-Cl(2)	95.985(15)

Selected Bond Lengths Å	
Cl(3)-Ti(1)	2.2379(4)
Cl(4)-Ti(1)	2.3070(4)
O(2)-Ti(1)	2.123(2)
O(1)-Ti(1)	2.1101(10)
C(4)-O(2)	1.2408(18)
Cl(1)-Ti(1)	2.2379(4)
Cl(2)-Ti(1)	2.3070(4)
C(6)-O(1)	1.2408(18)

3.3.2. Interaction of $TiCl_4$ with Triglyceride Analogue Glycerol Tribenzoate [4]

By using diesters and triesters as model compounds for the interaction of oils with $TiCl_4$, their ability to bind other metal chlorides, while leaving $TiCl_4$ can be better understood. By knowing the portion of the oil molecule responsible for the removal and how it happens, the most effective oil or combination of oils can be found, leading to improvements in the efficiency of the Chloride Process.

Glycerol tribenzoate is a triester, meaning that of all the ligands in this study, it is the most representative of the glycerol group of the oil used for purification of $TiCl_4$ in TiO_2 production. Rather than unsaturated hydrocarbon chains however, in this case each ester group is linked to a benzene ring. This simpler molecule serves as a close analogue to the structure and reactivity of the glyceride group of the oils used in the Chloride Process, however the absence of long alkyl chains makes the characterisation of the product, as well as the growth of single crystals, more facile. Glycerol tribenzoate was reacted with excess $TiCl_4$ under Schlenk conditions in hexane (Scheme 5). An excess of $TiCl_4$ was used as the product's lack of solubility in hexane means that the excess reagent could easily be removed *via* filtration. This is in fitting with the Chloride Process, where the oil is added stoiciometrically in far lower amounts. After two hours a yellow product was observed, which was washed with hexane and dried *in vacuo*. Crystals suitable for single X-ray crystallography were grown by making a concentrated solution of **4** in dichloromethane and cooling to -1 °C for 1 month.

The ^1H NMR spectrum for unreacted glycerol tribenzoate shows two sets of doublet of doublets around 4.7 ppm. These represent the inequivalent CH_2 environments situated on

the ends of the molecule's central propyl carbon chain, which couple to each other as well as the proton on the central carbon. Upon reaction of $TiCl_4$ with the glycerol.

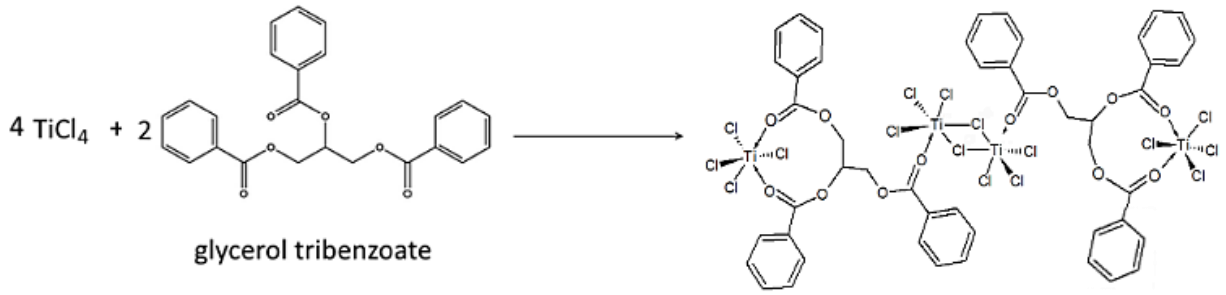

Scheme 5: Schematic of the synthesis of compound **4**, formed by the reaction of $TiCl_4$ in hexane with glycerol tribenzoate.

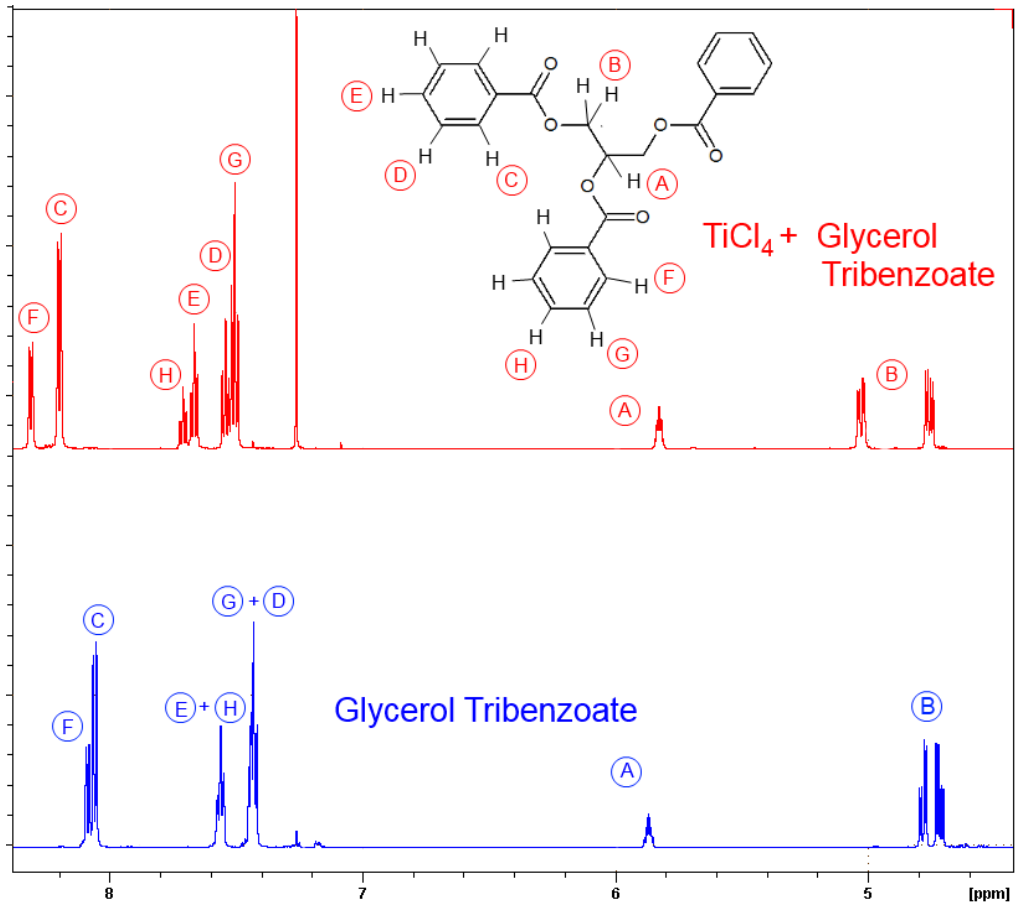

Figure 34: ^1H NMR spectra of glycerol benzoate and the product of its reaction with $TiCl_4$ **[4]**, all peaks exhibiting a downfield shift indicating coordination to the titanium metal centre.

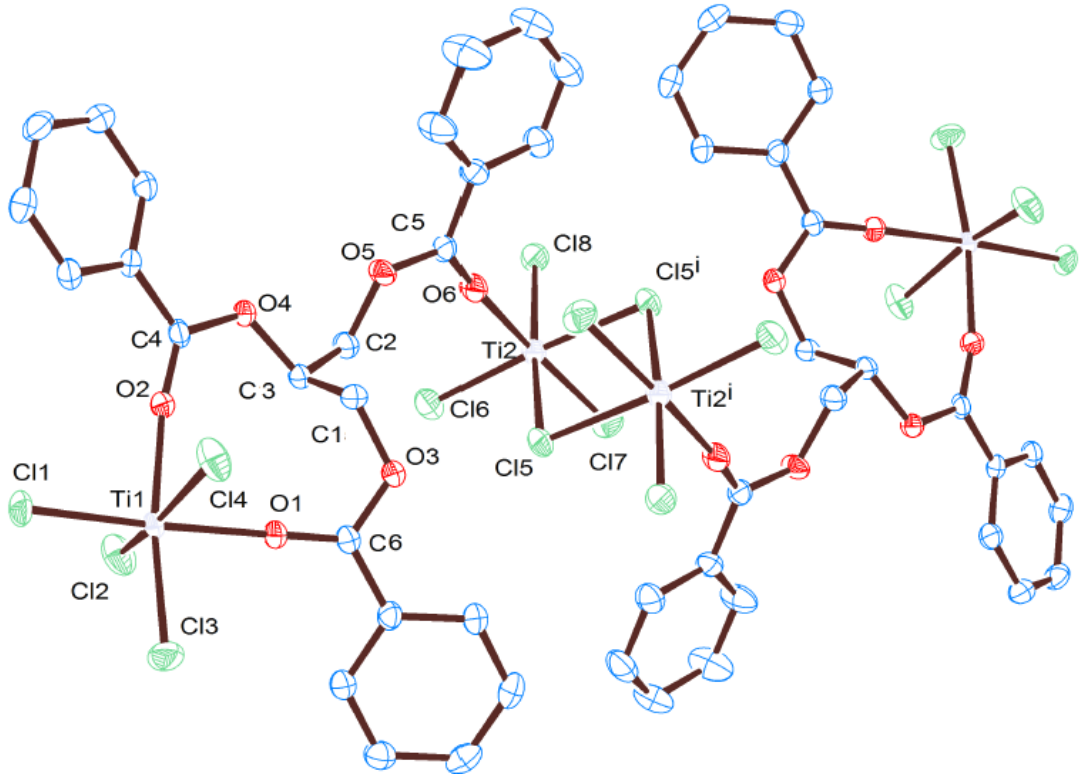

Figure 35: ORTEP representation of **4** as determined by single crystal X-ray diffraction, with thermal ellipsoids at the 50% probability level. Hydrogen atoms omitted for clarity.

Table 7: Crystallographic Data and Selected bond lengths angles for the crystal structure of 4 the product of reaction $TiCl_4$ and glycerol tribenzoate.

Structural Data	
crystal system	Triclinic
space group	P-1
a	9.9955(3) Å
b	13.9772(3) Å
c	14.4644(4) Å
α	71.868(2)°
β	76.307(2)°
γ	77.073(2)°
R_1	0.0381
wR_2	0.0977

Selected Bond Angles °	
C(4)-O(2)-Ti(1)	164.3(2)
C(6)-O(1)-Ti(1)	170.7(2)
O(1)-Ti(1)-O(2)	83.59(8)
O(1)-Ti(1)-Cl(3)	177.38(7)
O(1)-Ti(1)-Cl(4)	87.98(6)
Cl(1)-Ti(1)-Cl(4)	94.63(3)
O(1)-Ti(1)-Cl(1)	93.79(6)
Cl(1)-Ti(1)-Cl(3)	98.32(4)
O(1)-Ti(1)-Cl(2)	84.49(7)
Cl(3)-Ti(1)-Cl(2)	95.38(3)
O(6)-Ti(2)-Cl(7)	171.73(7)
O(6)-Ti(2)-Cl(6)	90.13(7)
O(6)-Ti(2)-Cl(5i)	84.62(7)
Cl(5)-Ti(2)-Cl(8)	167.70(4)
Cl(5i)-Ti(2)-Cl(8)	92.11(3)
Cl(5i)-Ti(2)-Cl(5)	78.41(3)

Selected Bond Lengths Å	
Cl(3)-Ti(1)	2.2258(9)
Cl(4)-Ti(1)	2.2756(9)
O(2)-Ti(1)	2.124(2)
O(1)-Ti(1)	2.101(2)
C(4)-O(2)	1.228(3)
Cl(1)-Ti(1)	2.2234(8)
Cl(2)-Ti(1)	2.2938(9)
C(6)-O(1)	1.227(3)
Ti(2)-Cl(5)	2.5002(8)
Ti(2)-Cl(7)	2.2328(9)
Ti(2)-O(6)	2.020(2)

tribenzoate one of these peaks was shifted upfield by 0.2 ppm whereas the other only shifts by 0.1 ppm, in comparison to the free ligand.

The ^{13}C {^{1}H} NMR shows a shift for the signal of the carbonyl, upfield from 174 to 168 ppm compared to the free ligand, which is due to the formation of a dative bond to the titanium centre reducing the shielding around the carbon (Figure 34).

The crystal structure of **4** shows two different environments for the $TiCl_4$ bound to the glycerol tribenzoate. In one of these environments titanium is bound to four chlorine atoms and also to two carboxyl oxygen atoms of the same glycerol tribenzoate (Figure 35). The bond distances and angles observed around this titanium centre which adopts a distorted octahedral coordination geometry, are similar to those observed for the diester complexes **1-3.**

The third carbonyl oxygen of the glycerol benzoate molecule, rather than coordinating to the same titanium centre, which would be sterically unfavourable, instead coordinates to a second $TiCl_4$ molecule. This leads to an electron deficient, 5 coordinate $TiCl_4$ centre. This species would be highly unstable as a monomer and thus dimerises. A two chloro-bridged dimeric species is formed, with the two central titanium atoms taking on edge sharing octahedral geometry. The bridging Ti-Cl bond distance of 2.5002(8) Å is longer than the terminal Ti-Cl bond distances observed to be on average 2.244(16) Å (Table 7). This is unsurprising as the electron density of the bridging chloride is shared between two metal centres rather than just one in the case of the terminal chlorine.

Furthermore among the terminal Ti-Cl bonds, it is observed that those *trans* to the ester carbonyl are notably shorter than the equivalent *cis*-chlorines. This is a result of

the carbonyl oxygen being less electron withdrawing than the chlorine and thereby increasing the electron density around the chlorine opposite. For example Ti(1)-Cl(1) (*trans*) and Ti(1)-Cl(2) (*cis*) are 2.2234(8) and 2.2938(9) Å respectively, a difference of 0.0704 Å. This is also the case for products **1-3**, all of which show a shortening of the Ti-Cl bond *trans* to the ester carbonyl of 0.7–1.0 ppm, due to the trans influence of the coordinating carbonyl group.

The formation of chloro-bridged bimetallic titanium species is relatively commonplace. Wu *et al.* reacted 2-propanol and $TiCl_4$ to produce a Ti_2Cl_8 dimer.[96] What is of note in the case of this species is that despite the complexity of the molecule formed, there is no elimination of any chloride species as a result of the reaction. Only addition followed by dimerisation of the resulting bimetallic species was observed. This is of interest in relation to the Chloride Process as the $TiCl_4$ is still intact within the molecule, and therefore at the high temperatures used in industrial synthesis, this coordination would be reversible.

3.3.3. Interaction of Glycerol Tribenzoate and Diesters With $VOCl_3$

Excess vanadium(V) oxytrichloride was reacted with the bidentate dicarbonyl ligands; 2,4-pentadione, diethyl malonate, bis-isopropyl malonate, and diethyl succinate and glycerol tribenzoate to yield compounds **5, 6, 7, 8** and **9** in anhydrous hexane under an atmosphere of nitrogen. Repeated attempts to grow single crystals of the resulting compounds were made, of which only **5, 6** and **7** were successful**.** These crystals revealed that the reactions had yielded a monomeric species, an oxo-bridged tetramer and a one dimensional coordination polymer, respectively.

In each case the loss of chlorine from the $VOCl_3$ was observed. This is significant as having lost a chlorine atom from the metal centre, dissociation of the ligand would not be enough to restore the staring material. This makes the reaction less reversible than those observed with titanium in complexes **1- 4**, when dissociation of the ligand would leave $TiCl_4$ completely intact.

In the production of TiO_2 *via* the Chloride Process, the addition of oil is carried out at around 200 °C, and hence all of the metal chlorides present are in the vapour phase. At this temperature, the dative coordination observed for titanium would likely be more reversible as the extreme conditions would make the ligand more labile. The reactions with $VOCl_3$, explain the preference with which the glyceride-containing oils are able to remove $VOCl_3$ from a gaseous $TiCl_4$ stream.

3.3.3.1. Dichloro(oxo) (2,4-Pentanedione) Vanadium(V) [$VOCl_2$(acac)] [5]

Excess $VOCl_3$ was reacted with 2,4-pentadione (acacH) and stirred for 2 hours under a nitrogen environment. A dark precipitate in a dark red solution formed immediately but the mixture was stirred for 2 hours to ensure full reaction. The dark purple product, [$VOCl_2$(acac)] (**5**), was dissolved in dichloromethane and layered with hexane. After a week, small black crystals were observed which were suitable for single crystal X-ray crystallography. The crystal structure for compound **5** is shown in Figure 37 along with selected bond lengths and angles in Table 5.

^{1}H NMR of **5** showed a peak at 2.39 ppm corresponding to the methyl groups on the acac ligand, which was upfield to the same peak, observed at 2.2 ppm, in uncoordinated acacH (Figure 36). Two further peaks were observed at 3.5 ppm and 5.4

ppm in uncoordinated acacH, which represent the H atoms bonded to the central bridging carbon. These normally equivalent protons are responsible for two different chemical shifts because one proton can freely dissociate, giving a conjugated system. When two protons are bound to the carbon atom the chemical shift is 3.5 ppm, however upon disassociation of one of the protons, shielding around the remaining proton increases, leading to a downfield shift to 5.4 ppm. This is a very useful tool in determining coordination. In the ^{1}H NMR spectrum of **5** only one further peak (in addition to the peak at 2.39 ppm) was observed at 6.13 ppm. The integral of this peak has a 6:1 ratio with the peak corresponding to the two methyl groups at 2.39 ppm. This provides clear evidence that one proton from the acac ligand has been lost on coordination to the vanadium centre with a concordant upfield chemical shift of 0.7 ppm. This suggests that the reaction of $VOCl_3$ with acacH proceeds *via* loss of HCl, as shown in Scheme 6.

The structure of compound **5** shows that the acac ligand is bound to the vanadium centre *via* the carbonyl oxygen atoms (Figure 37). The V-O bond lengths are 1.918(3)Å for O(2) and 1.904(3) Å for O(3). These are shorter than typical dative V-O bond distances of ~2.1 Å, as described for **6** and **7** (*vide infra*) and is the result of the increased electron density given from the carbonyl oxygen. A proton from C(3) was lost in the reaction and a delocalised system is therefore created between O(3), C(2), C(3), C(4) and O(2) (Table 8).

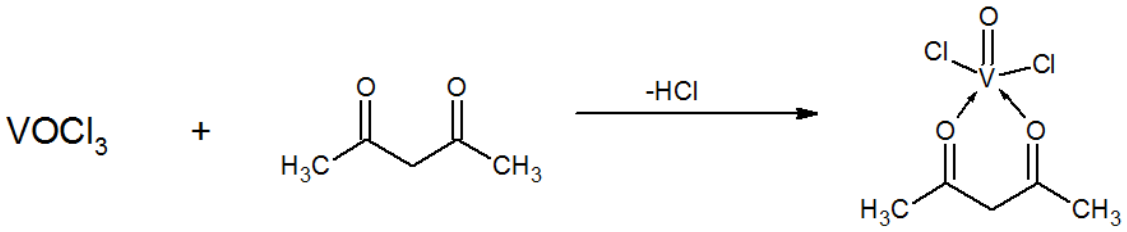

Scheme 6: Schematic of the synthesis of compound **5**, formed by the reaction of $VOCl_3$ in hexane with diethyl malonate

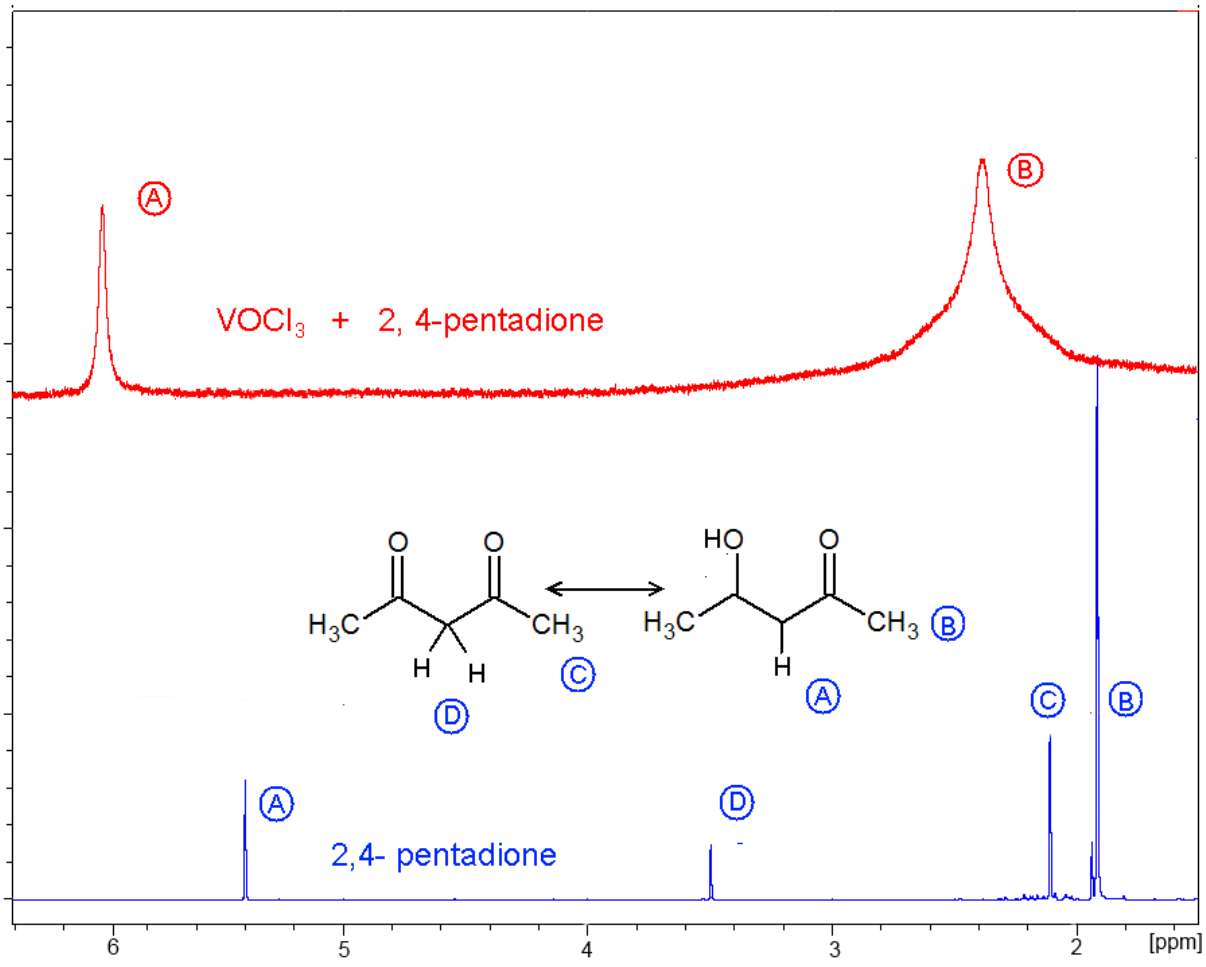

Figure 36: ^1H NMR spectra of 2,4 pentadione and the product of its reaction with $VOCl_3$ **[5]**, The signals relating to the non-conjugated variant of acac are completely removed in the spectrum of 5, indicating that coordinating to the $VOCl_3$ is responsible for loss of a proton. Both peaks exhibiting a downfield shift indicating coordination to the vanadium metal centre.

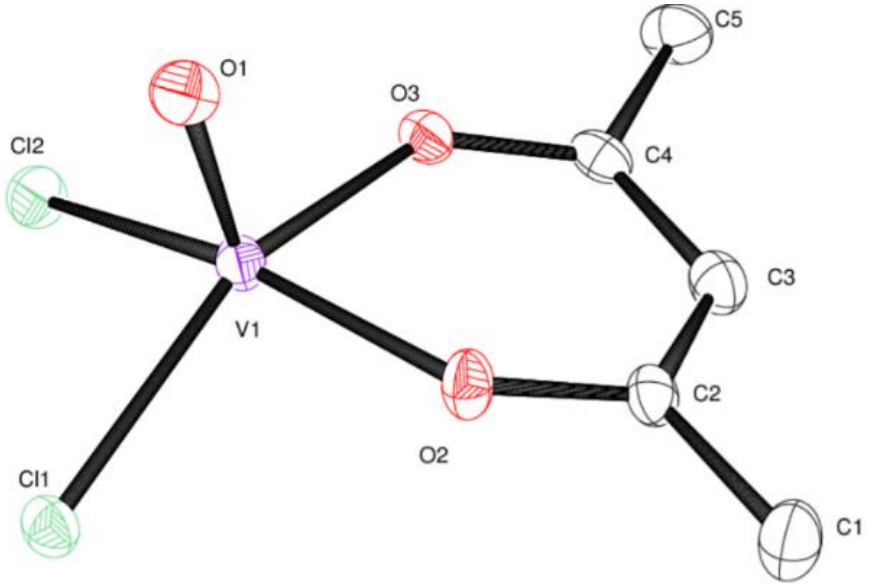

Figure 37: ORTEP representation of crystal structure of [$VOCl_2$(acac)] **[5]** with thermal ellipsoids at the 50% probability level. Hydrogen omitted for clarity.

Table 8: Crystallographic Data and Selected bond lengths angles for the crystal structure of **5** the product of reaction $VOCl_3$ and 2,4 pentadione.

Structural Data	
crystal system	monoclinic
space group	P21/c
a	15.3393(8) Å
b	9.7939(5) Å
c	8.6842(5) Å
α	90
β	94.664(5)
γ	73.746(5)
R Factor	3.21%

Selected Bond Angles °	
Cl2 - V1 - Cl1	93.45(3)
O1 - V1 - Cl1	99.58(9)
O1 - V1 - Cl2	99.94(9)
O1 - V1 - O2	100.11(10)
O1 - V1 - O3	101.11(10)
O2 - V1 - Cl2	159.64(7)
O2 - V1 - O3	84.62(9)
O2 - V1 - Cl1	86.68(8)
O3 - V1 - Cl2	88.12(7)

Selected Bond Lengths Å	
V1 - Cl1	2.2880(8)
V1 - Cl2	2.2275(9)
V1 - O1	1.569(2)
V1 - O2	1.903(2)
V1 - O3	1.918(2)
O2 - C2	1.290(4)
O3 - C4	1.283(4)
C2 - C3	1.398(4)
C3 - C4	1.398(4)

This results in the ligand having an overall negative charge, which is stabilised by the reaction with the $VOCl_3$ resulting in a stronger bond to the vanadium than seen in complexes of $VOCl_3$ with the diesters, diethyl malonate and diethyl succinate (*vide infra*). This is evidenced in the crystal structure of **5** in which the C2-C3 and C3-C4 bonds between the carbonyl groups appear shortened (1.398(5) Å and 1.382(5) Å

respectively).[22] This shows that the central carbon has been deprotonated leading to a conjugated 6 membered ring system as is frequently seen with coordination compounds of acac.[23]

Compound **5** is five coordinate, which is common for vanadium species, particularly when a V=O bond is present. This is also seen for $[VO(acac)_2]$, a five coordinate species in which the 4 carbonyl oxygen atoms take an almost square planar geometry with the double bond perpendicular.[24] In the case of compound **5**, the geometry is similar, with bond angles between the oxygen atoms in the acac O(2)–V(1)-O(3) at 84.59(12)°, whereas the angle between the chlorine atoms and the equivalent oxygen atoms on the acac are wider, at 86.68(8)° and 88.12(8)°, respectively for O(2)-V(1)-Cl(1) and O(3)-V(1)-Cl(2). The angle between the two chlorines (Cl(1)-V(1)-Cl(2)) is widest at 93.47(4)°. This is due to the increased repulsion between the chlorine atoms due to their greater electron density.

3.3.3.2. Dichloro(oxo) (diethyl malonate) Vanadium(V) $[\{VOCl_2(CH_2(COOEt_2)\}_4]$ [6]

Diethyl malonate was reacted with an excess of $VOCl_3$ at room temperature, which yielded dark red crystals of $[\{VOCl_2(CH_2(COOEt_2)\}_4]$ **[6]** after layering a concentrated solution of **6** in dichloromethane with hexane (Scheme 7).The ^1H NMR spectra of compound **6** shows that peaks corresponding to the coordinated ligand have shifted downfield compared with that of the unreacted malonate starting material (Figure 38). The protons on the central carbon showed the greatest shift, implying they are most heavily deshielded by the presence of the vanadium, with the signal shifting downfield to 3.5 ppm from 3.2 ppm for the unreacted ligand. NMR spectroscopy displayed strong

peak broadening may suggest the presence of a paramagnetic vanadium species, however the crystallographic data (*vide infra*) would suggest otherwise, as the malonate has not been deprotonated as with the acac, implying a redox exchange has not occurred. It is more likely that there is a degree of ligand exchange happening between the vanadium atoms in solutions, resulting in the loss of peak resolution.

Single crystal X-ray diffraction analysis of the red crystals revealed that the tetrameric complex $[\{VOCl_2(CH_2(COOEt))_2\}]_4$ **6** had formed, as shown in Figure 39. The crystal structure of compound **6** is a tetramer linked by four bridging oxygen atoms. From each of the bridged vanadium centres a chlorine atom has been lost and the coordination sphere filled with the bridging V-O bond. Around each vanadium atom there are 4 V-O bonds. The two longest bonds are the dative bonds to the carbonyl groups of the diethyl malonate. These are similar to the equivalent Ti-O bond lengths (2.112(4) Å and 2.102(4) Å) observed for the same malonate ligand coordinating to titanium tetrachloride.[97] In the case of the $TiCl_4$ however, all four chlorides are retained, giving a monomeric species. The C(2)-C(3) bond lengths of the central carbon chain are equivalent to those of the side group C(6)-C(7), (1.496(9) &1.498(7) Å respectivelty) suggest that no deprotonation as occurred (as with **1-3** but unlike with $VO(acac)_2$).

The other two V-O bond lengths represent the bridging oxygen bonds, this shows that the oxygen atom does not sit equidistant between the two vanadium atoms. The shorter of the two has a length of 1.623(3) Å, close to that expected for a V=O bond, for example 1.595(5) Å observed in $VOCl_3$.[25] The other bridging V-O bond distance was considerably longer at 2.036(3) Å, resembling the dative coordination of the malonate. This shows that the original V=O bond in the $VOCl_3$ has not been broken but datively

coordinates to another vanadium atom. This structure has been reported previously by Sobota *et al.* formed *via* reaction of $[V_2(\mu\text{-}Cl)_2Cl_2(MeCO_2Et)_2]$ with diethylmalonate to give $[V_2(\mu\text{-}Cl)_2Cl_2(MeCO_2Et)_4]$, which was exposed to air to give **6**.[98]

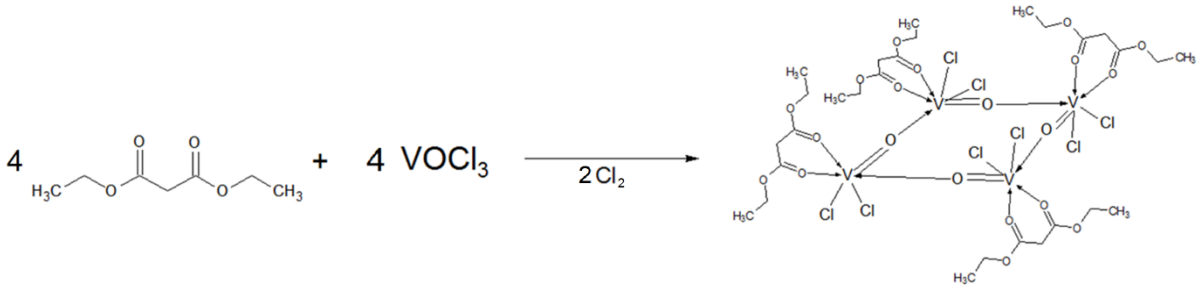

Scheme 7: Schematic of the synthesis of compound **6**, formed by the reaction of $VOCl_3$ in hexane with diethyl malonate

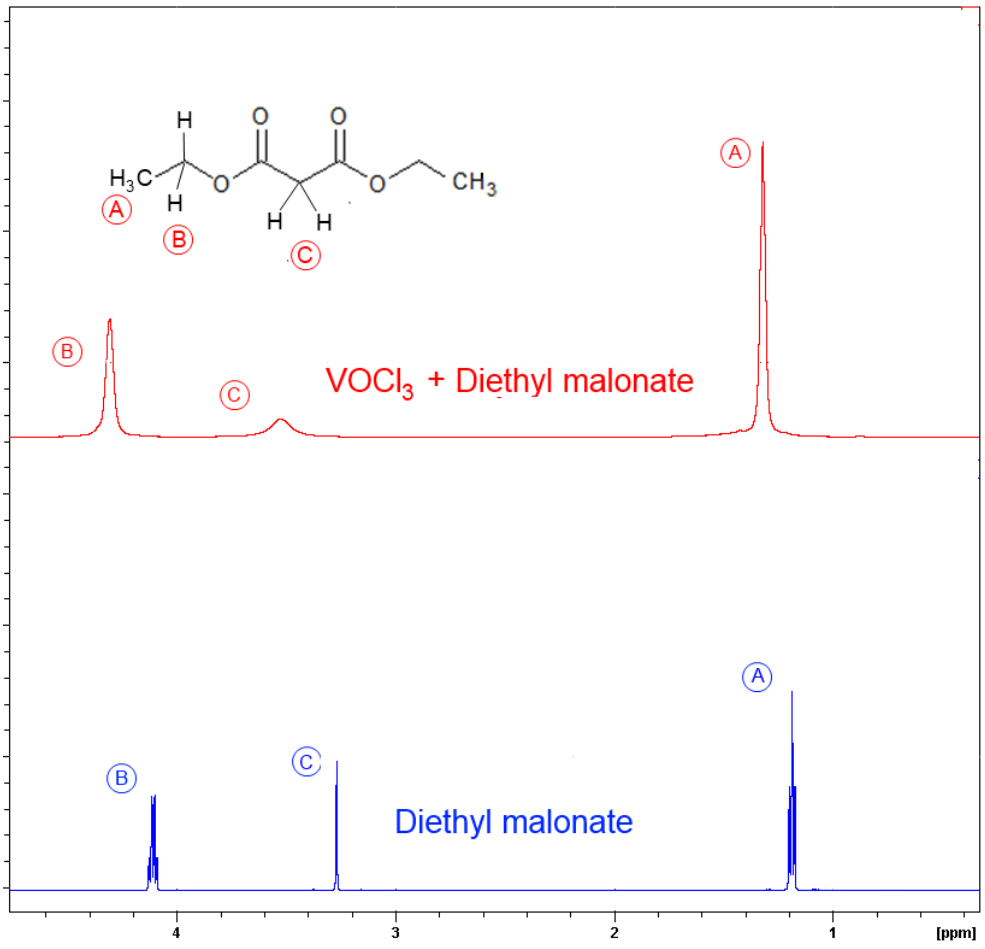

Figure 38: ^{1}H NMR spectra of diethyl malonate and the product of its reaction with $VOCl_3$ **[6]**, all peaks exhibiting a downfield shift and experiencing broadening indicating coordination to the vanadium metal centre

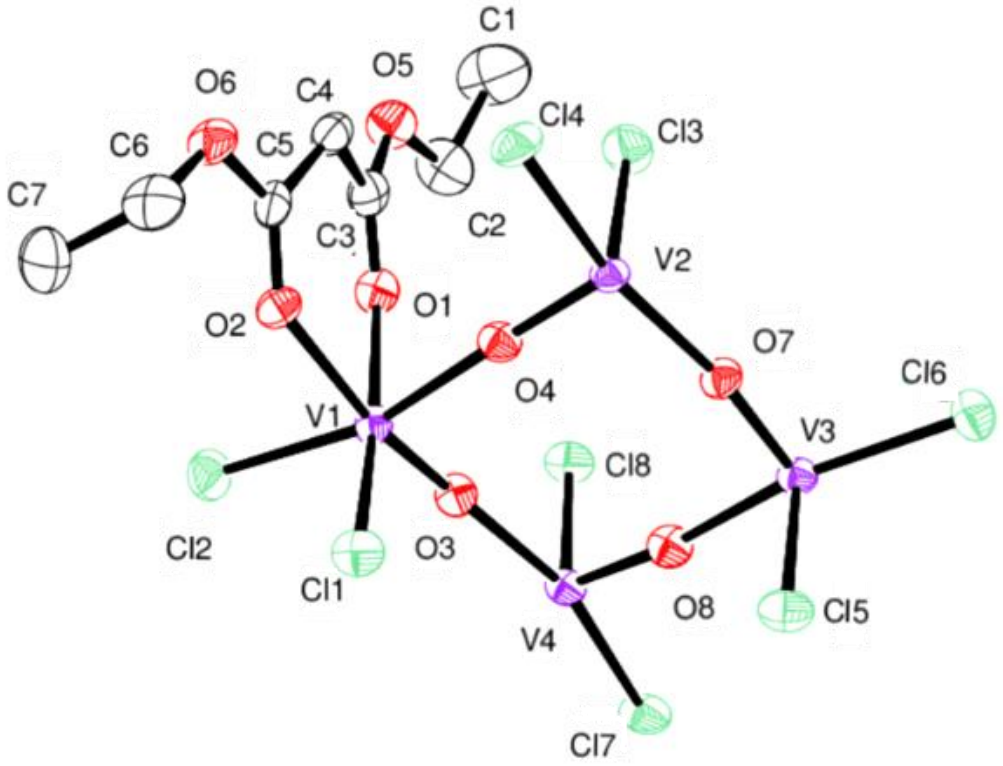

Figure 39: ORTEP representation of crystal structure of [{$VOCl_2(CH_2(COOEt_2)\}_4$] **[6]** with thermal ellipsoids at the 50% probability level. Three of the four diethyl malonate molecules and all hydrogen atoms omitted for clarity.

Table 9: Crystallographic Data and Selected bond lengths angles for the crystal structure of **6** the product of reaction $VOCl_3$ and diethyl malonate

Structural Data	
crystal system	Triclinic
space group	P-1
a	12.516(5) Å
b	13.338(5) Å
c	17.573(5) Å
α	85.751(5)
β	84.006(5)
γ	90.000(5)
R Factor	5.51%

Selected Bond Angles °	
O1–V1–Cl2	89.07(10)
O4–V1–O1	83.64(13)
O1–V1–O2	80.58(12)
O3–V1–O1	93.47(14)
O3–V1–O2	171.21(15)
Cl1–V1–Cl2	93.66(5)
V1–O3–V4	172.1(2)
O4–V1–O2	78.95(12)
C3–O1–V1	133.1(3)

Selected Bond Lengths Å	
V1 - O1	2.077(3)
V1 - O2	2.148(3)
V1 - O3	1.623(3)
V1 - O4	2.036(3)
V4 - O3	2.027(3)
O2 - C5	1.222(6)
C3 - C4	1.498(7)
C4 - C5	1.492(7)
C6 - C7	1.496(9)

In this work however, a direct route to **6** is reported from $VOCl_3$ and diethyl malonate. Despite **6** being the same the structure reported by Sobota *et al.*, with similar R factors (4.94% *cf*. 5.51%), the crystallographic data differs, which is likely a result of collection temperature (283-303 K *cf.* 150 K). This in turn has resulted in significant differences in the unit cell dimensions (Sobota structure has the unit cell dimensions: a = 12.655(4) Å, b = 13.735(3) Å, c = 18.141(3) Å, compared with: a = 12.5230(2) Å, b = 13.3895(2) Å, c = 17.5946(3) Å, reported here). The low temperature collection reported here has been submitted to the CCDC since there are noticeable differences in the majority of the bond lengths and angles of the two structures and we consider this of interest to the field. For example the V-O bond distance between the vanadium and the carbonyl groups on the malonate is 2.177(6) Å in the previously reported structure, but considerably shorter in this case at only 1.904(3) Å.

Dimeric oxo-bridged vanadium complexes have been produced in a similar way by reaction of $VOCl_3$ and pinacol. In this case one of the oxygen atoms of each pinacol ligand is coordinated to both vanadium centres, acting as bridges, with the other oxygen coordinating to one.[99] The V-O bond lengths observed for the bridging oxygen atoms are 2.0211(11) Å, resembling the dative coordination of the malonate, rather than a direct oxo bridge. This is likely due to the electron decent nature of the vanadium centre. The dative V-O bond length of 2.077(3) Å in **6** is still shorter than the V-Cl bonds at 2.3031(13) Å. This shows how the coordination sphere of the oxygen is important in these reactions, and until the oxygen is bound to two other elements it will be reactive when subjected to an electron poor metal centre.

In compound **6**, each of the vanadium atoms are coordinated to two chlorine atoms, having lost one on coordination to the ligand. The lengths of the C-C bonds between the two carbonyl groups are 1.492(7) and 1.496(9) Å which indicates that both are single bonds.[22] This implies that the coordination to the vanadium centre has not lead to the loss of a proton from the central carbon atom resulting in the evolution of HCl as would be expected and observed in the formation of compound **5**. Had this occurred the C-C bond lengths would be shortened to around 1.38 Å due to the increased electronic density resulting from the aromaticity of the resulting species. Therefore, the vanadium centre has been reduced to V(IV) from V(V) with concurrent oxidation of chloride ligands to elemental chlorine. This has been observed previously in the reaction of $VOCl_3$ with 2-ethoxy ethanol, which was shown to coordinate in a bidentate fashion to the vanadium whilst maintaining the ethanoic proton.[28] This reaction was found to result in the reversible loss of chlorine ligands *via* oxidation to Cl_2. Vapours from the reaction were found to test positive for Cl_2 gas.[100]

3.3.3.3. Dichloro(oxo)(diethyl succinate) Vanadium (V) $[VOCl_2\{C_2H_4(CO_2Et)_2\}]_n$ [7]

Excess $VOCl_3$ was reacted with diethyl succinate in hexane and stirred for 2 hours under nitrogen. The reaction mixture turned from orange to dark red over 5 minutes and was left to stir for 2 hours to ensure a full reaction. The reaction yielded a dark red oily product (Scheme 8). The flask was left under nitrogen for one month, during which time, green crystals of compound **7** were formed which were suitable for single crystal X-ray crystallography. The NMR spectrum of **7** showed customary peak broadening associated with coordination to a paramagnetic vanadium species (Figure 40).

The diethyl succinate acts as a bidentate ligand in **7**, with each carbonyl binding to a different metal centre rather than chelating as was observed with the malonate ligand in compound **6**. Likewise, each vanadium centre forms bonds with two different ester groups thus forming a polymer chain. This polymer chain is classed as a one dimensional coordination polymer. Coordination polymers are metal-ligand complexes that extend "indefinitely" into one, two or three dimensions *via* covalent metal-ligand bonding. Coordination polymers are also known as metal organic frameworks (MOFs).[101,102] One dimensional coordination polymers are of particular interest for their electronic properties, for use as nanowires.[103,104]

The first non-cluster vanadium coordination polymer was synthesised by Zhang *et al*. in 2001, with the synthesis of $[VO(dod)_2]X_2$ (X = Cl, Br; dod = 1,4-diazoniabicyclo[2,2,2]octane-1,4-diacetate].[105] There have been other reported 1-dimensional coordination polymers containing vanadium, one with *O*,*O*,*N*-dichelating ligands[106] and a further from the reaction of vanadium sulfate with 1,3-aryl-linked *bis*-β -diketones in aqueous alcohol and sodium acetate followed by 4,4-bipyridine, which stabilises formation of a polymeric species.[107] Furthermore, succinate has been used as a bridging ligand in a cobalt based MOF, forming a similar one dimensional chain, stabilised with benzadine ligands.[108]

This is the first mononuclear 1-dimensional vanadyl coordination polymer to be isolated as a single crystal and the structure probed by X-ray diffraction. The presence of the two V-Cl bonds makes the polymer extremely moisture sensitive. The vanadium centre is similar to that in **6** in that it is five coordinate, bound to three oxygen atoms and two chlorine atoms. The complexes differ in the way that the ligand is oriented. In

compound **5,** the carbonyl oxygen atoms are *cis* to each other since they are from the same acac ligand. In compound **7**, the carbonyl oxygen atoms originate from two different molecules and are positioned axial to each other, rather than equatorial, as in the case for **5**.

This is reflected in the O(1)-V(1)-O(2^1) bond angle of 167.72(6)˚ in **7**, whereas in compound **5** the equivalent O-V-O angle between the carbonyl oxygen atoms is 84.59(12)˚ (Figure 41).

Structure **7** differs from the related cobalt polymer synthesised by Roy *et al*.,[34] since the O-M-O bond angle was observed to be 180°. This is due to the electronegativity of the two chloride ligands, resulting in the Cl(1)-V(1)-Cl(2) bond angle being 131.62(3)°, as opposed to the expected 120° for a five coordinate geometry. Regardless of this the chain is linear due to the positioning of the succinate bridge.

The V-O bond lengths in **7** for the carbonyl oxygen atom are 2.0483(13) Å and 2.0370(13) Å respectively, which resembles the dative coordinative bonds observed with the malonate ligand in **6**. It is likely that $VOCl_3$ forms this polymer because of the two bridging carbon atoms between the ester groups. When there is one bridging carbon, as is the case with the malonate and the acac, both of the carbonyl oxygen atoms lie on the same side of the chain. In the case of the succinate ligand there are two bridging carbon atoms, the bond between which can rotate freely, allowing the carbonyls to lie on opposite sides due to steric hindrance. This appears to be the more favoured conformation of the ligand, most likely due to the presence of the relatively large, electron rich chlorine centres.

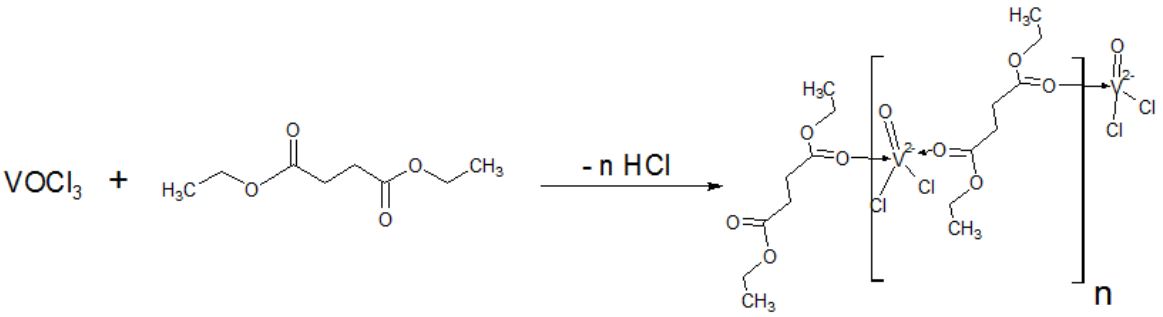

Scheme 8: Schematic of the synthesis of compound **7**, formed by the reaction of $VOCl_3$ in hexane with diethyl succinate.

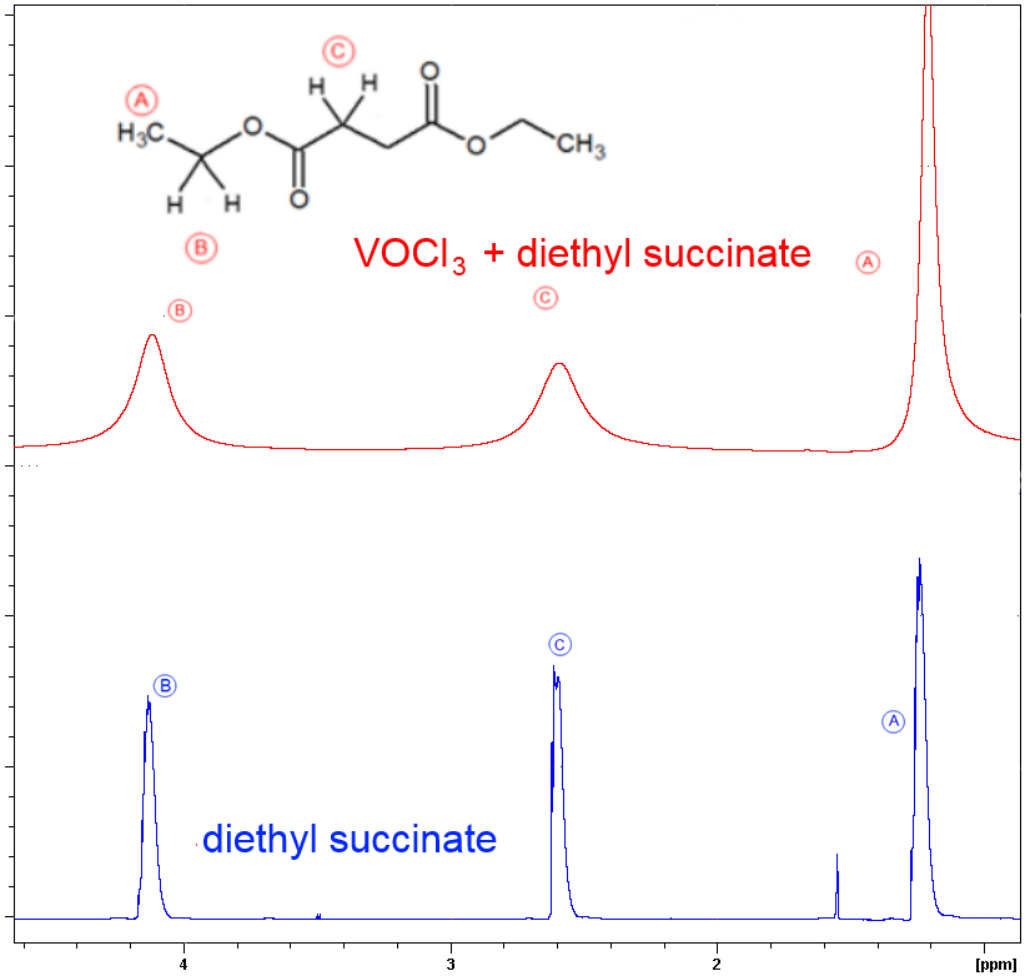

Figure 40: ^1H NMR spectra of diethyl succinate and the product of its reaction with $VOCl_3$ **[7]**, all peaks exhibiting a downfield shift and experiencing broadening indicating coordination to the vanadium metal centre.

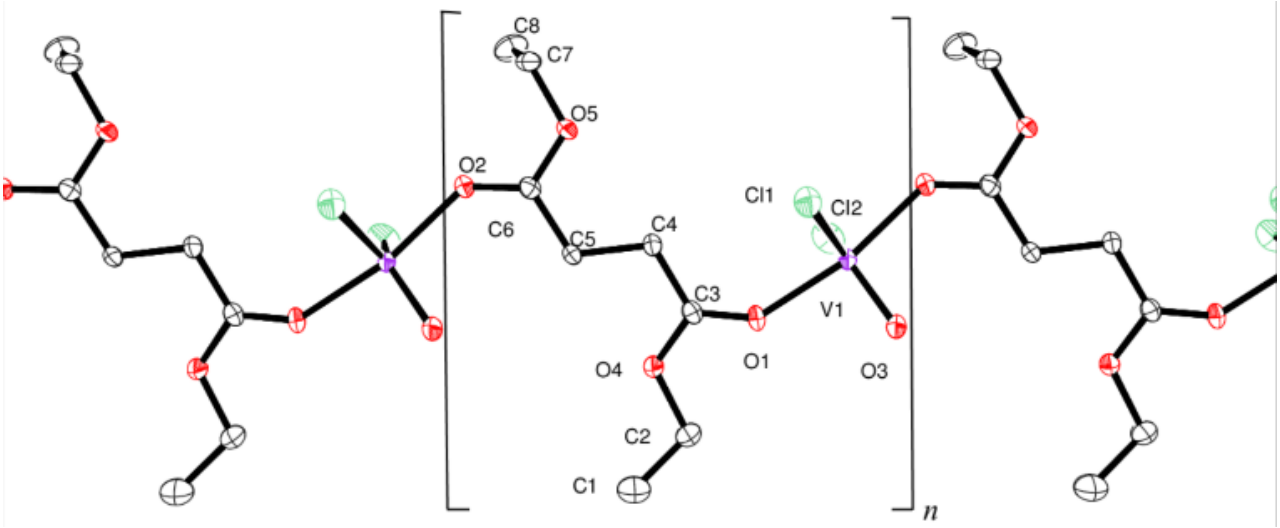

Figure 41: ORTEP representation of crystal structure of $[VOCl_2\{C_2H_4(CO_2Et)_2\}]_n$ (7) with thermal ellipsoids at the 50% probability level. Hydrogen omitted for clarity.

Table 10: Crystallographic Data and Selected bond lengths angles for the crystal structure of **7** the product of reaction $VOCl_3$ and diethyl succinate.

Structural Data	
crystal system	orthorhombic
space group	P212121
a	8.3503(3) Å
b	13.5046(4) Å
c	15.2041(5) Å
α	90.000(5)
β	90.000(5)
γ	90.000(5)
R Factor	3.40%

Selected Bond Lengths Å	
Cl2 - V1 - Cl1	131.62(3)
O3 - V1 - Cl1	113.26(6)
O3 - V1 - O1	93.40(7)
O3 - V1 - $O2^1$	98.62(6)
O1 - V1 - Cl2	85.88(4)
$O2^1$ - V1 - Cl2	86.74(4)
C3 - O1 - V1	142.20(13)
C3 - C4 - C5	113.60(16)
$O2^1$ - V1 - O1	167.72(6)

Selected Bond Angles °	
V1 - Cl1	2.2854(6)
V1 - Cl2	2.2776(6)
V1 - O3	1.5783(14)
V1 - O1	2.0483(13)
V1 - $O2^1$	2.0370(13)
C3 - C4	1.487(3)
O1 - C3	1.228(2)
O4 - C3	1.312(2)
O2 - C6	1.237(2)
O5 - C6	1.312(2)
O5 - C7	1.473(2)
C4 - C5	1.530(3)

Each of the diester molecules were observed to coordinate datively to the vanadium metal centre, facilitated by the loss of a chlorine ligand, as was observed for compound **6**. The structures differ greatly according to the ligand, with the malonate appearing to favour oxo-bridged oligomeric structures, whilst the less oxygen rich acac favours a simple monomeric species. This can be related to the effectiveness of the mineral oil as a means of removing $VOCl_3$ in the Chloride Process as opposed to other organic mixtures. By encouraging the formation of oligomeric species the likelihood of vanadium crashing out of the $TiCl_4$ as a solid or liquid in the Chloride Process rather than passing through the distillation column is increased, leading to a cleaner final product. Another interesting characteristic of the diester species is that both the ^1H NMR spectra and bond lengths observed suggests that there is no deprotonation of the ligand to form a conjugated species, as is observed in the acac ligand. This is unexpected, especially for the diethyl malonate ligand, the deprotonated state of which is widely used in organic synthesis.[35] This may relate back to the propensity for forming oligomeric and polymeric species, which could facilitate the loss of Cl_2 gas in the event of the dimerisation of two unstable $VOCl_3L$ centres as a preferable reaction pathway.[28]

3.3.3.4. Reaction of $VOCl_3$ with Other Species

In addition to the above three structures, $VOCl_3$ was reacted with other ester species, however it proved impossible to isolate crystals of these products. Bis-isopropyl malonate and glycerol tribenzoate were reacted with $VOCl_3$ to give **8** and **9** respectively. Compound **8** was formed under the same conditions as **5, 6** and **7** with the ligand added dropwise to a solution of $VOCl_3$ in hexane.

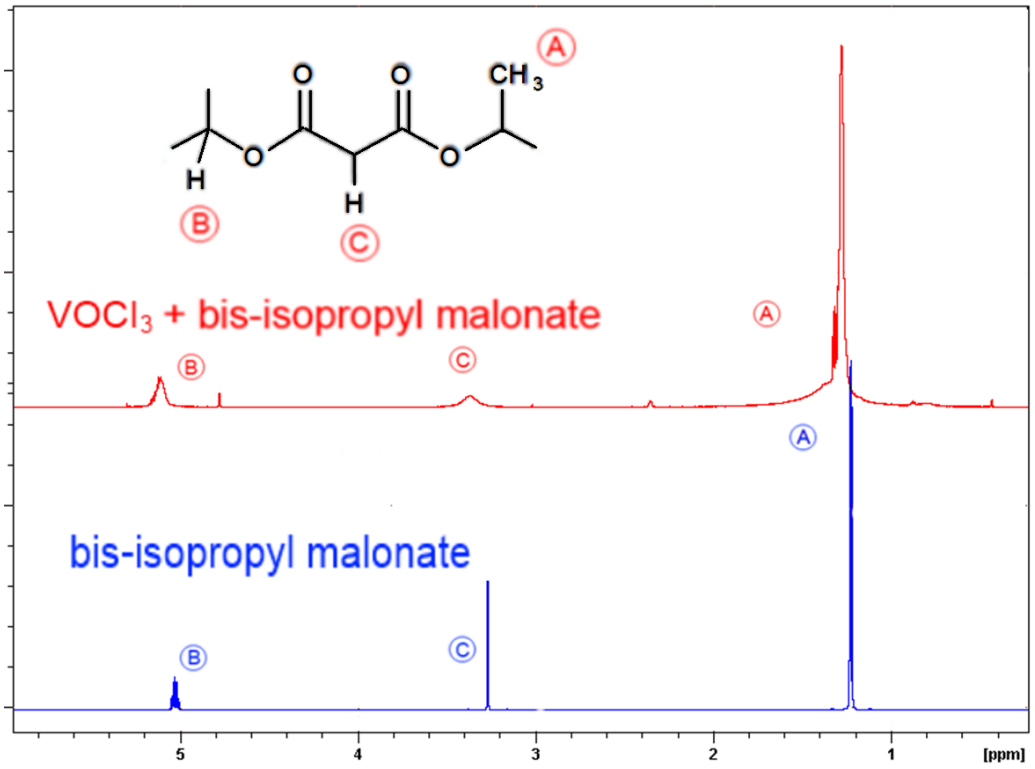

Figure 42: ^{1}H NMR spectra of bis-isopropyl malonate and the product of its reaction with $VOCl_3$ **[8]**, all peaks exhibiting a downfield shift and experiencing broadening indicating coordination to the vanadium metal centre.

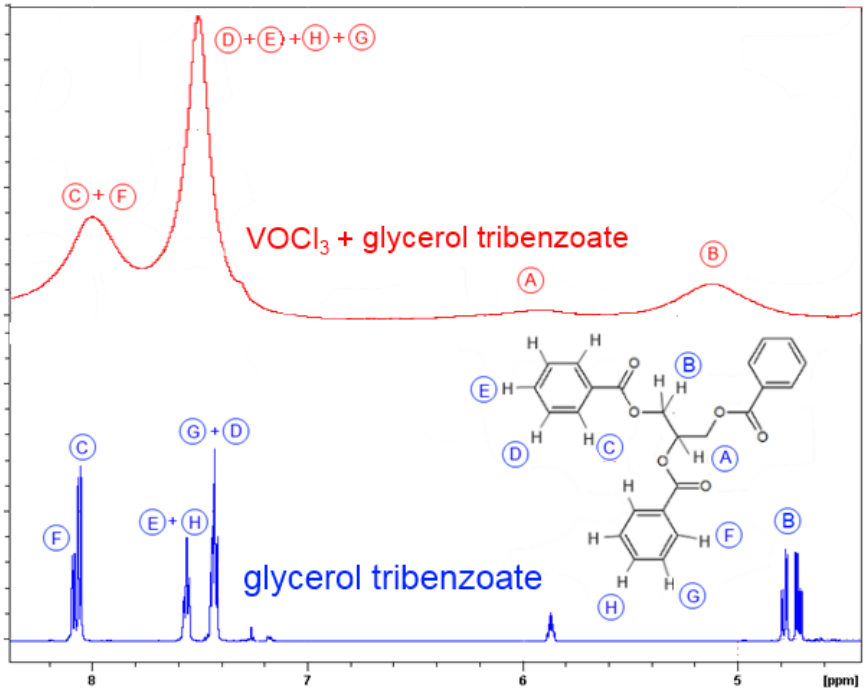

Figure 43: ^{1}H NMR spectra of bis-isopropyl malonate and the product of its reaction with $VOCl_3$ **[9]**, all peaks exhibiting a downfield shift and experiencing broadening indicating coordination to the vanadium metal centre.

This approach with glycerol tribenzoate was found to be ineffective as glycerol tribenzoate is highly insoluble in hexane and preventing the reaction from going to completion. The reaction was repeated in toluene and refluxed for 15 hours, at which point a black liquid was obtained. NMR of **8** (Figure 42) reveals considerable peak broadening in all three peaks, as well as a minor downfield directing effect relating to the electron poor desheilding nature of the $VOCl_3$, The most noticeable shift is, as expected, the central proton of the malonate, which is shifted from 5.05 to 5.44 ppm. Peaks at 1.25 and 3.31 ppm in the unreacted bis-isopropyl malonate spectra have also shifted downfield, however this is far less pronounced.

As a crystal structure could not be obtained due to the extremely air sensitive nature of the product, the NMR data confirms coordination of the malonate to the $VOCl_3$. The highly similar nature of the ligand would suggest that the mostly likely structure taken on by **8** would be cyclic, similar to **6**, with the vanadyl oxygen forming bridges between the metal centres.

The same is true for the glycerol tribenzoate and $VOCl_3$ complex. In this case the broadening and downfield shifting in the NMR spectrum (Figure 43) is far more pronounced than that seen in the bis-isopropyl malonate. The doublet peak of proton B has shifted from 4.78 to 5.10 ppm and broadened greatly. The single proton singlet at 5.9 ppm has also broadened to the point to where it is barely visible from the background. The signals for the aromatic species have homogenised to form two extremely broad peaks over the range of 7.3 to 8.3 ppm. This once again confirms coordination of the glycerol tribenzoate to the vanadium centre, however predicting the structure is considerably more challenging. The length of the bridging alkyl chain

between the carbonyls resembles that of the succinate species, and is long enough for polymerization to be possible. However the fact that there are three carbonyl groups would make the formation of a branched polymer species possible. The complexity of the resulting species would explain the extreme difficulty in forming crystals.

3.4. Conclusion

All of the diesters studied coordinated to the titanium(IV) chloride in the same way, forming complexes of an octahedral geometry, distorted by the presence of the chloride ligands. No chlorine was lost from the $TiCl_4$ upon formation of the complexes **1 - 3**. The same is true for glycerol tribenzoate titanium chloride complex **4**, with two of the ester groups datively coordinating *via* the carbonyl oxygen to a single titanium centre. This lead to a six coordiate octahedral centre with octahedral geometry. The third ester carbonyl group coordinates to a second titanium chloride molecule. The resulting species instability leads to dimerization. Formation of a two choro-bridged $Ti_2Cl_6(\mu\text{-}2)Cl_2$ centre was observed, with both titanium centres coordinated to a single carbonyl oxygen of a different glycerol benzoate molecule. As with the other structures, no chlorine loss is observed.

Conversely, with $VOCl_3$, all three molecules coordinating to the vanadium lead to the loss of a chlorine atom. This is significant as the reaction could not be reversed by simple dissociation of the ligand alone, which could occur for the $TiCl_4$ complexes at the high temperatures used in the Chloride Process.

Additionally, whilst all three diesters form monomeric species with $TiCl_4$ to compensate for the loss of the chlorine atom, the diester complexes of vanadium (4 + 5) form a ring and a

chain respectively, with the oxygen of the $VOCl_3$ forming a dative bond with another metal centre.

The addition of oil in the Chloride Process for the production of TiO_2 is carried out at around 200 ˚C, at which point all of the metal chlorides present are in the vapour phase. At this temperature, the dative coordination would likely be more reversible, as neither the $TiCl_4$ nor the esters are altered structurally by coordination. Conversely the addition of donor ligands to $VOCl_3$, the species removed by the oil, frequently causes the dissociation of one of the chlorine atoms.

This suggests that even though the Lewis acidy of the $TiCl_4$ is greater than $VOCl_3$, the $VOCl_3$ may be changed irreversibly by reaction with carbonyl groups in the oils, making it the preferred species for the reaction of the triglyceride group of the oil, despite being present in far lower concentrations in the gas stream. The group may coordinate briefly to many titanium(IV) chloride molecules before coming into contact with one vanadium oxytrichloride but having done so the energy barrier to reversibility would be greater and so the interaction leads to a permanent formation of a new species which is not able to pass through the distillation.

Chapter 4

Vanadium Removal Flow System

4.1. Introduction

Having analyzed the contents of various samples from different points along the Chloride Process using NMR spectroscopy, and modeled the interaction of $TiCl_4$ and $VOCl_3$ with diesters and triesters as analogues for the oils, the next step was to try and recreate the gas phase interactions of the heated $TiCl_4$ and $VOCl_3$. To achieve this, a piece of glassware was designed to mimic the distillation column of the Chloride Process, complete with the ability to cycle the same liquid through the distillation repeatedly. Samples of $TiCl_4$ and $VOCl_3$ that had been passed through this apparatus were analyzed using NMR using the same method described in Chapter 2.

In order to investigate the behaviour of oil in the Chloride Process on a laboratory scale, the conditions within the Chloride Process had to be emulated as closely as possible. This involved reacting mixtures of gaseous titanium(IV) chloride and vanadium(V) oxytrichloride with the liquid oil at over 140 ˚C under moisture free conditions. An additional challenge lies in the fact that the industrial scale production of TiO_2 is a cyclic process. Material that does not pass through the distillation columns is not discarded but recycled into the chlorinator, passing through the process repeatedly. This is done to minimize waste and production of harmful by-products as well as to maximize the yield of titanium dioxide obtained from the ore.

A potential problem with this method however is that byproducts, such as those formed by the breakdown of the oil, can be recycled repeatedly and build up in the system, leading to fouling or unwanted side reactions. To accurately recreate the addition of oil, the same sample of $TiCl_4/VOCl_3$ needs to react with the oil repeatedly, simulating possible build-up of breakdown products. In order to achieve this, a flow cell was designed by modifying a Soxhlet extractor (Figure 44) with the purpose of forcing gaseous $TiCl_4$ and $VOCl_3$ over a small amount of rapidly stirred oil, simulating the injection of the oil as a dispersion of liquid droplets into the gaseous $TiCl_4$ stream, as shown in the schematic of the process (Figure 45).

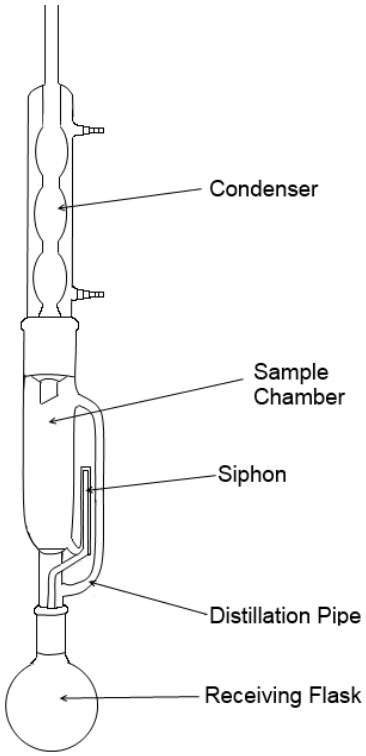

Figure 44: Schematic of a Soxhlet extractor.[109]

This was achieved by modifying the bottom pipe of the Soxhlet, through which the distillate drains in the flask. To the side of this tube was connected to a thinner glass pipe (0.5 cm diameter) that leads into a second two necked round bottom flask. From this flask, a second 0.5 cm wide pipe leads 10 cm directly upwards before connecting to the upper Soxhlet. This

set up effectively elongates the distillation tube of the Soxhlet to include a second round bottom flask to which oil can be added (Figure 45).

4.2. Experimental

Before each experiment, 5 ml of the selected oil (Tables 11 and 12) was added to flask 2. The flow cell was assembled as shown in Figure 45 and purged with nitrogen anhydrous nitrogen from a Schlenk line for 30 minutes whilst the bottom two flasks were heated to 140 ˚C using a silicone oil bath and a hot plate, in order to remove as much moisture from the system as possible, so as to more accurately emulate the conditions during industrial $TiCl_4$ removal.

The apparatus was fitted with an ice water condenser in order to ensure that all of the $TiCl_4$ remained inside the system, not escaping through the top of the Soxhlet extractor. The apparatus was also fitted with an oil bubbler in order to regulate the flow of nitrogen through the system, which was kept as low as possible. Following this, the condenser was removed from the top of the Soxhlet chamber and replaced with a rubber septum, through which 15 ml of $TiCl_4$, $VOCl_3$ or a mixture of the two were injected. This caused the Soxhlet to fill, leading to roughly 10 ml falling into flask one and 5 ml remaining in the top chamber of the Soxhlet. This was important as it prevented backflow of the hot vapour, forcing it through the system in the correct direction, ensuring interaction with the oil in flask 2. Following the addition of the $TiCl_4$, $VOCl_3$ or mixture, the rubber septum was removed and replaced with the condenser and oil bubbler. After the addition of the metal chloride species both flasks were stirred vigorously using magnetic stirrer bars. The movement of the metal chloride species within the system can be described as 5 steps. Throughout the process the system was heavily insulated using foil and thermal insulation material.

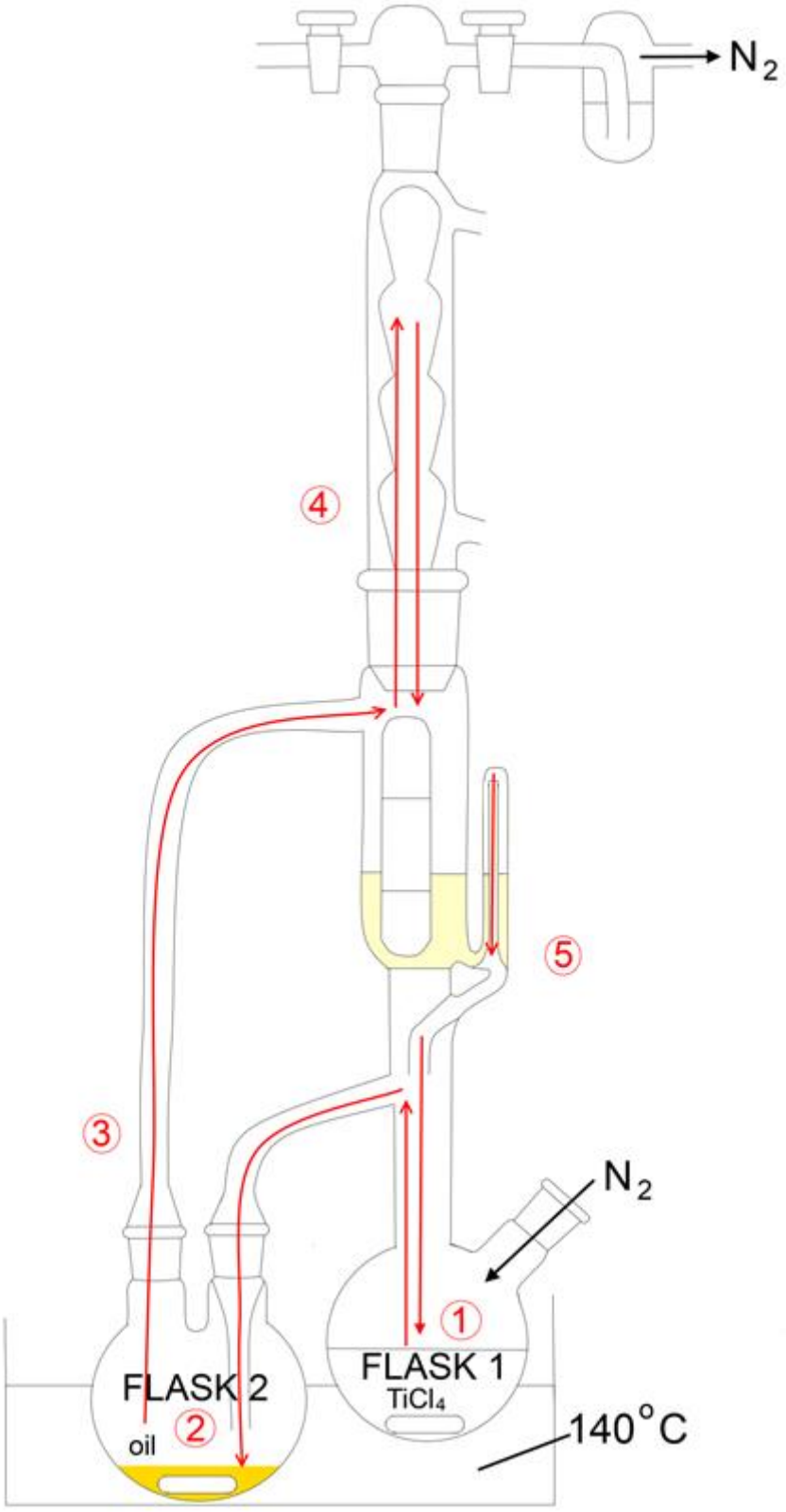

Figure 45: Gaseous metal chloride flowcell from a modified Soxhlet extractor.

The metal chloride species pass through the flowcell in five steps:

1) The titanium chloride was added *via* the top of the Soxhlet extractor into the flow cell whereupon it filled the Soxhlet before dropping through into flask one. The $TiCl_4$ was heated to 140 ˚C using an oil bath. This lead to evaporation of the $TiCl_4$. As some liquid $TiCl_4$ remain in the Soxhlet above, the path of least resistance was into flask 2.

2) Flask 2 contain roughly 5 ml of the selected oil, which was vigorously stirred at 140 ˚C. The heating caused the oil to become far less viscous and droplets were kicked up by the stirrer, emulating the dispersion of oil that is injected into the gas cleaning tank. The gaseous $TiCl_4$ interacted with the oil in flask 2 whist purely in the gaseous state as the inlet was not submerged in the oil.

3) Following reaction with the oil, the $TiCl_4$ and $VOCl_3$ were distilled through the 0.5 cm diameter glass tube, along with any volatile products that may have formed in flask 2.

4) The $TiCl_4$ and volatile products moved into the condenser. Here their temperature was reduced sufficiently to cause them to enter the liquid phase and drip down, filling the Soxhlet extractor sample chamber.

5) The full Soxhlet emptied into flask one beginning the cycle over. This simulates the cyclic nature of the Chloride Process, allowing possible byproducts to build up over multiple cycles.

Whilst the experiments were carried out, a third magnetic stirrer was kept inside the Soxhlet chamber above flask 1. This reduced the amount of liquid that was required to build up inside before emptying into flask 1 from 10 ml to around 5 ml. This was found to improve the flow of the gas and prevent either of the heated flasks from boiling dry.

Once the Soxhlet had filled and emptied a certain number of times the nitrogen flow was removed and the system left to cool to room temperature, at which point three NMR samples were taken.

- The contents of flask 1, which contained $TiCl_4$ and any by-products built up over several cycles.
- The contents of the Soxhlet extractor, which contained the freshly distilled $TiCl_4$
- The contents of flask 2, which contained the oil residue, which had often solidified as well as the vanadium oxytrichloride that had been removed from the gas stream.

4.2.1. Soya Bean Oil Experiments

The initial experiments all used soya oil as this is the oil currently used by Huntsman Pigments and Additives in the removal of $VOCl_3$. After some initial optimizing of the technique by running toluene, $SiCl_4$ and finally $TiCl_4$ through the system, a series of experiments were carried out. The details of these experiments are shown in Table 11. The 1000 ppm vanadium(V) oxytrichloride dosed titanium(IV) chloride was obtained from Huntsman. The 40,000 ppm $VOCl_3$ sample was made up in a separate Schlenk flask by adding 1 cm^3 of $VOCl_3$ to 25 cm^3 of $TiCl_4$.

Table 11: Key experiments involving soya oil carried out using the flow system

EXP no.	**Chloride flask**	**Oil flask**	**No. Cycles**	**Time /hrs**	**Results + Observations**
1	$TiCl_4$	soya	4	3	Oil becomes brown and viscous after 3 cycles. NMR shows chlorinated alkene species have distilled into Soxhlet.
2	$VOCl_3$	soya	3	4	Oil became black and viscous during first cycle. $VOCl_3$ that distills into Soxhlet identical to starting material by NMR.
3	$TiCl_4$ + $VOCl_3$ (1000ppm)	soya	4	3	Oil becomes brown and viscous after 2 cycles. NMR shows chlorinated alkenes species have distilled into Soxhlet.
4	$TiCl_4$ + $VOCl_3$ (40,000ppm)	soya	4	4	Oil becomes black and viscous after 1.5 cycles. ^1H NMR shows no broadening suggesting that $VOCl_3$ has been removed. Chloroalkane peaks only present in oil.
5	$TiCl_4$	-	4	3	NMR shows no reaction.

4.2.2. Analysis of Naphthenic Oils

Following the experiments with soya bean oil, a second flow cell study was carried out using various naphthenic oils (Table 12). All of these experiments were carried out as described in the previous section, with an NMR spectrum being obtained from each of the naphthenic samples for comparison. After initially sampling several naphthenic oils with only $TiCl_4$ it was decided that Flavex 977(s) would be reacted with the other metal chloride mixtures in the same way as the soya bean oil, as it possessed greater fluidity and was observed to become solid less rapidly upon exposure to $TiCl_4$.

Table 12: Experiments run through the flow cell apparatus using naphthenic oils

EXP no.	Chloride flask	Oil Flask	No. Cycles	Time (hrs)	Results + Observations
6	$TiCl_4$	Flavex 977(s)	4	2	Oil becomes dark red/brown, almost as soon as $TiCl_4$ begins boiling however remains fluid. $TiCl_4$ condensing in Soxhlet dark red
7	$TiCl_4$	EH L550	4	3	Oil becomes dark red/brown, almost as soon as $TiCl_4$ begins boiling however remains fluid. $TiCl_4$ condensing in Soxhlet dark red
8	$TiCl_4$	Gravex 926	4	3	Oil becomes dark red/brown, almost as soon as $TiCl_4$ begins boiling however remains fluid. $TiCl_4$ condensing in Soxhlet dark red
9	$TiCl_4$	Edelex 926(s)	3	4	Oil becomes dark red/brown, almost as soon as $TiCl_4$ begins boiling however remains fluid. $TiCl_4$ condensing in Soxhlet dark red
10	Toluene	Flavex 977(s)	4	1.5	NMR shows pure toluene
11	$TiCl_4$ + $VOCl_3$ (1000ppm)	Flavex 977(s)	4	4	Same as 8 except the oil is visibly darker during the initial cycle.
12	$TiCl_4$ + $VOCl_3$ (40,000ppm)	Flavex 977(s)	4	3	Oil goes from colourless to black as soon as it is exposed to the gaseous species. The distilled fraction appears to stain the apperattus orange (Figure 30). Precipitation of black solid is observed in distillate
13	$VOCl_3$	Flavex 977(s)	3	4	Oil initially appears less viscous, however over the course of the cycle it gradually becomes more solid. By the third cycle only 4 ml of $VOCL_3$ remains, the rest appears to have been taken up by the oil.

4.3. Results and Discussion

4.3.1. Soya Bean Oil Analysis

4.3.1.1. $TiCl_4$ + Soya Oil

$TiCl_4$ caused the oil to gradually go from light yellow to brown, becoming more viscous over time. After the Soxhlet had emptied and filled three times, the oil had become so thick that the stirrer could no longer move. The $TiCl_4$ passing into the Soxhlet was clear and colourless, lighter in colour than the starting material, which was a light yellow due to aging. The NMR spectra taken from flask 1 and the Soxhlet show a number of signals that were not present in the starting material.

These peaks were not present in any of the spectra from when the cell was run without oil, which only shows signals from the grease used on the joints. This suggests strongly that the peaks are a result of $TiCl_4$ breaking down the oil. Figure 46 shows enhanced images of two major new peaks, whilst Figure 47 shows the COSY (correlation spectroscopy) spectrum of the same two peaks. The two signals in question are a quartet of doublets at 3.95 ppm and a pentet at 5.2 ppm. These are the strongest peaks that appear as a result of the flow system experiment. The COSY shows that the two signals are from protons situated on adjacent carbons. This is in keeping with the ^1H NMR signal of a glycerol group, which shows both the pentet and quartet of doublets when coordinated to $TiCl_4$, however both were considerably more downfield shifted due to the presence of the three highly electron withdrawing ester groups (Figure 47). These signals strongly suggest that the glycerol group of the soya bean oil is responsible for these signals emerging.

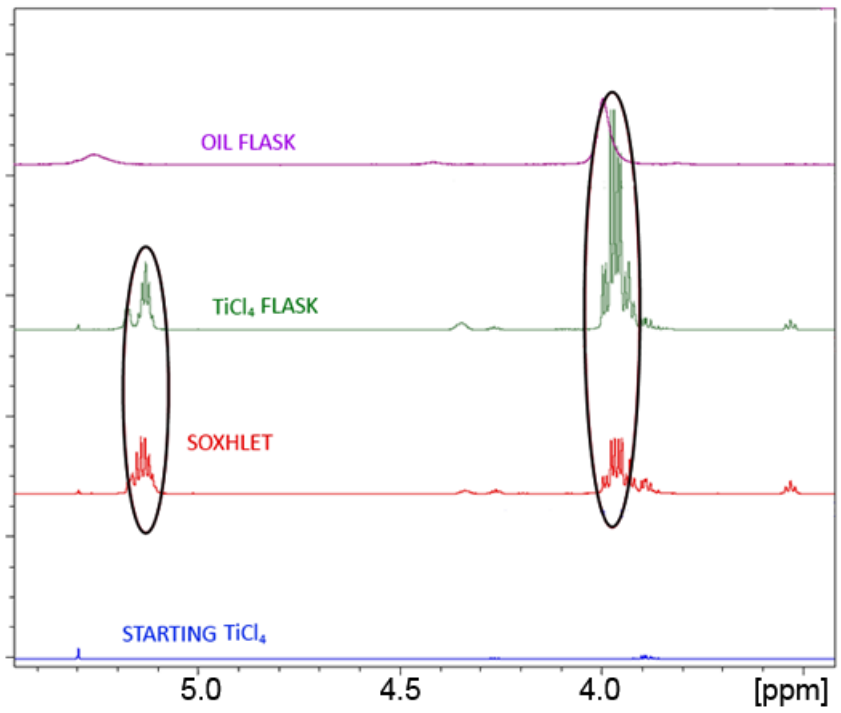

Figure 46: ^{1}H NMR spectra of the starting material and the contents of flasks 1, 2 and the Soxhlet extractor from experiment in which gaseous $TiCl_4$ was reacted in soya oil. Spectra taken in $CDCl_3$. The figure shows the region between 3.5 and 5.5 ppm.

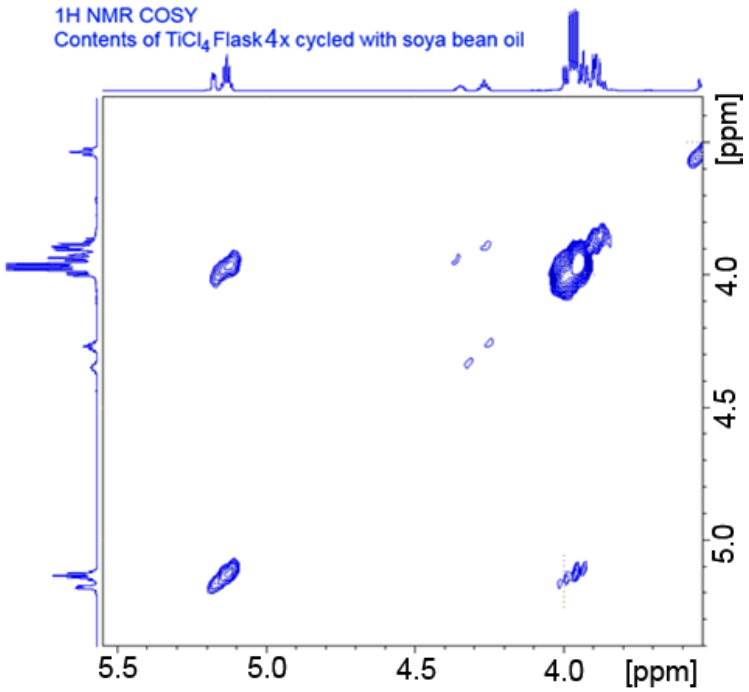

Figure 47:^{1}H NMR COSY spectrum of the contents of flask 1, from experiment in which gaseous $TiCl_4$ was reacted in soya oil, showing the region between 3.5 and 5.5 ppm. Spectra taken in $CDCl_3$.

Despite this it is unlikely that the soya bean oil was able to make it though the distillation intact. Neither the NMR spectra from the Soxhlet or flask 1 showed any trace of the unsaturated alkene peaks at 2.1, 2.4 and 2.8 ppm that were also seen in the NMR spectrum of the soya bean oil. Furthermore the signals have undergone an upfeild shift, with the equivalent signals in soya bean oil appearing at 5.4 and 4.3 ppm as opposed to the peaks at 5.1 and 3.9 ppm observed in this spectrum (Figure 46).

This evidence points to the molecules that produce these signals being the products of the breakdown of the soya bean oil, with the fatty acid chains separating from the glycerol.

The resulting molecule must still be able to provide the signals resulting from a 1, 2, 3 propane species whilst providing downfield shifts in the correct environments. The protons on the 1 and 3 carbons must also be equivalent as otherwise the signals from the carbons in the 1 and 2 positions of the propyl backbone would not be in the same position, as was observed in these spectra. The species that fits best in simulated NMR is that of a dichlorinated species in which the ester groups have been replaced by the chlorine in the 1 and 3 positions (Figure 48 and 49).

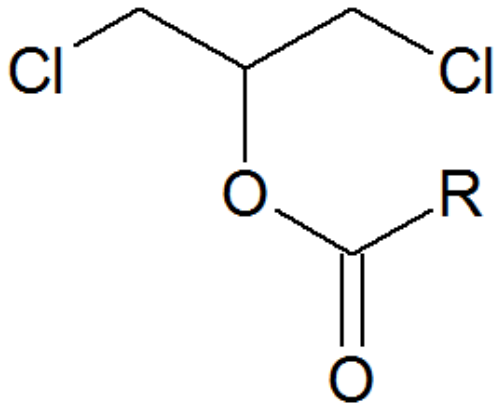

Figure 48: Proposed general structure of the main NMR product of the reaction of $TiCl_4$ and soya bean oil in the flow cell

This matches well with the product of the reaction of the $TiCl_4$ with glycerol tribenzoate as shown in the previous chapter. The $TiCl_4$ was found to coordinate to the two terminal ester groups or the central ester on two molecules forming a chloro-bridged tetra-titanium species. It is probable therefore that this species, formed in the gas phase, or at least part of it, should be the intermediate for the formation of the volatile molecule that would be able to distill over. The R group represents the carbon chain that would also need to be far shorter to make distillation possible.

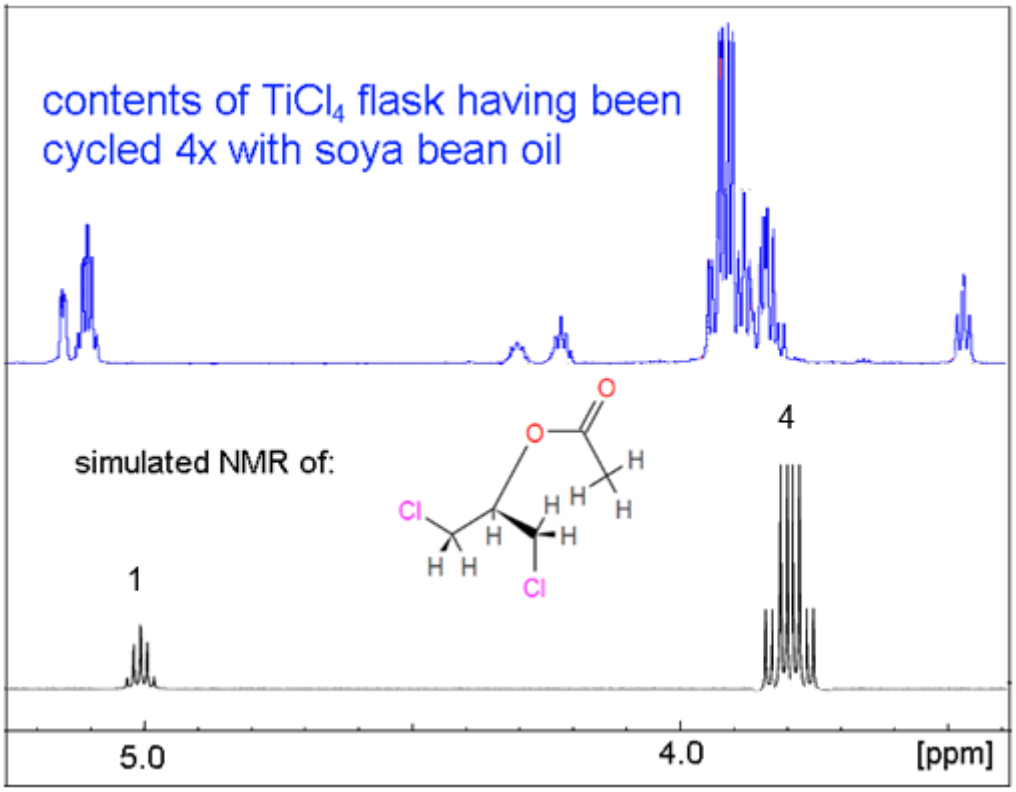

Figure 49: Comparison of the spectrum of the contents of flask 1 produced from putting $TiCl_4$ through 4 cycles with soya bean oil, compared with the simulated ^1H NMR spectrum of 1, 3 dichloro propan-2-acetate.The simulation does not factor In long range coupling of the 4H peak which was added manually. Simulation carried out using NMRDB NMR predictor software. [110–112]

The chlorination of an ester species from $TiCl_4$ would be unfavorable due to the greater bond enthalpy of the C-O linkage than the formed C-Cl (348 kJ mol^{-1} vs 328 kJ mol^{-1} respectively) as well as the large energy barrier of 373kJ mol^{-1} required o break the $TiCl_4$ bond. [113] However, it

should be noted that just because the formation of the above distillate product is unfavorable does not mean it should be discounted. The flowcell device is designed to allow for the buildup of marginal species over a period of hours, as was seen in the Chloride Process, with undistilled components cycled repeatedly through the entire system. Even if a very small amount of each 5 ml of distilled $TiCl_4$ reacts with the oil in this way, it would build up in the system, being removed from the oil flask *via* distillation preventing the reaction from reaching equilibrium. The spectrum also shows weaker signals that could be the same molecule but with different ester groups substituted. A postulated mechanism is shown in Figure 50, with the chlorine attacking the electron poor carbon adjacent to the ester and the resulting rearrangement leading to fission of the C-O bond. The resulting species rearranges giving a covalent structure similar to those observed by Barrow *et al*.[114] It should be noted that despite the species denoted by Barrow being bis-titanium dimers bridged by carboxyl ligands, with both carboxyl oxygen atoms coordinating to a titanium centre, a similar reaction could occur here, with the second stage facilitated by the presence of a second species.

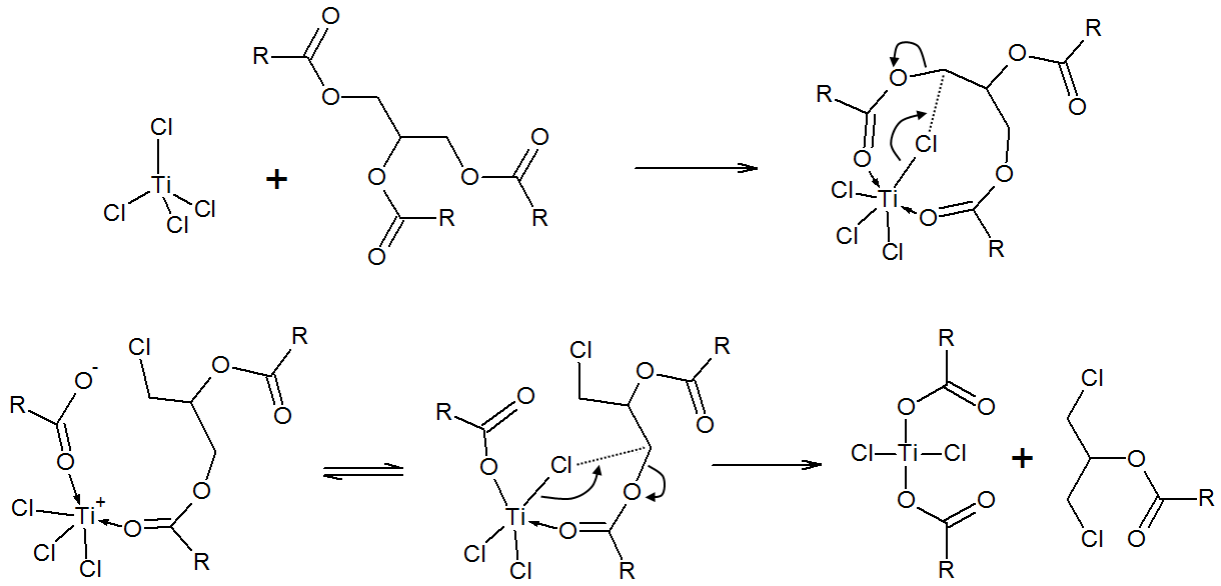

Figure 50: Suggested mechanism for the formation of the 1, 3 dichloro 2 acetyl propane species observed in the ^{1}H NMR of the flow-cell distillate.

Despite the unfavourable nature of this reaction due to the Lewis acid character of the titanium chloride, it would be irreversible and as the experiment involves cycling the same sample of $TiCl_4$ repeatedly, even a product that forms in minuscule amounts could be observed to build up.

Another explanation could be that the formation of HCl in the system plays a part in the chlorination and stabilizing the resulting $TiCl_4$ carboxylate species. The cause of this chlorination could either be the formation of small amounts of HCl from residual water, as well as the small amount of water in the nitrogen stream. This would not be entirely inaccurate to the process as before the addition of oil, a small jet of water vapour is injected in order to remove water.

4.3.1.2. $VOCl_3$ + Soya Oil

When the flow system was used with only $VOCl_3$ present, the oil was found to become viscous far more rapidly, becoming black and solid just after the first Soxhlet-full had passed through. It was observed that most of the $VOCl_3$ appeared to have been 'consumed' by the oil, with only around 5 ml flowing through the system by the third cycle. The distilled $VOCl_3$ in the Soxhlet appeared unchanged. This implied that all of the soya oil had reacted with the $VOCl_3$ allowing what remained to pass through the flow cell repeatedly undisturbed. This was confirmed by the ^1H NMR analysis (Figure 51). The $VOCl_3$ in the Soxhlet adaptor showed no significant change from the starting material, except for the removal of peaks at 0.5 – 0.7 ppm, which are the result of unsaturated alkyl impurities. These were apparently removed by the distillation.

The NMR spectrum of the oil flask was similar to that of unreacted soya oil, except broadened significantly, suggesting the presence of vanadium, coordinated to the oil. This is in keeping with current theory that the $VOCl_3$ coordinates to the double bonds and triglyceride backbone

irreversibly, rendering it unable to pass through the distillation column. Conversely the $TiCl_4$ coordinates in a more reversible manner, allowing it to pass through the distillation.

These findings support the work in which $TiCl_4$ and $VOCl_3$ were reacted with diesters. The reaction with the $VOCl_3$ was found to displace chlorine, which heavily reduces the reversibility of the reaction when compared with the $TiCl_4$, which remains intact upon coordination, simply adopting an octahedral moiety, maintaining all four chlorine atoms.

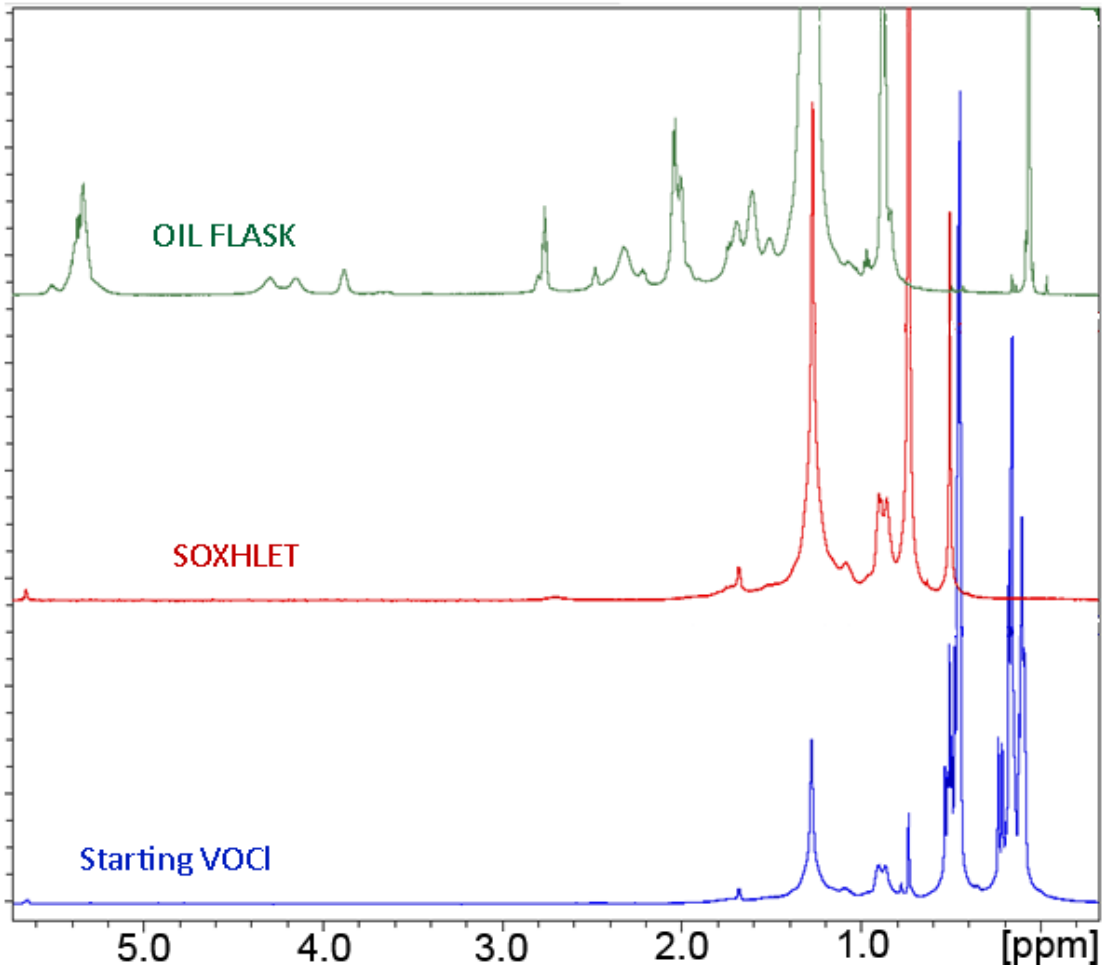

Figure 51: ^1H NMR spectra of the starting material and the contents of flask 2 and the Soxhlet extractor from experiment 2, in which gaseous $VOCl_3$ was reacted in soya oil. Spectra taken in $CDCl_3$. The figure shows the region between 0.6 and 5.5 ppm.

4.3.1.3. $TiCl_4$ + 1000ppm $VOCl_3$ + Soya Oil

Of the two mixtures put through the flow cell, the 1000 ppm $VOCl_3$ mixture was far more similar to the gas stream found in the actual Chloride Process. The results are highly similar to those obtained, using pure titanium chloride. The ^1H NMR spectra of flask 1 and the Soxhlet both show the same peaks between 3 and 6 ppm including the large quartet of doublets at 3.95 ppm (Figure 52). The lack of any broadening in the spectra as well as the colourless nature of the distillate suggests complete removal of the vanadium species by the oil. This is a promising result as it shows that the flow cell is able to emulate the distillation and removal of $VOCl_3$ in the plant effectively.

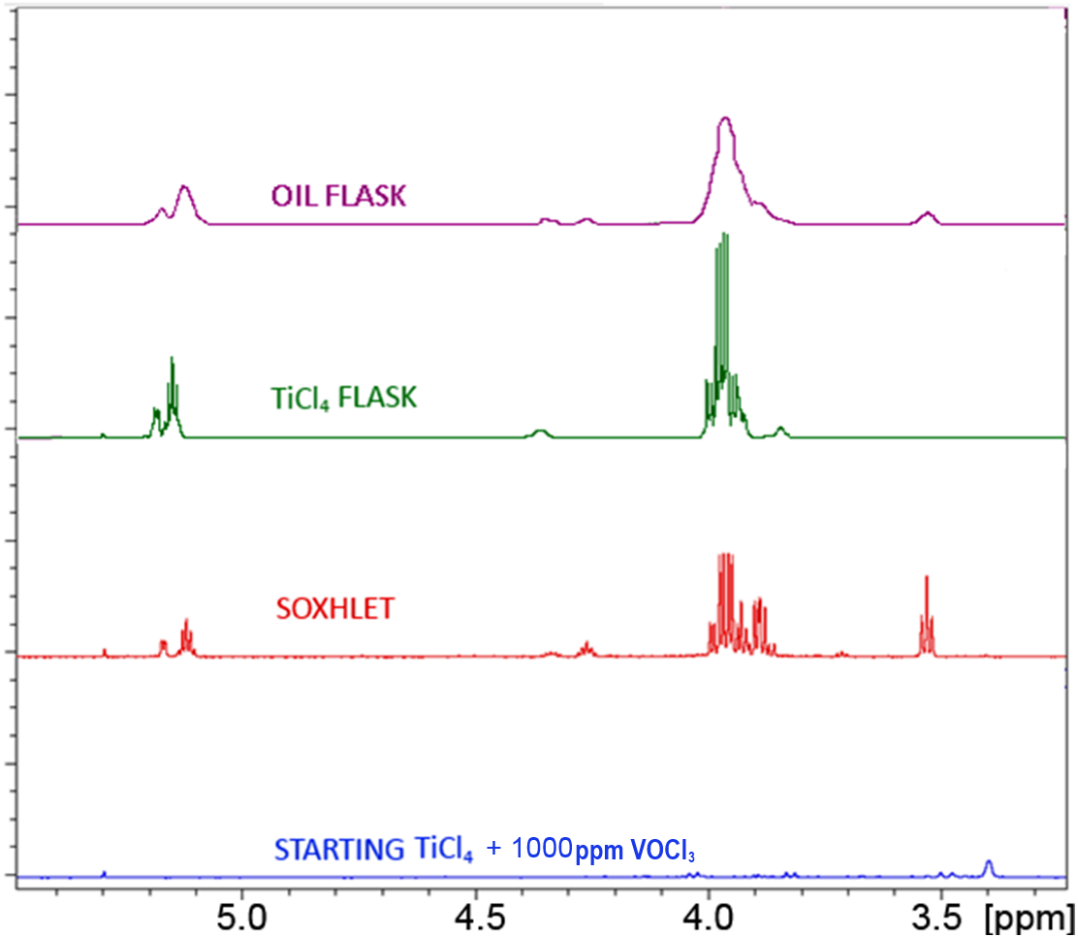

Figure 52: ^1H NMR spectra of the starting material and the contents of flasks 1, 2 and the Soxhlet extractor from experiment in which gaseous $TiCl_4$ with 1000 ppm $VOCl_3$ was reacted in soya oil. Spectra taken in CDCl3. The figure shows the region between 3.5 and 5.5 ppm.

4.3.1.4. $TiCl_4$ + 40,000ppm $VOCl_3$ + Soya Oil

The presence of a higher proportion of $VOCl_3$ in the distillation mixture lead to the oil solidifying far more rapidly, similar to when only $VOCl_3$ was passed through the system. However the distilled product in the Soxhlet remained colourless, suggesting successful removal of the $VOCl_3$. This is supported by the lack of peak broadening in any of the flask's spectra, save the oil suggesting that the $VOCl_3$ had been effectively removed as with the Chloride Process itself (Figure 53)

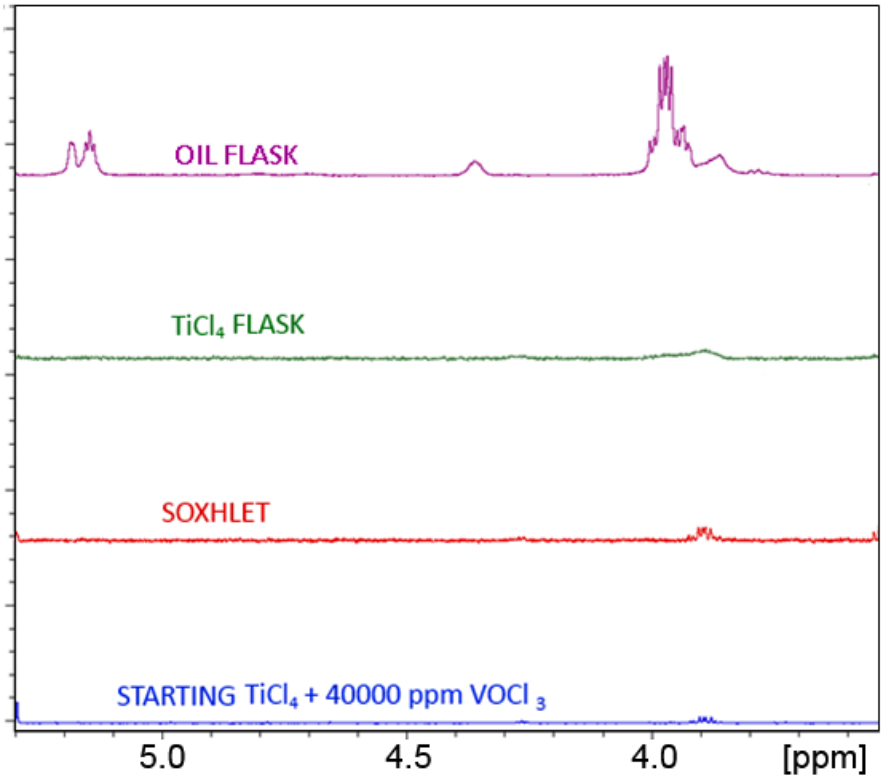

Figure 53: ^{1}H NMR spectra of the starting material and the contents of flasks 1, 2 and the Soxhlet extractor from experiment 4 in which gaseous 40,000 ppm $VOCl_3$ In $TiCl_4$ was reacted in soya oil. Spectra taken in $CDCl_3$. The figure shows the region between 3.5 and 5.5 ppm.

Interestingly, this far higher dose of $VOCl_3$ appears to prevent the carryover of the chloroacetate formed by reaction of the oil, with the $TiCl_4$. The signals relating to the chlorinated glyceride species are only present in the spectra of the oil and neither of the $TiCl_4$ samples from the Soxhlet or flask 1. This suggests that whilst the $TiCl_4$ may still be reacting with

the oil as seen in the previous experiments, it is impeded by the thickening of the oil and cannot pass through the distillation column. The lack of peak broadening in the quartet of doublets implies that although prevented from passing over, this species has not directly coordinated to the vanadium.

4.3.2. Naphthenic Oil Analysis

Following the successful study involving soya bean oil, the flow system was used to investigate a range of prospective oils that can be used to separate $VOCl_3$ from $TiCl_4$. The purpose of this study was less about defining the breakdown products of these species, but to investigate the ability of these oil to separate the two transition metal species, as well as to determine whether or not breakdown products formed by using NMR to observe them, as well as looking at the colour of the oil entering into the Soxhlet extractor. This study was carried out at the request of Huntsman Pigments and Additives in order to better understand their competitors method for refining TiO_2.

Naphthenic oils are produced from the naphtha fraction of crude oils. Naphthenics feature hydrocarbon chains containing ring systems, both saturated and conjugated. The oil's are made up of different blends of these species in order to control characteristics such as viscosity and lubricity. Structurally, all of these oils are therefore far more complex than soya-bean oil, which is formed of the same basic triglyceride structure, but with only four possible long unsaturated chains, all of which are linear An example of some of the commonly featured species in naphthenic oils are shown in Figure 54. Viscosity, boiling range and colour are all affected by the number and size of these groups, as well as their ratio to straight chain portions.

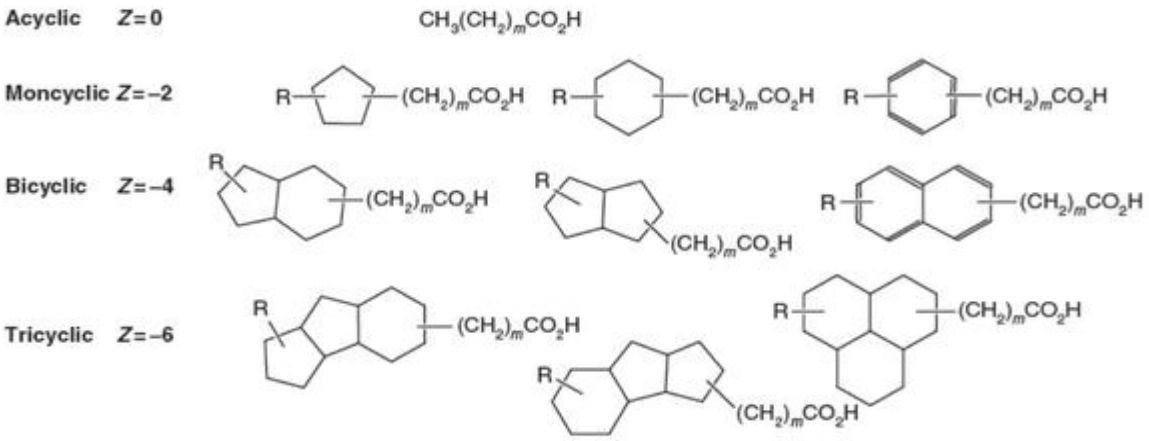

Figure 54: Example structures of naphthenic acids, derived from the hydrolysis of naphthenic oil.

Table 13: Comparison of acidity of naphthenic oils and soya bean oil.

Oil	pH
Soya bean Dec 13	7
Flavex 977(s)	5.9
Ergon Hygold L500	6.3
Gravex 926 (s)	6.6
Edelex 926	6.4

This study focussed on the oil Flavex 977(s) as a previous study at Huntsman Pigments and Additives concluded that it showed potential for the removal of $VOCl_3$. Other oils tested were Ergon-Hygold 550 (the worst performer in the aforementioned test, as well as Gravex 926 (s) and Edelex 926. These were chosen to represent the 'other end' of the naphthenics spectrum, being far lighter in colour and less viscous. The pH of all of the oils was tested using a pH meter. Each of the oils were found to be more acidic than soya bean oil (Table 13).

Unfortunately it was impossible to obtain information as to the exact or even approximate contents of each of these oils, as the companies that produce them, Shell, Nynas and Ergon Hygold, would not respond to any enquiries made about them.

4.3.2.1. NMR of the Naphthenic Oils

All of the oils tested give extremely similar NMR spectra (Figure 55). This is not to say that they are the same, simply that the number of proton environments are in the same region but slightly different, which broadens the spectrum peaks to the point where differences cannot be seen. All spectra showed a peak at 1 ppm representing the primary carbon at the end of the hydrocarbon chains, a large peak at 1.5 ppm for secondary carbons and cyclic chains. This peak is very broad at the base due to the number of different ring systems. Several other broad humps can be seen on the side representing either more stained rings or rings with a double bond. Finally a region between 7-8 ppm of many smaller peaks representing a small number of conjugated ring systems can be observed.

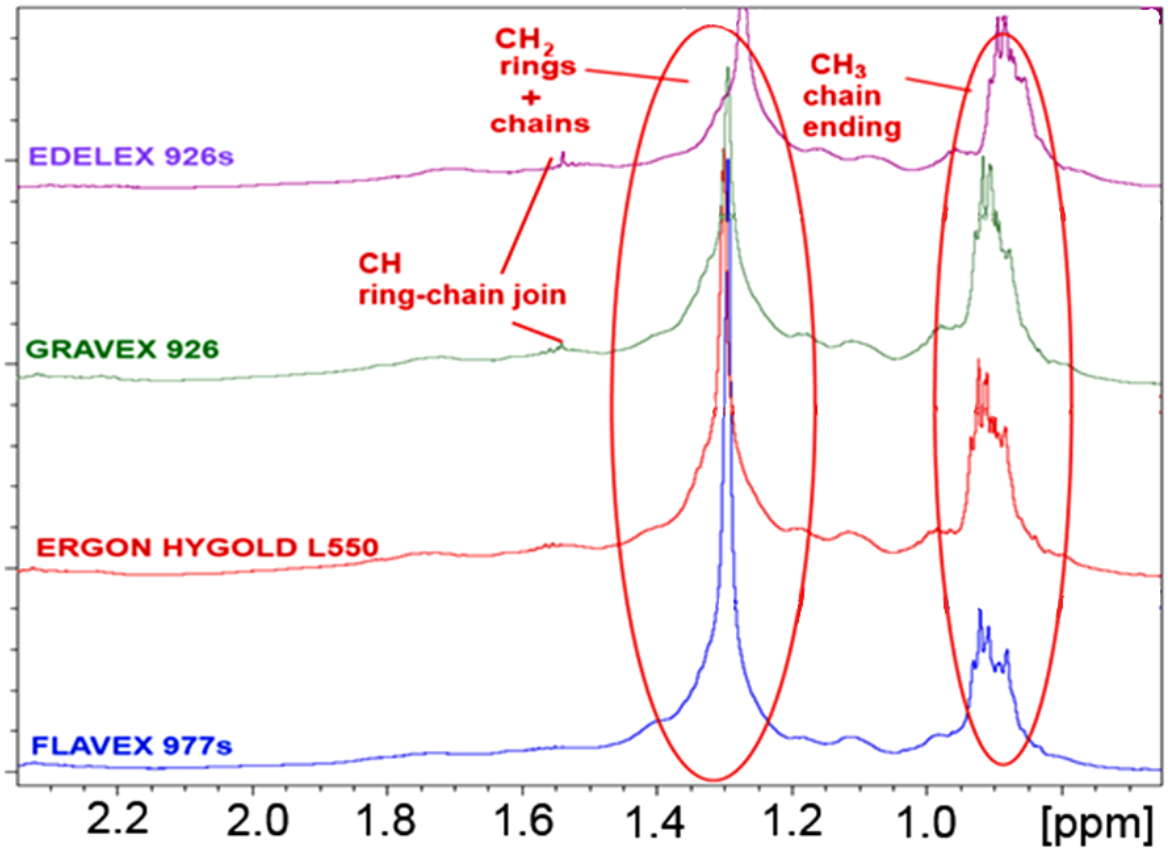

Figure 55: Comparison of the ^{1}H NMR spectra of four naphthenic oils: Flavex 977s (blue), Ergon Hygold L550 (red), Gravex 926 (green) and Edelex 926s (purple). Spectra taken in $CDCl_3$. The figure shows the region between 0.8 and 2.4 ppm

4.3.2.2. Flow Cell Experiments

In a setup identical to the previous section, 20 ml of $TiCl_4$ was pushed through the flow system with 5ml of oil stirred vigorously in the second flask. In each case the Soxhlet was allowed to fill four times when possible before the heater was turned off and the samples collected.

In the case of all 4 oils, regardless of the original oil colour and viscosity, interaction with the gaseous $TiCl_4$ caused the oil to immediately take on a dark red colour as the $TiCl_4$ began to boil and pass over it. The $TiCl_4$ that enters the Soxhlet having passed though the oil appears red in all four cases (Figure 56). The stained $TiCl_4$ was observed to layer on top of the clean $TiCl_4$ within the Soxhlet extractor, not mixing at all until the first emptying (Figure 57). This red colouring becomes more prominent with each emptying of the Soxhlet. This was never seen when soya bean oil was used.

The cause of this red staining was most likely related to the formation of a weakly bound charge transfer complex between the titanium chloride and the aromatic portions of the oil that had broken away from the molecule and carried over to distillation column. This is a commonly observed phenomenon with $TiCl_4$, most commonly observed in its interaction with toluene and tetrahydrofuran (THF). [115] This phenomenon is the result of the electron rich conjugated and double bond systems within the oils donating weakly to the Lewis acidic $TiCl_4$ centre, however not being able to bond directly due to the Lewis basic character of these species being too weak, as well as steric hindrance. This results in the formation of a weakly bound charge transfer complex, usually deep orange or red in colour. These species can only exist in solution, with solids unable to form and lower boiling aromatics still being separable by distillation. It has been observed that solutions of $TiCl_4$ with toluene do form small amounts of solid when left over long period.[115] Taking the red solution and refrigerating it does not result in the formation of a solid.

The Flavex 977s oil appeared to be able to effectively remove $VOCl_3$ from the gaseous $TiCl_4$. When the flow system was run with 15 ml of $VOCl_3$, only 4 ml remained after three cycles, the rest appeared to have been 'captured' by the Flavex 977(s). When $VOCl_3$ and $TiCl_4$ were run together, the distillate appeared dirtier, staining the pipe leading up to the Soxhlet with a black solid. This implies that gas phase reactions continue to occur throughout the distillation, resulting in the formation of a solid that crashes out in the liquid phase (Figure 58). When toluene was run through the system with Flavex 977(s) no oil was found to have passed through, implying that $TiCl_4$ and $VOCl_3$ were responsible for the breakdown and carry-over of the oil fragments, not simply the heating and agitation.

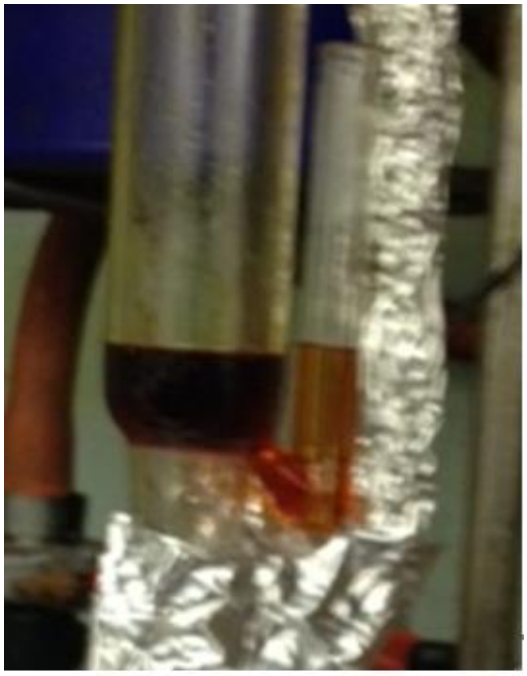

Figure 56: Pure $TiCl_4$ and Flavex 977(s) after 4 cycles, contents of Soxhlet adaptor. $TiCl_4$ appears to break down the naphthenic, which then carries over, staining the distillate red.

Figure 57: Gravex 926 with $TiCl_4$ during first cycle. The red distillate is seen to gather on top off the clean $TiCl_4$ that starts off in the Soxhlet, before falling though when it fills.

Figure 58: 25ml $TiCl_4$ and 1ml $VOCl_3$ with Flavex 977(s). Flow system is stained; solid in Soxhlet suggests that whatever carries over continues reacting.

4.3.2.3. NMR Experiments with Flavex 977s

Following the four initial experiments with $TiCl_4$ and the four naphthenic oils, all of which yielded extremely similar spectra, further experiments were carried out, focussed on the Flavex 977s oil, altering the contents of flask one, in order to study the effect of $VOCl_3$ on the oil, as well as its ability to separate it from $TiCl_4$.

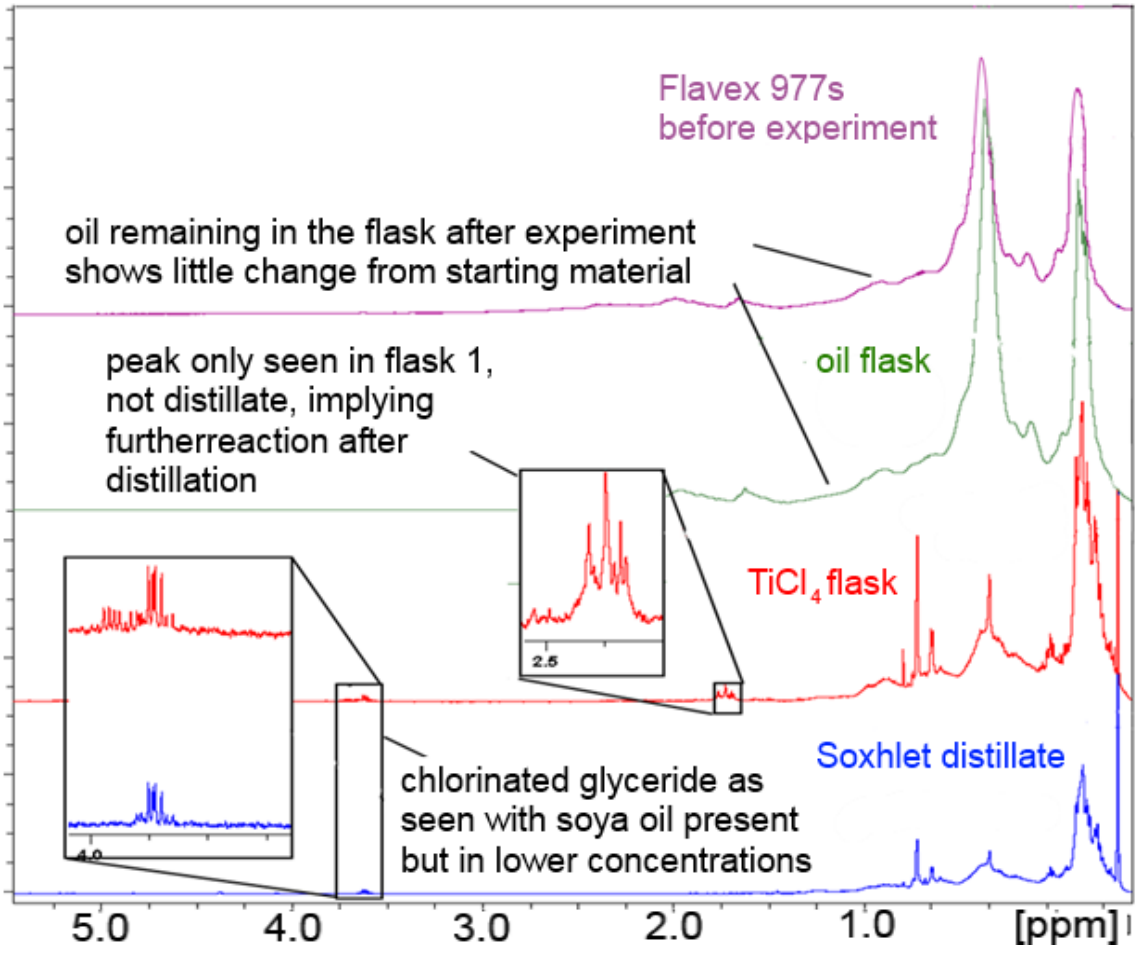

Figure 59: ^1H NMR spectra of the starting material and the contents of flasks 1, 2 and the Soxhlet extractor from experiment in which gaseous $TiCl_4$ was reacted in naphthenic Flavex 977(s) oil Spectra taken in $CDCl_3$. The figure shows the region between 0.0 and 5.4 ppm.

Figure 59 shows the NMR spectra of the contents of the Soxhlet, Flask 1 and the oil from flask 2 after four cycles of gaseous $TiCl_4$, as well as the unreacted oil. The familiar pattern of diminished CH_2 and enhanced CH_3 was seen. The $TiCl_4$ flask and Soxhlet flask also show traces of chloroakanes, implying that the chlorination of double bonds seen with soya oil was still

occurring, but less prevalent. Several peaks were only seen in the $TiCl_4$ flask spectra, implying continued reaction of the oil flask after distillation.

Pure $TiCl_4$, pure $VOCl_3$ and $TiCl_4$ containing 1000 ppm and 40,000 ppm of $VOCl_3$ were put through the flow system with Flavex 977s. The NMR spectra of the Soxhlet extractor's contents after each experiment are compared in Figure 60. The spectra from the Soxhlet were largely the same for each. The peak representing chain and cyclic species was reduced in relation to the straight chain peak. It can be inferred from this that the chains carrying over are considerably shorter than the ones in the starting oil.

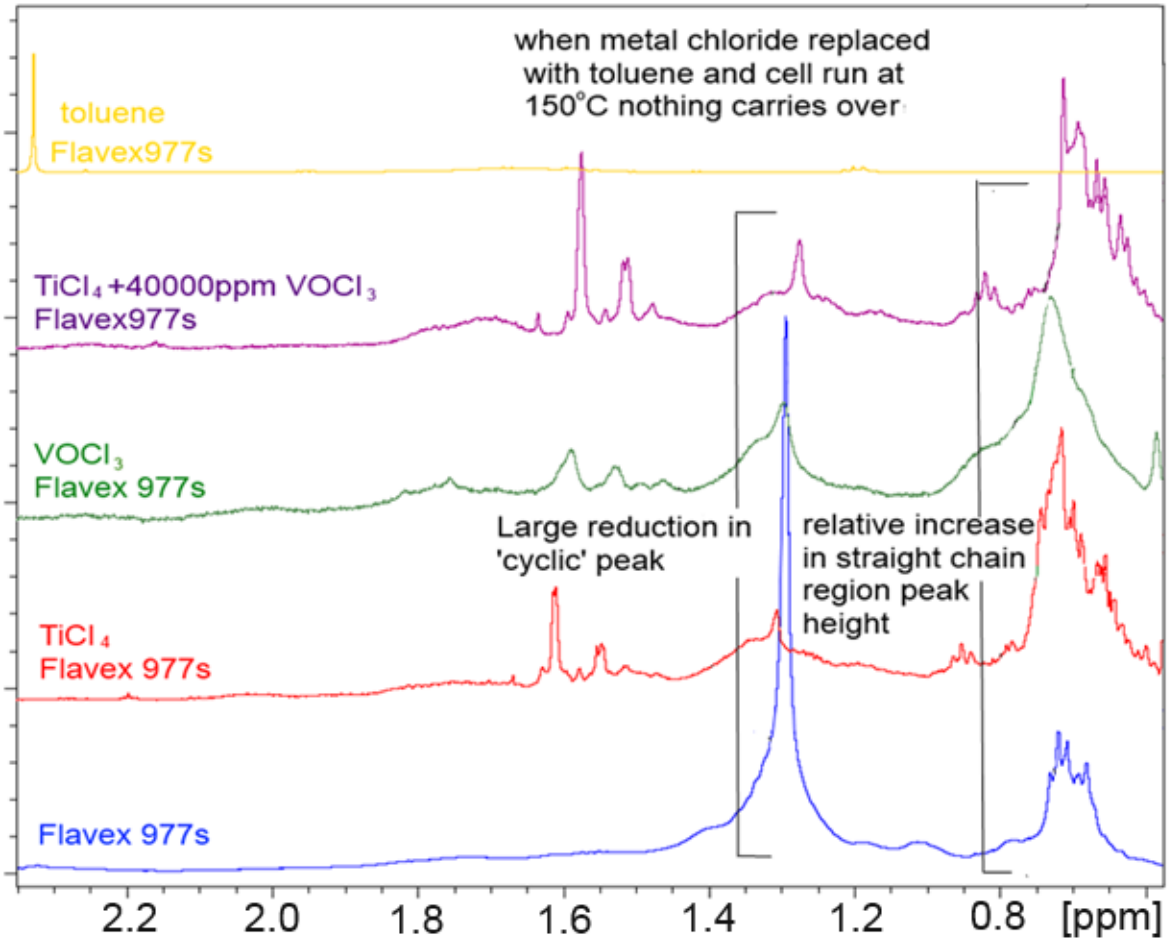

Figure 60: Comparison of the ^1H NMR spectra of Flavex 977s compared with the contents of the Soxhlet extractor after three cycles of $TiCl_4$ (red), $VOCl_3$ (green), $TiCl_4$ + 40000ppm $VOCl_3$ (purple) and toluene (yellow) . Spectra taken in $CDCl_3$. The figure shows the region between 0.8 and 2.4 ppm.

Firstly that the $TiCl_4$ is breaking down the oil into smaller fragments, similar to the soya oil. It could also be due to the distillation only carrying though the smaller chains, however as nothing was seen to carry through when $TiCl_4$ was replaced with toluene, this would still require an interaction with the $TiCl_4$ or $VOCl_3$, possibly in the form of complexation. Following this it is likely that the straight chain alkane fragments that carry through react further after distillation. This explains the solids carrying over, as seen in the Huntsman Pigments and Additives study.

The oil appears to be efficient at vanadium removal. Even with very high vanadium concentration in the starting material, there was not broadening in the final spectra. Furthermore, when using only $VOCl_3$ after three cycles, there was not enough to fill the Soxhlet, the rest appearing to have congealed with the oil in the second flask. The first flow system experiment carried out was that of pure $TiCl_4$ and Flavex 977s.

4.4. Conclusion

A lab bench scale system for removal of $VOCl_3$ from a gaseous stream of $TiCl_4$ using liquid phase oil was designed and built. This involved modifying a Soxhlet extractor so that the volatile products pass through a round bottom flask and an extended column further than directly into the sample chamber. This was done in order to analyse the side products formed during the vanadium removal process, with $TiCl_4$ reacting with the oil species to give unwanted volatile products.

The results conclusively show that $TiCl_4$ is capable of breaking down the soy oil into component fragments capable of passing through a distillation column. The most abundant species formed appears to be the result of the triester backbone of the oil being chlorinated at the 1, and 3 positions, which mirrors the way in which the species is observed to coordinate to $TiCl_4$ in the

case of glycerol tribenzoate. This suggests that the $TiCl_4$ is capable of chlorinating the triglyceride. This reaction is not likely to be favorable and therefore this only happens in small amounts, however, it is likely that this species could build up over time within the Chloride Process due to the recycling of the undistilled fractions.

This is not how $TiCl_4$ usually behaves with alkenes, showing that the state of the reactants in the process is important, as well as the absence of water from the system. It has also been demonstrated that the flow system is capable of separating $VOCl_3$ from the $TiCl_4$ in doses both equal to and far higher than found in industry.

As well as soya bean oil, naphthenic oils were also reacted with $TiCl_4$ using the flowcell. These we also found to produce the chlorinated glyceride species, as well as forming a red charge transfer complex with the $TiCl_4$ which was able to distil over, staining the products and also to continue reacting with the $TiCl_4$ after distillation, forming a black precipitate both of which would have been disastrous were they to occur in industrial production.

Chapter 5

Using Mass Spectrometry to Study Gas Phase Reactions in Chemical Vapour Deposition

5.1. Introduction

The work described in this chapter involved using a molecular beam mass spectrometer to study the hot vapours within an atmospheric pressure CVD reactor. This was designed with the goal of furthering the work with the flow-cell in the previous chapter by detecting and characterising the intermediates of gas phase metal chlorides and carbonyl containing ligands, similar to the reactions seen within this Chloride Process.

Whilst related to the work carried out studying the production of TiO_2, this work is of greater scope, contributing to the understanding of several of the most common CVD reactions studied worldwide. Using a specialised mass spectrometer able to withstand heated corrosive gaseous species and a custom designed mass spectrometer/ CVD adaptor apparatus the deposition of TiO_2, VO_2 and SnO_2 were studied from a variety of precursors.

5.1.1. Atmospheric Pressure CVD

Atmospheric pressure chemical vapour deposition (APCVD) is one of the earliest forms of chemical vapour deposition,[116] and is the building block from which many more complex varieties arise such as atomic layer deposition (ALD)[117] and plasma enhanced CVD (PECVD).[118] The process involves the heating of a precursor molecule containing the metal atom for which the film is to be comprised, often with the bonds to be present in the film pre formed.[119–121]

The vapours of these materials form a thin film on a substrate at high temperatures inside a heated reactor vessel.

APCVD is thought to occur in 6 stages (Figure 61):[122]

1. Evaporation of precursors and transport of gaseous molecules in the bulk gas flow.
2. Precursor vapour enters the heated reactor leading to the formation of reactive intermediates and by products.
3. Some of the gaseous intermediates come into contact with the surface of the heated substrate.
4. Adsorption of precursor/reactive species onto substrate surface.
5. Reactive species diffuse across the surface to growth sites, such as imperfections in the substrate or existing crystals of the product material. This leads to nucleation of the thin film as the reactive species break down.
6. Gaseous by-products of the thin film formation desorb from the surface and are carried out the reactor *via* the exhaust. [123]

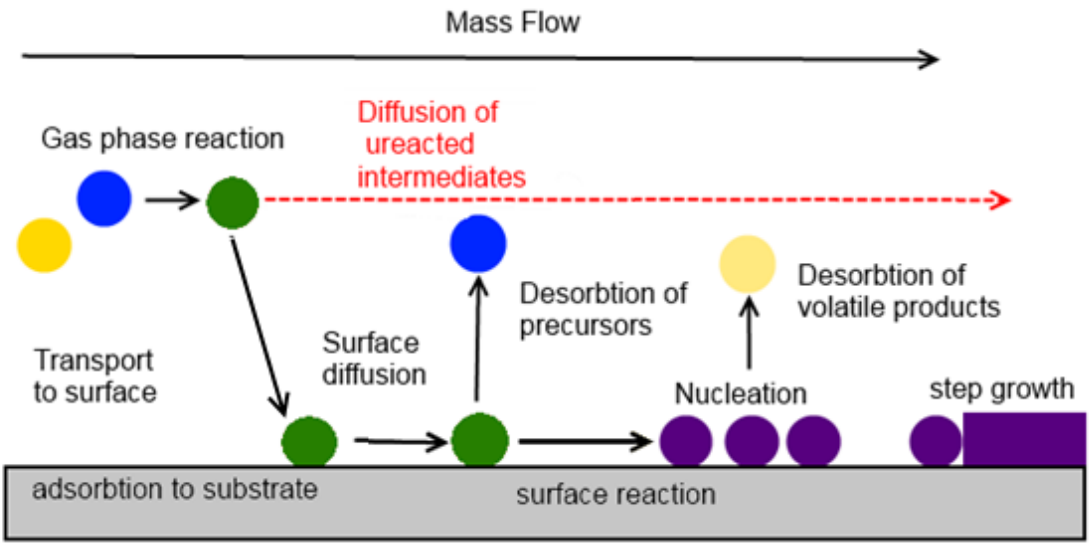

Figure 61: Schematic of basic model of film growth in APCVD[122]

APCVD has been used extensively in the deposition of a wide range of metal oxide thin films. Films of TiO_2,[124–126], VO_2(M),[127–129], SnO_2, [130–132] Fe_2O_3, [133] WO_3, [134,135], ZnO,[136–138], α-Al_2O_3,[139,140] as well as many others. [141] Composite films of two or more of these species that combines the advantageous properties of its components have also been fabricated. [142–144] Furthermore, doping small amounts of metallic or main groups species into a thin film has proven highly effective in APCVD, for instance fluorine doped tin oxide[142] as a transparent conducting oxide, N doped TiO_2 as a photocatalyst [16,145] and W doped VO_2 (M).[146] This can either be achieved by the introduction of a separate bubbler full of co-material/dopant, or they can be deposited from the same vessel if the thermal conditions to generate the desired amount of precursor vapour match closely enough.

Many of the above examples of metal oxide thin film deposition involve using metallic chloride precursors. These are highly prized in APCVD due to their relatively low boiling point as well as being more volatile and reactive than other transition metal species. [147] The advantages of these precursors are however counteracted by their lack of stability in air making handling the precursors challenging.[148] Additionally, unlike with metal alkoxides, another heavily used precursor group[120,128,134,140,149] there are no preformed metal oxygen bonds. This means that the precursor needs to be oxidised by an outside source. This can be achieved using a stream of water,[144] or air.[150]

Another method is to co-deposit the metal precursor with a second, oxygen-heavy organic precursor that provides oxygen by supposedly coordinating to the metal centre and having the excessive organic material 'burnt off'. A common organic oxidising agent is ethyl acetate.[151] This has been used extensively in the oxidation of $TiCl_4$,[152,153] however it has also been used in the deposition of VO_2 from VCl_4.[154] Ethyl acetate is used in this study as the predominant oxidising agent, due to its similarity to diethyl malonate, as the malonate themselves were

observed to lead to blockages.

In APCVD the concentrations of the precursors are controlled by the vapour pressures generated. By altering the temperature of the bubbler, the amount of vapour formed is controlled. This is determined by the Clausius-Clapeyron equation (equation 1).[155]

$$ln(P1/P2) = (\Delta H_{vap}/R)((1/T2) - (1/T1)) \quad (1)$$

where:

ΔH_{vap}= The enthalpy of vaporization of the liquid

R = The real gas content, or 8.314 J/(K × Mol).

T1 = The temperature at which the vapour pressure is known

T2 = The required vapour pressure

P1 & *P2* = The vapour pressures at T1 and T2, respectively.

This equation is used to generate vapour pressure curves of the precursors in order to determine the pressure evolved at a given temperature.[156] In general the precursor vapour is generated at roughly half of its boiling point [157] By controlling the temperature of the bubbler the amount of each precursor reaching the reactor can be manipulated. This is especially useful in dopant studies, wherein only a very small amount of the dopant precursor can make it to the reactor.

APCVD offers the ability to uniformly coat large areas of substrate with a repeatability that is hard to obtain for other CVD techniques such as aerosol assisted (AACVD). It is also highly tuneable, with the flow rates and temperature of the bubblers controlling precursor flows effectively.[158] These factors lead to the most compelling reason to choose APCVD over other means of depositing thin films: industrial applications. As well as simplicity and reliability the fact that it is carried out entirely at ambient pressures means that the process involves no

vacuum pumps, that are expensive to procure and maintain. Cold wall and hot wall industrial reactors for the deposition of SiO_2 barrier layers onto float glass has been in existence for many years.[159]

The major drawback of APCVD is the limited number of precursors available. Precursors must be suitably volatile to generate a vapour and suitably reactive to deposit a film. This means that for every material there are only a few options, for instance with TiO_2 there are few studies outside of $TiCl_4$ and titanium isopropoxide. Furthermore there can be major issues with the purity of some films,[160] particularly with carbon contamination.

This study seeks to study the gas phase interactions (Figure 61), in order to determine the intermediates that lead to the formation of films at different temperatures, by examining three frequently deposited thin films, namely TiO_2, V_xO_y and SnO_2.

5.1.2. Using Mass Spectrometry to Study CVD

Chemical vapour deposition is a widely used means of depositing metal oxide thin films onto a variety of substrates.[161,162] Despite widespread use in the deposition of metal oxide coatings, little is known about reactions within the gas phase during the deposition of the thin film.[122] Part of the reason for this is the challenge in taking *in-situ* measurement from the inside of a chemical vapour deposition reactor, as well as the potentially damaging nature of those vapours to analytical equipment.

Although relatively few in number, mass spectrometry studies of vapour phase deposition have been carried out previously. Turgambaeva *et al.* studied the gas phase reactions of copper(I) cyclopentadienyltriethylphosphine for the deposition of cuprous films. This was achieved by heating a small sealed ampoule of the precursor, whilst attached to the front of a time of flight mass spectrometer that measured the content of the evolved gas.[163] Time resolved spectra

showed how the evolution of fragments over time as the sample was heated, similar to thermogravimetric analysis.

Li *et al.* used mass spectrometry to study the deposition of silicon carbide from a tetraethyl silane precursor using hot-wire CVD. This is a technique whereby the decomposition of the gaseous precursor is catalysed by the heated substrate it is deposited onto, usually tungsten wire or stainless steel.[164] Measurements were obtained by placing the hot – wire apparatus into a chamber with a time of flight (TOF) mass spectrometer. This study revealed the formation of four membered rings of alternating silicon and carbon in the gas phase.[165]

Numerous mass spectrometry studies have been undertaken by Rego, Petherbridge and Tsang *et al.* on the mechanism for the CVD of diamond from methane. Using a Hiden HPR-60, the same model spectrometer as this study, the levels of CH_4, C_2H_6, C_2H_4 and C_2H_2 and CH_3 in the gas phase were analysed. [166] Additionally the device was employed to measure the effects of nitrogen,[167] chlorine,[168] and phosphine[169] on the growth mechanics. Furthermore low temperature plasmas of methane and CO_2 were analysed, in order to determine the ideal conditions for formation of the $\bullet CH_3$ radical, which is believed to be the major species in the formation of diamond thin films.[168]

Analysis of titanium containing precursors has been carried out using mass spectrometry previously. Rahtu *et al*. used a four vacuum chamber quadrupole assisted MBMS system, sampling directly from the exhaust of a thin quartz tube hot wall reactor to examine the formation of Ti-N-Si composite thin films from $Ti(NMe_2)_4$, NH_3, and SiH_4, examining the decay of the SiH_4 peak in order to construct an Arrhenius plot and in doing so propose a mechanism for the interaction of the precursors and subsequent thin film deposition.[170]

Additionally Rahtu and Matero *et al.* used a similar system combined with a quartz crystal mass balance to analyse atomic layer deposition of titanium tetrachloride,[171] titanium(IV)

isopropoxide[172] and trimethyl aluminium[170] with deuterated water. These studies provided insight into the breakdown of the precursors within the gas chamber, showing how loss of ligand is affected by the presence of water. The use of a deuterated solvent also allowed for the differentiation of side products evolved from reaction of the precursor with the D_2O and those evolved from the thermal decay of the precursor itself.

The main difference between the system proposed in these experiments and those discussed above is that of versatility and scale. Most of the above studies were on heavily modified systems, that do not resemble an unmonitored deposition, with the exception of the work on diamond. That work whilst similar, only focused on the use of methane as a precursor, scanning in very low mass ranges (below 100 amu). A problem with this is that spectra can be noisy in this region. The system designed for this work seeks to emulate thin film deposition on a laboratory scale as closely as possible, whilst still sampling continuously and safely from within the reactor. The work also focuses on a wider range of precursors than seen in previous studies, with multiple titanium and vanadium precursors analysed as well as additional work with tin oxide and silicon oxide precursors carried out.

5.1.3. Mass Spectrometry

Mass spectrometry is the technique used mainly in the characterisation of the organic materials, with uses in chemistry[173] as well as widespread use in the fields of art restoration and archaeology.[174]

The general principal of mass spectrometry is based around the ionization of a parent molecule, forming a charged species, usually positive (equation 2)[175]

$$M + e^- \longrightarrow M^{+\bullet} + 2e^- \qquad (2)$$

This radical cation then decays by numerous possible pathways that can be categorized into two paths, shown in equation 3. The species either breaks down to form a radical (R) and a

positively charges species $[EE]^+$ as is the case with equation 3a or the parent ion can lose a neutrally charged species (equation 3b), with the other species remains a radical cation.[176]

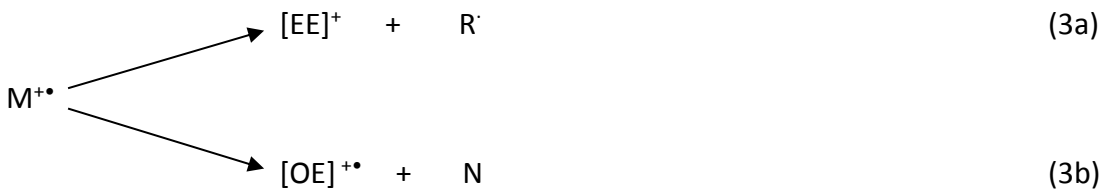

(3a)

(3b)

The sample can be ionised by a wide range of different techniques. The simplest of these is electron ionisation (EI), as is used in this study. This involves subjecting the sample to a beam of high energy electrons from a filament. The current applied to the filament is used to control the energy of the electrons, which is usually set in the region of 70 eV. [175,177]

Higher energy electrons lead to more fragmentation. A method of ionisation is judged 'hard or soft' depending on the level of fragmentation it produces (hard being more fragmentation). EI is considered overall to be a hard ionisation method.

Soft ionisation methods include chemical ionisation (CI), which involve creating a charged cloud of molecules. The most common chemical ionisation agent is methane, which forms highly unstable CH_5^+ and $C_2H_5^+$.[178] These species go on to ionise the sample. Another soft method is electrospray ionisation (ESI), in which a solution of the material to be studied is pushed through a thin, charged tube into a heated vacuum chamber. The solvated analyte exists as an ion in solution. Upon entering the chamber the solvent evaporates and the now gaseous ions are accelerated through the spectrometer. [179] These techniques are frequently used in biology in the study of protein molecules as they allow the base structure of the macromolecule to be maintained.

The charged species are separated according to their mass to charge ratio in the mass analyser portion of the device. There are several types of mass analyser including magnetic sector, where the charged species pass through a curved tube with a variable magnetic field applied so that only species of a certain mass can pass through, the others colliding with the walls.[180] There are also time of flight (TOF) detectors, which separate ions by velocity.[181] This method struggles to separate ions of high mass. To counteract this most modern TOF analysers have a reflectron, a series of high voltage ring electrodes, creating an electrostatic field at the end of the flight tube that reflect the particles in the opposite direction, heavier molecules being able travel further into the magnetic field before being repelled. Quadrupole spectrometers offer advantages in terms of reproducibility and cost, however unlike TOF, quadrupoles must scan a range of masses in succession, not all masses simultaneously. A result of this is that scans take longer to complete the wider scan range.

In the case of the Hiden HPR-60 the spectrometer, this is fitted with a quadrupole mass analyser. This consists of four metal rods arranged parallel in a square pattern (Figure 62) inside a cylindrical chamber.[182] These rods act as electrode with a constant DC voltage and a variable radiofrequency (RF) voltage applied across them. Ions that pass along this path oscillate according to this frequency however for each frequency only ions of a certain mass/ charge ratio can pass through, with heavier or lighter species 'spinning out' and colliding with the chamber walls.[183] The quadrupole in the spectrometer used in this work is a triple filter quadrupole. These devices feature a smaller quadrupole in front of and behind the main unit, arranged in tandem (Figure 63). This is beneficial as it can increase resolution in detection of high mass species.[184] Other triple quadrupole can be used to filter ions and then break down the filtered ions into fragments, the second quadrupole acting as a collision chamber, before filtering again. [185]

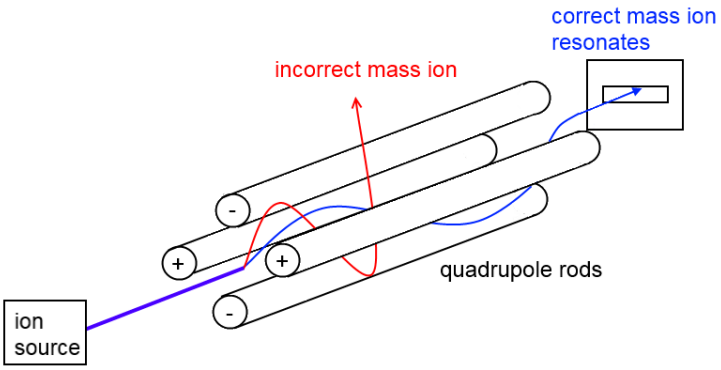

Figure 62: Diagram of a quadrupole mass analyser

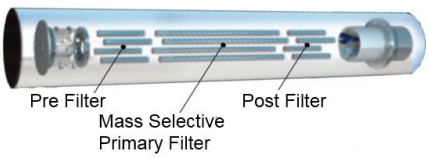

Figure 63: Schematic of the triple filter analysers used in the Hiden HPR-60[368]

In this study, all mass spectrometry measurements were taken using a modified quartz tube CVD reactor containing a heated stainless steel pipe. This pipe carried a stream of the reactive vapour inside the system into a heated, airtight chamber attached to the front of a Hiden HPR60 molecular beam mass spectrometer (MBMS). This spectrometer has an inlet approximately 0.25 mm in diameter. This leads to three consecutive vacuum chambers of increasingly low pressure. This focuses the gas entering the system into a beam of singular molecules that enter the ionisation chamber. The species are then ionised using a dual source low profile electron ionisation source, before separation by Quadrupole mass analyser. The device uses an Off-Axis Positive and Negative Ion Pulse Counting Single Channel Electron multiplier detector with a maximum threshold of 1000 Da. This system allows for examination of extremely low concentrations of analyte compared to traditional spectrometers, enabling the analysis of transition metal species that would damage the detector in larger quantities. The MBMS system is ideal for high energy gas phase studies as upon entering the system the gaseous molecules undergo no further reaction, not coming into contact with each other or the walls of the detector.

The detector was set to positive ion RGA mode for all measurements meaning that all species analysed are positively charged (cations or radicals). The energy of the ionizing electrons was set to 70 eV for all experiments.

5.2. Experimental

Argon (Puresheild 99.998%) was obtained from BOC and used as supplied. Films of TiO_2 were deposited using a modified cold wall CVD reactor, onto 60 × 40 × 4 mm silicon coated float glass substrates, from Pilkington Glass Plc. The argon carrier gas was delivered into the system using stainless steel tubing. All of the tubing making up the rig was heated to 150 °C using heater tape, monitored using by Pt-Rh thermocouples. The precursor was introduced into the gas stream using stainless steel bubbler, heated to roughly half the boiling point of the precursor using a heater jacket. Hot argon or nitrogen was passed through this bubbler, the gas stream carrying the precursor molecules to the reactor. When used, ethyl acetate was introduced through a second bubbler, heated to 35 °C (Figure 64). The amount of precursor was controlled using the flow rate of argon through the bubbler. This was kept as low as possible whilst still seeing data on the mass spec readout as to avoid dealing with unnecessary damage to the detector.

The precursor vapour enters into the reactor, which is held at an elevated temperature, between 300 and 600 ˚C. A stainless steel tube above the substrate carried a sample of the reagent gas out of the reactor with the majority passing out of the rear of the reactor as exhaust, as with regular vapour deposition. Stainless steel tube passes through a chamber bolted to the front of the mass spectrometer, where a small amount entered the chamber through a hole in the tube (Figure 65). Both the chamber and the tube were heated to 170 ˚C, however due to the flow of hot air from the reactor, it is estimated the temperature inside the tubing is far higher. A small amount of the vapour entered the spectrometer through a ¼ mm

hole in the front end, which then formed the molecular beam. The remainder was carried back into the fume hood through the heated tube or a secondary exhaust built into the front chamber (Figure 66). There is added protection for the spectrometer in the form of a weak flow of nitrogen or argon over the spectrometer's inlet, known as the purge flow, which can be used to dilute the gas stream further.

In most experiments the mass spectrometer was set to continuously scan over a set range. After collecting a background of at least 10 scans, the precursor bubbler was opened in order to view the spectrum of the precursor only. Following this the ethyl acetate oxidising agent bubbler was opened (if used), and the spectra of both reagents in the gas stream was observed. Each time either of the bubblers was turned on or the flow rates altered, the mass spectrometer would be allowed to take 10 scans if the range was between *m/z*- 50 - 300 and 5 scans if it was between *m/z*- 50 – 500. This was decided as it allows for enough scans to identify anomalous results, which can be the result of impurities or build-up of charge on the quadrupole, whilst still preventing overexposure of the detector to the gas stream, which can lead to blockages and damage.

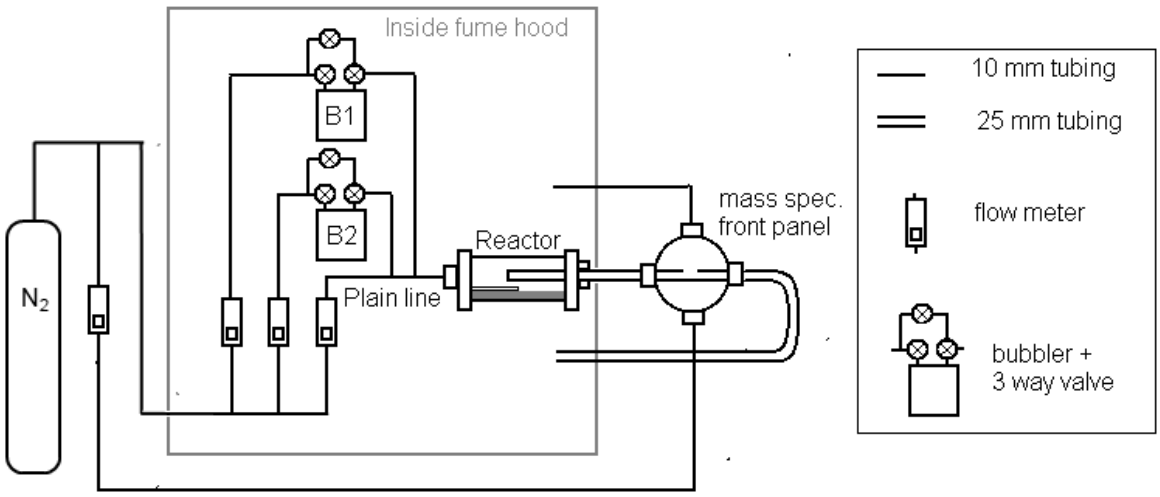

Figure 64: Schematic representation of entire mass spectrometry CVD setup.

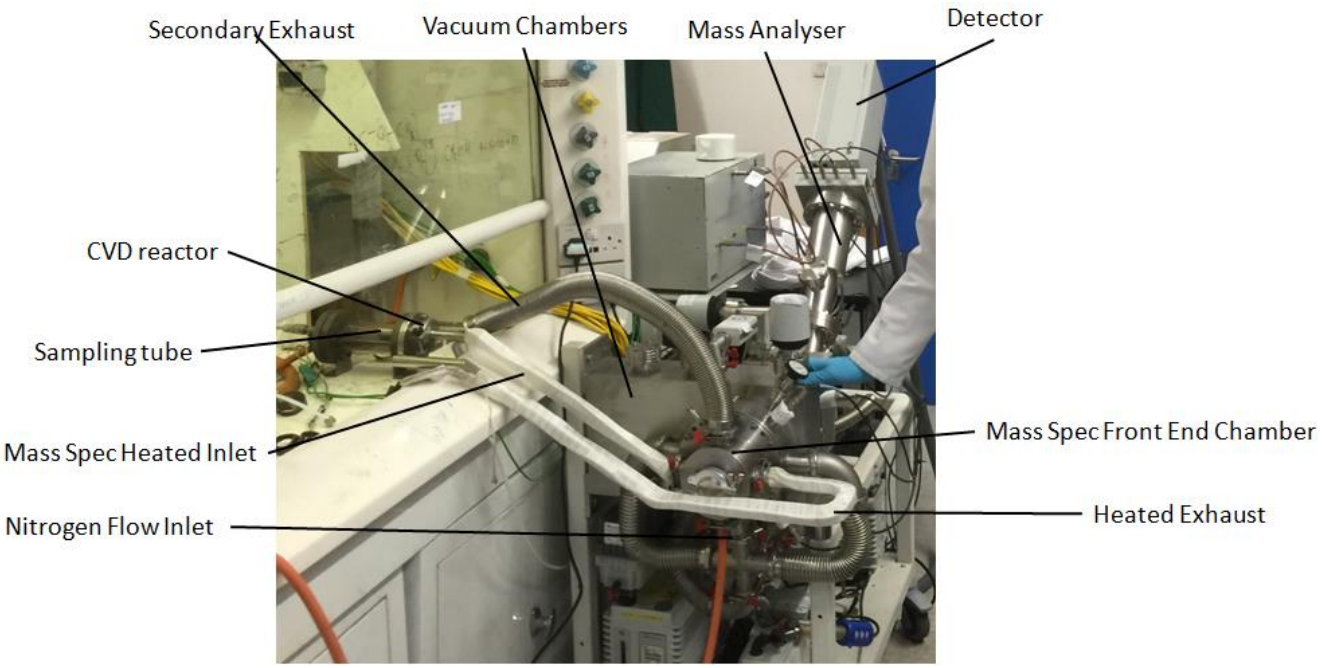

Figure 65: Annotated photograph of mass spectrometer CVD setup.

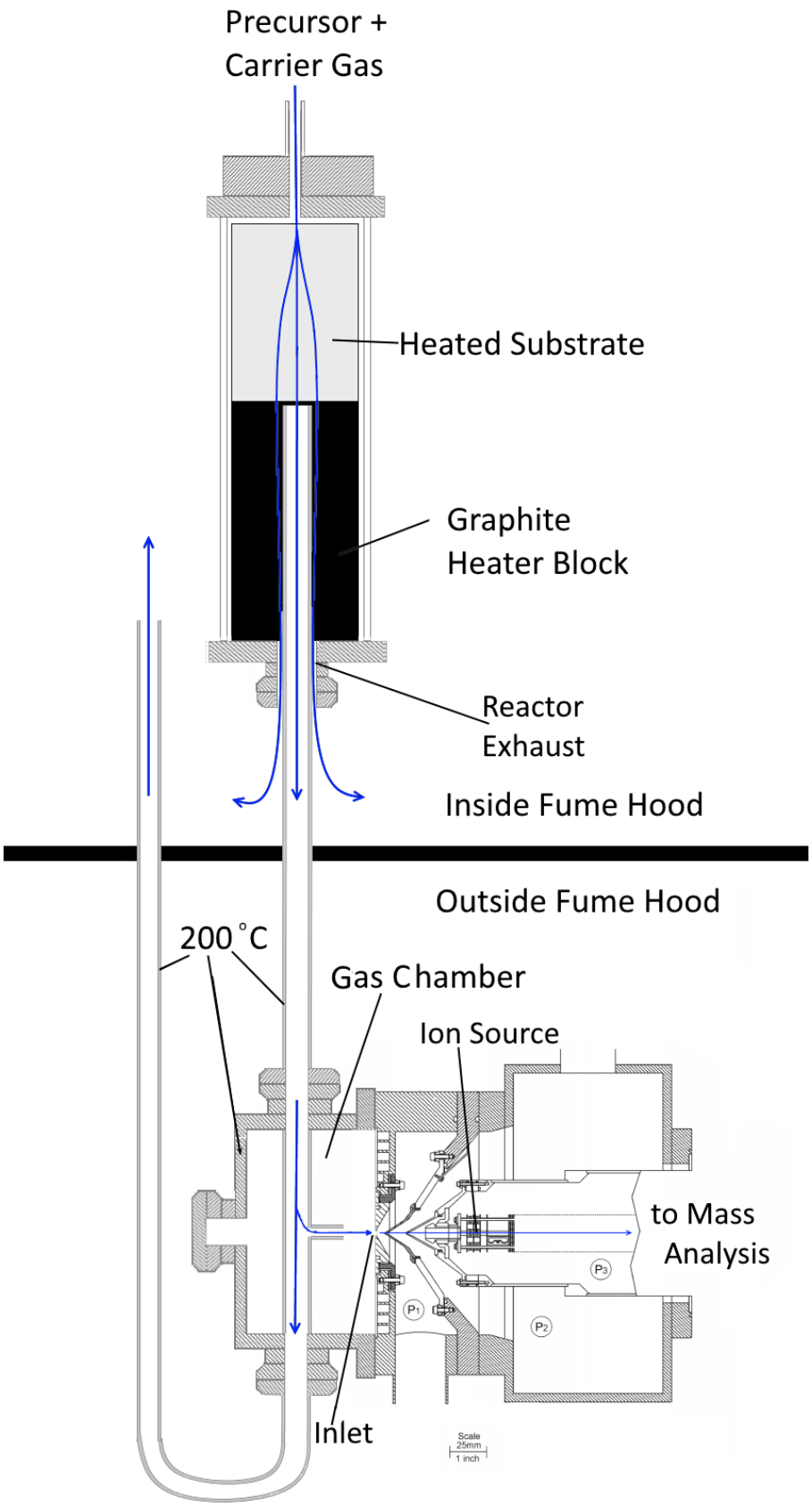

Figure 66: Schematic of CVD apparatus and mass spectrometer setup.

In the majority of experiments scanning began at 50 amu, so as to avoid sampling the carrier gas N_2 (mass = 28 amu) or argon (mass = 40 amu). Due to their extremely high concentration, sampling these numbers for long period can age the detector extremely quickly. Furthermore if too high a concentration of a single mass is obtained, the detector will automatically shut off in order to prevent damage. By not sampling the highly abundant carrier gasses, the system can be opened to allow more analyte into the system, improving the signal to noise ratio of the spectra. For these reasons scans were only taken below 50 amu when specifically searching for lower mass fragments.

5.2.1. Preliminary Experiments

Before using the apparatus to study thin film depositions, two proof of concept experiments in which toluene was passed through the reactor in order to test the devices sensitivity were carried out.

5.2.1.1. Toluene Test Run

In order to test the spectrometer's ability to sample a mobile gas stream, toluene was heated in a bubbler to 60 ˚C. Scans were taken between 1 and 100 amu. The bubbler was opened and closed alternately every 10 scans, each time increasing the flow rate through the bubbler by 0.2 L min^{-1} from 0.2 up to 1 L min^{-1}. The reactor was kept at 150 ˚C and the plain line flow at 6 L min^{-1} over the whole experiment. Figure 67 shows the effect of the different flow rates on the number of counts per second for the mass number corresponding to the intact toluene molecule (91amu).

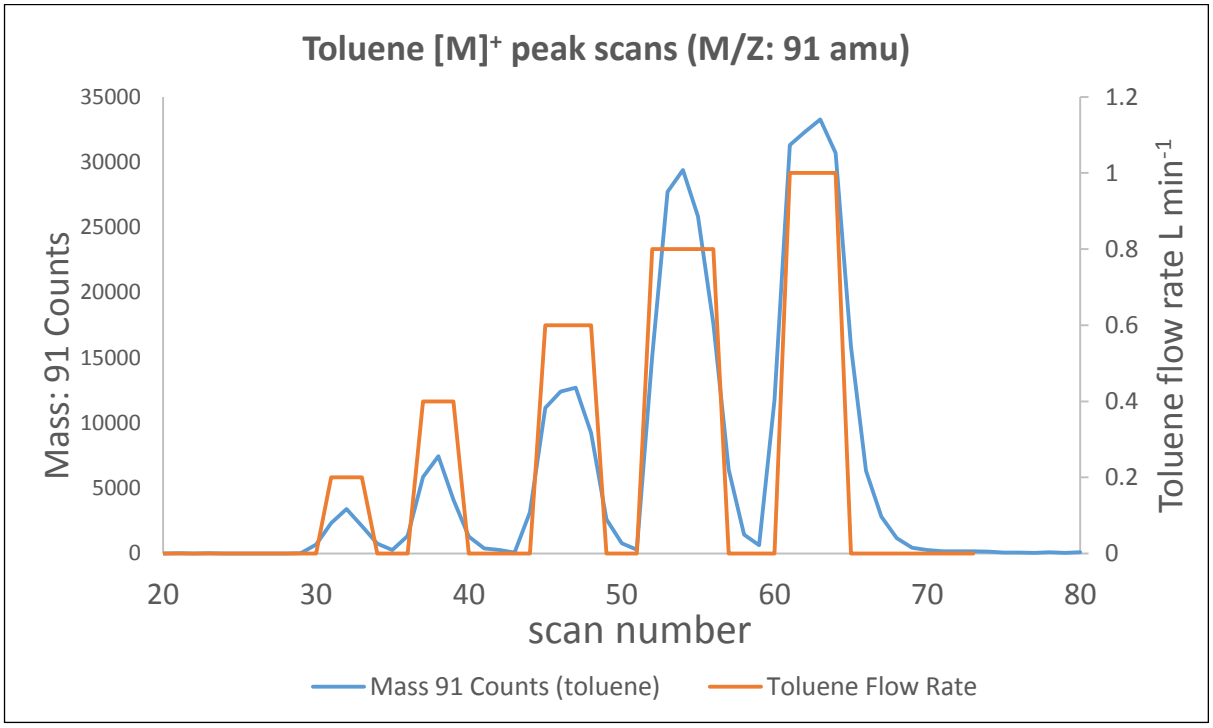

Figure 67: Intensity of the mass spec peak at *m/z*- 91 representing the molecular mass of toluene plotted alongside the flow rate through the toluene bubbler.

This study shows that the spectrometer was able to pick up a signal of toluene across the entire range of flow rates, as well as that the signal increases roughly proportionately with flow rate. This is an encouraging result as toluene has a boiling point of 110 ˚C, similar to that of many CVD precursors.

5.2.1.2. Purge Flow Test

Toluene was also used to the test the effectiveness of the purge flow system in lowering the concentration of harmful vapour species. As before, toluene was heated in a bubbler to 60 ˚C with the reactor kept at 150 ˚C and the plain line flow at 6 L min^{-1}. Scans were carried out over the range of *m/z*- 1 -100. Every 5 scans the purge flow rate was increased by 0.5 L min^{-1}, from 0 – 2 L min^{-1}. Over this range the signal was observed to fall from ~22000 to ~15000 counts, a reduction in signal of around 30 % (Figure 68).

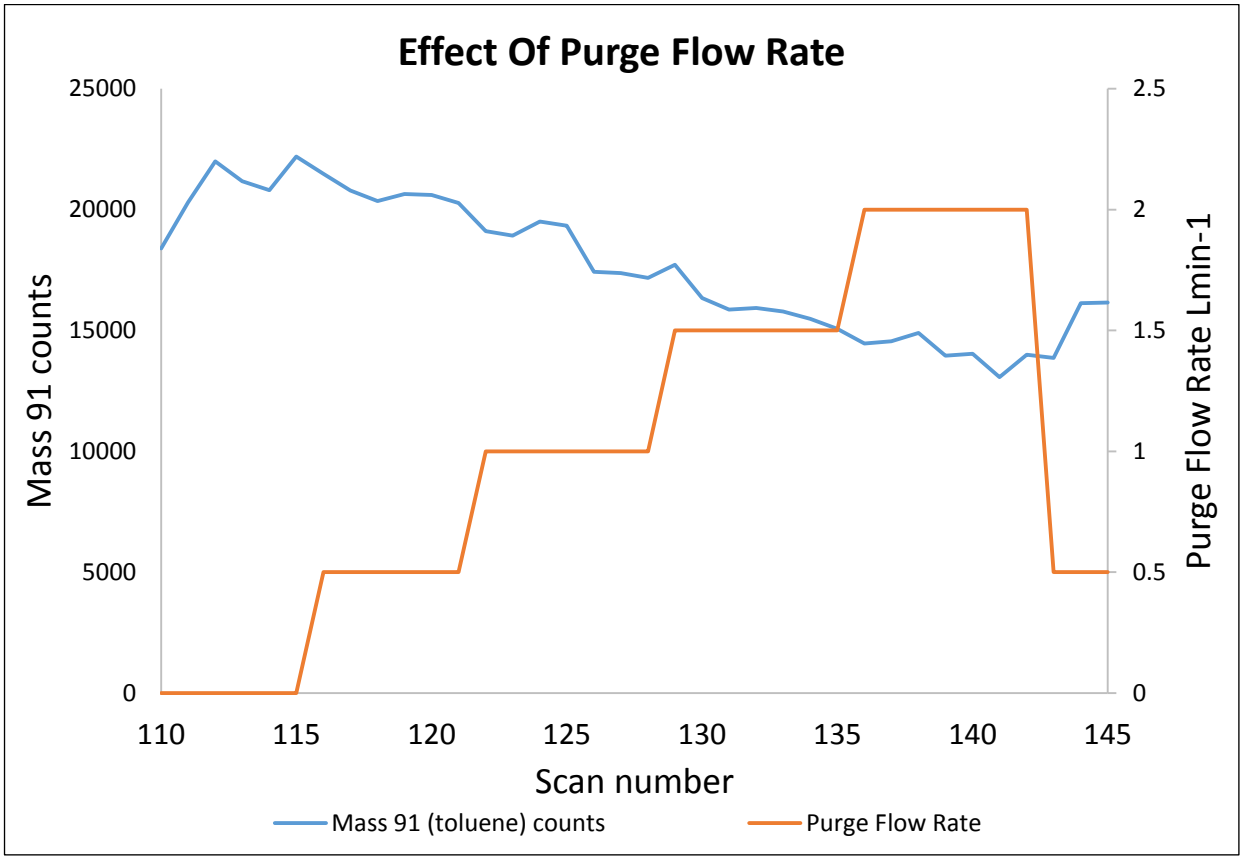

Figure 68: Intensity of the mass spec peak at *m/z*- 91 representing the molecular mass of toluene plotted alongside the flow rate of the purge flow.

5.2.2. Precursor Deposition

Table 14 shows the experiments carried out using the CVD mass spectrometry apparatus that successfully produced spectra of the precursors. Initially the reaction of titanium and vanadium oxytrichloride with ethyl acetate was studied. Ethyl acetate was chosen as it is a common oxidising agent in CVD, with a low boiling point allowing it to be easily manipulated. Attempts were made to use diethyl malonate to which would have been a better fit with the crystallography study, however blockages within the tubing were found to form quickly upon opening the bubbler in both cases. Ethyl acetate can be thought of as half of a diethyl malonate molecule. Although lacking the chelating properties of diethyl malonate, the increased reactivity of such was the likely cause of the blockages.

Following the study with $TiCl_4$ and $VOCl_3$, titanium(IV) isopropoxide (TTIP) were studied, along with butyltin trichloride, a common SnO_2 precursor.

Finally a study was carried out investigating the reactivity of VCl_4 with ethyl acetate. This common vanadium oxide precursor has been found to be extremely sensitive to the presence of an oxidising agent, with the formation of thermochromic VO_2 occurring with roughly equal mass flow rates of the precursor and ethyl acetate. Increasing the flow of ethyl acetate has been found to result in growth of V_2O_5 films. Using mass spectrometry, the different gas phase species forming as the ratio of ethyl acetate to VCl_4 changes has been analysed in order to determine a possible the cause of this sensitivity.

Table 14: List of precursors and conditions used in the mass spectrometry analysis of CVD experiment.

Number	Precursor	Reactor Temp (˚C)	Scan Range	Bubbler Temp (˚C)	Bubbler Flow rate (L min^{-1})	Plain Line Flow Rate (L min^{-1})	Ethyl acetate bubbler flow rate (L min^{-1})	Observations
1	Ethyl Acetate	300, 400, 500 +600	1-100	35	0.4	6	n/a	Strong peaks visible immediately. No film deposited no discernible difference between spectra at different temperatures
2	Titanium tetrachloride	300 + 600	50 - 300	60	0.4	2	0	Spectrum of $TiCl_4$ fully visible
3	Titanium tetrachloride	300 + 600	50 - 500	60	0.4	2	0.4	At 600 ˚C Coordination peaks of ethyl acetate to $TiCl_4$ visible. Only $TiCl_4$ and ethyl acetate peaks seen at 300 ˚C
4	Vanadium Oxytrichloride	300 + 600	50 - 300	60	0.4	2	0	Spectrum of $VOCl_3$ fully visible
5	Vanadium Oxytrichloride	300 + 600	50 - 300	60	0.4	2	0.4	Coordination peaks of ethyl acetate to vanadium oxytrichloride visible at 300 ˚C and 600 ˚C
6	Titanium(IV) isopropoxide	300 + 600	50 - 300	110	0.2	6	0	Major issues with blockages above 300 ˚C, little difference between temperatures
7	Butyltin Trichloride	300 + 600	50 - 500	120	0.4	6	0	Spectrum of $BuSnCl_3$ fully visible
8	Butyltin Trichloride	300 + 600	50 - 500	120	0.4	6	0.4	Coordination peaks of ethyl acetate to $BuSnCl_3$ visible at 300 ˚C and 600 ˚C
9	Vanadium Tetrachloride	300 + 600	50 - 500	35	0.4	2	0	Spectrum of VCl_4 fully visible
10	Vanadium Tetrachloride	550	50 - 500	35	0.4	2	0.05	Spectrum of VCl_4 fully visible. Small peaks match those of $VOCl_3$
11	Vanadium Tetrachloride	550	50 - 500	35	0.4	2	0.2	Spectrum of VCl_4 fully visible. Small peaks match those of $VOCl_3$ stronger than in 10
12	Vanadium Tetrachloride	550	50 - 500	35	0.4	2	0.6	Spectrum of VCl_4 fully visible. $VOCl_3$ peaks now more intense that VCl_4 peaks of similar mass/charge ratio. Intermediate VCl_4 + ethyl acetate complex observed

5.2.2.1. Ethyl Acetate

Ethyl acetate (anhydrous 99.8%, Sigma Aldrich) was placed in a stainless steel bubbler equipped with a heater jacket and a thermocouple. This bubbler was connected to the CVD system. The bubbler was heated to 35 ˚C whilst the mass spectrometer scanned the range of 1-100 mass numbers. The bubbler was opened and a flow of nitrogen (0.6 L min^{-1}) transported the gaseous ethyl acetate to the plain line through an 80 ˚C 10 mm stainless steel tube. Once inside the plain line the vapour joined a 6 L min^{-1} flow of nitrogen heated to 150 ˚C, carrying it into the reactor. From the reactor the sample was transported to the mass spectrometer *via* the 20 mm sampling tube and analysed, with the excess vapour transported back into the fume hood through the exhaust tubes. Following the opening of the bubbler, 10 scans were taken of the reagent gas before closing the bubbler and increasing the reactor temperature by 100 ˚C. This was repeated 4 times, from 300 up to 600˚C.

5.2.2.2. Titanium Tetrachloride

Titanium tetrachloride (anhydrous 99%, Sigma Aldrich) was placed in a stainless steel bubbler (B1) equipped with a heater jacket and a thermocouple that was then connected to the CVD apparatus. The bubbler was heated to 60 ˚C. Ethyl acetate (anhydrous 99.8%, Sigma Aldrich) was added to a second identical bubbler (B2), attached in the same way as the first and heated to 35 ˚C. The mass spectrometer scanned the range of 50 to 500 mass numbers. The $TiCl_4$ bubbler was opened and a flow of nitrogen (0.4 L min^{-1}) transported the gaseous $TiCl_4$ to the plain line through a 150 ˚C, 10 mm stainless steel tube. Once inside the plain line the gaseous $TiCl_4$ joined a 2 L min^{-1} flow of nitrogen heated to 150 ˚C, carrying the precursor into the reactor, which was heated to 600 ˚C. A sample of the atmosphere within the reactor was transported to the mass spectrometer *via* the 20 mm sampling tube and analysed, with the excess vapour transported back into the fume hood through the exhaust tubes. Five scans were taken of the

$TiCl_4$ vapour before B2 was opened as well, releasing a stream of ethyl acetate carried by a 0.4 L min^{-1} stream of N_2 into the plain line, where it mixed with the $TiCl_4$ before entering the reactor. Five scans were obtained of the $TiCl_4$ / ethyl acetate mixture before both bubblers were closed. The reactor temperature was lowered to 300 ˚C and the atmosphere in the detector allowed to return to its previous state before the process was repeated. Only five scans were obtained for each set of conditions as the highly reactive nature of the $TiCl_4$ lead to rapid oxidation to solid TiO_2. This lead to the formation of blockages, which would then clog the mass spectrometer inlet, preventing further scans.

5.2.2.3. Vanadium Oxytrichloride

Vanadium oxytrichloride (99%, Sigma Aldrich) was placed into bubbler B1 and attached to the CVD apparatus. The bubbler was heated to 60 ˚C. Ethyl acetate (anhydrous 99.8%, Sigma Aldrich) was added to B2, attached and heated to 35 ˚C. The reactor vessel was heated to 600 ˚C. The mass spectrometer scanned the range of 50 to 500 mass numbers. B1 was opened first, allowing a stream of gaseous $VOCl_3$, to be carried through the 150 ˚C, 10 mm stainless steel tubing with a flow of N_2 (0.4 L min^{-1}) towards the plain line, joining a 2 L min^{-1} nitrogen gas stream at 150 ˚C. The precursor passed into the reactor where a sample of the atmosphere within was transported to the mass spectrometer *via* the heated 20 mm sampling tube. The excess reagent gas passed back into the fume hood through the exhaust tubes. $VOCl_3$ was judged to be far slower to block the spectrometer than $TiCl_4$ allowing for 10 scans to be obtained. Following this, ethyl acetate was released into the gas stream from B2 (heated to 35 ˚C , with a gas flow of 0.4 L min^{-1}). Ten more scans were taken before both bubblers were shut off. The reactor temperature was lowered to 300 ˚C and the signals given by the previous experiment observed to dissipate until the spectrum resembled that of the carrier gas only. At

this point the process was repeated, capturing 10 scans of $VOCl_3$ and $VOCl_3$ / ethyl acetate at the lower temperature.

5.2.2.4. Titanium(IV) Isopropoxide

Titanium(IV) isopropoxide (TTIP) (97%, Sigma Aldrich) was placed in B1 and connected to the CVD system at which point it was heated to 110 ˚C. The reactor temperature was set to 300 ˚C and the mass spectrometer scanned the range of 50 to 300 mass numbers. B1 was opened and a 0.4 L min^{-1} stream of nitrogen carried the gaseous titanium(IV) isopropoxide through stainless steel tubing heated to 150 ˚C to the plain line, heated to the same temperature with a 6 L min^{-1} flowing towards the reactor. A sample of the atmosphere within the reactor was transported to the mass spectrometer *via* the 20 mm sampling tube and analysed, with the excess vapour transported back into the fume hood through the exhaust tubes. Five scans were taken of the TTIP vapour before B1 was closed and the reactor temperature increased by 300 ˚C to 600 ˚C. The process was repeated with five scans of TTIP vapour collected at 600 ˚C.

5.2.2.5. Butyltin Trichloride

Butyltin trichloride (95%, Sigma Aldrich) was placed into bubbler B1 and the vessel attached to the line of the CVD system, sealing it shut. The bubbler was heated to 120 ˚C. Ethyl acetate (anhydrous 99.8%, Sigma Aldrich) was added to B2, attached and heated to 35 ˚C. The reactor vessel was heated to 600 ˚C. The mass spectrometer was set to scan the range of 50 to 500 mass numbers. B1 was opened first, allowing a stream of gaseous $BuSnCl_3$, to be pass through the 150 ˚C, 10 mm stainless steel tubing with a flow of N_2 (0.4 L min^{-1}) towards the plain line, mixing with the 2 L min^{-1} plain line flow of nitrogen at 150 ˚C. The precursor passed into the reactor where a sample of the atmosphere within was transported to the mass spectrometer *via* the 20 mm stainless steel sampling tube, heated to 150 ˚C. The excess reagent gas passed back into the fume hood through the exhaust tubes. Unlike the titanium precursors, $BuSnCl_3$

was found not to block the detector at all, allowing for more numerous scans over a longer range. After ten scans, ethyl acetate was released into the gas stream from B2 as described in the method for the $TiCl_4$ and $VOCl_3$ depositions. 10 more scans were taken before both bubblers were shut off. The reactor temperature was lowered to 300 ˚C and the signals given by the previous experiment observed to dissipate until the spectrum resembled that of the carrier gas only. At this point the process was repeated.

5.2.2.6. Vanadium(IV) Chloride

The study of VCl_4 consisted of four different depositions. In each, VCl_4 was placed into bubbler B1, connected to the APCVD system and heated to 35 ˚C. A 0.6 L min^{-1} flow of N_2 pushed the VCl_4 through the 10 mm stainless steel tubing into the plain line, which were heated to 100 and 150 ˚C respectively. The gaseous VCl_4 flowed into the reactor which was set to 550 ˚C from which some of the atmosphere within passed along the 20 mm stainless steel sampling tube into the mass spectrometer front chamber. This atmosphere was sampled by the mass spectrometer and the remaining gas passed harmlessly back into the fume hood through the exhaust pipes.

This process was repeated three times, between which the reactor was switched off and the substrate replaced. For the subsequent scans, in addition to the VCl_4 vapour stream, a stream of ethyl acetate from B2, heated at 30 ˚C was also used. The flow of nitrogen through B2 was varied between each deposition, altering the mass flow of ethyl acetate. The first of these three depositions used a flow of 0.6 L min^{-1} ethyl acetate, roughly 2 x the mass flow of VCl_4 the second and third depositions used flows of 0.2 L min^{-1} and 0.05 L min^{-1}, roughly equal and half the mass flow of VCl_4, respectively. As with the first experiment five scans were obtained at 550 ˚C, with both the VCl_4 and ethyl acetate bubblers open.

5.3. Results and Discussion

A Hiden HPR-60 quadrupole mass spectrometer was connected to a CVD reactor in order to sample the gaseous species within during atmospheric pressure vapour deposition reactions. Depositions using $TiCl_4$, $VOCl_3$, VCl_4, $SnBuCl_3$, TTIP and were carried out, and the atmosphere within the reactor sampled at different temperatures and with different levels of the oxidising agent ethyl acetate in the atmosphere to determine the gas phase intermediates that form during high temperature deposition reactions.

5.3.1. Ethyl Acetate

Initial depositions used ethyl acetate without a metal oxide precursor. This was in order to establish a 'baseline' as ethyl acetate's role as an oxygen donor meant that it would be present in the spectra of all further depositions. Furthermore, due to ethyl acetate's interesting fragmentation pattern, its mass spectrum is well studied and provided a good means of establishing the effectiveness of the mass spectrometer at picking up low mass signals spectrometer.

Ethyl acetate has a simple but telling set of peaks at *m/z* 88(M+), 70, 61, 45, 31 and 18. All of these are clearly visible in the spectra obtained using the CVD MS apparatus (Figure 69a). This combined with its interesting fragmentation pattern sees ethyl acetate frequently used as an example in mass spectrometry training courses. Rather than simple fragmentation, ethyl acetate undergoes condensation of water resulting in the loss of the ethyl oxygen and subsequent rearrangement to form a methyl vinyl ketone species. The formation of this is not fully understood.

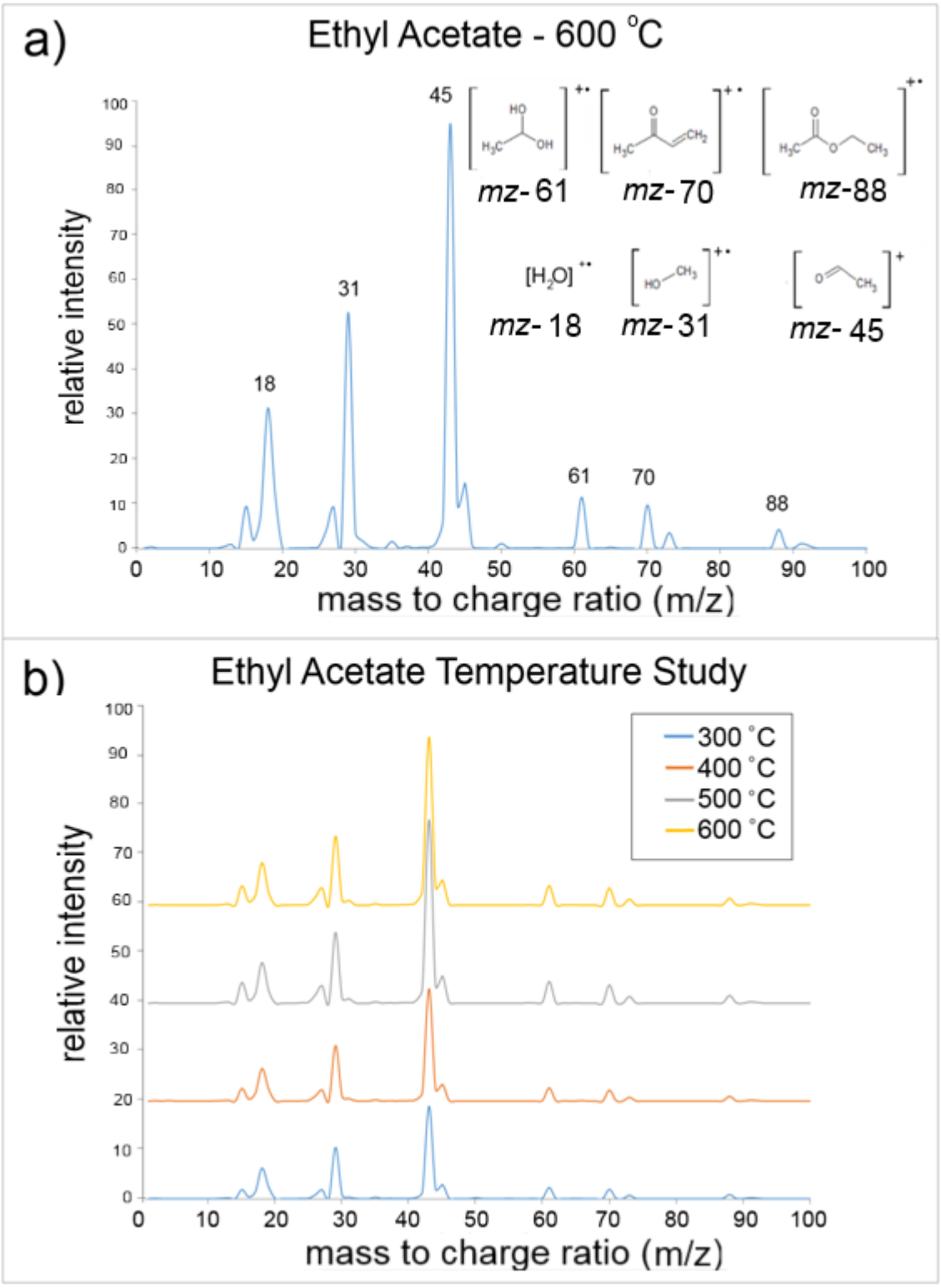

Figure 69: Assigned mass spectrum of ethyl acetate as passed through an atmospheric pressure chemical vapour deposition reactor at 600 ˚C (a) and comparison of ethyl acetate fragmentation patterns over the temperature range of 300 to 600 ˚C (b).

The spectrum of the ethyl acetate was observed to be very stable to temperature. The spectra remained identical with variation in reactor temperature from 300 to 600 ˚C in 100 ˚C increments (Figure 69b).

5.3.2. Titanium Tetrachloride

5.3.2.1. Mass Spectra Analysis

In the first instance titanium chloride was passed through the reactor without the presence of ethyl acetate at 600 ˚C. The spectrum recorded matches well to that taken for $TiCl_4$ first taken by Hogg in 1954 that features in the NIST Webbook.[186]

The four major peaks at *m/z* 189, 154, 118, and 83 accounts for titanium(IV) chloride having lost 0, 1, 2 and 3 chlorine atoms respectively. In each case the isotope pattern for the correct number of chlorines was observed, with the peaks representing the presence of one and two mass 37 chlorine atoms increasing in size as more chlorine is present (Figure 70).

An additional peak was visible at *m/z* 225, which represents a titanium atom with five chlorine ligands present. This is most likely caused by the extremely high energies within the ionisation chamber, giving discarded chlorine radicals enough energy to react with the parent molecule, allowing for the formation of the highly energetically unfavourable $TiCl_5$. Although surprising, side reactions involving fragments and the parent ion are relatively common in mass spectrometry, (although usually in high energy ionisation sources) and are not relevant to this study.

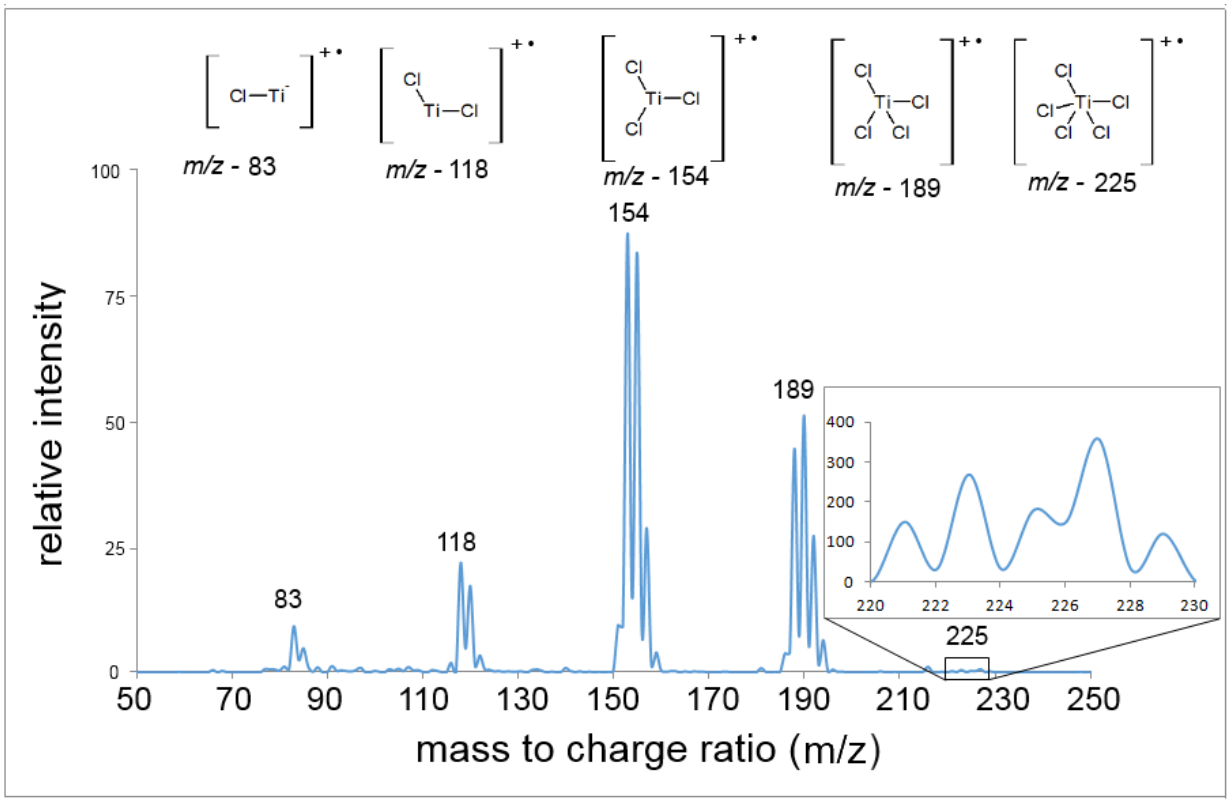

Figure 70: Mass spectrum of titanium(IV) chloride as passed through an atmospheric pressure chemical vapour deposition reactor at a temperature of 600 ˚C.

When the experiment was repeated with a flow of ethyl acetate joining that of $TiCl_4$, the fumes passing out of the reactor, as well as the two exhaust tubes of the mass spectrometer chamber, were observed to be far thicker and denser. The inlet to the spectrometer was found to block more rapidly as well, demonstrating that the presence of the oxygen rich organic species facilitates TiO_2 formation. The spectra collected (shown in Figure 71), contained a number of new peaks, representing intermediates formed *via* coordination of the ethyl acetate to the $TiCl_4$.

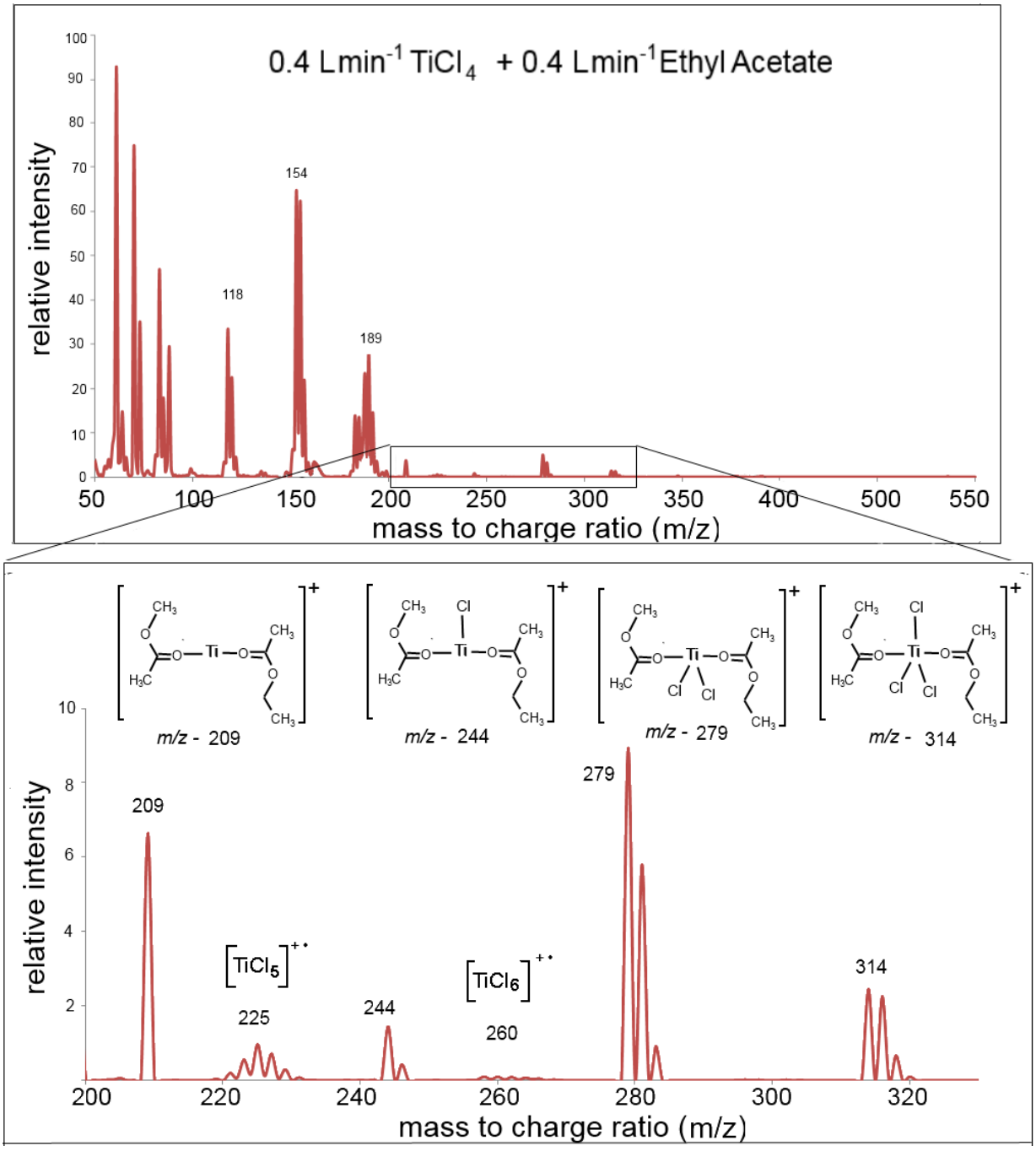

Figure 71: Mass spectrum of titanium(IV) chloride and ethyl acetate as passed through an atmospheric pressure chemical vapour deposition reactor at a temperature of 600 ˚C, with an enhanced image of the peaks between *m/z* 200 and 330, showing the newly formed adduct peaks.

Spectra collected for the same experiment at 300 ˚C do not show these peaks, suggesting that the formation of these intermediate species is conducive to the formation of TiO_2 films.

The peak at *m/z* 314 possesses the isotope pattern of a trichloride, and is *m/z*- 159 heavier than the $TiCl_3$ ion. This suggests that the species present is likely to be a $TiCl_3$ centre complete with two ethyl acetate molecules coordinated to the titanium centre, one of which is missing a methyl group, a common fragmentation pathway for the molecule.

This suggests that the $TiCl_4$ is able to coordinate to one ethyl acetate without loss of chlorine, with subsequent coordination by ethyl acetate molecules leading to displacement of a chloride ion in the gas phase. It is however plausible that the tetrachlorotitanium bis-ethylacetate species exists, but is simply too unstable to make it to the spectrometer intact. The remaining peaks at *m/z* 279, 244 and 209 represent the same species following the loss of a second third and fourth chlorine, respectively, as confirmed by the clear isotope patterns. Their presence as single charge cations demonstrates that this loss of chlorine is taking place at the ionisation source following formation of a radical cation parent ion, as with the $TiCl_4$ molecule.

5.3.2.2. Thin Film Analysis

The film deposited from $TiCl_4$ and ethyl acetate at 600 ˚C appeared largely transparent, displaying the birefringence common with titanium dioxide films. A dark, hazy patch formed immediately before the position of the gas sampling tube, which is likely the result of the obstruction leading to a build-up of product in that area. The deposition at 300 ˚C gave no film, instead yielding a very thin grey powder, easily removed from the substrate.

i) X-ray diffraction

The X-ray diffraction pattern of the film deposited at 600 ˚C from $TiCl_4$ and ethyl acetate revealed that the film consisted of TiO_2 in the anatase phase (Figure 72). X-ray diffraction of the material deposited at 300 ˚C gave a largely amorphous pattern, several small signals suggesting the faint presence of anatase TiO_2.

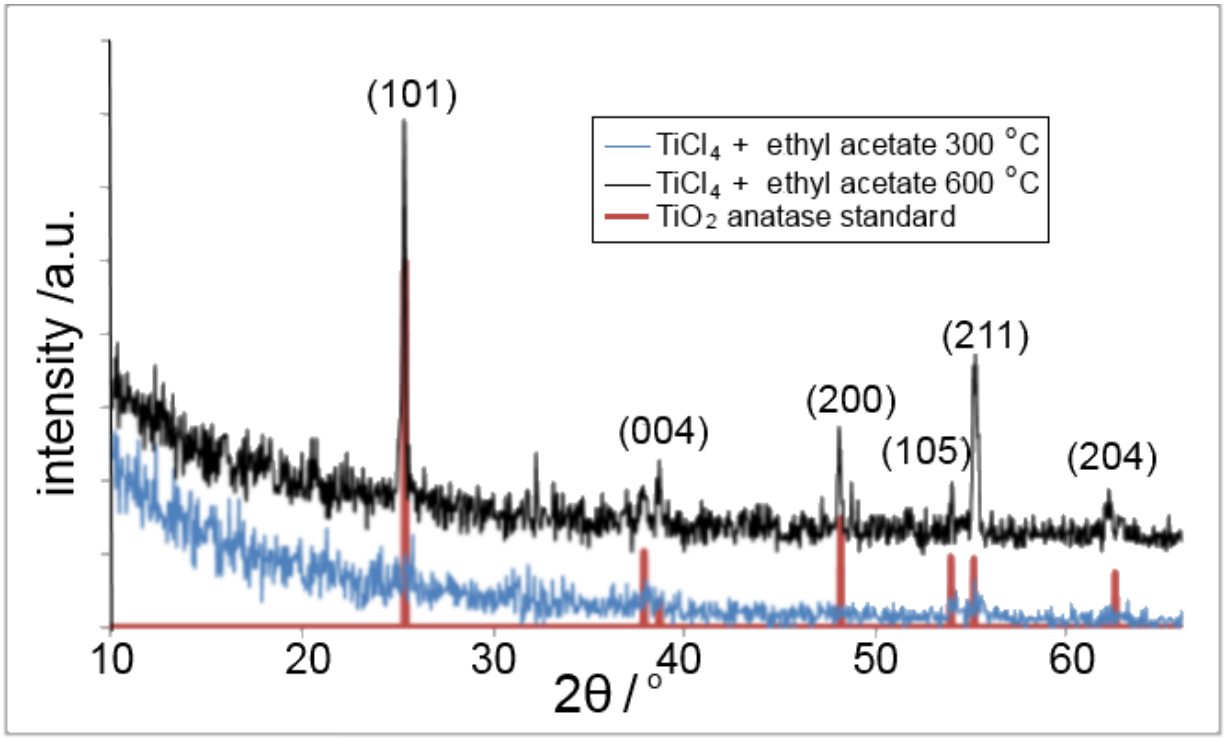

Figure 72: X-ray diffraction pattern of the films deposited from $TiCl_4$ and ethyl acetate onto float glass at 300 and 600 ˚C using the APCVD / mass spectrometry apparatus, alongside an anatase TiO_2 standard.[187]

ii) Scanning Electron Microscopy

SEM images were obtained for the films deposited from $TiCl_4$ at 600 and 300 ˚C. The film deposited at 600 ˚C revealed a dense microstructure consisting of a mixture of thin plates roughly 200 nm in diameter and protruding rods of approximately 50 nm in diameter (Figure 73). Imaging of the powdery substance deposited at 300 ˚C shows a substrate sparsely populated with roughly square particulates of around 100 nm in diameter.

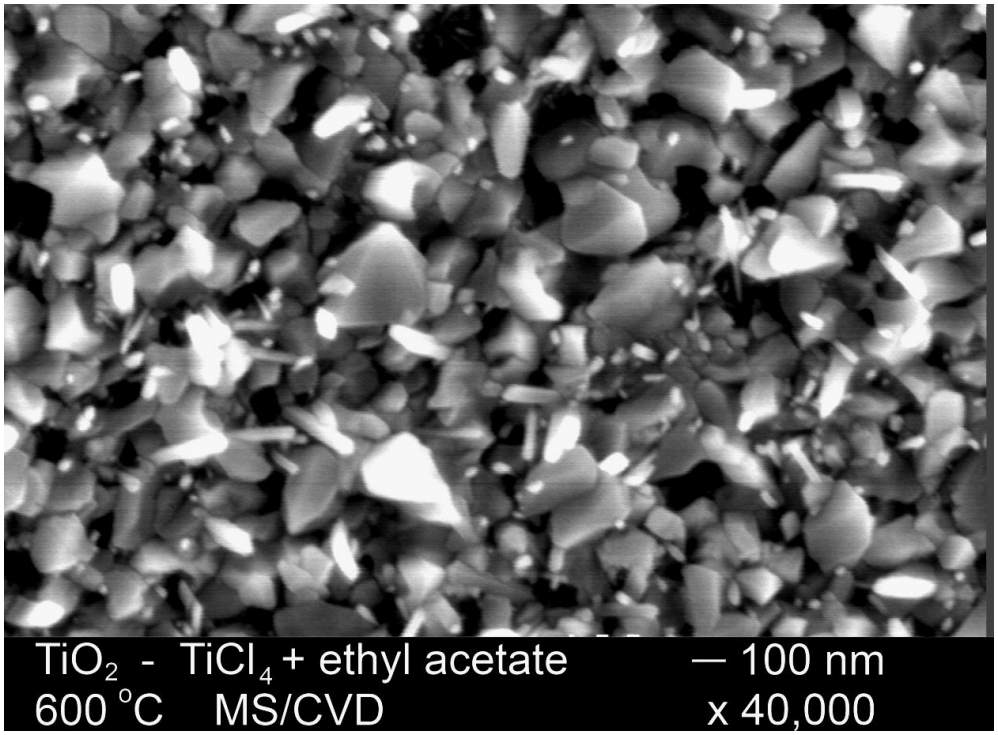

Figure 73: SEM image of the film deposited from $TiCl_4$ and ethyl acetate onto float glass at 600 ˚C using the APCVD / mass spectrometry apparatus.

SEM and XRD analysis confirms the formation of TiO_2 thin films at elevated temperatures when $TiCl_4$ was deposited with an oxidising agent, as is well documented in the literature.[151] The pronounced difference in the mass spectra taken during depositions at 300 ˚C and 600 ˚C, as well as the resulting films, is strong evidence that the formation of the TiO_2 on the substrate surfaces relates to the formation of the gas phase $[TiCl_3(CH_3COOC_2H_5)_2]$ intermediate observed in the mass spectrum of the reactor atmosphere.

5.3.3. Vanadium Oxytrichloride

5.3.3.1. Mass Spectrometry Analysis

Scanning the atmosphere when only $VOCl_3$ was present in the gas stream alongside the carrier gas shows that the precursor predominantly makes it through to the detector intact (Figure 74). The peaks at *m/z* 172, 137, 102 and 67 represent the intact parent ion and the loss of one,

two and three chlorine ligands respectively. This is confirmed by the very clear isotopic patterns of the chlorine for all three peaks. The signals at *m/z* 102 and 86 represent the parent molecule minus the double bound oxygen, as well as the loss of one and two chlorines,respectively. These species appear considerably less abundant than that of those only missing chlorine, likely due to the energy required to break the V=O double bond.

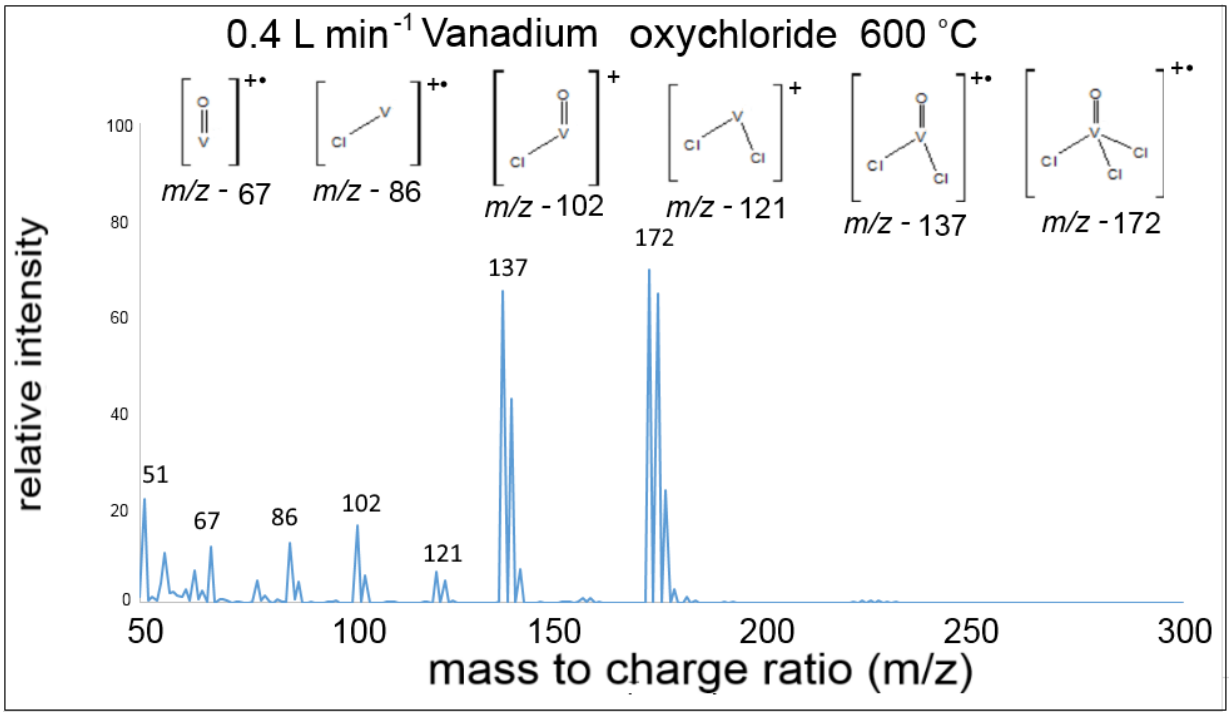

Figure 74: Mass spectrum of vanadium(V) oxytrichloride as passed through an atmospheric pressure chemical vapour deposition reactor at a temperature of 600 ˚C.

Similarly to $TiCl_4$, when an equivalent amount of ethyl acetate was run through the reactor alongside the $VOCl_3$ stream at the same temperature, new peaks at a mass greater than that of $VOCl_3$ were observed relating to the products of gas phase reactions (Figure 75).

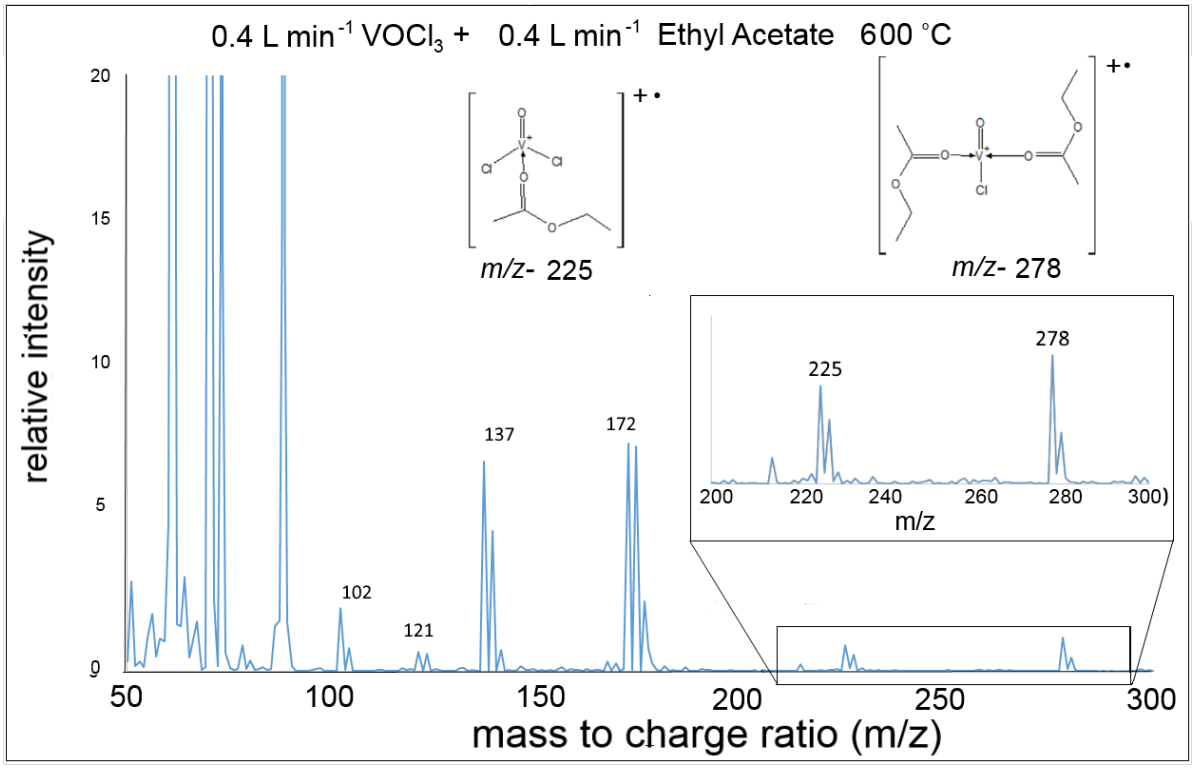

Figure 75: Mass spectrum of vanadium(V) oxytrichloride and ethyl acetate as passed through an atmospheric pressure chemical vapour deposition reactor at a temperature of 600 ˚C, with an enhanced image of the peaks between *m/z*- 200 - 330, showing the newly formed adduct peaks.

As with the $TiCl_4$ experiment, the new peaks relate to the $VOCl_3$ coordinating to the ethyl acetate in the gas phase. In this case only two peaks were visible, both of which were the result of ethyl acetate coordinating to the vanadium, presumably *via* the carbonyl oxygen, displacing a chlorine atom on the vanadium. This has occurred twice in the species represented by the *m/z* 278 peak and in the species represented by the peak at *m/z* - 225. This is confirmed by the isotope patterns of the chlorine in both cases.

This presents an interesting difference in the reactivity of the $TiCl_4$ and $VOCl_3$, previously alluded to in this thesis. In the case of $TiCl_4$, the peak at *m/z*- 314 represents the $TiCl_4$ having coordinated to two ethyl acetate molecules with the loss of one chloride. It can be inferred from this that, although perhaps unstable, the $TiCl_4$ is capable of coordinating to a single ethyl acetate without

the loss of any chlorine. In the case of $VOCl_3$ in the case of each new species involves coordination to an ethyl acetate molecule comes at the expense of a chlorine ligand.

This pattern relates closely to that seen with the diester species reacting with $TiCl_4$ and $VOCl_3$ where the coordination of a diester ligand to the titanium saw no loss of chlorine, making it far more reversible than the same reaction with $VOCl_3$ which would always result in the displacement of chlorine.

Furthermore, unlike $TiCl_4$, the formation of the intermediate species with $VOCl_3$ was visible at both 300 ˚C and 600 ˚C, with the ratio of intermediates to unreacted $VOCl_3$ in fact higher at 300 ˚C. This suggests that gas phase reactions of the ethyl acetate and $VOCl_3$ either possess a lower activation energy barrier than the equivalent reaction with $TiCl_4$, or have greater stability ty in the gas phase and able to make it to the detector at the lower temperature, rather than simply dissociate, both of which fit well with the chemistry observed in the chloride process.

5.3.3.2. Thin Film Analysis

Both depositions at 600 ˚C and 300 ˚C yielded films. The film deposited at 600 ˚C was completely opaque, with a matte dark blue/black appearance and complete coverage of the substrate. The film deposited at 300 ˚C was lighter in colour with translucent brown areas around the edges likely due to the temperature being lower, leading to incomplete oxidation of the precursor to V_2O_5. The film appeared only on the back half of the substrate. The films were both very thick, likely the result of the very long deposition time taken to obtain 10 scans.

i) X-Ray Diffraction

XRD patterns were obtained for both the films deposited at 300 and 600 ˚C (Figure 76). Both films appear to be predominantly VO_2, however the different temperatures appear to result in the formation of different polymorphs. This is an interesting development as the vanadium is entering the reactor in the 5+ oxidation state, implying that the ethyl aceate, whilst providing

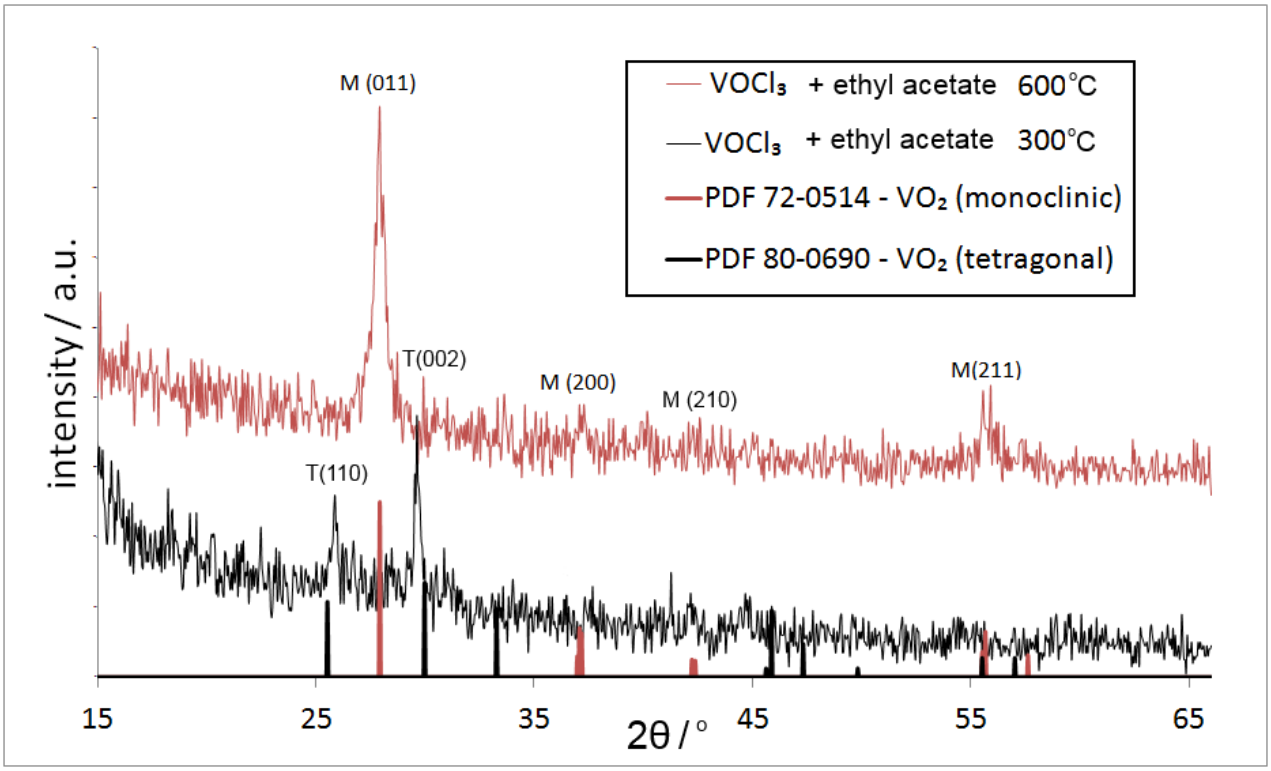

Figure 76: X-ray diffraction pattern of the films deposited from $VOCl_3$ and ethyl acetate onto float glass at 600 ˚C (top) and 300 ˚C (bottom) using the APCVD / mass spectrometry apparatus, alongside standards for monoclinic (PDF 72-0514)[188] and tetragonal (PDF 80-0690) VO_2.[189]

oxygen is not an oxidising agent. It is plausible that it could be attributable to the donation of electron into the d empty shell by the dative coordination of the acetate, or it could be a more complex chain or reactions occurring at the surface of the substrate.

At 600 ˚C, the monoclinic polymorph appear to be the dominant phase, with strong reflections of the (001), (200) and (211) planes. Although there is less work done on the use of $VOCl_3$ as a precursor for the deposition of VO_2 than for VCl_4, due to the vanadium being in the +5 oxidation state, this is in keeping with literature findings of depositions with $VOCl_3$ and water.[190] At the lower temperature of 300 ˚C, the dominant phase appears to be the tetragonal polymorph of VO_2. Although both patterns are fairly broadened, the lower temperature film gave far weaker reflections. This is reflected in SEM images taken of the film *(vide infra)*, in which the higher temperature films appear to have a far more crystalline morphology.

ii) Scanning Electron Microscopy

Scanning electron micrographs of the films reveal a striking difference in the morphologies of the deposited films with deposition temperature. At both temperatures, the films were thick and dark in appearance due to the length of depositions time. This is reflected in the morphologies with both films featuring densely packed particles.

At both temperatures, the films consist of elongated particles of between 1 and 2 μm in length with no preferred orientation (Figure 77a). At 600 ˚C the film consists of fairly uniform, rod-like structures roughly 100 nm wide. These crystallites have flattened edges, indicating preferred growth of certain faces. Formation of vanadium oxide nanorods has been observed in several cases, including previously with APCVD of $VOCl_3$. [191–193] The particles formed at 300 ˚C were considerably wider and less uniform with rounded edges and diameters ranging from 200 to 600 nm (Figure 77b).

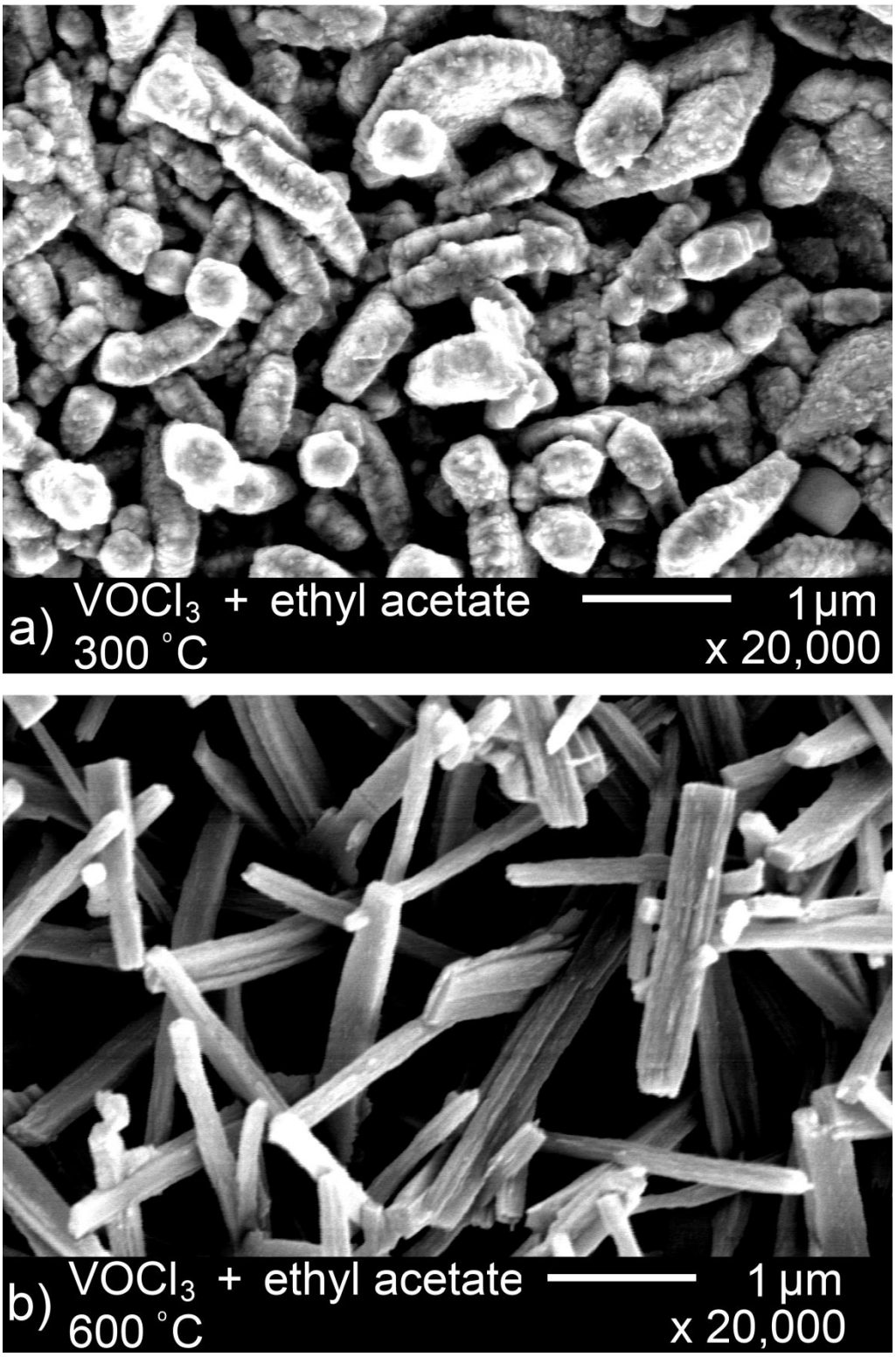

Figure 77: SEM images of the film deposited from $VOCl_3$ and ethyl acetate onto float glass at 300 (a) and 600 ˚C (b) using the APCVD / mass spectrometry apparatus.

5.3.4. Butyltin Trichloride

5.3.4.1. Mass Spectrometry Analysis

Unlike the previous two species, the presence of the butyl group on the butyltin trichloride makes the spectrum far more complex. Furthermore, isotope patterns of the chlorine ligands are far more unclear due to the overlapping of peaks from which one or two protons are lost creating complex multiplets (Figure 78). Nevertheless as there is only one alkyl group present the fragments are relatively facile to deduce.

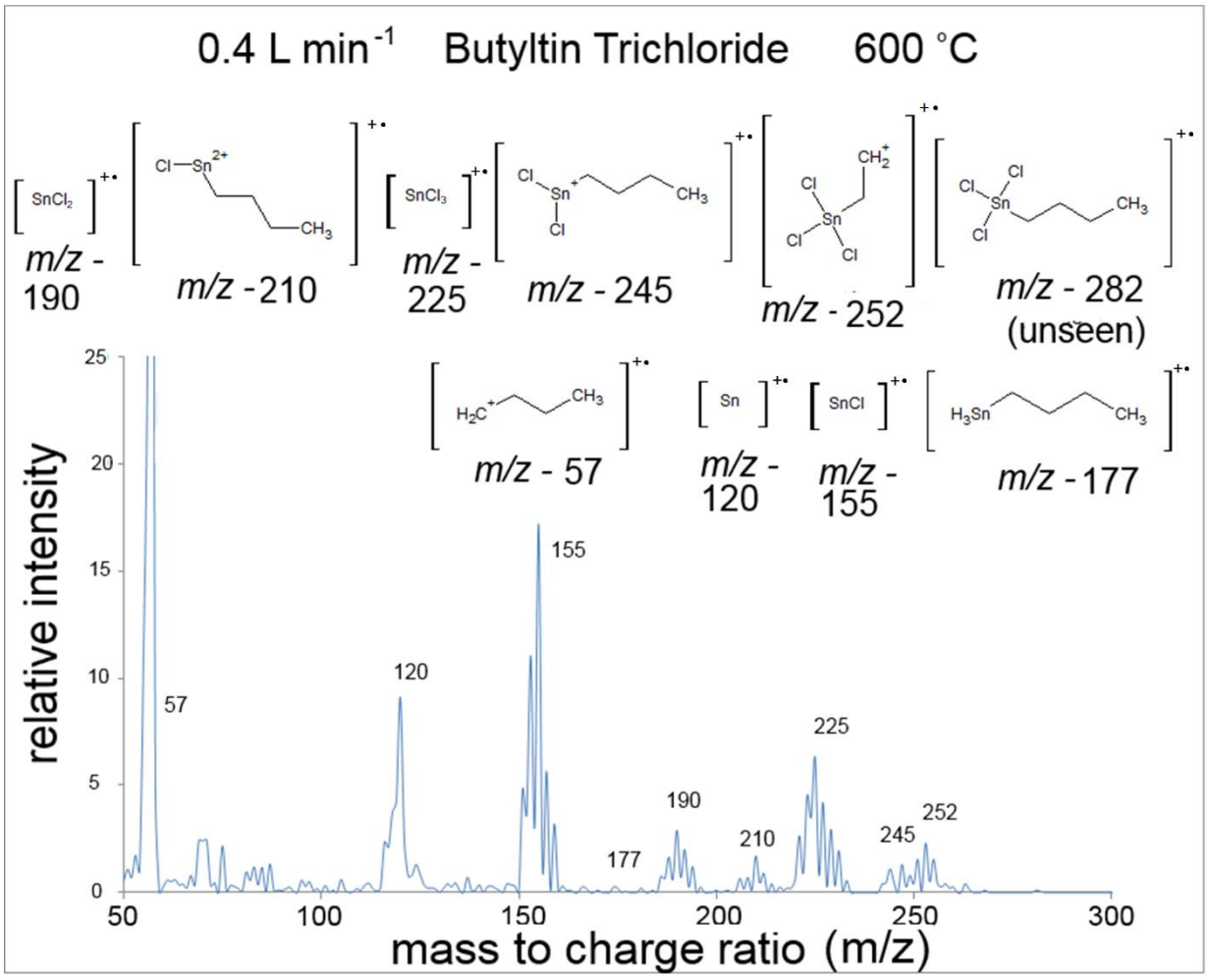

Figure 78: Mass spectrum of butyltin trichloride as passed through an atmospheric pressure chemical vapour deposition reactor at a temperature of 600 ˚C.

The parent ion peak was not seen in this spectrum. Instead the highest molecular weight peaks has a signal at of *m/z* 252, which relates to the parent ion having lost a $[CH_3CH_2]^+$ from the butyl species.

This peak overlaps with another set of peaks at around *m/z* 245, resulting from the parent ion having lost a chlorine ligand. The peaks at *m/z* 210 and 177 (extremely faint) represent the subsequent loss of two more chlorine atoms. Of these three species the only one with a relatively clear isotope pattern is that at *m/z* 210. Peaks at *m/z* 225, 190 and 155 likewise represent the parent species having lost the butyl group and subsequently losing a chlorine ligand, giving $[SnCl_3]^{+\cdot}$, $[SnCl_2]^{+\cdot}$ and $[SnCl]^{+\cdot}$ species respectively. These are presumably radical species as otherwise the multiple charges would cause them to appear at far lower mass numbers.

When gaseous ethyl acetate was flowed through the reactor chamber alongside the $BuSnCl_3$, A host of new peaks, formed from reaction of the two species were visible in both the scans collected at 300 and 600 ˚C (Figure 79). Similarly to the titanium chloride, the highest mass peak at *m/z* 423 relates to that of $BuSnCl_3$, having coordinated to two ethyl acetate ligands, leading to the loss of a single chloride. The peak at *m/z* 335 represents the same molecule following the loss of one of those ethyl acetate molecules.

The ethyl acetate also appears to be able to displace the butyl group, with an equilvalent pair of peaks at *m/z* 401 and 313, generated by the coordination of two ethyl acetate ligands and the loss of a butyl group and the subsequent loss of a one ethyl acetate in the ion source, as well as a peak at *m/z* 366 relating to the loss of one chlorine and one butyl group following the coordination of two ethyl acetate groups.

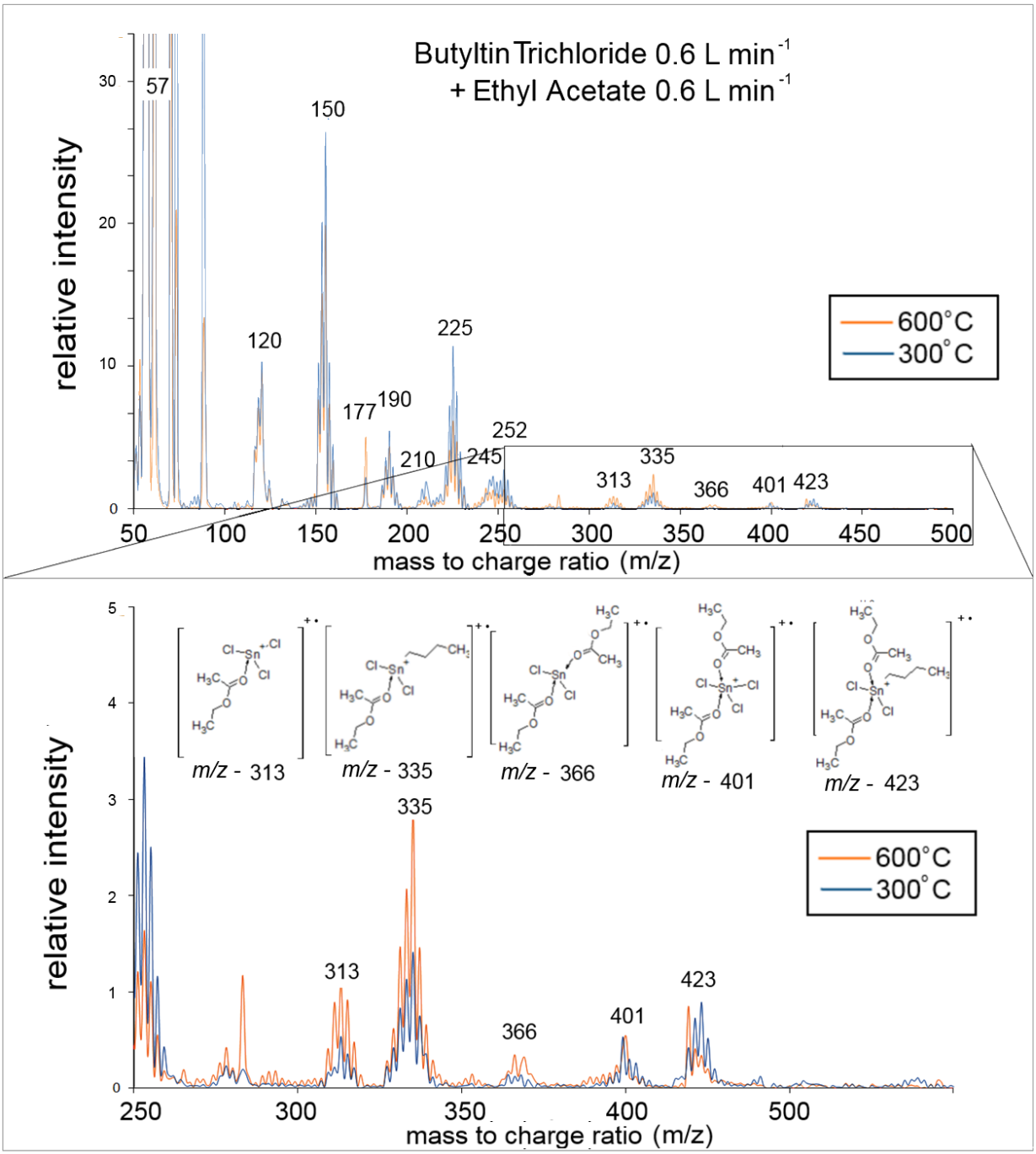

Figure 79: Mass spectrum of Butyltin trichloride and ethyl acetate as passed through an atmospheric pressure chemical vapour deposition reactor at a temperature of 600 ˚C and 300 ˚C, with an enhanced image of the peaks between *m/z*- 250 and 500, showing the newly formed adduct peaks.

The fact that these adduct peaks appear in both the low and high temperature runs is hard to explain as $BuSnCl_3$ will only deposit tin oxide at above 400 ˚C,[194] implying that the formation of the intermediates is not enough to guarantee film deposition. It should be noted that all peaks

relating to unreacted $SnBuCl_3$ have greater relative intensity in the depositions at 300 ˚C, whereas the products of the ethyl acetate and $SnBuCl_3$ have a higher intensity in the 600 ˚C deposition, suggesting that a greater proportion of the $SnBuCl_3$ is reacting with the ethyl acetate at higher temperatures. It is possible to consider that at 300 ˚C the intermediates are capable of forming; however this does not mean that they have enough energy to fully oxidise. This could explain why despite most of the intermediate peaks in the spectrum taken at 300 ˚C are roughly half the relative intensity of those taken at 600 ˚C, the peaks at *m/z* 401 and 423, representing the fully intact intermediates, are the same intensity as those in the high temperature and low temperature spectrum. This increase in relative height could be the result of a failure to react in the gas phase inside the reactor, leading to a greater concentration on the ensuing mass spectrum. This experiment was repeated, with the flow rate of ethyl acetate lowered from 0.6 L min^{-1} to 0.2 L min^{-1}, resulting in an excess of $BuSnCl_3$ entering the reactor. This yielded the same result, with intermediates visible in both the higher and lower temperature spectra.

5.3.4.2. Thin film Analysis

The depositions with butyltin trichloride and ethyl acetate at 600 ˚C yielded a colourless transparent thin film, with slight haze just before the entrance to the sampling tube. Depositions at 300 ˚C appeared to yield no visible deposition onto the substrate.

i) X-ray Diffraction Analysis

The XRD pattern of the film deposited from 0.6 L min^{-1} $BuSnCl_3$ and 0.6 L min^{-1} ethyl acetate at 600 ˚C are shown in Figure 80. The XRD patterns of the films confirm the deposition of rutile SnO_2, as compared to a standard. The peak for the (101) miller plane is present although that plane appears heavily disfavoured by the particles making up the film. The deposition under

the same conditions at 300 ˚C shows no visible peaks, suggesting that had a film formed it was highly amorphous.

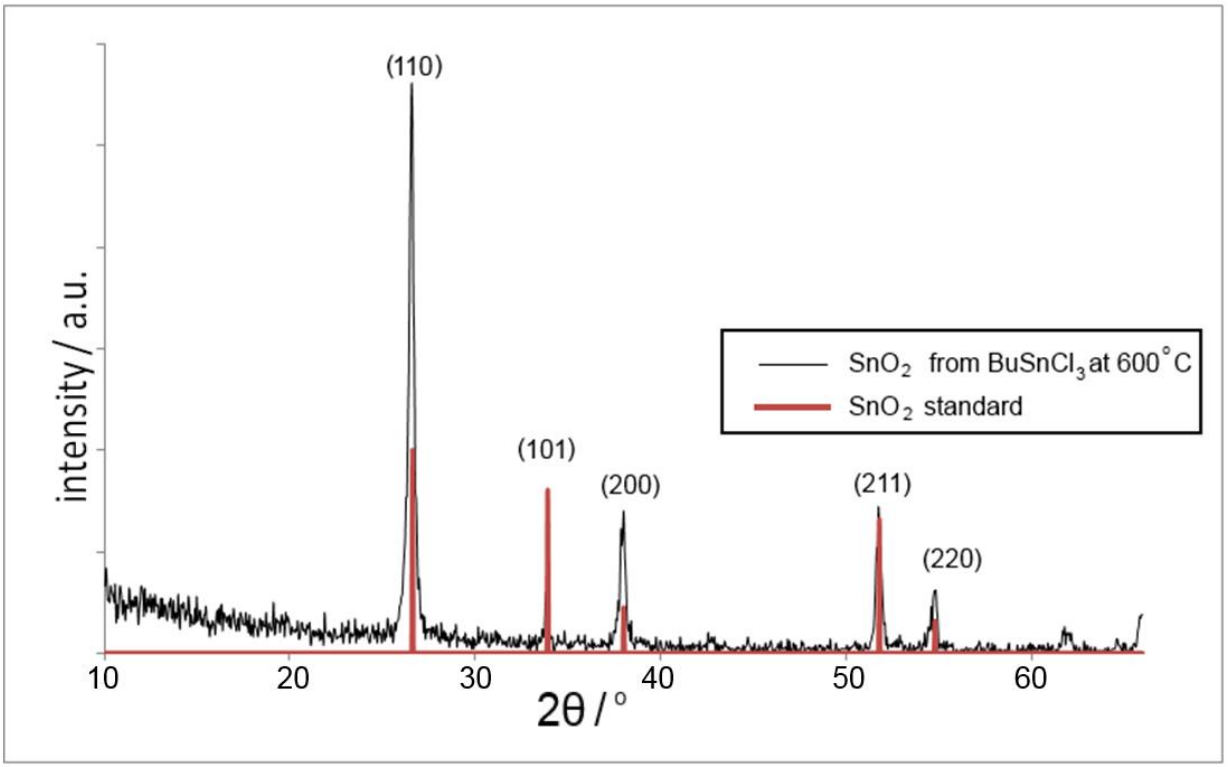

Figure 80: X-ray diffraction pattern of the film deposited from $BuSnCl_3$ and ethyl acetate onto float glass at 600 ˚C using the APCVD / mass spectrometry apparatus, alongside a rutile SnO_2 standard. [195]

ii) Scanning Electron Microscopy

SEM imaging of the film deposited at 600 ˚C shows a leaf-like microstructure consisting of flattened, pointed particles, packed tightly together on the substrate (Figure 81). This is a similar morphology to fluorine doped tin oxide reported in the literature, as grown from $BuSnCl_3$ from atmospheric pressure and aerosol assisted CVD.[196,197]

The substrate from the equivalent experiment at 300 ˚C was also imaged by SEM, revealing a sparse scattering of sphere like particulates of what is likely amorphous SnO_2.

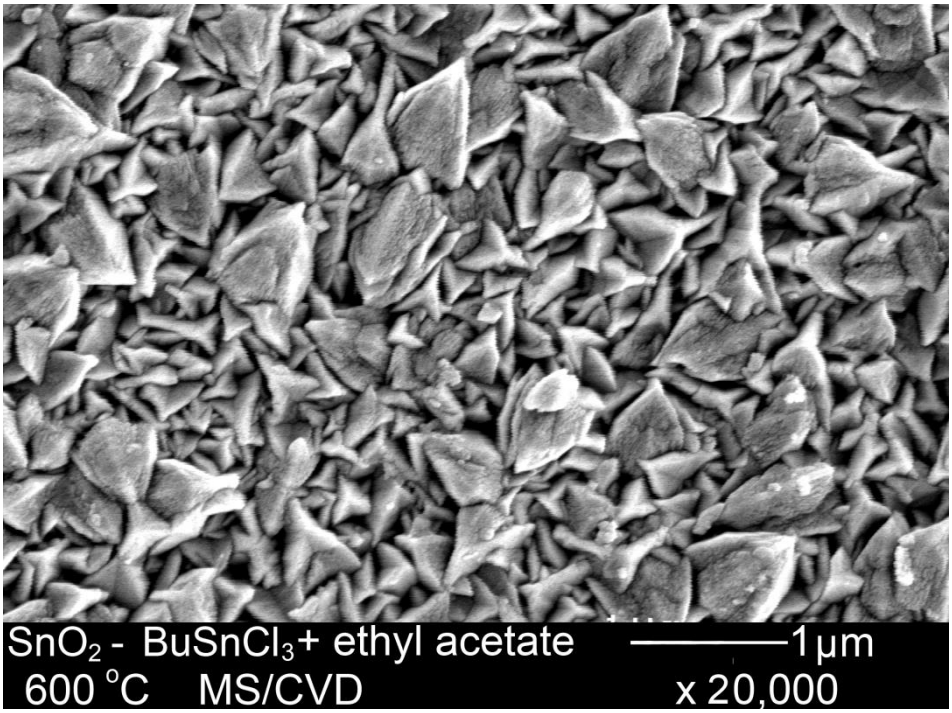

Figure 81: SEM image of the film deposited from $TiCl_4$ and ethyl acetate onto float glass at 600 ˚C using the APCVD / mass spectrometry apparatus.

5.3.5. Titanium Isopropoxide

Depositions were carried out using titanium isopropoxide (TTIP) at 600 ˚C and 300 ˚C, both yielding thin films. The film deposited at 600 ˚C was far thicker and more adherent, appearing transparent with a circular area of haziness at the point of the substrate positioned in front of the sampling tube. This film passed the Scotch tape test and was observed to be fairly resistant to surface abrasion.

The film deposited at 300 ˚C was far more powdery and easily wiped from the surface by touching. The opaque film was white in colour as is customary with TiO_2.

Ethyl acetate was not added as an oxygen source in these experiments as it is not commonly used in conjunction with TTIP depositions in the literature, as the precursor molecule already contains four Ti-O bonds, making oxygen plentiful enough to deposit TiO_2 without an additional

oxygen source. This was observed in the depositions, with TTIP depositions blocking the machine far more rapidly than any other precursor.

5.3.5.1. Mass Spectrometry Analysis

The deposition carried out at 300 ˚C gave the expected spectra of TTIP, with no additional gas phase interactions visible (Figure 82). In this case the TiO_2 forming is simply the result of the alkyl side groups burning off to leave TiO_2. (Scheme 9)

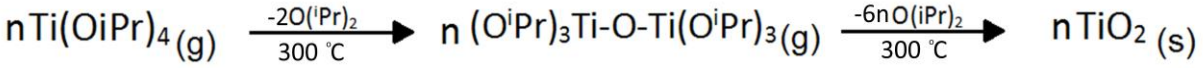

Scheme 9: Schematic of the decomposition of TTIP at high temperatures to give TiO_2. [198]

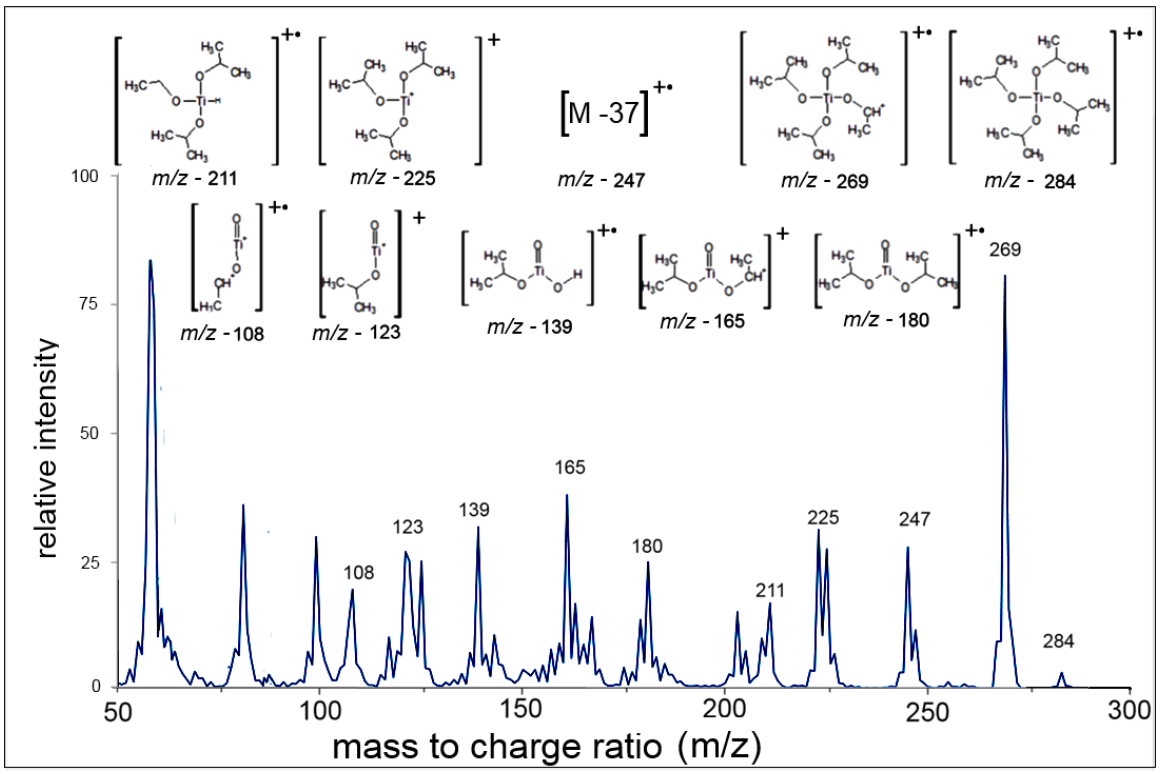

Figure 82: Mass spectrum of titanium isopropoxide as passed through an atmospheric pressure chemical vapour deposition reactor at a temperature of 300 ˚C.

Despite being far more stable than $TiCl_4$ and $VOCl_3$ the molecular ion peak was extremely weak, instead the dominant peak of the spectrum was the one corresponding to the loss of a single methyl group from one of the isopropoxide ligands. This is a phenomenon commonly seen in

the ionisation chambers of EI mass spectrometers,[199] suggesting that the spectrum seen here is a very close approximation to putting TTIP through an EI instrument directly. This spectrum is similar to one taken from an atomic layer deposition reactor at 250 ˚C, the major difference being the signal at *m/z* 247 which could not be assigned to a fragmentation peak of the TTIP molecular ion. The following fragmentation is complex although the major peaks have been assigned based on the idea that there are three bond at which fragmentation could occur: the Ti-O bond, the O-C bond and the C-C bonds, resulting in the loss of a methyl (mass = 15 amu), propyl (mass = 43 amu) or isopropyl (mass = 59 amu) group respectively (Figure 83).

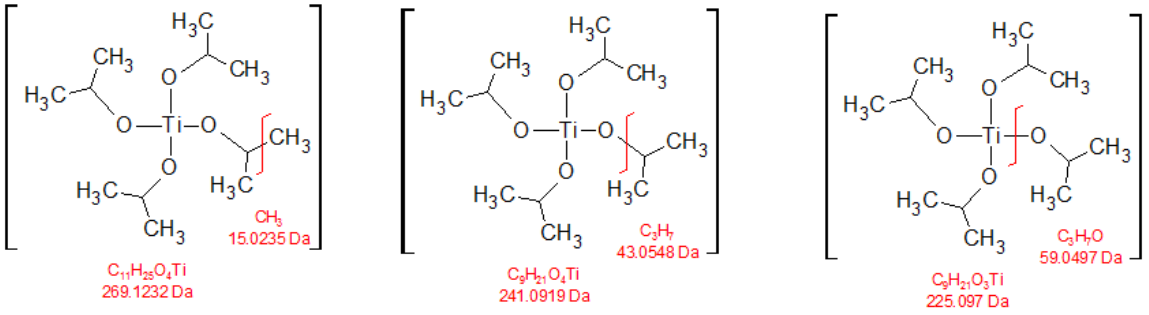

Figure 83: Possible fragmentation points on the TTIP parent ion with the formulas and masses of the fragments denoted in red

The deposition at 600 ˚C gave an extremely different pattern to that observed at 300 ˚C. In this case a totally new set of peaks, many above the mass of the parent ion were observed (Figure 84). The initial assumption when observing the repeating pattern of 60 amu decreases in the fragment masses, was that the product was simply a polymer consisting of removed isopropoxide ligands potentially polypropylene glycol.

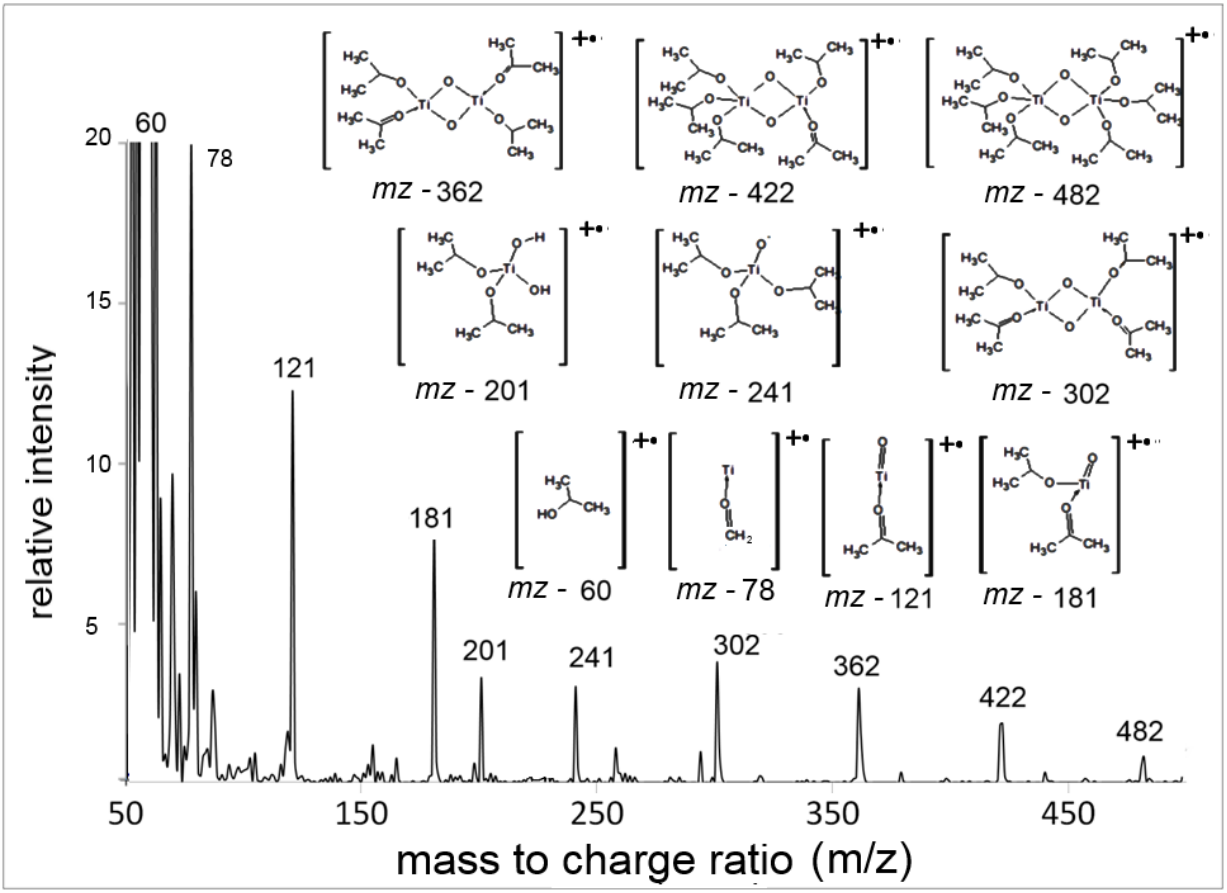

Figure 84: Mass spectrum of titanium isopropoxide as passed through an atmospheric pressure chemical vapour deposition reactor at a temperature of 600 ˚C.

However the difference in mass between the fragments would then be *m/z* 58, as a proton would have to be lost from either end of the monomer.[200] The formation of an oxo-bridged dimer species in titanium isopropoxide has been proposed as a possible mechanism for the formation of nanoparticles *via* the solvothermal synthesis of TiO_2 from TTIP and benzylamine.[201]

It is thought that the high temperature leads to the loss of the propyl group leaving an unstable $(O^iPr)_3TiOH$. In this case it appears as though a dioxo bridge has formed between the two titanium centres (Figure 85) with electron density shared over the two oxygen atoms forming a four membered ring.

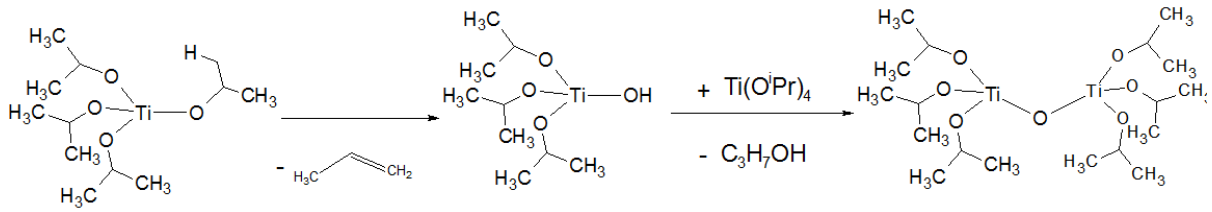

Figure 85: Proposed formation of an oxo-bridge between two titanium isopropoxide molecules at high temperatures.[201]

The formation of the two oxo bridges without the loss of the isopropyl ligands would be highly disfavoured due to the maximum oxidation state of titanium being 4+, therefore this is likely not the whole picture. Two bridging oxygen atoms could potentially be hydroxyl ligands themselves, both of which could easily lose a proton in the mass spectrometer ionisation chamber. The mass of this species would be 228, which is a peak present in the spectrum taken at 300, however it is masked by a cluster of peaks bringing another fragment molecule so it is unknown if it relates to this species also. This would explain how such a species would be stable. A small peak at *m/z* 484 could explain this, however it is too weak to be seen as proof of this species forming. If this is indeed the case, deprotonation of the bridging species could be a *via*ble path for the loss of the isopropanol fragments.

Following the formation of the dimer species, fragments are lost of *m/z* - 60 . As with the polymer this is not simply a case of heterolytic fission causing loss of the ligand, as would occur in an ionisation chamber, as the fragments would have *m/z* - 59. Whilst 1 mass unit below the expected value is common due to subsequent proton loss, one heavier is harder to explain. The isopropoxide ligand group must be abstracting a proton as it leaves, forming isopropanol. This is corroborated by the presence of a large peak at *m/z* 60 in the spectrum, however it cannot be ruled out that the ligand would coordinate to a proton later.

The most likely pathway for the loss of isopropanol from the ligand is *via* the abstraction of a proton from another isopropyl ligand (Figure 86). The central proton would be the most likely

provider of a proton due to the tertiary nature of the carbon providing greater stability for the negative charge was well a being adjacent to the oxygen. The oxygen from one isopropoxide abstracts the central proton from the adjacent ligand, resulting in the formation of an acetone group which remains coordinated to the metal centre.

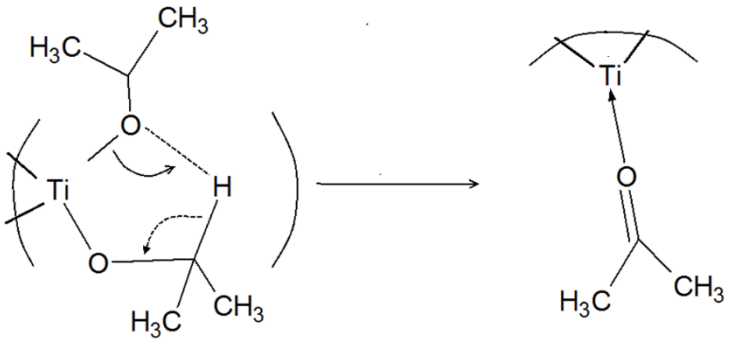

Figure 86: Proposed mechanism for the loss of the elimination of an isopropanol molecule from TTIP and its dimer at high temperatures.

This reaction can be assumed to happen into the gas phase in the CVD reactor, as these peaks were not observed during the deposition at 300 ˚C. Further reactivity occurs in the loss of more isopropanol molecules in this way, with the dimer eventually splitting apart. The lowest main fragment featuring titanium involves coordination to an acetone molecule and an oxygen atom. Should the dimer species be forming inside the CVD reactor it is likely a precursor for the deposition of crystalline TiO_2 at higher temperatures.

5.3.5.2. Thin Film Analysis

i) X-ray Diffraction Analysis

As with the films deposited from $TiCl_4$ and ethyl acetate the film deposited at 600 ˚C was considerably more crystalline than the film deposited at 300 ˚C (Figure 87). In both cases, the film appears to be anatase phase TiO_2, with the (200), (211) and (204) miller planes present in

both films. The usually dominant (101) plane however appears to be disfavoured at the lower temperatures.

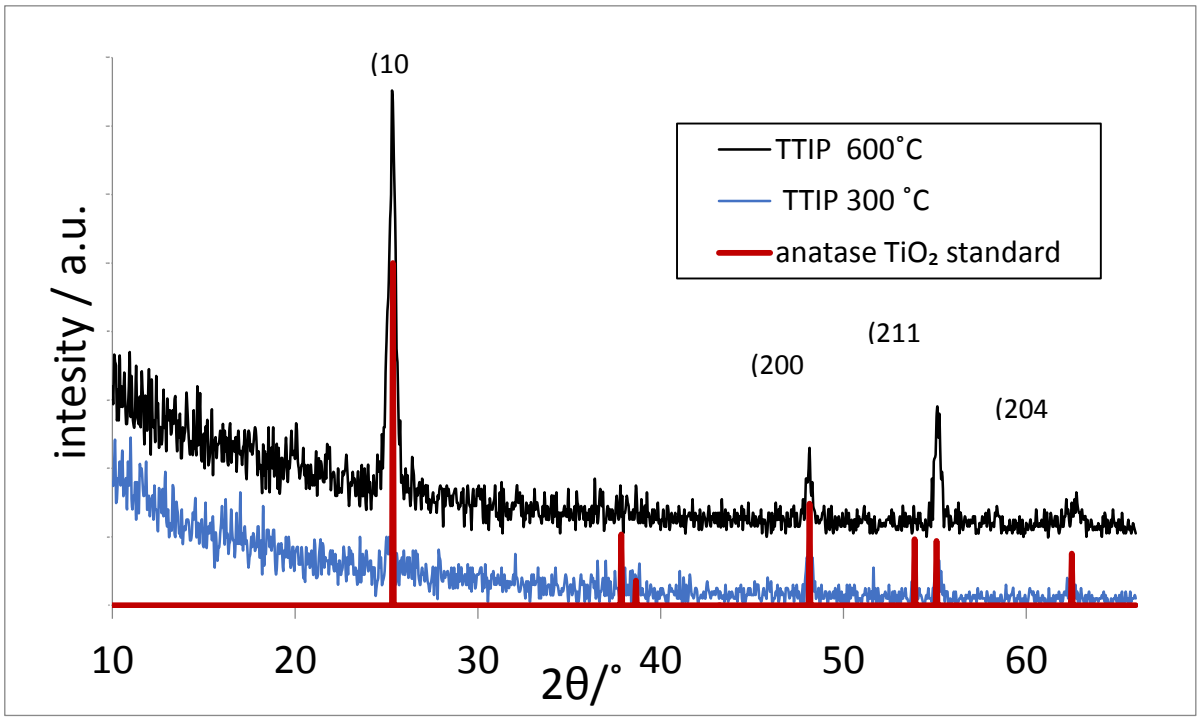

Figure 87: X-ray diffraction pattern of the films deposited from $TiCl_4$ and ethyl acetate onto float glass at 300 and 600 ˚C using the APCVD / mass spectrometry apparatus, alongside an anatase TiO_2 standard.[187]

ii) Scanning Electron Microscopy

SEM micrographs were taken of the films deposited from TTIP at 300 and 600 ˚C (Figure 88). At 300 ˚C the film appears to display more pores and a disordered microstructure constructed of small grains of approximately 100 nm in diameter forming pseudo dendritic protrusions.

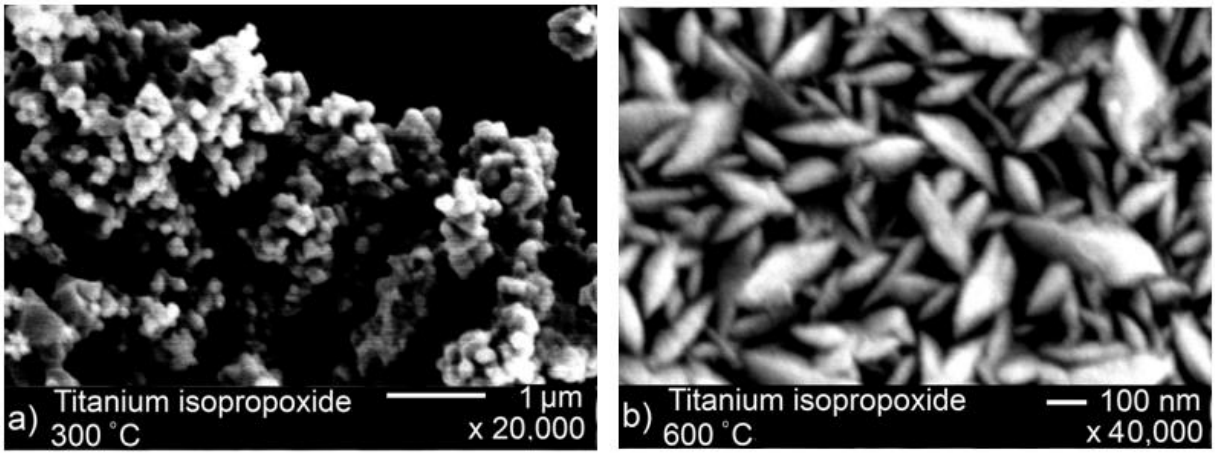

Figure 88: SEM images of the film deposited from titanium isopropoxide onto float glass at 300 (a) and 600 ˚C (b) using the APCVD / mass spectrometry apparatus.

The film deposited at 600 ˚C consisted of flattened diamond shaped crystallites roughly 100 nm in width and between 200 and 300 nm in width, in a disordered arrangement with some perpendicular to the substrate an others lying flat.

5.3.6. Vanadium Tetrachloride

Thin films were deposited using the APCVD mass spectrometer apparatus VCl_4 and ethyl acetate as a precursors. Four depositions were carried out, the first with only a 0.2 L min^{-1} flow of VCl_4 and the following three with 0.6 L min^{-1}, 0.2 L min^{-1} and 0.05 L min^{-1}, giving approximate ratios of 2.5:1, 1:1 and 1:4 ethyl acetate to vanadium chloride respectively. Upon removal of the thin films from the reactor, films deposited with a 0.6 L min^{-1} flow of ethyl acetate appeared pale yellow and opaque. The film was fairly adherent to the substrate surface, resisting the Scotch tape test. The film deposited from a 0.2 L min^{-1} flow of ethyl acetate was transparent and light orange in colour, strongly resembling those deposited from $VOCl_3$ in section 5.3.3. The film deposited from the lowest flow rate of ethyl acetate was opaque and dark red, with no adherence to the substrate. Upon exposure to the atmosphere the film changed, becoming green and oily within twenty minutes of deposition. This implied that the vanadium chloride was not fully oxidised within the reactor, most likely depositing as a partially oxidised vanadium

chloride species that upon exposure to air reacted with atmospheric water to give an oily vanadium hydroxide species. Deposition with no oxidising agent gave no deposition.

5.3.6.1. Mass Spectrometry Analysis

Figure 89 shows the mass spectrum of VCl_4. Initially, VCl_4 was passed through the reactor at 600 ˚C without any oxidising agent and a predictable spectrum, with peaks at *m/z* 192, 155, 122 and 86 representing the parent ion VCl_4 and the subsequent loss of one, two and three chlorine atoms respectively was observed. Furthermore, the presence of peaks at *m/z* 227 and 264 indicates that chlorination of the parent ion *via* the fragmented Cl· radicals, as observed for $TiCl_4$ was also occurring with VCl_4.

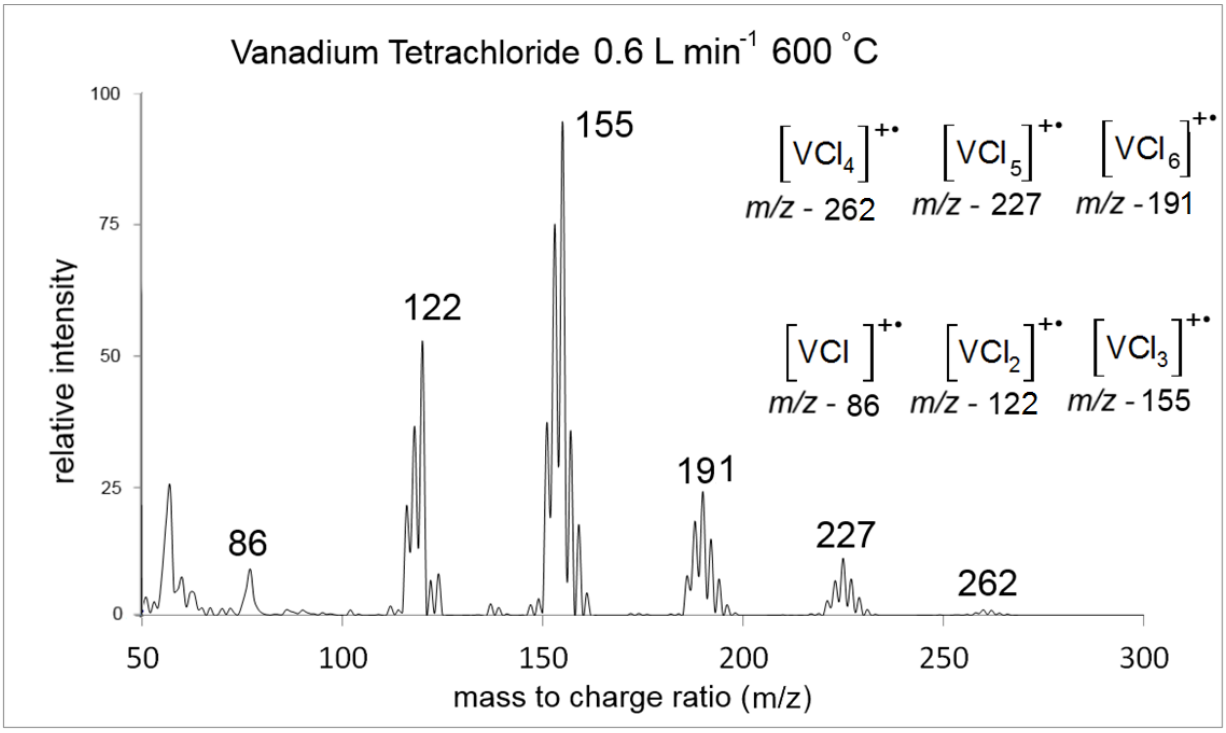

Figure 89: Mass spectrum of titanium isopropoxide as passed through an atmospheric pressure chemical vapour deposition reactor at a temperature of 600 ˚C

Following the deposition using only VCl_4, spectra were collected for depositions with the same pressure of VCl_4 with different pressures of ethyl acetate passing through the reactor. In the case of this study, the mass flows of VCl_4 and ethyl acetate were closely monitored as the final

product has been found to relate closely to the stoichiometry of VCl_4 and the oxidising species. The mass flows of all three experiments are shown in Table 15.

By tuning the flow rates, atmospheres were tailored so that VCl_4: ethyl acetate ratios of 2.5:1, 1:1 and 1:4 were used (experiments 11, 12 and 13 respectively), in order to observe the effect of increased levels of oxidising agent on the atmosphere inside the reactor.

Table 15: Approximate vapour pressure and molar flow rates of VCl_4 and ethyl acetate during mass spectrometry APCVD depositions 11-13

	VCl_4				ethyl acetate			
Deposition	Bubbler Temp /˚C	Flow rate L min^{-1}	Vapour pressure mmHg	Mass flow Mol min^{-1}	Bubbler Temp /˚C	Flow rate L min^{-1}	Vapour pressure mmHg	Mass flow Mol min^{-1}
11	70	0.6	60	0.002	30	0.05	120	0.0005
12	70	0.6	60	0.002	30	0.2	120	0.002
13	70	0.6	60	0.002	30	0.6	120	0.005

The results are shown in Figures 90 and 91. As the flow rate of ethyl acetate increases, relative heights of the ethyl acetate peaks to the vanadium species increases, however the ratios do not reflect the amount entering the reactor, as in all three cases the highest peaks in the spectrum are those at *m/z* 88, 70 and 66, commonly associated with ethyl acetate. This is due to both the ethyl acetate having fewer breakdown products and a lower boiling point and reactivity than VCl_4 meaning it is far more likely to reach the detector and not deposit or breakdown on the walls of the sampling tube or mass spec chamber. In all three cases the

presence of the ethyl acetate appears to lead to the emergence of peaks that relate to $VOCl_3$, as observed in Figure 91.

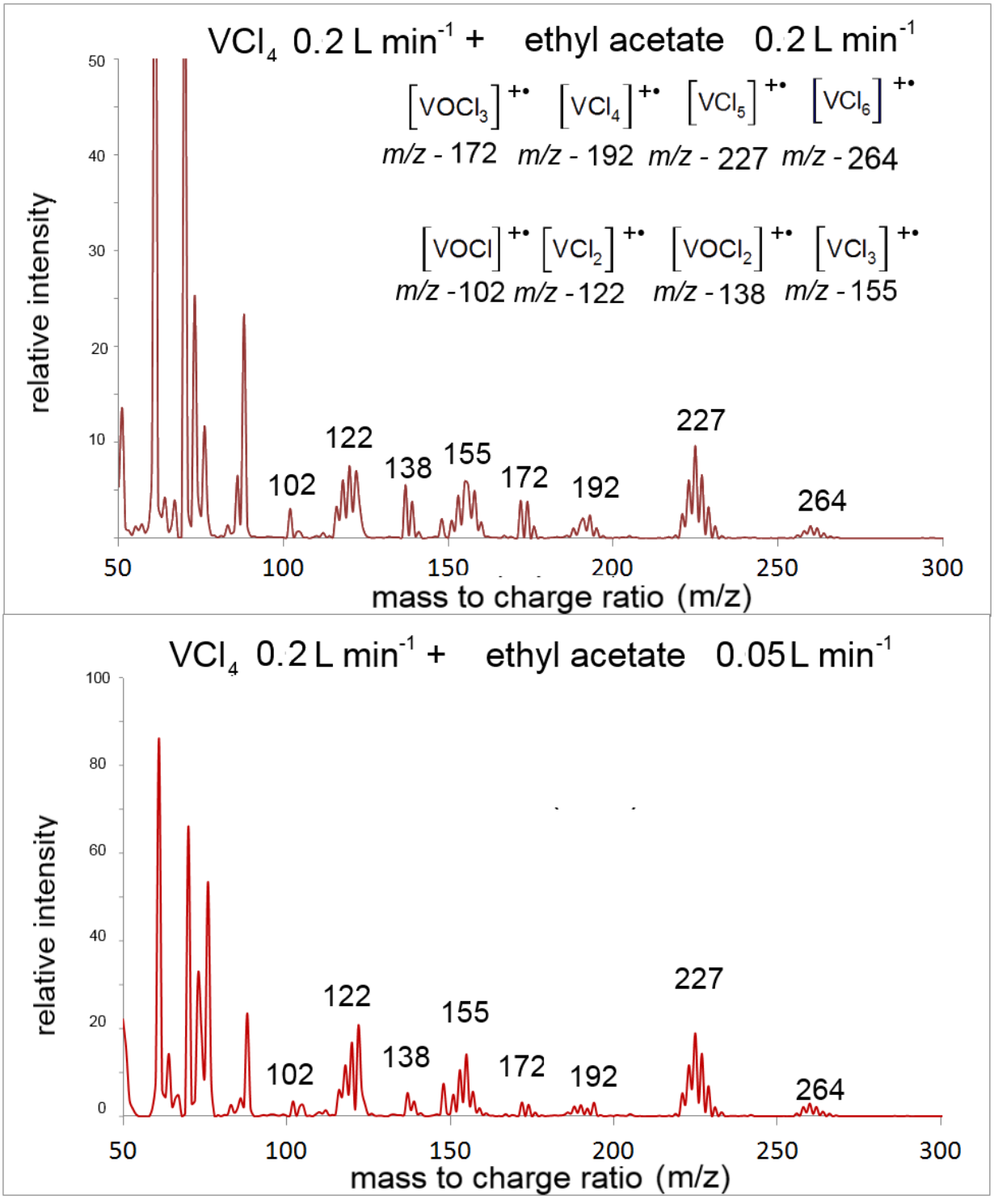

Figure 90: Mass spectra of APCVD depositions of VCl_4 at 600 ˚C with flows of ethyl acetate at 0.2 L min^{-1} (top) and 0.05 L min-1 (bottom).

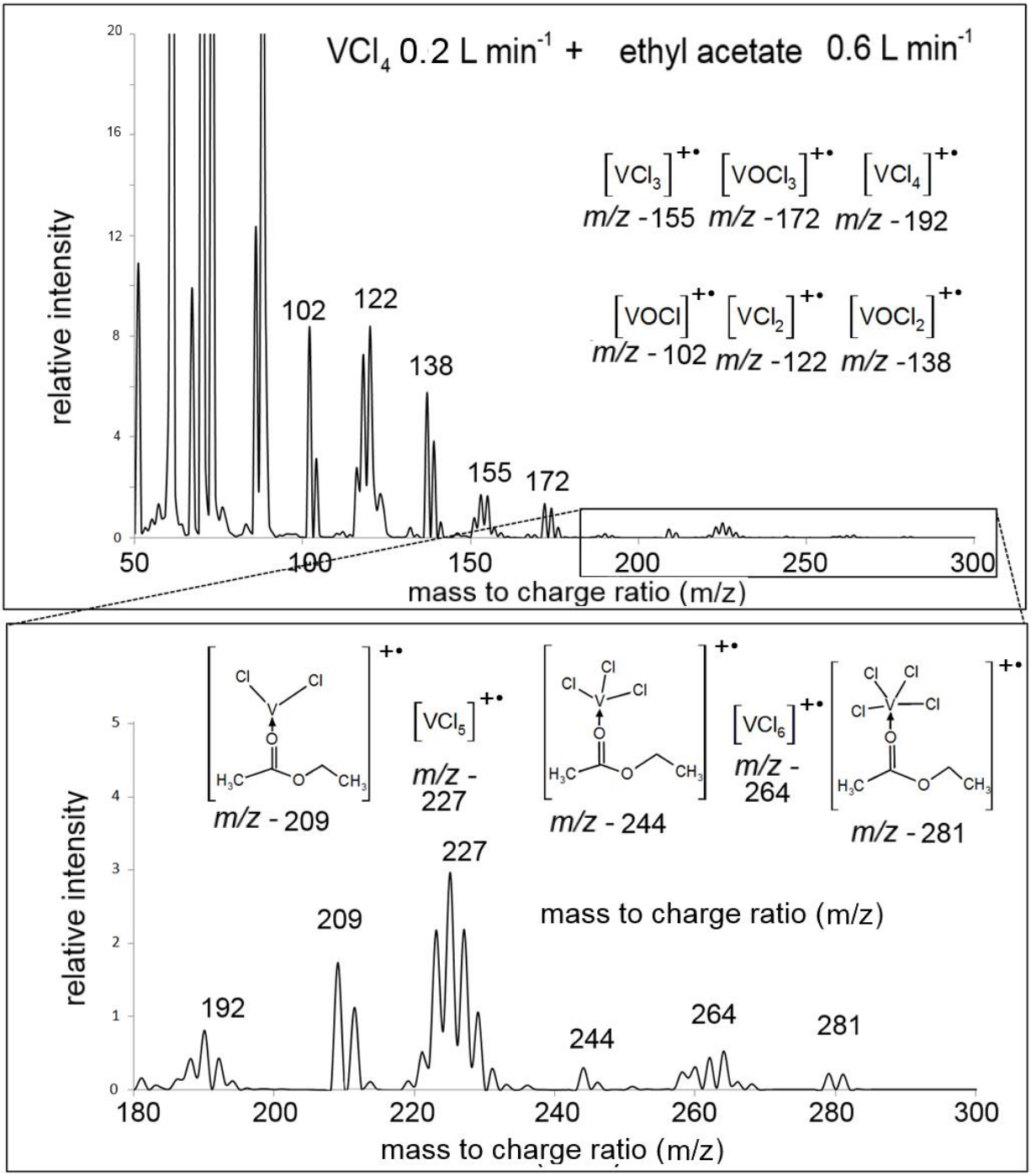

Figure 91: Mass spectra of APCVD depositions of VCl_4 at 600 ˚C with flows of ethyl acetate at 0.6 L min^{-1} with peaks in the range of *m/z*- 180 to 300 enhanced.

Peaks at *m/z* 172, 138 and 102 with isotope patterns matching those of three, two and one chlorine ligands can be seen in all three spectrum with the intensities increasing as the mass flow of ethyl acetate increases.

In the depositions carried out with ethyl acetate, flow rates of 0.2 L min^{-1} and 0.05 L min^{-1}, only those peaks and the peaks of the unreacted VCl_4 and ethyl acetate were observed (Figure 91). When the ethyl acetate level is highest, the flow rate of 0.6 L min^{-1} , however, new peaks are observed at *m/z* 281, 244 and 209. These are thought to relate to the VCl_4 with one intake ethyl acetate ligand coordinated to the metal centre *via* the carbonyl oxygen, along with the same species having lost one and two chlorine ligands respectively. The very low intensity of these peaks indicates that this structure is somehow unstable and likely breaks down in the gas phase to form $VOCl_3$.

5.3.6.2. Analysis of Thin Films

i) X-ray Diffraction

X-ray diffraction patterns of the thin films confirmed that increasing the level of ethyl acetate and by extension the amount of $VOCl_3$ forming within the reactor increased the oxidation state of the final deposition product (Figure 92). The film deposited with 0.6 L min^{-1} ethyl acetate flow shows a clear pattern for V_2O_5. The film deposited using a 0.2 L min^{-1} shows a pattern very similar to that resulting from the $VOCl_3$ depositions, that of monoclinic VO_2. In both cases the patterns were considerably broadened, suggesting low crystallinity in the films.

The film deposited from the lowest flow of ethyl acetate appears to be largely amorphous, with small peaks that may represent V_2O_5 just visible below the baseline. This is in keeping with the

incomplete removal of chlorine in the reactor resulting in slow oxidation of an intermediate oxychloride species on the substrate in air to vanadium (V).

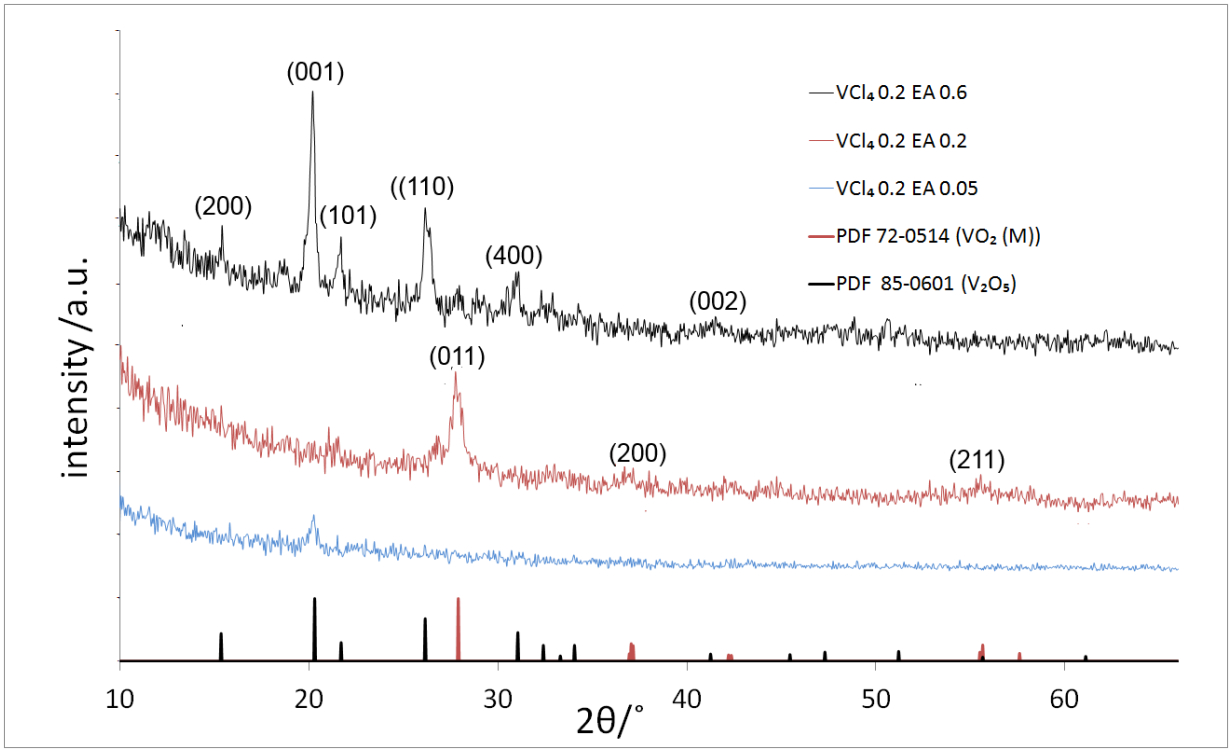

Figure 92: X-ray diffraction pattern of the films deposited from VCl_4 and ethyl acetate onto float glass at 600 ˚C using the APCVD / mass spectrometry apparatus with ethyl acetate flow rates of 0.6 L min^{-1}(top), 0.2 L min^{-1} (middle) and 0.05 L min^{-1} (bottom) and alongside standards for monoclinic (PDF 72-0514)[188] and tetragonal (PDF 80-0690) VO_2.[189]

ii) X-ray Photoelectron Spectroscopy

X-ray photoelectron spectroscopy (XPS) of the thin films deposited from VCl_4 and ethyl acetate further confirm the pattern of greater oxidation as a result of higher levels of ethyl acetate. The film deposited with a flow of 0.6 L min^{-1} of ethyl acetate gave the largest signal for the V(V) oxidation state over V(IV), with a ratio of 3.2:1. The presence of some V(IV) in the film shows that the vanadium in the material has not been completely oxidised from the 4+ state (Figure 93a).

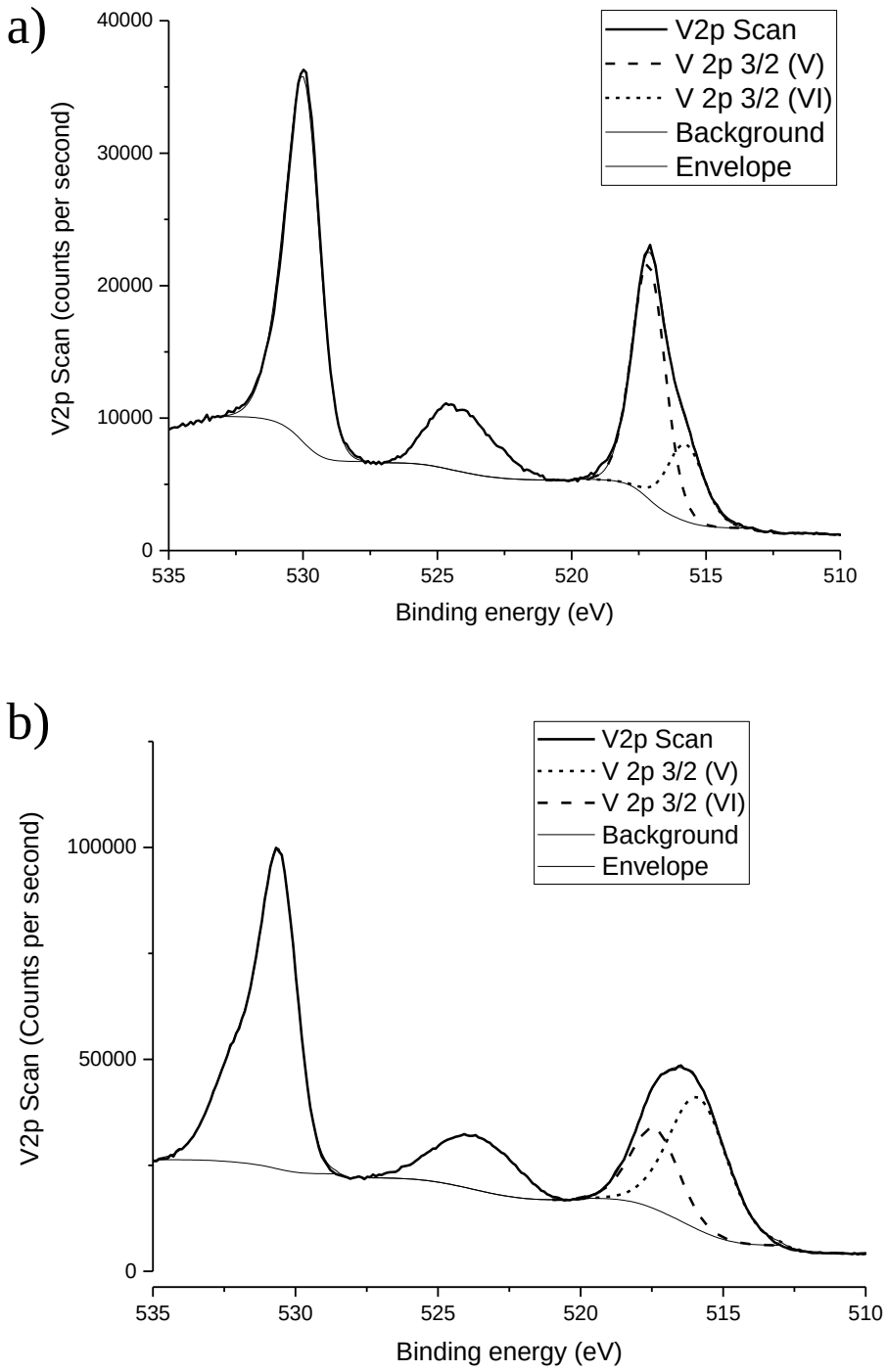

Figure 93: Detailed XPS scans of: a) V 2p of film deposited from 0.2 $Lmin^{-1}$ VCl_4 and 0.6 L min^{-1} ethyl acetate and b) V 2p of film deposited from 0.2 $Lmin^{-1}$ VCl_4 and 0.2 L min^{-1} ethyl acetate, V(IV) (dotted line) vs. V(V) (dashed line).

The film deposited from 0.2 L min^{-1} flow rate of ethyl acetate gave a predominantly V(IV) signal, with the ratio of the 5+ to 4+ oxidation states at 1:2.1. The presence of some V_2O_5 in any VO_2 film is explained by surface oxidation of the film (Figure 93 b). This is exacerbated by the nature of XPS which is a highly surface sensitive technique.

XPS of the film deposited from 0.05 L min^{-1} of ethyl acetate gave a film that was roughly 1:1 V(V) to V(IV), which is in keeping with the idea that the material deposited was only partially reacted, and that a large amount of vanadium chlorine bonds remained, which is evidenced by the colour change and non adherent nature of the film deposited. The resulting oily film would likely contain a number of different species, especially following exposure to air. XPS was also taken of the film deposited from VCl_4 without any ethyl acetate, revealing that the glass, which appeared uncoated, contained a very small amount of V(IV).

iii) Scanning Electron Microscopy

SEM imaging of the films deposited from VCl_4 appears to show a considerable difference in the morphology as a result of increased levels of ethyl acetate present in the gas flow. When the amount of ethyl acetate was maximised and the mass flow ratio to VCl_4 was roughly 5:2 (Figure 94a), the films are at their most porous and disordered, consisting of roughly spherical particulates of roughly 100 nm in diameter, adhered together to form protruding structures.

When the ethyl acetate flow was set to 0.2 L min^{-1} and the mass flow ratio to VCl_4 was around 1:1, the morphology was observed to consist of vertical columns, roughly cylindrical in shape and 200 nm in diameter, densely packed together on the substrate surface. When the mass flow of ethyl acetate was reduced even further, with the flow rate set to 0.05 L min^{-1} and the mass

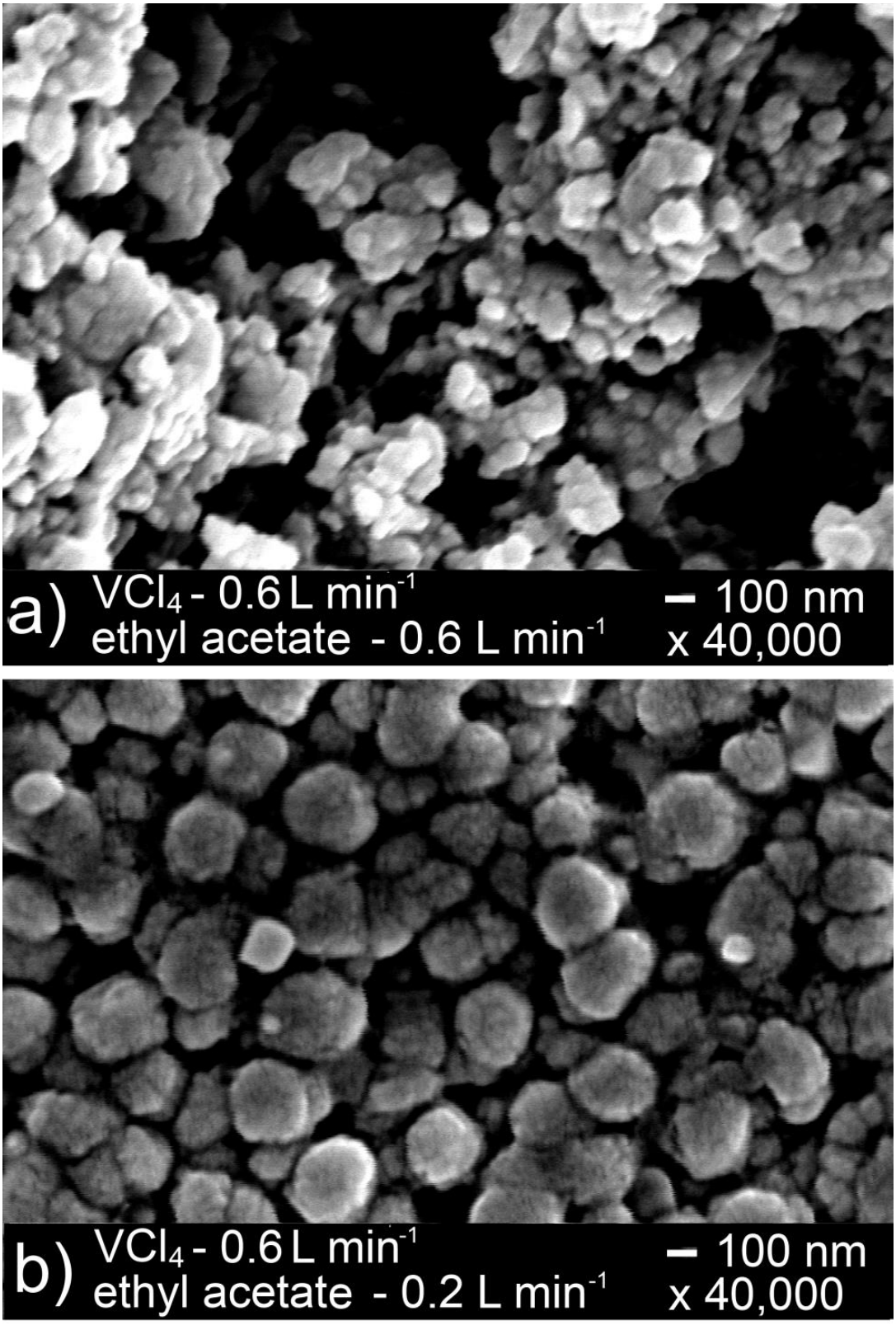

Figure 94: SEM images of the film deposited from a 0.6L min^{-1} flow of VCl_4 onto float glass with 0.6 L min^{-1} (a), 0.2 L min^{-1} (b) and 0.05 L min^{-1} (c) flows of ethyl acetate using the APCVD / mass spectrometry apparatus.

flow ratio to VCl_4 at 1:4 ethyl acetate to VCl_4, square plate- like particles of between 200 – 800 nm in width and no more than 50 nm in thickness were seen, arranged in a disorganised fashion across the surface with some flat to the surface, some perpendicular. Some cube shaped particles of roughly 500 nm in width were also observed

5.4. Conclusion

This chapter details a novel, sensitive and versatile approach to analysing the contents of an APCVD reactor using mass spectrometry, during high temperature depositions. The approach has proved robust enough to sample highly reactive metal chloride species that would be beyond the scope of most spectrometers. The methodology has also been shown to be capable of 'capturing' species that form in the gas phase from the reaction of the metal oxide precursors and the oxygen source, giving new insight into the intermediate phases observed in APCVD.

Initial testing using $TiCl_4$ and $VOCl_3$ with ethyl acetate as a source of carbonyl oxygen appear to reaffirm what was previously postulated with regards to the reactivity of the two species. In the case of the $TiCl_4$ a species featuring two ethyl acetate species coordinated to the titanium species was observed with only the loss of a single chlorine atom from the metal centre. An analogous complex with $VOCl_3$ was not observed. In that case with each ethyl acetate molecule that was observed to have coordinated to the metal centre, chlorine was lost, as observed with the diethyl malonate. This is important as it shows that the metal chloride species behave the same way in the gas phase, as in the solid phase. The ability to observe the intermediate gaseous species *in-situ* rather than in solution, (as with the NMR) and solid, (as with the crystallography) gives new weight to these conclusions.

In addition to this, new light has been shed on numerous other APCVD precursors. Depositions using butyltin chloride reveal that the reaction with the ethyl acetate can proceed *via* two

pathways, either displacing the butyl group, or the chloro group first, with the latter being the more favourable of the two.

In the case of titanium isopropoxide, deposited alone, at high temperatures the possible formation of a dimeric intermediate to deposition of TiO_2 was observed. Ti-O-Ti linkages were observed to form in the gas phase, before contact with the substrate surface. These intermediates are then likely to nucleate on the substrate surface, resulting in the TiO_2 thin film product.

Finally, with VCl_4 when deposited alongside ethyl acetate, the observation of $VOCl_3$ as an intermediate in the deposition of vanadium oxide thin films were observed, with the height of the $VOCl_3$ peaks correlating to the quantity of ethyl acetate in the system. Increasing the level of ethyl acetate increases the vanadium: oxygen ratio in the final film. This could mean that $VOCl_3$ is the gaseous intermediate to VO_2, the vanadium oxygen bonds forming in the gas phase before depositing.

The range of applications of this apparatus is broad and has by no means been fully explored. In addition to work with APCVD, the mass spec CVD linkage has been utilised in the study of aerosol assisted chemical vapour deposition reactions, gas sensor arrays and low pressure chemical vapour deposition applications. Further work would likely involve increasing the range of precursors studied with iron oxide precursors being a likely candidate, as well as investigation of dual source co-depositions, although the resulting spectra would likely be extremely complex.

Chapter 6

Aerosol Assisted CVD of Photocatalytically Active TiO_2-SiO_2 Microfractal Thin Films

6.1. Introduction

The work presented in this chapter is based around a continuation of the coordination chemistry of carbonyl ligands with $TiCl_4$. In addition to the malonate and triglyceride examined in chapter 4, several carbonyl species featuring silane groups were reacted with $TiCl_4$. Whilst initially linked to the discovery of organosilanes within the industrial samples for $TiCl_4$, the emergence of one compound in particular was found to be highly effective as an aerosol assisted CVD precursor for the deposition of TiO_2-SiO_2 composite thin films, which show increased photocatalytic activity over TiO_2 deposited from $TiCl_4$ using the same deposition technique. The results of the reaction of four silyl-keto species, methyltrimethylsilyl acetate, trimethylsilyl acetate, silicon tetraacetate and bis-trimethylsilyl malonate with $TiCl_4$ to produce complexes **10** [Ti{OC(OMeCH_2SiMe_3}Cl_3(μ-Cl)]$_2$, **11, 12** [$Ti_3O_2Cl_3(CH_3CO_2)_5$ and **13** are presented. Additionally the resulting TiO_2-SiO_2 composite thin films fabricated from the deposition of **10** onto float glass using AACVD are characterised and tested from photocatalytic efficiency and hydrophilicity.

6.1.1. Aerosol Assisted CVD

Aerosol Assisted CVD differs from conventional chemical vapour deposition in that transportation of the precursor is primarily a liquid phase process. The precursor is dissolved or suspended in a solvent, from which an aerosol is generated using an ultrasonic humidifier.[202] This creates a mist of aerosol droplets containing solvated precursor molecules that are then

transported into the reactor *via* a carrier gas (Figure 95). In this case nitrogen was used. Upon entering the reactor chamber, the aerosol droplets evaporate, leaving the precursor, which deposits onto the substrate.[203]

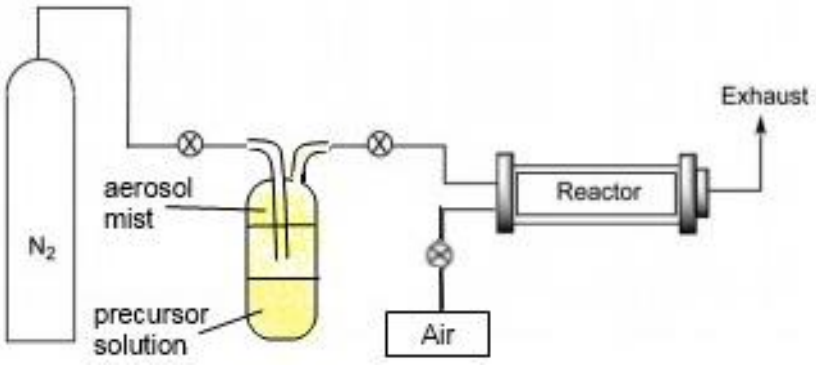

Figure 95: Schematic diagram of the AACVD apparatus.

AACVD has a number of advantages over conventional methods of CVD, most notably that it opens up a new range of precursors as the primary prerequisite for an AAVCD precursor is its solubility rather than its volatility, as is the case with other methods.[204] The process is also far simpler to set up, requiring no heated tubing to carry the hot precursor, simply an aerosol generator and a reactor. AACVD has been used to deposit a large number of metal oxide coatings. These include titanium dioxide,[205,206] thermochromic vanadium dioxide,[207–209] tin oxide ,[210–212] zinc oxide[213] and tungsten oxide,[214,215] as well as composites[216,217] and doped films.[218–220]

The use of a solution based medium allows for greater control over the composition of doped/ composite films and also the deposition of mixed metal oxides by allowing the pre-mixing of the precursors in solution.[221] These one pot depositions allow the correct stoichometery of the two components to be achieved before the deposition of the material. [222] The wider range of precursors available also means that there is a much more expansive combination of precursors that can be combined in order to give the desired properties.[223,224]

AACVD is a highly tunable technique, with many variants.[225] In general a piezoelectric mister is used to generate aerosol droplets of a solution of the precursor in a solvent. The deposition can be altered by the frequency of the ultrasound used to generate the mist, with higher frequency producing more numerous, finer droplets.[162] The use of a solution based technique allows for control over deposition speed and/or film thickness by altering the concentration of the precursors within the solution.[226]

AACVD has also been shown to produce different morphologies compared to films deposited by traditional CVD methods.[227] AACVD has been used to produce wide a range of nanostructures from the same precursor, for instance tungsten oxide from $W(OEt)_6$ which has been deposited as particles, wires, hollow tubes, rods and even 'nanoflowers'.[228,229] Further control of morphology can be demonstrated by use of surfactant additives to the precursor solution, such as substituted ammonia salts. These have been found to favour certain growth patterns.[230]

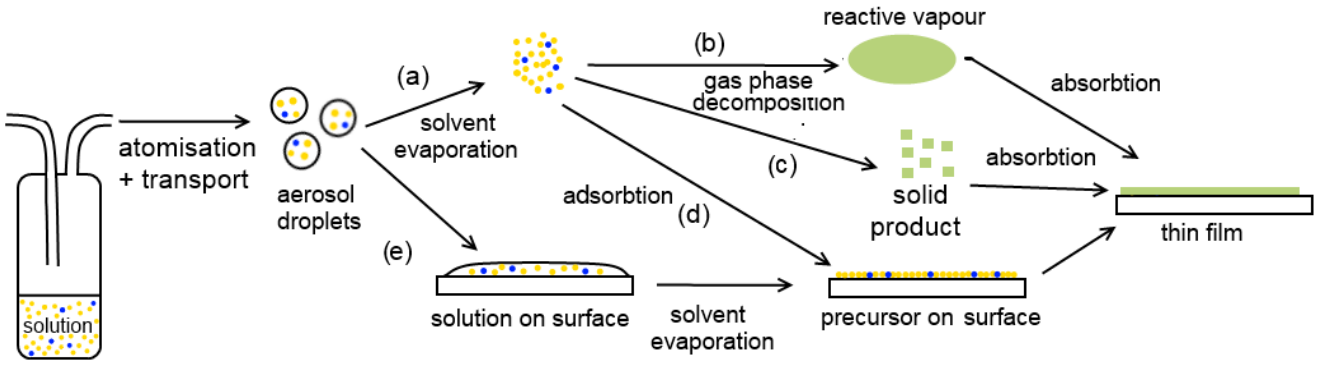

Figure 96: Schematic representation of various deposition pathways possible in AACVD.

Depositions within an AACVD process can occur *via* a number of pathways, relating to the substrate temperature, concentration of precursor, solvent used and other factors (Figure 96). In each case the precursor arrives at the reactor solvated in droplets of the chosen solvent. The solvent either evaporates before reaching the substrate (a) or afterwards (e).[231] In the case of

(a) the precursor species commonly decomposes in the gas phase, forming a reactive intermediate vapour or particles of the desired product ((b) + (c) respectively), similar to atmospheric pressure chemical vapour deposition.[225] Following this, in both cases the products are absorbed onto the substrate to form the film. The gaseous reagents can also adsorb onto the substrate intact before decomposing and coordinating onto the surface of the substrate (d).[231] In the case of (e) the solution deposits onto the heated substrate and spreads out before rapidly evaporating, leaving the precursor species to react as seen in (d).[232]

Problems with this method are mainly based around the time taken for the deposition to complete, taking anywhere from ten minutes to over an hour depending on the ease with which an aerosol of the solvent is generated. There are also issues with industrial scale up [233] and reproducibility.[234]

6.1.2. TiO_2-SiO_2 Composite Films

The photocatalytic properties of TiO_2 are widely recognized[235] and have received much literature attention.[236] Irradiation of TiO_2 with UV light causes the excitation of electrons to the conduction band, leaving a positive hole that can migrate to the surface, oxidising water to form highly reactive hydroxyl radical species capable of breaking down surface organics.[237] Efforts to improve the photocatalytic properties of TiO_2 have focussed on the use of dopants such as nitrogen,[238] fluorine,[239] and tungsten,[240] as well as composite materials such as TiO_2-SiO_2, which have been produced in the form of both thin films[241] and nanoparticles,[242] both of which are frequently doped to further improve catalytic activity.[243]

TiO_2-SiO_2 thin films have themselves been widely studied for a number of uses. These films have been shown to have exceedingly high wettability.[244,245] Work by Hourmard *et al.* showed that films of 20:80 and 60:40 composites of TiO_2:SiO_2, prepared *via* sol gel of tetraethylorthosilicate and isopropyl orthotitanate show increased superhydrophilicity

compared to TiO_2 prepared in the same manner.[246] This was attributed to increased surface roughness of the composites, as well as the presence of charged TiO_x^- and SiO_x^+ at the interfaces.[247]

SiO_2 / TiO_2 composite films have also been shown to have the potential for excellent photocatalytic behaviour. Films with a TiO_2:SiO_2 ratio of 1:1, deposited onto ethylene terepthalare *via* dip coating using a peroxotitanium acid/(aminopropyl) triethoxysilane sol, were shown to photocatalytically degrade Rhodamine B under UV light at a rate roughly twice that of pure TiO_2 deposited in the same way. This was attributed to the generation of surface acid sites, as well as smaller grain size.[248] Likewise, a study by Yu *et al.* found that a 5% composite film of SiO_2 in TiO_2 was more effective at degrading methyl orange under UV/Vis conditions than TiO_2 prepared in the same way, however at concentrations greater than 5% the performance became poorer.[249]

Chemical vapour deposition has been widely used in the deposition of TiO_2 thin films, using a variety of methods such as atmospheric pressure (APCVD),[250] aerosol assisted (AACVD),[251] and plasma enhanced (PECVD).[252] Examples of TiO_2-SiO_2 thin films grown *via* CVD are limited. Klobukowski *et al.* succeeded in depositing a 1:1 TiO_2-SiO_2 film onto float glass *via* APCVD using a $[Ti(O^iPr)_2\{OSi(O^tBu)_3\}_2]$ precursor.[253] Additionally, Yoon *et al.* fabricated a TiO_2-SiO_2 composite film from the co-deposition of tetraethylorthosilicate (TEOS) with titanium isopropoxide at 400 ˚C using AACVD.[254]

This work describes the reactions of $TiCl_4$ with methyl trimethylsilyl acetate (mtmsa) to form a novel single source precursor for the deposition of photocatalytically active TiO_2-SiO_2 thin films onto glass *via* AACVD over a range of temperatures. AACVD has a number of advantages over conventional methods of CVD, the most notable being that it opens up a new range of precursors as their effectiveness is dependent on solubility rather than volatility as is the case

with other methods. The process is also far simpler to set up, requiring no heated tubing to carry the precursor vapour, simply an ultrasonic humidifier and a reactor.[225]

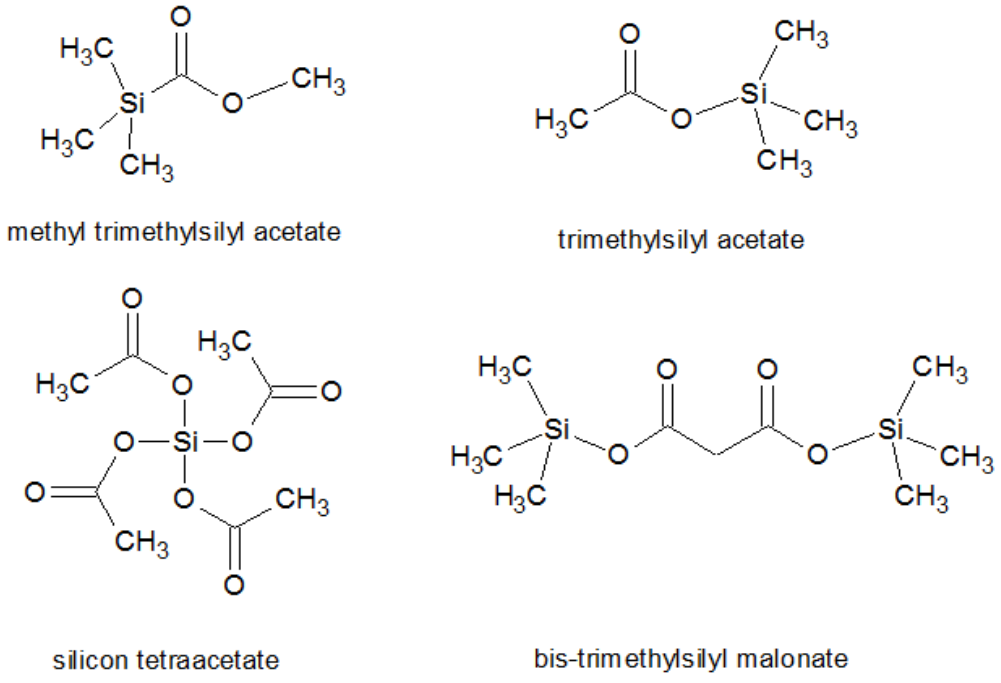

Figure 97: Silicon containing ligands reacted with $TiCl_4$ used in the synthesis of **10** (top left), **11** (top right) **12** (bottom left) and **13** (bottom right)

In this section $TiCl_4$ was reacted with four silicon containing carbonyl species, methyl trimethylsilyl acetate, trimethylsilyl acetate, bis-trimethylsilyl acetate and silicon tetraacetate (Figure 97) to produce compounds **10** $[Ti\{SiMe_3CH_2CO_2Me\}Cl_3(\mu\text{-}Cl)]_2$, **11, 12** $[Ti_3O_2Cl_3(O_2CCH_3)_5$ and **13** respectively. The resulting species were characterised by NMR spectroscopy and single crystal X-ray diffraction analysis where possible. Following this, **10** was used as a single source precursor for the deposition of TiO_2-SiO_2 films for use as self cleaning coatings as evidenced by their enhanced propensity for the breakdown of stearic acid when compared with TiO_2 films deposited from $TiCl_4$ in the same manner. This is the first deposition of a TiO_2-SiO_2 composite film using a single source precursor *via* AACVD. Depositing in this manner lead to films with novel fractal like morphologies.

6.2. Experimental

All starting materials were purchased from Sigma Aldrich and used without further purification. The solvents were dried over activated alumina by the Grubbs method using anhydrous engineering equipment, such that the water concentration was 5 – 10 ppm.[83] All products were synthesised under an atmosphere of nitrogen obtained from BOC in anhydrous solvents using standard Schlenk techniques.

6.2.1. Synthesis of $[Ti\{OC(OMeCH_2SiMe_3\}Cl_3(\mu\text{-}Cl)]_2$ [10]

Methyl trimethylsilyl acetate (1 g, 0.006 mol) was added to an excess of titanium(IV) chloride (1 ml, ~ 10 mmol), dissolved in anhydrous hexane (30 ml) in a Schlenk flask under nitrogen. The resulting mixture was stirred for two hours. Following this the solvent was removed *via* filtration, and the product washed three times with anhydrous hexane and dried under vacuum in order to ensure the complete removal of all remaining $TiCl_4$, leaving a light yellow, free-flowing powder product [**10**] (1.931 g, 92.1%). Single crystals of **10** were grown from a 5 ml saturated solution of the product in anhydrous toluene, layered with 10 ml of anhydrous hexane and left under nitrogen for one week. ^{1}H NMR ($CDCl_3$): δ 4.04 (s, 2H, C**H$_2$**Si), 2.54 (s, 3H, OC**H**$_3$), 0.44 (s, 9H, Si**Me$_3$**) ^{13}C {^{1}H} NMR ($CDCl_3$): δ 184.8 (C=O), 56.5 (CH_2), 28.8 (CH_3), 2.4 ($SiMe_3$). MS: *m/z* = 671.46 [M + H$^+$].

6.2.2. Reaction of $TiCl_4$ with trimethylsilyl acetate to produce [11]

Trimethylsilyl acetate (1 g, 0.006 mol) was added to an excess of titanium(IV) chloride (1 ml, ~ 0.01 mol), dissolved in anhydrous hexane (30 ml) in a schlenk flask under nitrogen. The resulting mixture was stirred for two hours. Following this the solvent was removed *via* filtration, and the product washed three times with anhydrous hexane and dried under vaccum in order to

ensure the complete removal of all remaining $TiCl_4$, leaving a bright yellow powder product (**11**) (1.344 g, 55.3%). Attempts were made to grow single crystals of **11** by layering a 5 ml saturated solution of **11** in $CHCl_2$ with hexane, an leaving for one week, and by freezing a 5 ml saturated solution over one month, however in both cases the product was observed to break down into a white solid over time, without the formation of crystals. ^{1}H NMR ($CDCl_3$): δ 2.63 (s, 3H, C**H₃**), 0.44 (s, 9H, Si**Me₃**), 0.6 (s, 3H), 2.1 (s, 0.5), 2.3 (s, 0.5), 2.4 (s, 0.8). ^{13}C {^{1}H} NMR ($CDCl_3$): δ 173.3 (C=O), 22.76 (CH_3), 3.6 ($SiMe_3$), (Appendix 11). The NMR spectra of **11** shows a number of minor peaks adjacent to the product (0.6, 0.8, 2.1, 2.3) peaks that are likely the result of unreacted starting material remaining in solution.

6.2.3. Reaction of $TiCl_4$ with silicon tetraacetate to produce $[Ti_3O_2Cl_3(O_2CCH_3)_5]$ [12]

Silicon tetraacetate (1 g, 0.004 mol) was added to an excess of titanium (IV) chloride (1 ml, ~ 0.01 mol), dissolved in anhydrous hexane (30 ml) in a schlenk flask under nitrogen. The resulting mixture was stirred for two hours. Following this the solvent was removed *via* filtration, and the product washed three times with anhydrous hexane and dried under vaccum in order to ensure the complete removal of all remaining $TiCl_4$, leaving a white powder product (**10**) (1.701 g, 93.87%). Single crystals of **10** were grown from a 5 ml saturated solution of the product in anhydrous toluene, layered with 10 ml of anhydrous hexane and left under nitrogen for one week. ^{1}H NMR ($CDCl_3$): δ 2.32 (COC**H**$_3$) (s, 3H). ^{13}C {^{1}H} NMR ($CDCl_3$): δ 184.8 (C=O), 23.1 (C**H**$_3$).

6.2.4. Reaction of $TiCl_4$ with bis-trimethylsilylmalonate to produce [13]

Bis-trimethylsilylmalonate (1 g, 0.004 mol) was added to an excess of titanium (IV) chloride (1 ml, ~ 0.01 mol), dissolved in anhydrous hexane (30 ml) in a Schlenk flask under nitrogen. The resulting mixture was stirred for two hours. Following this the solvent was removed *via* filtration and the product washed three times with anhydrous hexane and dried under vacuum in order to ensure the complete removal of all remaining $TiCl_4$, leaving an orange, powder

product [**11**] (1.068 g, 79.2%). The product was found to be insoluble in $CHCl_2$ and $CDCl_3$ with NMR showing only signals for the trimethylsilyl chloride formed as a side product (0.5 ppm), hexane, toluene and vacuum grease.

6.2.5. Deposition of Thin Films

Following characterisation of **10** – **13** as well as some test runs it was determined that only **10** was a suitable precursor for the AACVD of TiO_2-SiO_2 composite thin films, as the other three were found to be unsuitable precursors. Compounds **11** and **12** were found to decay rapidly upon exposure to a dynamic flow of nitrogen. In the case of **13,** despite being air stable, the compound did not dissolve in any common AACVD solvents and did not contain any silicon in the crystallised product.

For all three depositions using **10**, 0.5 g (0.00071 mol) was dissolved in 20 ml of anhydrous toluene and transferred to a glass bubbler under nitrogen using a cannula. The resulting solution was atomized for 5 minutes to ensure complete solvation of the precursor. An aerosol was generated using a Piezo Liquifog® ultrasonic atomiser. The deposition was carried out using nitrogen as the carrier gas at a flow rate of 0.5 L min^{-1}. The glass substrate was standard float glass of 4 mm thickness. A top plate was suspended level, 0.5 cm above the substrate to ensure a laminar flow.

A stream of air was introduced into the baffle *via* a second tube, from the house line fitted with a filter. Air is frequently used in AACVD rather than nitrogen as a carrier gas in order to ensure that the product is fully oxidised in the reactor chamber. [255] In this case however, due to the air sensitive nature of the precursor, using air as the main carrier gas would result in the pre oxidation of the precursor, forming TiO_2 before the materials could enter the chamber and deposit. By using the split baffle and two streams, one of nitrogen through the bubbler and one of air directly into the chamber the benefits of both carrier gasses can be achieved without loss

of product to oxidation before entering the chamber. The depositions were carried out at 450, 500 and 550 °C, each taking approximately 30 minutes. A final deposition using a solution of $TiCl_4$ (0.5 ml, 0.005 mol) in 20 ml of anhydrous toluene was carried out at 500 °C using the same conditions as the above reactions in order obtain a control film of TiO_2.

6.2.6. Analytical Methods

X-ray crystallography, both obtaining and solving the spectra was carried out by Dr. Caroline Knapp. Single crystal diffraction patterns were collected on a *SuperNova, Dual*, *Cu*, *Atlas* diffractometer. The crystal was kept at 150 K during data collection. Data was processed with Olex2,[87] the structure was solved with the olex2.solve[88] structure solution program using Charge Flipping and refined with the ShelXL[89] refinement package using Least Squares minimisation. X-ray diffraction (XRD) patterns of the deposited films were obtained using a Bruker-Axs D8 (GADDS) diffractometer equipped with a monochromated (Kα1 and Kα2) Cu X-ray source and a 2D area X-ray detector with a resolution of 0.01°. The films were analysed with a glancing incident angle of 5°. The diffraction patterns obtained were compared with database standards. X-ray photoelectron spectroscopy (XPS) was performed using a Thermo Scientific™ K-alpha™ spectrometer, with monochromated Al Kα radiation, a dual beam charge compensation system and consta pass energy of 50 eV. Survey scans were collected in the energy range of 0 – 1200 eV.

^1H and $^{13}C\{^1H\}$ NMR spectroscopy was carried out on a Bruker A-600 Mz spectrometer, operating at 295 K and 600.13 MHz (^1H). Signals are reported relative to $SiMe_4$ (δ = 0.00 ppm) and the following abbre*via*tions are used s (singlet), d (doublet), t (triplet), q (quartet), m (multiplet), b (broad). Deuterated $CDCl_3$ was obtained from GOSS Scientific and was degassed and dried over 3 Å molecular sieves. Liquid Chromatography Mass spectroscopy of **10** was recorded using a Thermo Finnigan LTQ two-dimensional ion-trap mass spectrometer operating

in ESI mode. High-resolution peaks were used for the principal peaks Ti (2p), O (1s), C (1s), Si (2p) and Cl (2p) with a spot size of 400 µm. Elemental composition was inferred from the integral of the peak corresponding to the signal of that particular element. A Renishaw 1000 spectrometer equipped with a 514 nm laser was used to obtain Raman spectra of the samples. The Raman system was calibrated using a silicon reference. Transmission and reflectance UV/Vis spectroscopy were performed using a double beam; double monochromated Perkin Elmer Lambda 950 UV/vis/NIR Spectrophotometer. The absorption spectra were recorded directly on the films as deposited on quartz slides, clamped against an integrating sphere in perpendicular position to the beam path. A Labsphere reflectance standard was used as reference in the UV/vis measurements. SEM analysis was carried out using secondary electron image taken using a JEOL 6301 field-emission instrument (5 kV).

6.2.7. Photocatalytic Testing

The photocatalytic activity of the films was measured by their ability to break down stearic acid, a layer of which was applied to the films *via* dip coating from a stock solution of 0.005 M stearic acid in dichloromethane. The degradation of the stearic acid was measured by Fourier transform infrared (FTIR) spectroscopy in the range 2700–3000 cm^{-1}, using a Perkin Elmer RX-I instrument. The area beneath the peaks relating to stretching vibrations of C-H bonds in the stearic acid (2820-2970 cm^{-1}) was integrated giving an estimation of the number of molecules of stearic acid degraded using a conversion factor reported in the literature (1 $cm^{-1} \equiv 9.7 \times 10^{15}$ mol)].[256] The photoactivity rates were estimated from line regression of the initial 30–40% degradation steps (zero-order kinetics). These rates are expressed as formal quantum efficiency (FQE) values, which are defined as the number of acid molecules degraded per incident photon. This degradation of the stearic acid is shown in equation 1.

$$CH_3(CH_2)_{16}CO_2H + 26O_2TiO_2 \xrightarrow{(h\nu \geq Ebg)} 18CO_2 + 18H_2O \qquad (1)$$

A blacklight-bulb UVA lamp (Vilber-Lourmat) 2 × 8 W, was used to irradiate samples during the photocatalytic tests. The irradiance of the UV lamp (4.1 $mWcm^{-2}$) was measured using a UVX meter (UVP). The films were cleaned under wet air conditions under a 365 nm UV lamp for 24 hours and kept in the dark for another 24 hours prior to the photocatalysis testing.

6.3. Results and Discussion

$TiCl_4$ was reacted with methyltrimethylsilyl acetate, trimethylsilyl acetate, silicon tetraacetate and bis-trimethylsilyl malonate complexes in hexane at room temperature under nitrogen to form **10** $[Ti\{SiMe_3CH_2CO_2Me\}Cl_3(\mu\text{-}Cl)]_2$, **11, 12** $[Ti_3O_2Cl_3(CH_3CO_2)_5$ and **13** in good yield. Following this, product **10** was deposited onto plain glass using aerosol assisted CVD in toluene over a range of temperatures. The films all had excellent coverage, evenly coating the entire substrate, and showed good adherence, being resistant to scratching and the 'Scotch tape test'.

6.3.1. Reaction of $TiCl_4$ with methyl trimethylsilylacetate to give $[Ti\{OC(OMeCH_2SiMe_3\}Cl_3(\mu\text{-}Cl)]_2$ [10]

Methyl trimethylsilyl acetate (Sigma Aldrich, 97%) was added to a solution of $TiCl_4$ and stirred under nitrogen to give $[Ti\{SiMe_3CH_2CO_2Me\}Cl_3(\mu\text{-}Cl)]$ [**10**], a bright yellow powder in good yield. Yellow crystals were grown by layering a solution of **10** in toluene with dichloromethane. NMR analysis shows a downfield shifting of all of the proton signals of the uncoordinated ligand, with the magnitude of the shift decreasing with distance from the carbonyl group (Figure 98). This is indicative of the dative coordination of the ligand to the $TiCl_4$ centre observed for the malonate species reacted with $TiCl_4$ in Chapter 3.

This hypothesis was confirmed by the X-ray diffraction analysis of the crystal grown. The crystal structure of the precursor of $[Ti\{OC(OMeCH_2SiMe_3\}Cl_3(\mu\text{-}Cl)]_2$ (**10**) comprises of a dimeric species, bridged by two chloride ligands (Figure 99). Each titanium atom adopts a distorted octahedral geometry, having retained all four chlorine atoms, with the silyl acetate molecule

coordinating *via* the carbonyl oxygen. This structure is very common with titanium chloride species, seen frequently for complexes of $TiCl_4$ with carbonyl ligands, such as 2-propanone[257] and acetate.[258]

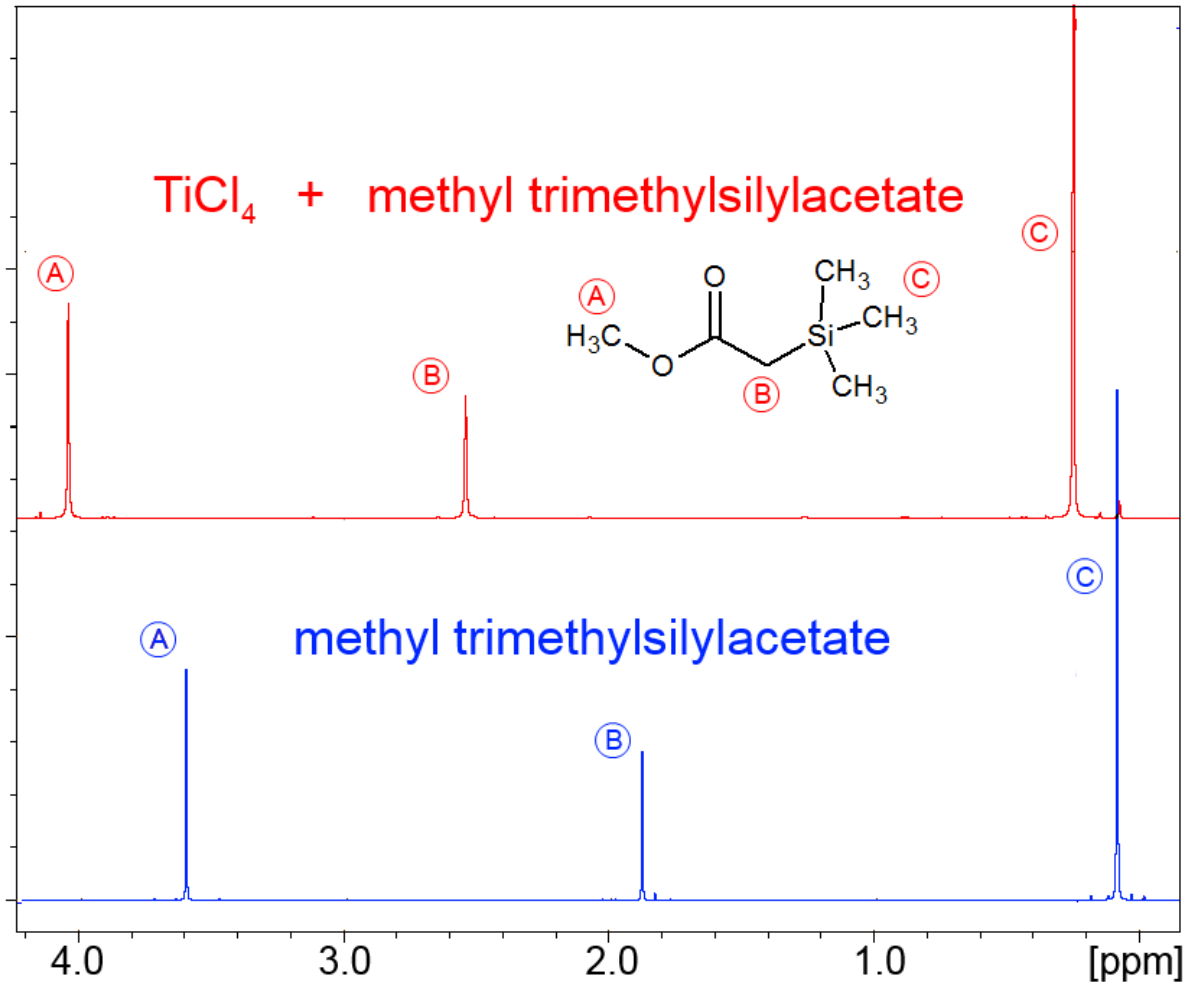

Figure 98: ^{1}H NMR spectra of methyl trimethylsilylacetate and the product of its reaction with $TiCl_4$ **[10]**, all peaks exhibiting a downfield shift indicating coordination to the titanium metal centre.

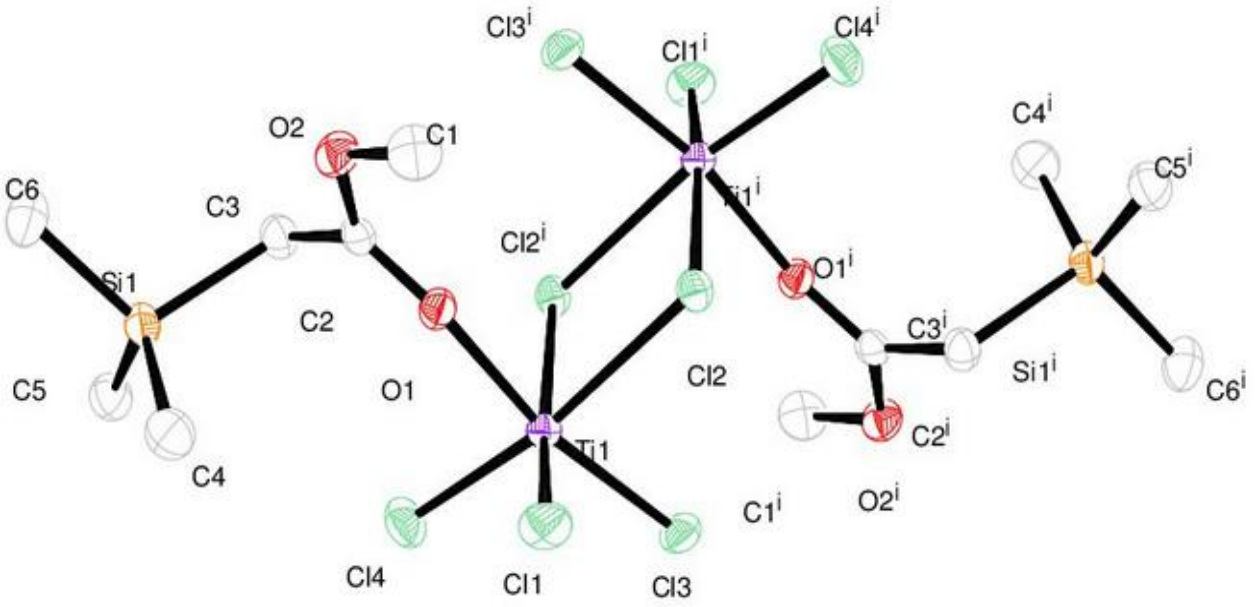

Figure 99: ORTEP representation of crystal structure of **10** with thermal ellipsoids at the 50% probability level. Hydrogen omitted for clarity.

Table 16: Crystallographic Data and Selected bond lengths angles for the crystal structure of 1a the product of reaction $TiCl_4$ and methyltrimethylsilyl acetate [**10**]

Structural Data	
crystal system	monoclinic
space group	C2/c
a	16.98585(13)
b	15.68339(10)
c	24.15174(15)
α	90
β	95.1852(6)
γ	90
R_1	0.0289
wR_2	0.0756

Selected Bond Angles /˚	
$Cl(2^1)$-Ti(1)-Cl(1)	166.816(18)
Cl(2)-Ti(1)-Cl(1)	88.766(16)
Cl(4)-Ti(1)-Cl(1)	99.810(18)
Cl(4)-Ti(1)-$Cl(2^1)$	90.860(16)
Cl(4)-Ti(1)-Cl(2)	169.677(18)
Cl(3)-Ti(1)-Cl(1)	96.526(16)
Cl(3)-Ti(1)-$Cl(2^1)$	89.995(15)
Cl(3)-Ti(1)-Cl(2)	88.729(14)
Cl(3) -Ti(1)-Cl(4)	95.930(17)
O(1) -Ti(1)-Cl(1)	87.55(3)
O(1) -Ti(1)-$Cl(2^1)$	84.11(3)
O(1) -Ti(1)-Cl(2)	81.33(3)
O(1) -Ti(1)-Cl(4)	93.23(3)

Selected Bond Lengths /Å	
Ti(1)-Cl(1)	2.2327(4)
Ti(1)-Cl(2)	2.5157(4)
Ti(1)-$Cl(2^1)$	2.4615(4)
Ti(1)-Cl(4)	2.2085(4)
Ti(1)-Cl(3)	2.2349(4)
Ti(1)-O(1)	2.0238(10)

The Ti-O bond lengths present (Table 16) are 2.0238(10) and 2.0238(10) Å, indicating covalent coordination to the titanium centre by the acetate species, as observed with the similar structure of di-chloro-bis[(allylacetate-O)trichlorotitanium(IV)]. The Ti-Cl bond lengths to the μ-2 bridging chlorides were 2.5157(4) and 2.4615(4) Å, longer than that of the terminal chloride ligands, all of which are between 2.20 and 2.25 Å. This is expected due to the electron density being shared over two metal centres, which in turn reduces the attractive forces felt between the individual titanium centres and the electron cloud around the chlorine.

The decreased electron density also results in the bridging chlorides lying closer to the other ligands. The bond angle between the terminal Cl(3) and the bridging Cl(2) is 88.729(14)˚, whereas the angle between two mutually adjacent terminal chlorines Cl(1) and Cl(3) is 96.526(16)˚. This is due to the reduced electron density around the bridging chlorines resulting in a decrease in electronegativity of the ligand and therefore a decreased repulsion between the ligands.

6.3.2. Reaction of $TiCl_4$ with trimethylsilylacetate to give [11]

Trimethyl silylacetate (TSA) (Sigma Aldrich, 97%) was added to a solution of $TiCl_4$ in hexane under an atmosphere of nitrogen and stirred for two hours. The resulting off-white powder was washed with hexane and dried under vacuum and a ^{1}H NMR spectrum of **11** was obtained. Attempts were made to grow crystals by layering saturated solutions of **11** in $CHCl_2$ and toluene with hexane, as well as storing saturated solutions of **11** in $CHCl_2$ and toluene in a freezer for one month however in all cases, a white, powdery, non-crystalline precipitate was observed. The NMR spectrum of **11** (Figure 100) shows a range of products with the signal at 0.2 ppm in the starting material shifting from 0.2 to 0.5 ppm, and the emergence of a range of new peaks at 0.55, 2.25, 2.40, 2.48, 2.51, 2.57 and 2.68 ppm. The integrals of these peaks do not align, suggesting that a range of products are present. The large peak at 0.5 ppm, is likely to be that

of trimethylsilylchloride, the trimethylsilyl (TMS) group having undergone ligand exchange with the $TiCl_4$. TSA is a well used acylating agent and has been shown in the literature to readily form trimethylsilyl chloride.[259] The peaks in the 2.2 – 2.7 ppm range suggest a number of ethyl species could have been formed, perhaps coordinating to the titanium centre in different numbers or forming clusters, such as the one shown in Figure 102 (*vide infra*). This explains the difficulty in isolating a crystalline product. It also suggests that this species would be inappropriate for use as a TiO_2 / SiO_2 thin film precursor.

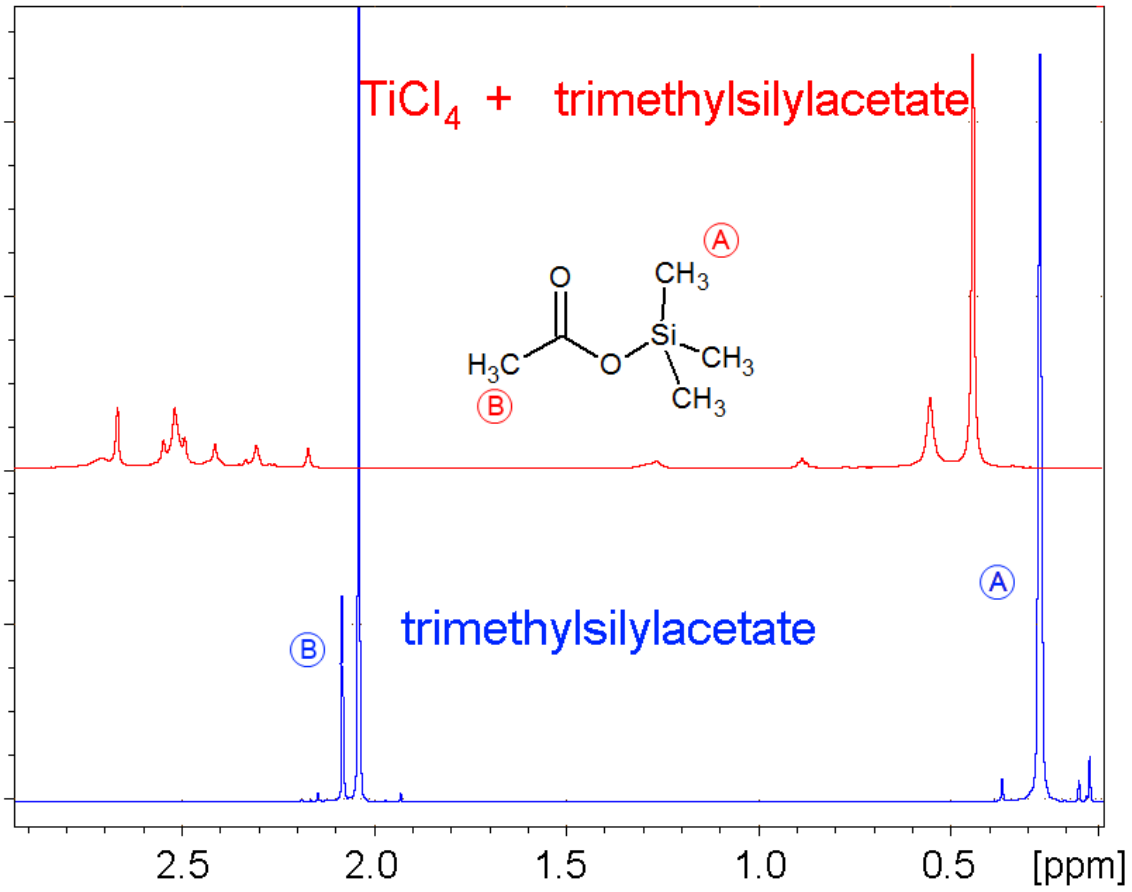

Figure 100: ^{1}H NMR spectra of trimethylsilylacetate and the product of its reaction with $TiCl_4$ **[11]**, showing a series of new peaks suggesting that multiple products form.

6.3.3. Reaction of $TiCl_4$ with silicon tetraacetate to give $[Ti_3O_2Cl_3(O_2CCH_3)_5]$ [12]

Silicon tetraacetate (STA) (Sigma Aldrich, 96%) was added to a solution of $TiCl_4$ in hexane and stirring for two hours under nitrogen, leading to the precipitation of a pale yellow product

$[Ti_3O_2Cl_3(O_2CCH_3)_5$ **[12]**. Crystals were obtained by layering a 5 ml saturated solution of **12** in anhydrous toluene with 10 ml of anhydrous hexane. Over a period of one week, pale yellow crystals formed.

As with the previous experiment, the NMR strongly suggests displacement of the acetate groups on the silicon by the $TiCl_4$ (Figure 101). The NMR of the starting material shows a single major peak at 2.15 ppm with satellites suggesting that the silicon tetraacetate is prone to loss of the acetate groups in solution, as well as suggesting strong presence of impurities. The product shows a slight shift in the acetate CH_3 peak to 2.3 ppm, as well as a broadening that could hide the formulation of multiple species. The new peak at 0.1 ppm is very likely to be from vacuum grease as there are no methyl silyl species present in the starting material and the formation of a methyl silane species in solution is highly unlikely.

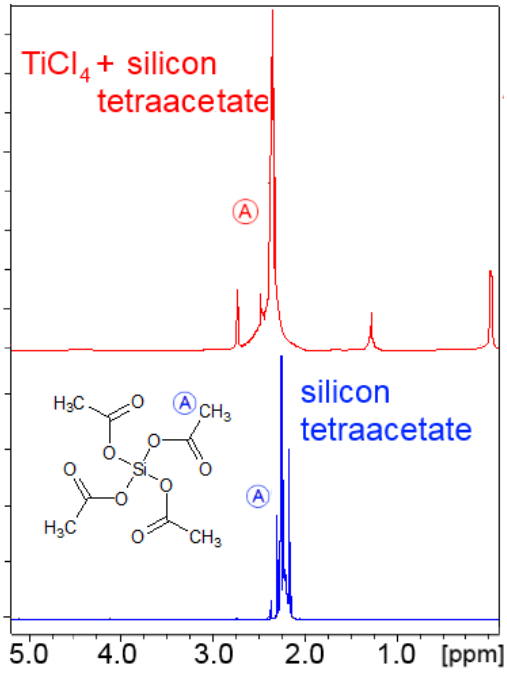

Figure 101: ^{1}H NMR spectra of trimethylsilylacetate and the product of its reaction with $TiCl_4$ **[12]**, showing a series of new peaks suggesting that multiple products form.

Unlike **11**, crystals of **12** could be grown *via* solvent layering, suggesting that although the reaction does not follow a simple coordination pathway as per **10**, a product formed in great

enough abundance to nucleate as crystals. These crystals were surprisingly facile to produce, meaning it is likely that **12** favours ordered crystalline growth. Analysis of the crystal revealed that rather than the silicon tetraacetate coordinating to the titanium chloride, the titanium displaces the silicon, coordinating to the acetate ligand. This leads to the formation of a trimeric cluster with two central oxygen atoms, one bridging all three titanium centres, the other bridging only two (Figure 102). The bonds between the titanium and the central oxygen atoms are all in the region of 1.87 Å, similar to other Ti-O bond lengths calculated for TiO_x cluster molecules. [260,261]

One titanium atom is coordinated to four acetate groups, with the remaining two coordinated to three, each titanium centre retaining one chlorine atom. The two oxygen atoms in the carboxylate groups of the acetate ligands coordinate to different metal centres. This leads to the formation of highly distorted, six membered rings featuring the two titanium centres linked by the central oxygen atom and the carboxylate group of the acetate.

The Ti-O-C bond angles are all between 132° and 138°, rather than 120° as is conventional for a six membered ring, in order to accommodate coordination to both metal centres. This relates to the highly differing bond lengths, Ti(1)-O(3) is 1.9697(11) Å, fitting with a dative Ti-O bond compared with the considerably shorter C(1)=O(3) bond in the acetate ligand at 1.2806(19) Å.

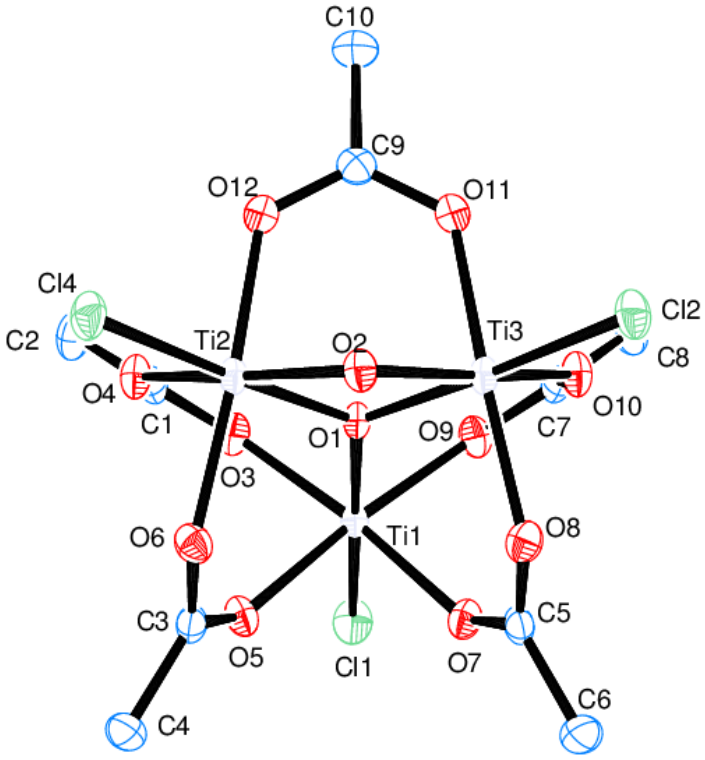

Figure 102: ORTEP representation of crystal structure of **12** with thermal ellipsoids at the 50% probability level. Hydrogen omitted for clarity.

Table 17: Crystallographic Data and Selected bond lengths angles for the crystal structure of 1a the product of reaction $TiCl_4$ and silicon tetraacetate [**12**]

Structural Data	
crystal system	monoclinic
space group	P21/c
a	8.4469(3)
b	13.6092(4)
c	12.4255(4)
α	90.00(5)
β	98.424(3)
γ	90.00(5)
R_1	2.70
wR_2	7.40

Selected Bond Angles /˚	
O(1)-Ti(1)-Cl(1)	175.03(4)
O(1)-Ti(1)-O(3)	87.04(5)
O(1)-Ti(1)-O(7)	90.44(5)
O(1)-Ti(1)-O(9)	86.97(5)
O(3)-Ti(1)-Cl(1)	89.84(4)
O(3)-Ti(1)-O(5)	87.72(5)
O(3)-Ti(1)-O(7)	171.57(5)
O(5)-Ti(1)-Cl(1)	92.90(4)
O(7)-Ti(1)-Cl(1)	93.19(4)
O(9)-Ti(1)-Cl(1)	89.69(4)
O(9)-Ti(1)-O(3)	98.96(5)
O(9)-Ti(1)-O(5)	172.85(5)
O(9)-Ti(1)-O(7)	88.93(5)
O(7)-C(5)-O(8)	123.06(14)
Ti(1)-O(1)-Ti(2)	130.53(5)
Ti(1)-O(1)-Ti(3)	130.92(5)

Selected Bond Lengths /Å	
Ti(1)-Cl(1)	2.2820(5)
Ti(1)-O(1)	1.8733(11)
Ti(1)-O(3)	1.9697(11)
Ti(1)-O(5)	1.9929(11)
Ti(1)-O(7)	1.9889(11)
Ti(1)-O(9)	1.9603(11)
Ti(2)-O(1)	1.9868(10)
Ti(3)-O(1)	1.9885(10)

The reason for the formation of **12**, as well as the likely failure of the other reactions to produce an acceptable precursor is the propensity of $TiCl_4$ to simply displace the silicon species, rather than coordinating directly to the acetate species carbonyl group. The reaction likely begins with a ligand exchange step, the titanium coordinating to the acetate, which in turn leads to the displacement of Cl^- from the metal centre as unlike the coordination to $TiCl_4$ seen in previous structures, the oxygen atom would be negatively charged. This chlorine would be attracted to the newly positive silyl acetate species.

The methyl trimethylsilylacetate ligand used to form **10** features a trimethylsilyl (TMS) group bound to carbon, not oxygen. The carbon oxygen bond of the methyl trimethyl silyl acetate is more stable than the silicon oxygen of bond in the trimethylsilylacetate.[262] Furthermore there is a far greater bond polarity between the carbon-oxygen bond ($\chi_C = 3.4$ vs $\chi_{Si} = 1.9$)[263] than the carbon - silicon bond ($\chi_C = 2.5$ vs $\chi_{Si} = 1.9$)[264]. The greater electronegativity of the oxygen facilitates the coordination of the titanium leading to the ligand exchange.

6.3.4. Reaction of $TiCl_4$ with bis-trimethylsilylmalonate to give [13]

Bistrimethylsilyl malonate (BTMSM) was added to a solution of $TiCl_4$ in hexane under an atmosphere of nitrogen and stirred for two hours. The resulting orange product was washed with hexane and dried under vacuum. This material was found to be highly unstable and sensitive to atmospheric oxygen and water, breaking down to a white, insoluble powder (presumable TiO_2) over time even when stored under nitrogen and almost instantaneously if the flask was opened. This made obtaining an NMR spectrum impossible as the white precipitate would crash out of the $CDCl_3$ as soon as the solution was made up. Attempts were made to grow crystals by layering saturated solutions of **13** in $CHCl_2$ and toluene with hexane, as well as well as storing saturated solutions of **13** in $CHCl_2$ and toluene in a freezer for one month however in all cases, a white, powdery, non crystalline precipitate was observed.

6.3.5. Characterisation Thin Films

A range of thin films were deposited from the single source precursor $[Ti\{SiMe_3CH_2CO_2Me\}Cl_3(\mu\text{-}Cl)]_2$ [**10**] in toluene at temperatures 450, 500 and 550 °C. The films were observed to display increasing opacity as deposition temperature increased, with those deposited at 450 °C being fully transparent, at 500 °C also transparent but with a slight fogginess in places and at 550 °C having a cloudy, almost opaque appearance. The film deposited from $TiCl_4$ was largely transparent but somewhat hazy, with fogginess around the edges of the substrate. All four films were left undamaged by the "Scotch Tape" test.

The morphology of the films was found to vary considerably with deposition temperature (Figure 103). The most notable of the films were those deposited at 500 °C. These films consisted of a base of cubic grains of approximately 100 nm in diameter as is commonly seen in the deposition of TiO_2 films.[265] However on top of this film additional growth in the form of snowflake-like fractal structures was observed. These growths also consisted of more homogenised, less defined grains that were more reflecting than those upon which they were grown. The micro-fractals ranged in size from 5-50 µm and appear to grow outward from a central point, from which nucleation occurs. This two tiered morphology would result in an increased surface area compared to that of a simple nanostructured thin film (Figure 103).

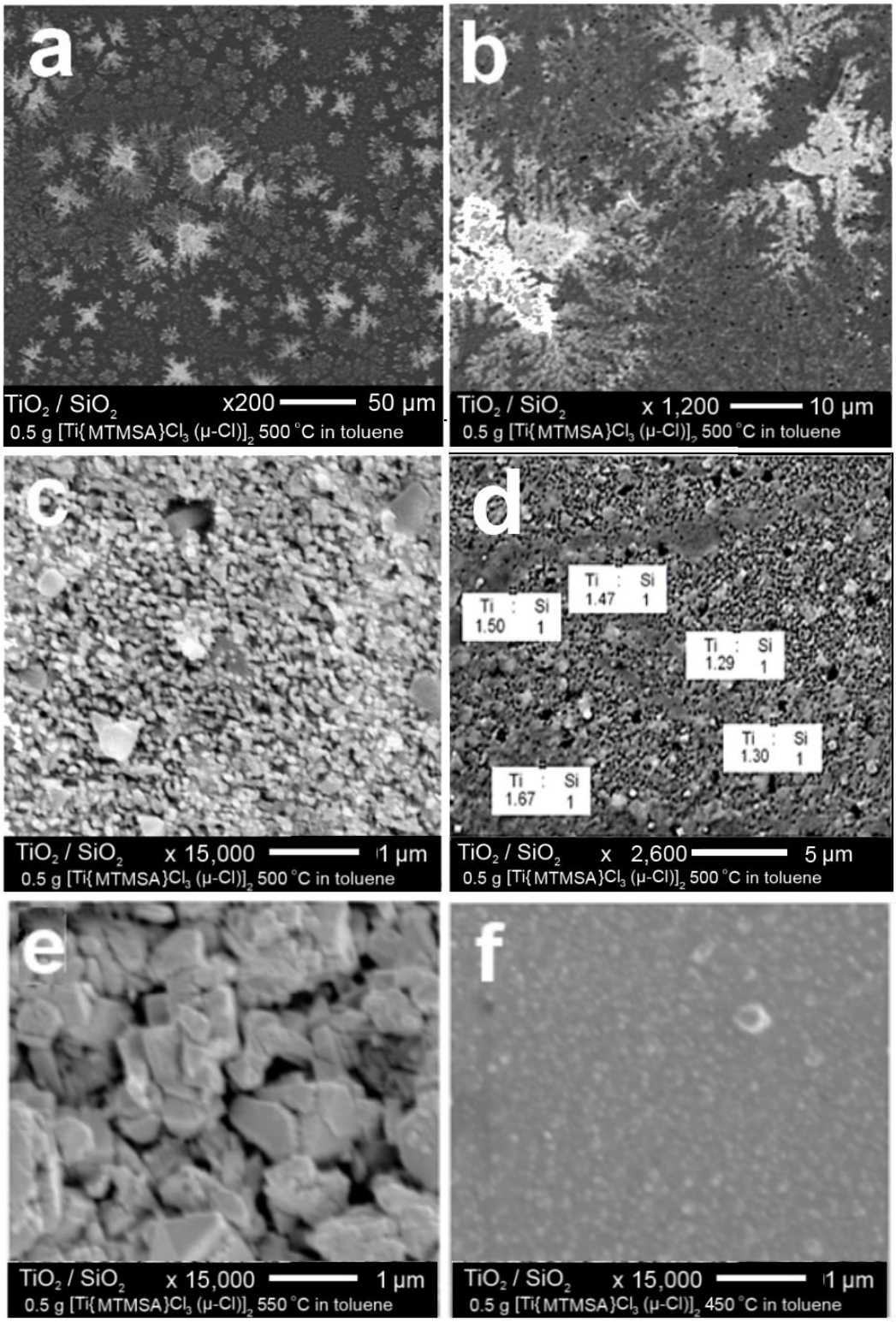

Figure 103: SEM images of the microstructure of film deposited from [Ti{$SiMe_3CH_2CO_2Me$}Cl_3(μ-Cl)]$_2$ (**10**) at 500 ˚C at magnifications of x200 (a), 1,200 (b), x15,000 (c) and 2,600 x (d) with addition of ratios of titanium to silicon at different points in the film, as measured by EDX spectroscopy. x15,000 magnified images of films deposited at 550˚C and 450˚C (e) + (f) respectively.

Films deposited at 450 °C were by comparison extremely flat and featureless, with protruding spherical grains of diameter 200 – 500 nm appearing sporadically across the surface. Depositions at 550 °C have a more textured morphology consisting of plate-like crystals of lengths between 0.5 and 1 μm. Only films deposited at 500 °C showed any sort of fractal growth, the others appearing homogenous across the surface. EDX spectroscopy carried out on the film deposited at 500 °C showed that the brighter fractal areas (Figure 103) at the top left and bottom left contain more titanium that other parts of the film with Ti: Si ratios of 1.67:1 and 1.50:1 compared with around 1.3:1 for the other parts of the film. This suggests that although the surface of the film consisted of a mixture of SiO_2 and TiO_2 particles, the area of fractal growth on top of the films base surface morphology are more titanium rich, potentially pure TiO_2.

Side-on SEM images show that film thickness increases with temperature, with the depositions at 450 °C giving a film of approximately 600 nm thickness and deposition at 500 °C leading to films of around 1 µm. The depositions at 550 °C showed the thickest and also most varied film thickness, varying from approximately 1 - 3 µm across the substrate.

Depth Profile XPS of the thin films showed that the vast majority of the silicon was situated at the surface, with films across the temperature range showing between 15-18 at.% silicon at surface level (Figure 106). The opposite was true of titanium, with initial concentrations of around 20 at.% more than doubling in all three films below surface level to 40 at.%, 48 at.%, 52 at.% for films deposited at 450, 500 and 550 °C respectively (Figure 104). This is in keeping with the EDX data, where the ratio of Ti:Si at the surface of the film was around 1.5:1, as EDX is a more penetrative technique than XPS, which would result in it picking up on some of the higher concentrations of titanium in the bulk. The bulk ratio of TiO_2:SiO_2 in films deposited at 500 °C is far lower than other films, at 12:1, compared with 21:1 (450 °C) and 24:1 (550 °C). The ratio

of TiO_2: SiO_2 at the surface of the films was highest in the 550 °C deposited film, at 1.68:1, whereas with the two lower temperature deposited films this ratio was 1:19 and 0.96 for 500 °C and 450 °C respectively.

XPS shows that the percentage of silicon making up the bulk of the film was considerably lower than at the surface, with titanium being 12-24 times more abundant. This composition is more consistent silicon doped TiO_2,[266,267] suggesting that the bulk phase of the film is largely Si doped TiO_2 with a composite of TiO_2 and pure phase SiO_2 at surface level.

The XRD patterns of all three films are shown in Figure 104. All were dominated by the peak pattern of anatase TiO_2, the phase commonly formed at this temperature range. XRD analysis of the films showed that the depositions using **10** at 500 and 550 °C lead to the formation of a mixed system of anatase and brookite TiO_2 polymorphs. Of the three common structures of TiO_2, brookite is the least studied due to its lower refractive index of approximately 2.5 and reddish brown colour being less desirable for use in pigments.[268]

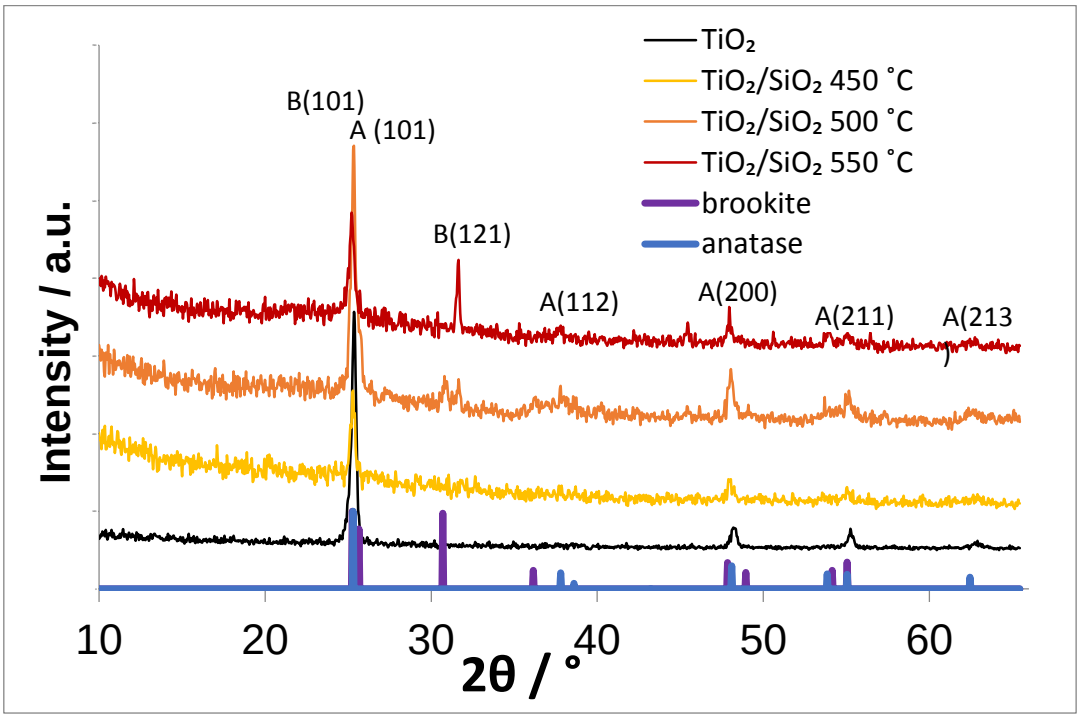

Figure 104: XRD patterns of films deposited from AACVD of $[Ti\{SiMe_3CH_2CO_2Me\}Cl_3(\mu\text{-}Cl)]_2$ (**10**) at various temperatures compared with that of anatase TiO_2 (bottom).

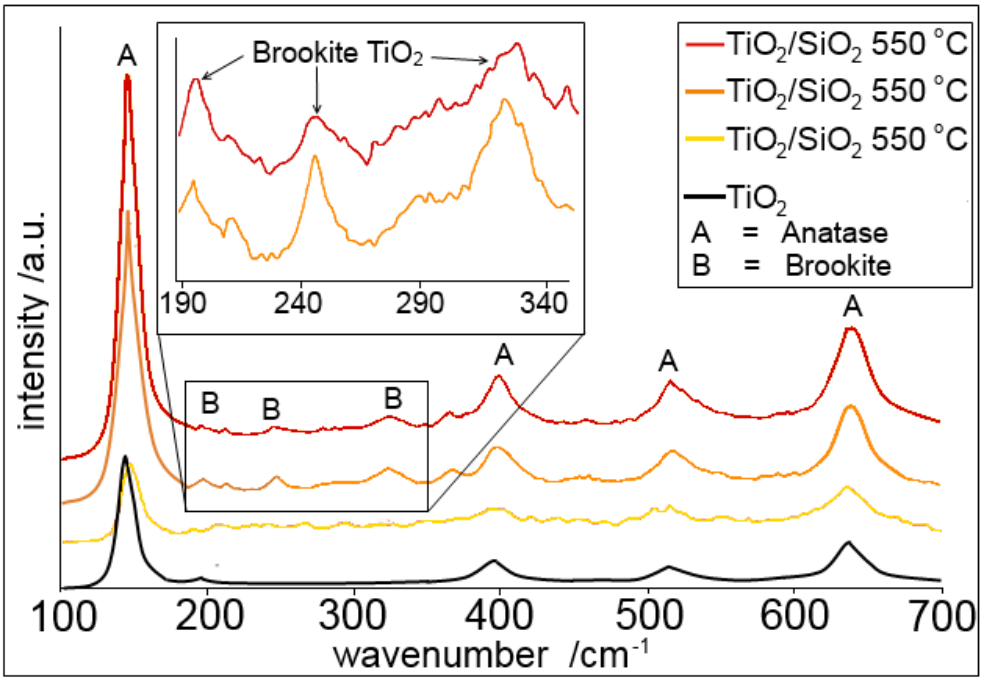

Figure. 105: Raman Spectra of films deposited from AACVD of $[Ti\{SiMe_3CH_2CO_2Me\}Cl_3(\mu\text{-}Cl)]_2$ (**10**) at various temperatures compared with that of anatase TiO_2 (bottom)

Despite this it does possess a narrower band gap than anatase (2.9 eV), and therefore its inclusion could be beneficial to photocatalytic applications. This is confirmed by Raman spectroscopy, once again showing that whilst the main TiO_2 polymorph deposited was anatase TiO_2, brookite signals were visible in films deposited from **10** at 500 and 550 °C (Figure 105). The film deposited at 450 °C gave a weak Raman spectrum with high background noise.

This is most probably due to the relatively low surface concentration of TiO_2. Transmission and reflectance UV/Vis spectroscopy was carried out on all of the films (Figure 108). The data was then used to determine the absorption coefficient in order to construct Tauc plots[269] and in turn approximate the band gap of the films. The absorbance characteristics of the TiO_2-SiO_2 films are strongly affected by the deposition temperature.

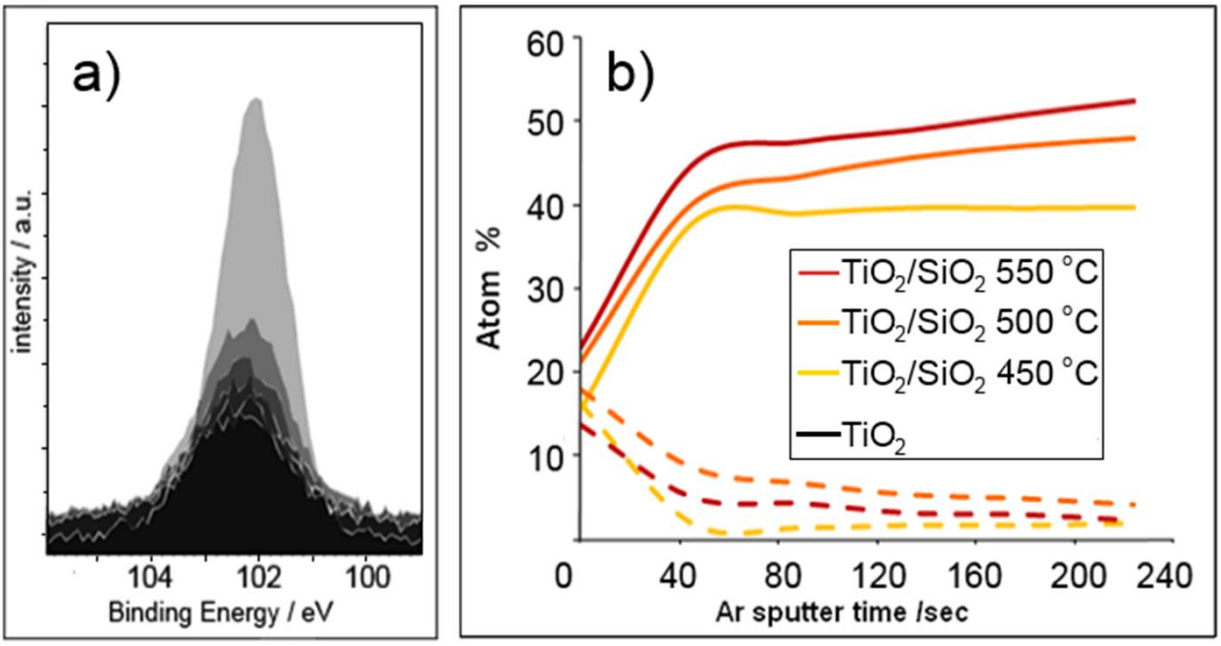

Figure. 106: Overlay of the depth profile XPS peaks for Si (2p) with darkening colour representing deeper penetration below the films surface a), Atomic percentages of titanium and silicon in the Composite films as measured using depth profile XPS b).

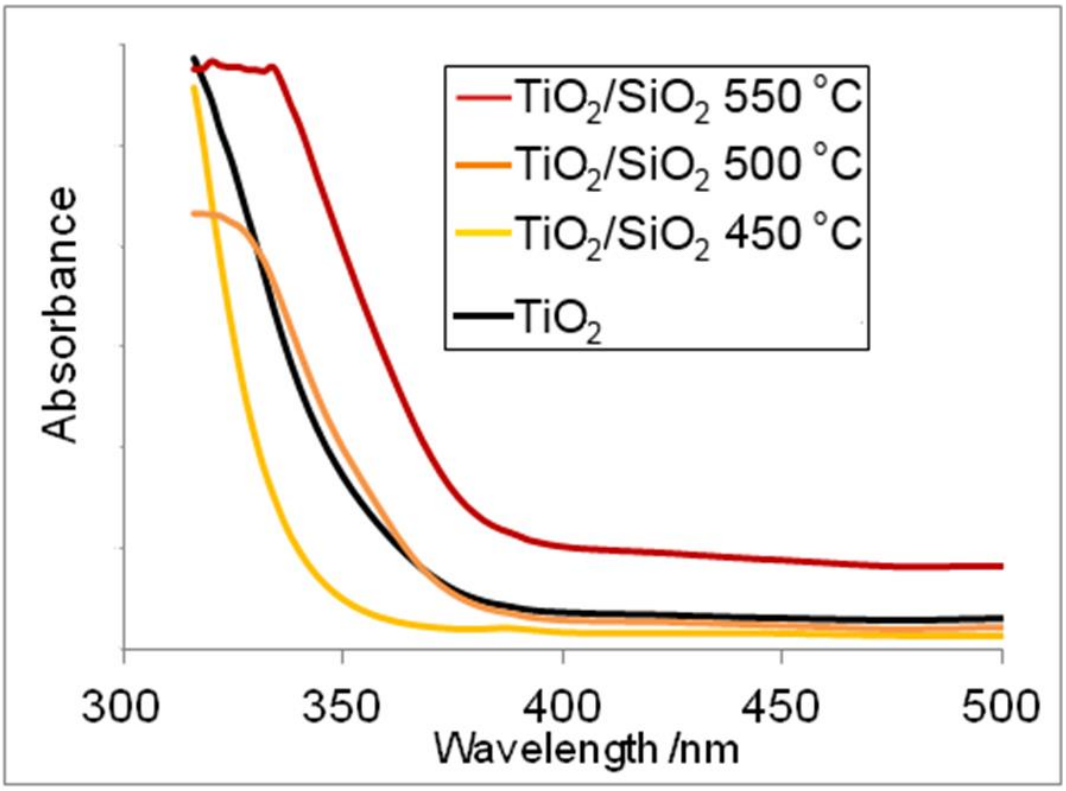

Figure 107: UV/Vis Absorption spectra of films deposited from AACVD of [Ti{$SiMe_3CH_2CO_2Me$}Cl_3(μ-Cl)]$_2$ (**10**) at various temperatures compared with That of anatase TiO_2.

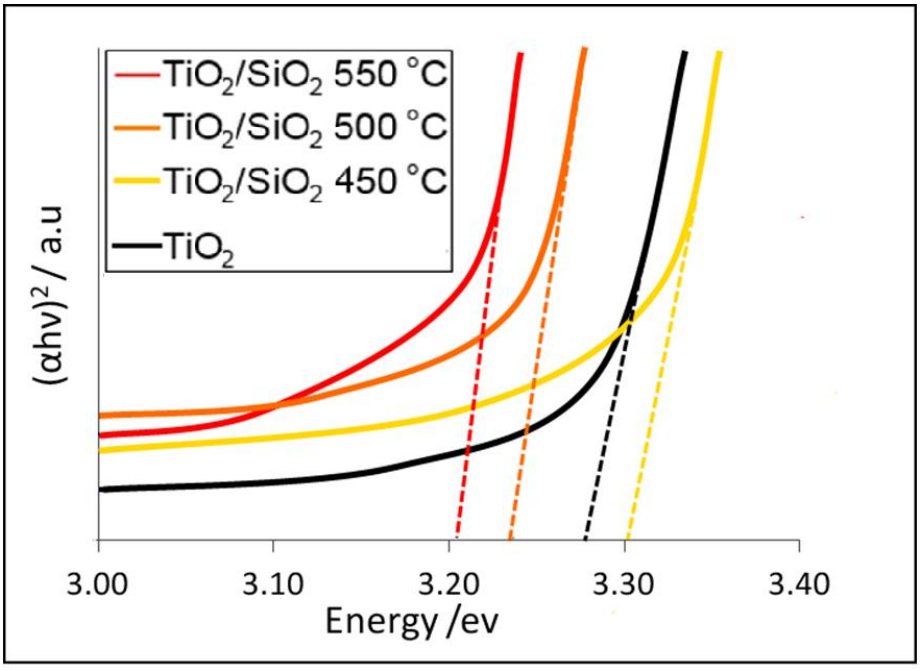

Figure. 108: Tauc plots of films deposited from AACVD of [Ti{$SiMe_3CH_2CO_2Me$}Cl_3(μ-Cl)]$_2$ (**10**) at various temperatures used to estimate the band gap of these films.

The film deposited at 550 °C saw the optical band gap reduced from 3.27 to 3.20 eV (Figure 108). This is a considerable difference in band gap, mirrored in the results of the photocatalysis testing (*vide infra),* especially as the ratio of TiO_2:SiO_2 in the bulk in the two films is similar.

Films deposited from **10** at 500 °C also appear to undergo a reduction in the band gap, although it is less pronounced than the film deposited at 550 °C, with the band gap estimated to be 3.23 eV. The deposition at 450 °C was found to increase the size of the band gap to 3.31 eV. This is in agreement with previous studies on TiO_2-SiO_2 composite thin films. [270]

The presence of SiO_2 as a separate phase is unlikely to lead to a reduction in band gap, due to SiO_2 having a substantially larger band gap at 9.3 eV.[271]

The reduction in band gap from the film deposited from $TiCl_4$ was found to correlate well with the results of the photocatalytic testing. The reduction in bandgap for films grown at 550 °C is explained by the incorporation of more silicon into the TiO_2 lattice at higher temperatures as demonstrated in the shifting of the anatase (101) peak of the XRD pattern for the film deposited

at 550 °C. The presence of silicon within the TiO_2 lattice leads to a narrowing of the optical band gap due to the introduction of strain into the TiO_2 lattice, which has previously been observed in both theoretical and experimental studies. [272]

6.3.6. Water Contact Angle Measurements

Water contact angles for the TiO_2 film and the three TiO_2-SiO_2 composites were taken by casting a 2.5 µL droplet of water onto the surface and imaging them with a high speed camera. The drop shape and contact angle were obtained using FTA3.2 software. The results are shown in Figure 109, as well as Table 18.

The contact angle for the TiO_2 film behaves as expected based on previous studies of anatase phase TiO_2 wettability,[206] initially displaying somewhat hydrophilic behaviour, which is greatly enhanced by exposure to UV irradiation, the contact angle falling from 73.9° to 11.2°. This thought to be due to the presence of surface- OH sites being deprotonated by the UV irradiation, as well as the UV catalysed breakdown of organic on the surface that would prevent contact with the TiO_2 surface.[273] This behaviour is not shared with the TiO_2 /SiO_2 films. All three films show no hydrophilicity in their non-irradiated state, with contact angles between 90 and 110°. Upon irradiation, a minor increase in the hydrophilicity of the films deposited at 500 and 550 °C was observed, the contact angles decreasing by 6.1° and 6.9° respectively. No discernible change was observed in the contact angle of the film deposited at 450 °C. This corresponds with the findings from the XPS studies, where the film deposited at 450 °C was observed to have the lowest surface concentration of TiO_2 as well as the highest SiO_2:TiO_2 ratio. Furthermore the SEM images of the films shows that the films deposited at higher temperatures have a protruding microstructure giving increased surface roughness, whereas the film deposited at 450 °C has a flat, featureless microstructure that is not conducive to wetting.[14,274] the lack of UV induced hydrophilicy is supported by the XPS data which shows a

considerable amount of SiO_2 at the surface of the films, which is considerably reduced just below. This would greatly reduce the presence of these acid sites to which the water is able to weakly adhere to

Table 18: Contact angles of before and after UV irradiation

Film	Contact angle before irradiation (°)	Contact angle after irradiation (°)
TiO_2	72.1 ± 1.5	10.4 ±1.4
TiO_2 /SiO_2 450 °C	109.1 ± 1.2	109.9 ± 2.4
TiO_2 /SiO_2 500 °C	94.8 ± 1.0	87.4 ± 1.6
TiO_2 /SiO_2 550 °C	102.0 ± 0.7	96.1 ± 0.4

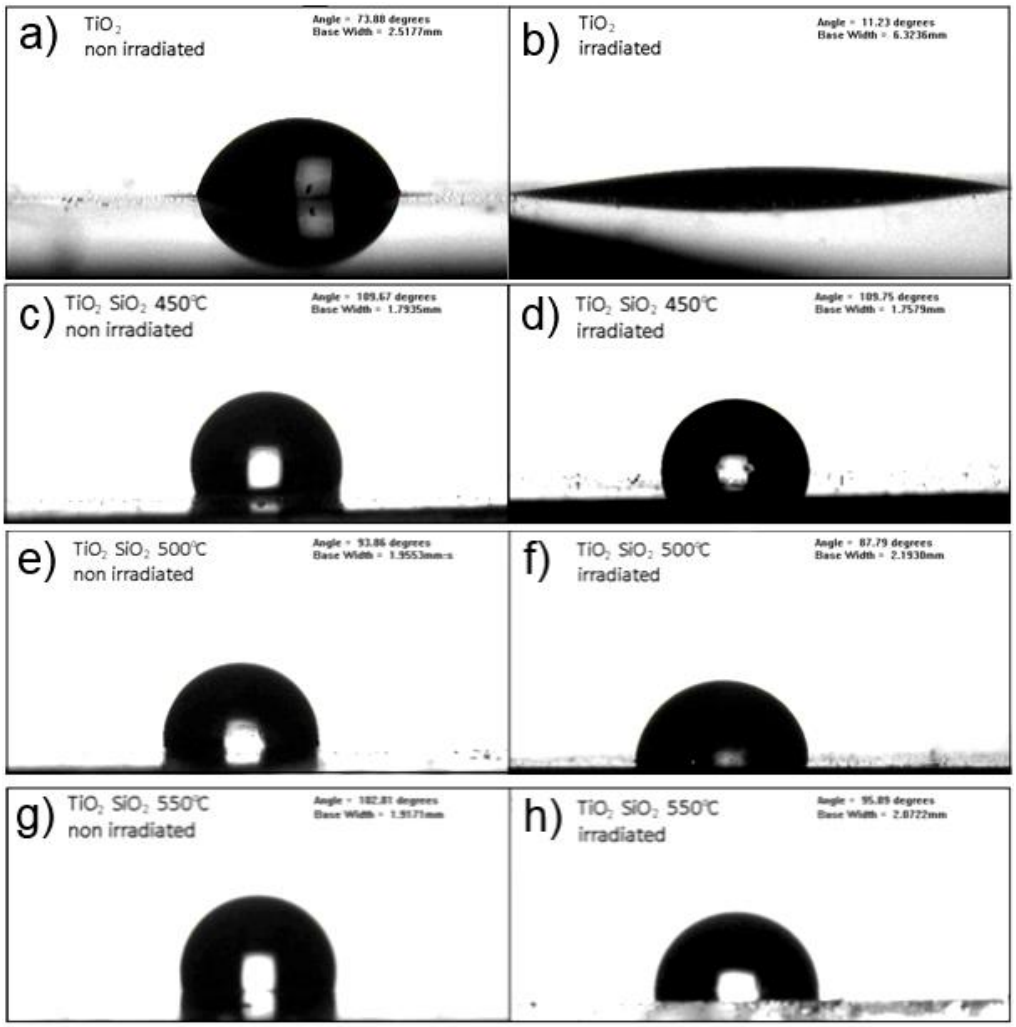

Figure 109: Comparison of the behaviour of water droplets on thin films of TiO_2 and the TiO_2-SiO_2 composite deposited at 450 °C, 500 °C and 550 °C before UV irradiation (a, c, e and g respectively) and after UV irradiation. (b, d, f, h respectively).

6.3.7. Photocatalytic Testing

Photocatalytic degradation of a coat of stearic acid applied to the films under λ = 365 nm UV irradiation was carried out on the films over the course of three hours (Figure 110). It was observed that of the three depositions, two yielded films that displayed a greater propensity to break down the organic material than the TiO_2 deposited in an equivalent manner, *via* AACVD of $TiCl_4$. The formal quantum efficiency (FQE) of TiO_2 deposited from $TiCl_4$ was 9.04 $x10^{-5}$ which is slightly lower than values found in the literature for undoped TiO_2[238] and can be explained by the patchier nature of the films. Figure 110 shows that the TiO_2-SiO_2 films deposited from **10** improved as photocatalysts with deposition temperature. At 450 °C the film deposited gave an FQE of 4.4532 $x10^{-5}$, roughly half that of the plain TiO_2. Films deposited at 500 °C give an FQE of 1.6764$x10^{-4}$ 81% superior to that of TiO_2 from $TiCl_4$.

Film	FQE (molecules photon^{-1})	error (molecules photon^{-1})
450 °C	4.4532E-5	4.85783E-6
500 °C	1.6764E-4	1.32888E-5
550 °C	3.06624E-4	2.78684E-5
TiO_2	9.04305E-5	7.3104E-6

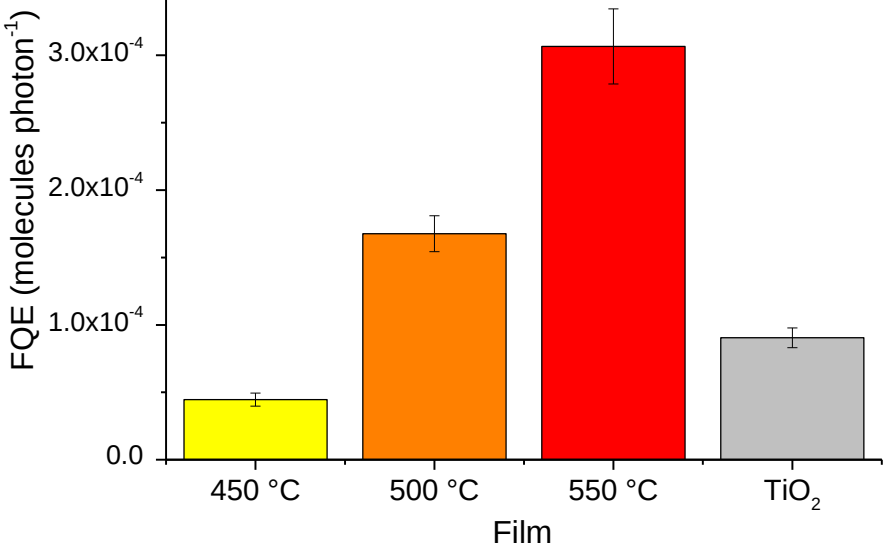

Figure 110: Bar graph showing the Formal Quantum Efficiency (FQE) of films deposited from AACVD of [Ti{$SiMe_3CH_2CO_2Me$}Cl_3(μ-Cl)] (1) at various temperatures compared with That of anatase TiO_2 and plain glass, as measured by the UV catalysed decomposition of the stearic acid on the films surface.

The optically opaque films deposited at 550 °C performed best with an FQE of 3.0662×10^{-4}, an improvement of over 250% above the film deposited from $TiCl_4$ with air. UV/Vis analysis suggests that in the case of the 500 °C deposited film the improved photocatalytic activity was not the result of tuning the optical properties of the film, as the band gap was effectively the same as the undoped TiO_2. It is more likely that the improved performance is in fact the result of the surface area of the film being greater due to the small grain size and the fractal structures growing on top providing a greater capacity for catalysis.

Depositing at 550 °C saw a narrowing of the band gap to 2.93 eV, compared with the 3.15 eV observed for pure TiO_2. This is reflected in its improved catalytic activity. Reducing the difference in energy between the highest occupied state and lowest unoccupied state means that more electrons are capable of overcoming the energy barrier to excitation, resulting in the formation of a greater number of positive holes in the valence band migrating to the film surface. This in turn leads to an increase in the rate at which surface organics are decomposed. The lowering of the band gap is likely a combination of the incorporation of the silicon which distorts the matrix to lower the band gap, and the presence of small amounts of brookite in the film. This is further corroborated by the shifting of the anatase peaks observed into the XRD of the film deposited at 550 °C, not seen in any of the other films.

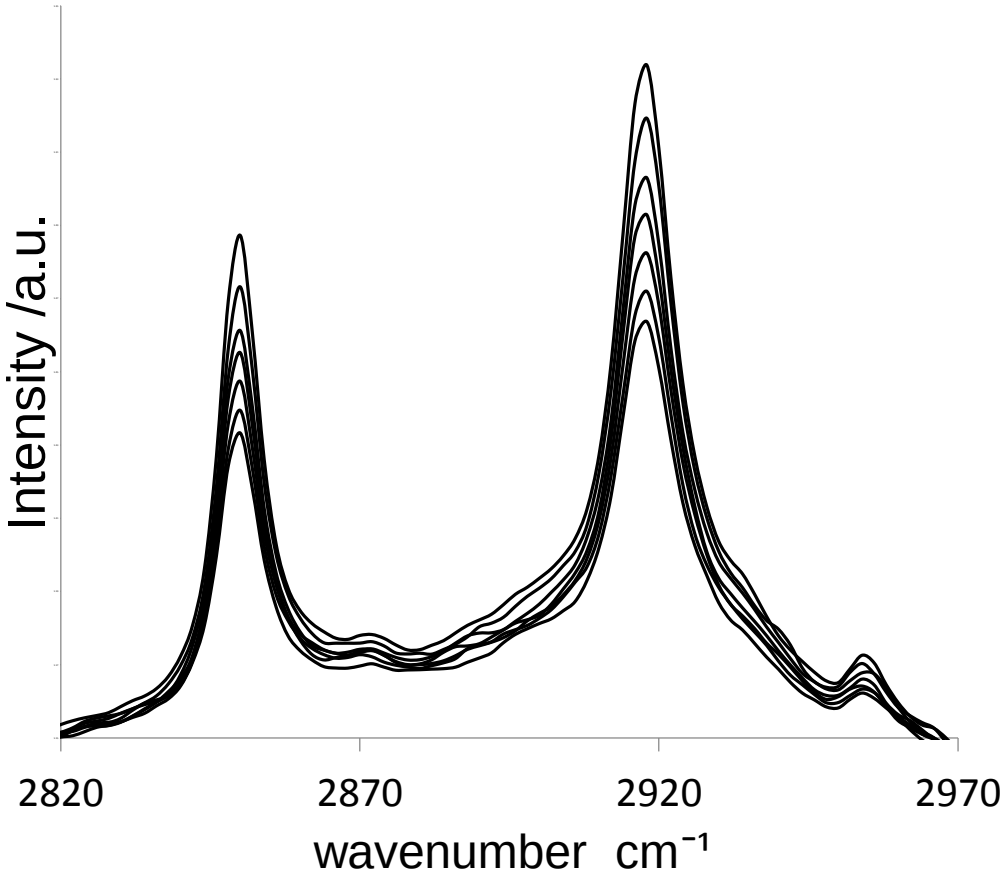

Figure 111: Overlay of the FT-IR spectra of the stearic acid on the surface of the 500 ˚C film over a two hour period of UV irradiation with spectra taken every 20 minutes

6.4. Conclusion

A novel precursor for the deposition of TiO_2 / SiO_2 composite films has been synthesised by reacting $TiCl_4$ with methyl trimethylsilyl acetate to give a chloro-bridged dimeric species $[Ti\{SiMe_3CH_2CO_2Me\}Cl_3(\mu\text{-}Cl)]_2$ **[10]** . The structure of the precursor was confirmed using single crystal X-ray crystallography. Using the aerosol assisted chemical vapour deposition technique, films were successfully deposited at 450, 500 and 550 °C from a solution of **10** using nitrogen as a carrier gas and a flow of air entering the reactor in order to oxidise the precursor.

The resulting films were found to have ratios of TiO_2: SiO_2 of between 2:1 and 1:1 at the surface and 12:1 and 24:1 in the bulk. In films deposited at higher temperatures the films were found

to contain both Anatase and Brookite phases of TiO_2. SEM revealed a novel morphology of 'microfractals' of material nucleating out from central points across the films surface, leading to improved surface area.

Studying the UV catalysed decomposition of stearic acid on the films surface; it was revealed that films deposited at 500 °C and 550 °C showed formal quantum efficiencies 73% and 150% higher than TiO_2 films deposited *via* the same method using $TiCl_4$ as a precursor. This work shows that SiO_2 has potential as an additive for improving photocatalytic efficiency of TiO_2 thin films.

Chapter 7

Derivatives of $VOCl_3$ and Their Uses in Materials Synthesis

7. Introduction

7.1.1. VO_2 Thin Films

Monoclinic vanadium dioxide thin films and nanoparticles for energy saving, infrared radiation reflecting windows has come under considerable attention in the literature, due to its considerable potential to help curtail energy intensive means of heating and cooling homes, thereby reducing pressure on the world's non-renewable energy resources.[275–278] By developing windows that can promote and prevent heat loss at different temperatures the need to use such resources can be lessened, reducing both household bills and global energy usage.

The monoclinic phase of vanadium(IV) oxide (VO_2 (M)) undergoes a structural transition to the rutile vanadium(IV) oxide (VO_2 (R)) at 68˚C. The temperature at which this change occurs is known as the metal to semiconductor transition temperature (MST). This phenomenon, in which the permittivity of electromagnetic radiation is dependent on temperature, is known as thermochromism.[203,279] VO_2 (M) is of particular interest as its MST is relatively close to room temperature, unlike other thermochromic V_xO_y species, such as V $2O_3$.[280] Below the MST, VO_2 (M) is a semiconductor that transmits infrared and ultraviolet radiation consistently, whereas above the MST, VO_2 (R) exhibits metallic conduction, reflecting in the same region.[281] This property is crucial in the design of smart window coatings, that are transmissive of sunlight at low temperatures, but reflective at high temperatures, thus alleviating the use of expensive and energy-intensive air conditioning units in hot countries (Figure 112).[282]

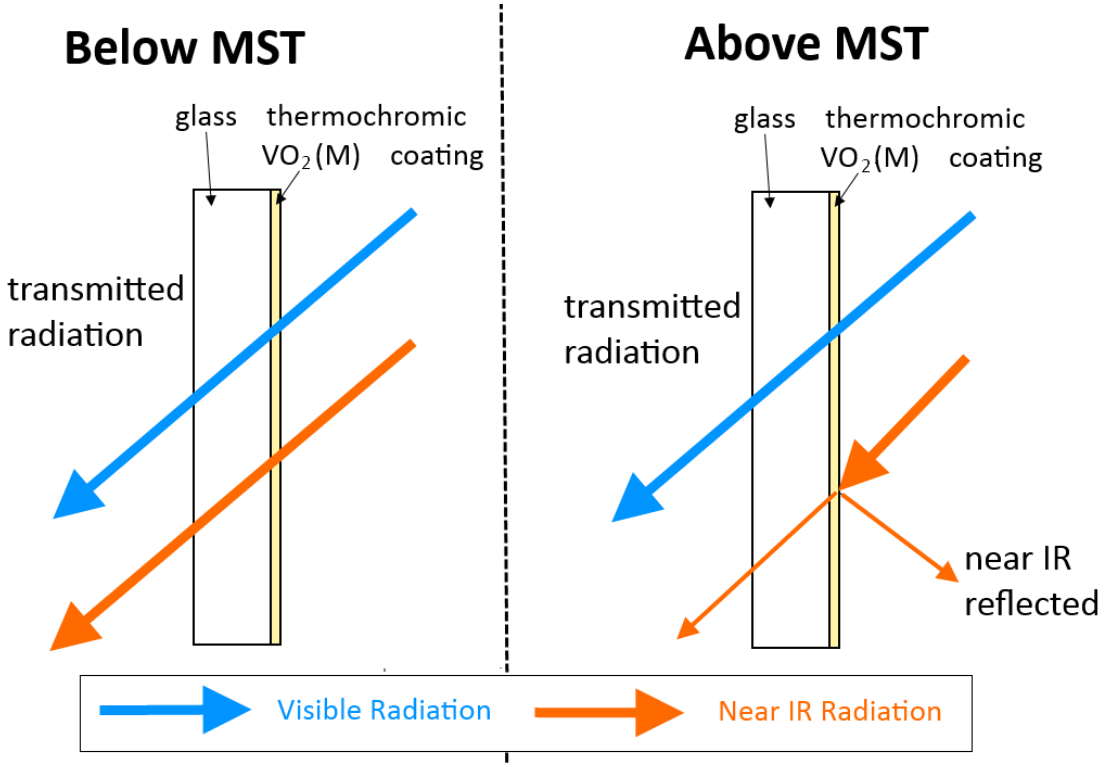

Figure 112: Diagram of the behaviour of visible and near infrared radiation upon contact with a VO_2(M) coated window, at below (left) and above (right) the MST[275]

Although close to room temperature, the MST must still be reduced in order to make the application applicable to everyday life. The most common means of achieving this reduction is the incorporation of dopant atoms into the VO_2 matrix. Tungsten is by far the most widespread and effective dopant in lowering the MST. Furthermore, incorporation of tungsten lends the windows a blue green tint as a result of a narrowing of the optical band gap due to lattice strain, altering the absorption of energy in d-d transitions that give the material its colour. This masks the less aesthetically acceptable brown/ yellow of VO_2 (M).[146,282–284] Other dopants such as: niobium,[285] fluorine,[286] magnesium[287] and molybdenum[288] have also been shown to reduce the MST. The incorporation of higher valence atoms with large atomic radii, such as tungsten, is thought to reduce the MST by introducing distortions into the VO_2 lattice around the dopant atom centre,[289] as well as introducing areas of greater electron density into the system.[290]

The production of thin films of VO_2 (M) is synthetically challenging due to the large number of stable oxide polymorphs of vanadium that can form under CVD conditons.[280] This has led to a wide variety of methods for the synthesis of VO_2 (M) thin films and nanoparticles.[291–293] Thin films of VO_2 have been very well studied, with highly effective thermochromic VO_2 (M) and doped VO_2 (M) films deposited on a variety of substrates.[129,291,294] The scarcity of low molecular weight, volatile precursors containing vanadium(IV), suitable for APCVD has led to the use of air-sensitive VCl_4 [295,296] and stable $[VO(acac)_2]$[297] precursors. $VOCl_3$ is also a well used VO_2 (M) thin film precursor in APCVD, even though the vanadium present is in the +5 oxidation state.[295,298]

Thin films of VO_2 (M) have also been deposited *via* aerosol assisted chemical vapour deposition (AACVD) methods.[220,299,300] The advantage of AACVD is that a wider range of precursors can be employed, giving a greater scope to tailor the vanadium precursor, potentially leading to the formation of more effective thin films.[144]

Synthetic methods for nanoparticles formation vary greatly.[292,293,301] Vanadium oxide nanoparticles have been synthesised using a variety of methods, including pyrolysis,[302] sol-gel,[303] hydrothermal methods[304] and ball milling[305] for use in coatings. Hydrothermal (and sol-gel methods) have been shown to produce highly crystalline VO_2 (M) nanostructures, from vanadium precursors in the presence of reducing agents.[301,191,306] Manipulating the environment inside the high temperature synthesis vessel by tailoring the amount of oxygen present preventing the over/under oxidation of vanadium(IV) species is crucial in nanoparticle synthesis, a technique that is employed here as well, in the AACVD of the VO_2 thin films. [307–309]

The majority of VO_2 (M) synthesis focuses on a vanadium precursor that is reacted with an oxygen-containing species *in situ*. This work however, shows the fabrication of doped and

undoped VO_2 (M) thin films using AACVD, and surfactant controlled anisotropic vanadium oxide nanomaterials from the previously synthesised single source precursor dichloro(oxo) Vanadium(V) diethyl malonate [{$VOCl_2(CH_2(COOEt_2)\}_4$] **(6)**. The films were doped with tungsten by adding small amounts of tungsten(VI) hexaphenoxide [$W(OPh)_6$] to the precusor solution, and a lowering of the MST was observed. Vanadium oxide nanostructures were synthesised by the thermal decomposition of **6** in the presence of a high boiling point solvent (1-octadecene) and structure directing surfactants (oleic acid and oleylamine). The structure of **6** was determined by X-ray crystallography, elemental analysis and ^{1}H NMR spectroscopy in chapter 4. Thin films and nanostructures were characterised using X-ray diffraction (XRD), scanning electron microscopy (SEM), transmission electron microscopy (TEM), X-ray photoelectron spectroscopy (XPS) and Energy-dispersive X-ray spectroscopy (EDS). Thermochromic measurements were measured using UV-Vis spectroscopy with a variable temperature stage.

7.1.2. Synthesis of Vanadium Carbide and Vanadium Nitride

Vanadium nitride (VN) and vanadium carbide (VC) are the subject of investigation by materials scientists due to their exceptional hardness, high melting points, high thermal conductivities and solid lubricating properties.[310] The Vickers hardness of VC[311,312] has been measured at 2600 - 3200 kg mm^{-2} considerably harder than tungsten carbide[313] and similar to titanium carbide (2400 kg mm^{-2} & 1900 - 3200 kg mm^{-2} respectively)[314] as well as a measured Young's modulus comparable with that of tungsten carbide.[311,315,316] VN exhibits similar properties, with a Vickers hardness of 1500 kg mm^{-2} and a melting point (2619 K) comparable to VC (3103 K).[310,317]

VN is widely used to harden steel, with the surface of the steel treated in such a way that a thin layer of VN is present by annealing at high temperatures under a flow of nitrogen. This increases

wear resistance for use in high performance steels.[318,319] VN is also a strong coupled superconductor, with potential use in supercapacitors.[320]

VN is often synthesised by controlled direct nitridation of vanadium containing species using nitrogen or ammonia gas at varying temperatures. Using this technique, foams of VN were formed through the nitridation of vanadium oxides with ammonia gas with high control over morphology.[321] Other methods that have proved successful include microwave synthesis,[322,323] hydrothermal synthesis[324] and high temperature plasma routes.[325]

VN thin films have been synthesised using molecular precursors with pre formed V-N bonds, for instance $V(NEt_2)_5$, with a carrier gas composed of 10% NH_3 in He using AACVD[326]. VN has also been produced from a variety of molecular precursors including the direct reaction of vanadium tetrachloride with sodium amide,[327] ammonia[328] and hexamethyldisilazane[329] vanadium-urea complexes,[330] as well as chloroimidovanadium compounds and metal oxide nanoparticles with cyanamide and urea.[331]

VC has been shown to be a highly effective additive to tungsten carbide in improving the hardness and thermal conductivity of highly durable ceramic-metal "cermet" composites,[332] and an ideal material for improving the wear resistance of tools.[333] Furthermore, precipitation of vanadium carbide nanoparticles into ferrite-martensite dual phase steel has been shown to lead to a consistent improvement to Vickers hardness over a range of synthesis conditions.[334–336] It has been reported that depositing a layer of vanadium carbide onto the surface of high carbon steel *via* a salt bath improves its surface hardness by six times.[337] Similar results have been reported for VC coatings deposited onto a die steel substrate *via* high temperature reactive diffusion using NH_4Cl/ferro-vanadium/naphthalene precursor with surface hardness improved approximately fivefold.[338]

There are numerous methods for the synthesis of vanadium carbide nanoparticles. Preparations can involve vanadium(V) oxide (V_2O_5) with various carbonaceous species at high temperatures in a reducing gaseous environment.[332,339,340] Refluxing V_2O_5 powder in *n*-dodecane has been shown to produce VC nanoparticles.[341] Furthermore V_2O_5 can be decomposed with magnesium filings and acetone in an autoclave.[336,342–344] Nanostructured thin films of vanadium carbide have been deposited using the CVD of single source precursors such as vanadocene[345] and cyclopentadienyl vanadium tetracarbonyl.[346]

In this study, the products of the experiments involving $VOCl_3$ and the bidentate ligands 2,4-pentadione, diethyl malonate, and diethyl succinate (**5**, **6** and **7**) were used as precursors for vanadium nitride and carbide formation. Each of the precursors was converted to vanadium nitride and carbide *via* heating in a furnace under an inert atmosphere at 1200 °C, similar temperatures to those used in the formation of austenitic steel. [347,348] Conversion to the carbide or nitride was dependent on the carrier gas used, with argon giving a carbide and nitrogen predictably producing a nitride species. The conversion of the precursor molecules to vanadium carbide/ nitride was determined by X-ray diffraction (XRD) (carried out by Dr. Michael Powell), X-ray photoelectron spectroscopy (XPS), energy dispersive X-ray spectroscopy (EDS) and transmission electron microscopy (TEM) (carried out by Dr. Joseph Bear).

7.2. Formation of VO_2 (M) thin films and VO_x Nanoparticles Using the Single Source Precursor [{$VOCl_2(CH_2(COOEt_2)\}_4$] (6)

Solutions of [{$VOCl_2(CH_2(COOEt_2)\}_4$] **[6]** in toluene were used to deposit films across a range of temperatures, resulting in the deposition of thermochromic VO_2(M). Preliminary attempts were made to deposit in the same way with dichloro(oxo)(diethyl succinate) vanadium(IV) **[7]** and dichloro(oxo)(2,4-pentanedione) vanadium(V) **[5]**, however the films deposited by, these

precursors were found to be thinner and more uneven than those from **6.** This is likely due to the higher stability of **5** and the lower solubility of **7** in toluene.

7.2.1. Experimental

$[VOCl_2(CH_2(COOEt_2)\}]_4$ **[6]** was synthesised as described in Chapter 3. Oleic acid (techn. grade, 90%), oleylamine (techn. grade, 70%), 1-octadecene (techn. grade, 90%) (dried over sodium) and 1,2-tetradecanediol (techn. grade, 90%) were purchased from Sigma Aldrich Ltd. and used as received. Laboratory solvents were purchased from Sigma Aldrich Ltd. and were of analytical grade. The solvents were dried over activated alumina *via* the Grubbs method using anhydrous engineering equipment, ensuring that the concentration of water in the solvents was below 5 – 10 ppm.[83] Deuterated chloroform ($CDCl_3$) was obtained from GOSS Scientific and was degassed and dried over 3 Å molecular sieves.

7.2.2. Deposition of Thin Films

All films were deposited using AACVD. Compound **6** (0.30 g, 0.25 mmol) was dissolved in anhydrous toluene (20 ml) and transferred to a glass bubbler under nitrogen using a cannula. The resulting solution was atomized for 5 minutes to ensure complete solvation of the precursor. An aerosol was generated using a piezoelectric humidifier (Ultrasonic Liquids Atomizer LIQUIFOG®). The depositions were carried out using a carrier gas of 2% O_2 in N_2 at a flow rate of 3 L min^{-1}. A separate 1 L min^{-1} flow of air was introduce *via* a second inlet in the baffle, from the house line fitted with a filter. The glass substrate was standard float glass of 4

mm thickness. A top plate of the same glass was suspended 0.5 cm above the substrate to ensure a laminar flow of the precursor/solvent vapour. Depositions were carried out at 540 °C, 550 °C and 560 °C, each taking approximately 30 minutes.

7.2.3. Tungsten Doping

Tungsten doping was affected by the addition of tungsten(VI) ethoxide [$W(OEt)_6$] or tungsten(VI) hexaphenoxide [$W(OPh)_6$] into the precursor solution prior to an AACVD deposition. The amounts used in each depsotion, as well as the atomic percentage of W present in the precursor solution, are detailed in Table 19. [$W(OEt)_6$] was purchaseed from Sigma Aldrich and added unmodifed to the precursor solution. [$W(OPh)_6$] was synthesised using a literature procedure first published by Cross *et al.*[349]

7.2.4. Synthesis of Nanoparticles

Nanoparticle samples were prepared using the thermal decomposition of **6** in the presence of high boiling point solvents and alkyl surfactants. Compound **6** (0.5 g, 0.41 mmol) was weighed out into a nitrogen-purged three-necked 250 ml flask with a condensor. 1-octadecene (dried over sodium) (20 ml), oleylamine, oleic acid and 1,4-tetradecanediol were added in varying amounts as described in Table 20. The flask was put under vacuum and then back filled with nitrogen 3x to purge any residual water from the system. Following this the flask was heated to the required synthesis temperature at a heating rate of 3.3 °C min^{-1} under a flow of nitrogen. Once reached, the reaction temperature was maintained for 1 hour before allowing the mixture to cool to room temperature. The reaction remained under nitrogen until completely cooled. The nanoparticles were precipitated with ethanol (*ca.* 100 ml) and centrifuged at 3000 × g. This was repeated three times in order to ensure maximum purity before the products were stored

in a vacuum dessicator overnight to remove any residual moisture. Due to the presence of the alkyl surfactants, the nanomaterials exhibited a high level of dispersibility in organic solvents such as chloroform and *n*-hexane.

7.2.5. Annealing to produce VC + VN powders

Samples were annealed in a tube furnace under a constant argon flow of 0.6 L min^{-1} for 10 hours at 550 °C at a heating rate of 10 °C min^{-1} and allowed to cool to room temperature naturally under argon flow before analysis.

7.2.6. Results and Discussion

7.2.7. Film deposition

All films were deposited using AACVD, in which the precursor is dissolved in a suitable solvent, from which an aerosol was generated using a piezoelectric mister. The precursor-containing aerosol droplets were transported into the reaction vessel *via* a flow of carrier gas, at which point the high temperature inside the reactor causes the solvent to evaporate bringing the precursor in contact with the substrate. The precursor was then free to decompose, nucleate and grow crystals to form a thin film. In all the depositions, toluene was used as a solvent. The precursor for both the VO_2 film and the tungsten dopant were both dissolved in the same solution and transported to the reactor using a carrier gas consisting of 98% nitrogen and 2% oxygen. It was found that in order to encourage film deposition and to attain VO_2 (M), a separate oxygen source had to be introduced in the form of a separate flow of air from the house line, in order to counteract the reducing nature of an almost total azotic atmosphere.

Key depositions using solutions of **6** in toluene are denoted in Table 19. The best results were found to be at 550 ˚C using a carrier gas of 2% O_2 in N_2 at a flow rate of 3 L min^{-1}. (experiments 3 + 4). Depositing using the same conditions but with the temperature lowered to 500 ˚C yielded patchy films whilst at 600 ˚C the temperature was too high encouraging the full oxidation of the product, giving V_2VO_5thin films (experiments 1 and 7 respectively). The films deposited at 550 ˚C were of good coverage and pale yellow in colour, with some darker, metallic patches formed at higher concentrations of **6**. The optimum concentration of **6** was found to be 0.3 g in 20 ml of toluene, or a concentration of 0.533 mol dm^{-3} (experiment 4).

Following the optimising of the precursor concentration and successful formation of thermochromic VO_2 (M), depositions were carried out at 540 and 560 ˚C in order to ensure the process was fully optimised. Thermochromic testing with UV/Vis spectroscopy found neither film performed as well as the one deposited at 550 ˚C. Films deposited under these conditions, over the temperature range of 540 to 560 ˚C displayed good optical transparency as well as durability, passing the Scotch tape test. They were however fairly easy to remove by scratching with a coin. Films deposited outside this temperature range on the other hand showed poor adherence and were more powdery.

Table 19: AACVD depositions carried out using $[VOCl_2(DEM)]_4$ [6] with and without the presence of tungsten dopants.

No.	Amount of $[VOCl_2(DEM)]_4$ [6] (g)	Amount of $W(OEt)_6$ (g)	Amount of $W(OPh)_6$ (g)	V:W proportion	Flow Rate of carrier (2%O_2 in N_2) (L min^{-1})	Temp ˚C	Observations
1	0.5	0	0	0.00	2	500	Patchy + uneven mixed phase film
2	0.5	0	0	0.00	2	550	Thermochromic VO_2 covers half substrate
3	0.5	0	0	0.00	3	550	Thermochromic VO_2 full coverage
4	0.3	0	0	0.00	3	550	thermochromic VO_2 full coverage + film thinner and more transparent than 3
5	0.3	0	0	0.00	3	540	thermochromic VO_2 full coverage, less thermochromic than 4
6	0.3	0	0	0.00	3	560	thermochromic VO_2 full coverage, less thermochromic than 4
7	0.3	0	0	0.00	3	600	Full coverage of black V_2O_5
8	0.3	0.032	0	0.066	3	550	Blue film, not thermochromic
9	0.3	0.022	0	0.045	3	550	Yellow VO_2 film. thermochromism not observed
10	0.3	0.028	0	0.058	3	550	Weakly thermochromic film Tc = 60˚C
11	0.5	0	0.025	0.019	3	550	Termochromic film Tc = 60˚C
12	0.5	0	0.018	0.014	3	550	Yellow VO_2 film. thermochromism not observed
13	0.5	0	0.03	0.023	3	550	Thermochromic film Tc = 40˚C
14	0.5	0	0.05	0.038	3	550	Thermochromic film Tc = 30˚C

Tungsten was doped into the films over a range of concentrations (Table 19) by adding small amounts of tungsten(VI) ethoxide [$W(OEt)_6$] or tungsten(IV) hexaphenoxide [$W(OPh)_6$] into the precursor solution. The concentration of [$W(OEt)_6$] as a percentage of **6** present in the precursor solution ranged from 4.5 to 6.6%, whereas the concentration of [$W(OPh)_6$] in the solutions ranged from 1.8 to 5.0%. The W doped films each had greater optical transparency than the undoped films deposited at the same temperature, with colours ranging from pale yellow to azure, becoming more blue with increased concentration. All W doped films were fairly adherent, resisting the "Scotch Tape" test.[250,350] [$W(OPh)_6$] was observed to be the superior tungsten dopant precursor of the two, as the MST was found to be far less sensitive to the presence of the precursor, giving a 'larger window' with which to alter the concentration.

The thermochromic transition (MST) was observed to decrease linearly from 60 ˚C to 30 ˚C as the amount of [$W(OPh)_6$] added to the solution increased from 0.025 to 0.05 g. The use of [$W(OEt)_5$] resulted in not enough dopant present at 0.022 to having far too much at 0.032 g, which made finding the ideal amount highly challenging. This is partially due to the far greater molecular weight of [$W(OPh)_6$] than [$W(OEt)_6$] (746 g mol^{-1} and 454 g mol^{-1} respectively), meaning that the amount of actual tungsten per gram of precursor is lower allowing for more control. [$W(OPh)_6$] is also more soluble in toluene, allowing for better incorporation into the VO_2 film and therefore resulting in more even coverage as well as being a more reliable precursor with greater reproducibility.

SEM images were obtained for films of VO_2 deposited at 550˚C, both with and without the incorporation of tungsten into VO_2 film. The W-free film consisted of highly disordered rod-like particles of width approximately 50 nm and length 300 - 500m (Figure 113a).

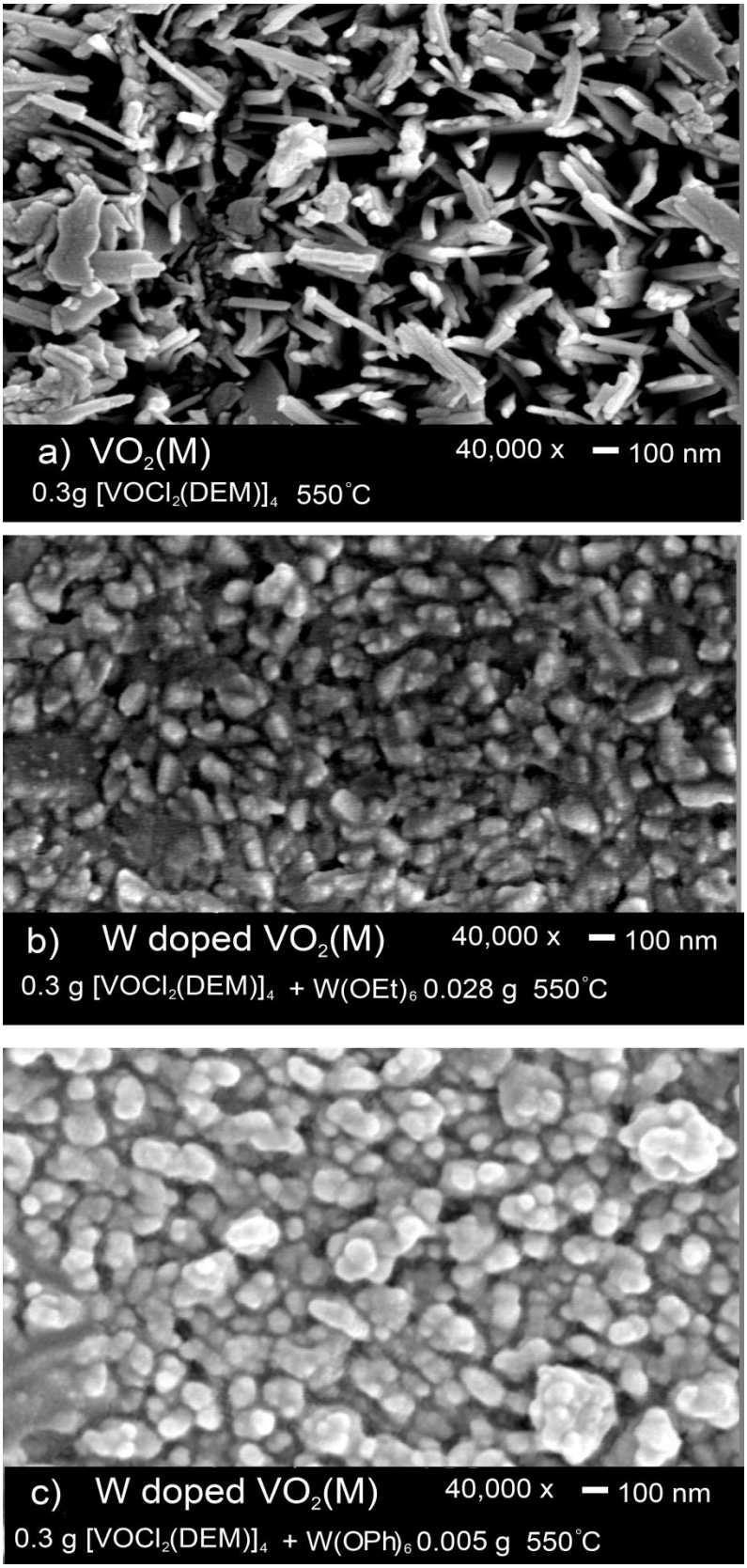

Figure 113: SEM images of the VO_2 film deposited from **[6]** in toluene at 550 °C using a 2% O_2 in N_2 carrier gas with no dopant (a), 2.8% [$W(OEt)_6$] (b) and 5.0% [$W(OPh)_6$] (c).

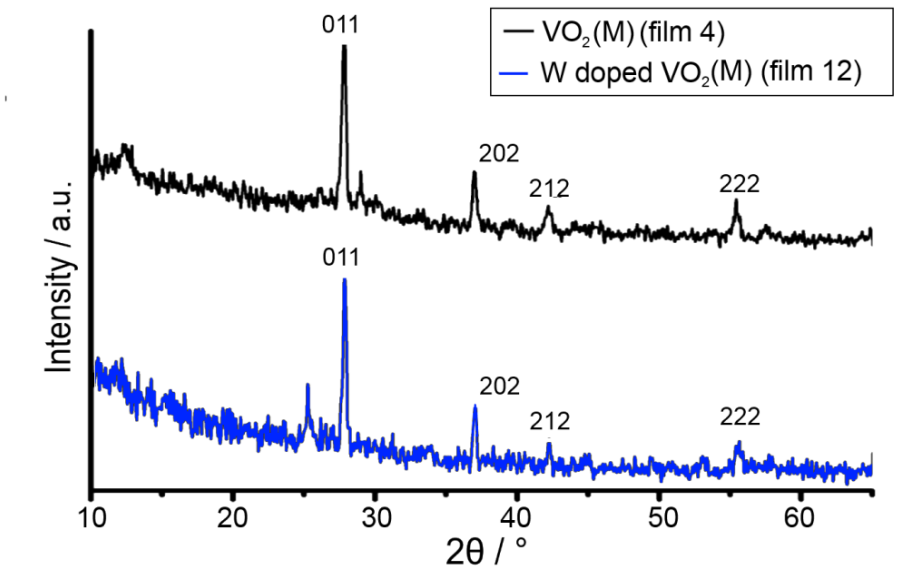

Figure 114: XRD patterns of the VO_2 film deposited from **[6]** in toluene at 550 °C using a 2% O_2 in N_2 carrier gas, both with and without 5.0% $[W(OPh)_6]$.

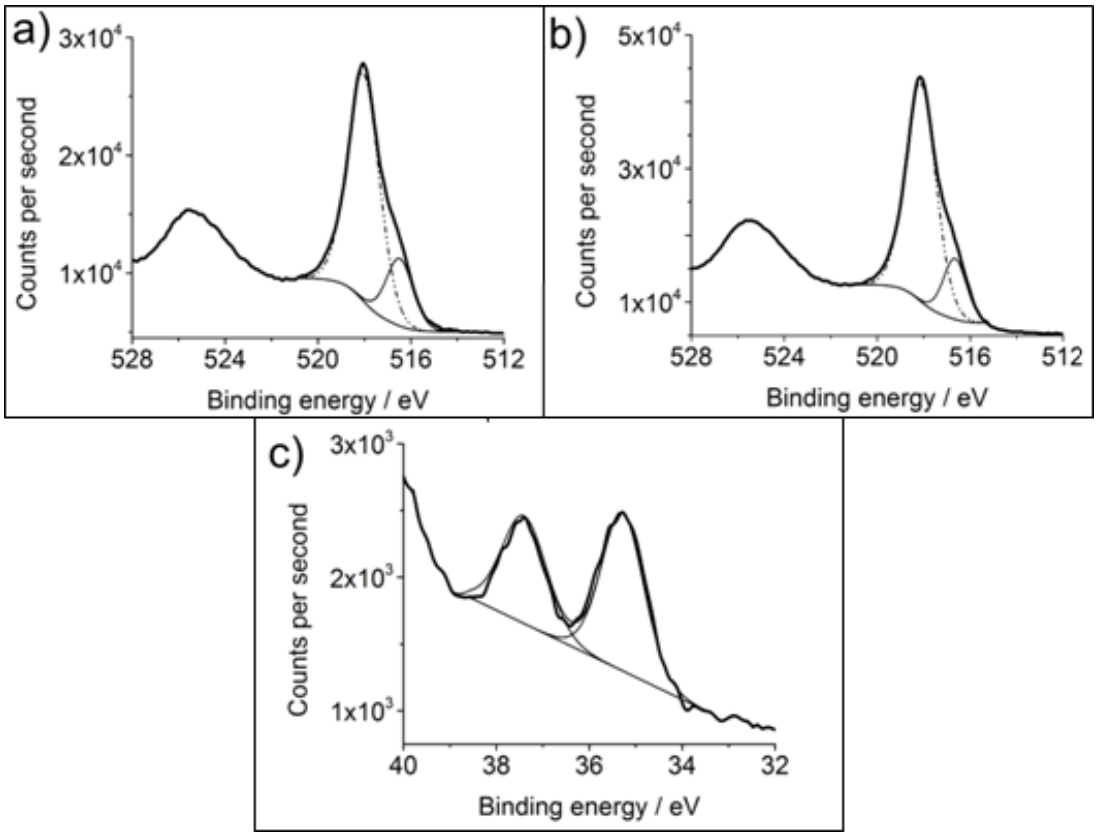

Figure 115: XPS scans of: a) V $2p_{3/2}$ of a VO_2 (M) thin film from the AACVD of $[\{VOCl_2(CH_2(COOEt_2)\}_4]$ **[6]** at 550 ˚C (showing $V^{(IV)}$ at lower binding energy (thin solid line) vs. $V^{(V)}$ (dotted line)), b) V $2p_{3/2}$ of a W-doped VO_2 (M) thin film (film 12) at 550 ˚C and c) corresponding W4f scan.

Incorporation of tungsten into the film appears to greatly alter the morphology, with the film depositing densely packed, rounded, vertical protrusions with a width of around 100 nm (Figure 113b). This is in keeping with the more smooth and even appearance of the doped films.

XRD patterns were referenced against those of VO_2 (M) (ICSD: 34033), VO_2 (A) (ICSD: 51213), VO_2 (B) (ICSD: 199) V_2O_5(ICSD: 15798) and V_2O_3 (ICSD: 1473). Films deposited at 550°C were found to be exclusively VO_2 (M) as seen in Figure 114. Tungsten incorporation induces a slight shift in the XRD pattern (27.8° for undoped VO_2 versus 27.9° for W-doped) and a loss of crystallinity. This, coupled with the lowering of the MST is highly indicative of successful doping.

Typical XPS data from VO_2 (M) and W-doped VO_2 (M) thin films are shown in Figure 115. The V 2p spectra are split into two regions which were then fitted with two separate environments as it was clear that more than one oxidation state was present. The visible shoulders of the main V $2p_{3/2}$ peak indicate the presence of V(IV) in the films. XPS is highly surface sensitive, and the VO_2 on the surface of the films had fully oxided, creating a thin layer as V_2O_5, as a higher proportion of V_2O_5 was present at the surface than in the film, hence a large V(V) peak. The fitted peak positions of 516.5 eV and 516.7 eV for V $2p_{3/2}$ in the undoped and doped films respectively are indicative of V(IV) in VO_2.[44] The second feature at higher binding energy in both spectra (518.1 eV and 518.2 eV respectively) can be attributed to V_2O_5.[44]

The W 4f environment showed the presence of only one oxidation state. This gave a value of 35.28 eV (W $4f_{7/2}$) and 37.38 eV (W $4f_{5/2}$) which is consistent with W(VI). This has been previously seen for W-doped VO_2 in both thin film and nanoparticle synthesis.[275, 283, ,351]

Variable temperature transmission UV/Vis spectroscopy was carried out on the films deposited from **6** in order to determine whether the films underwent the structural transition associated

with VO_2 (M) (Figure 6). A spectrum was taken of the film at room temperature. Following this the films were rapidly heated to 90 ˚C and the measurement repeated. The films were then cooled to room temperature and the initial measurement repeated to ensure that the sample has remained in the same position throughout the heating as heating the ample can cause the sample to slip downward in the heater cell, which would affect the UV/Vis data.

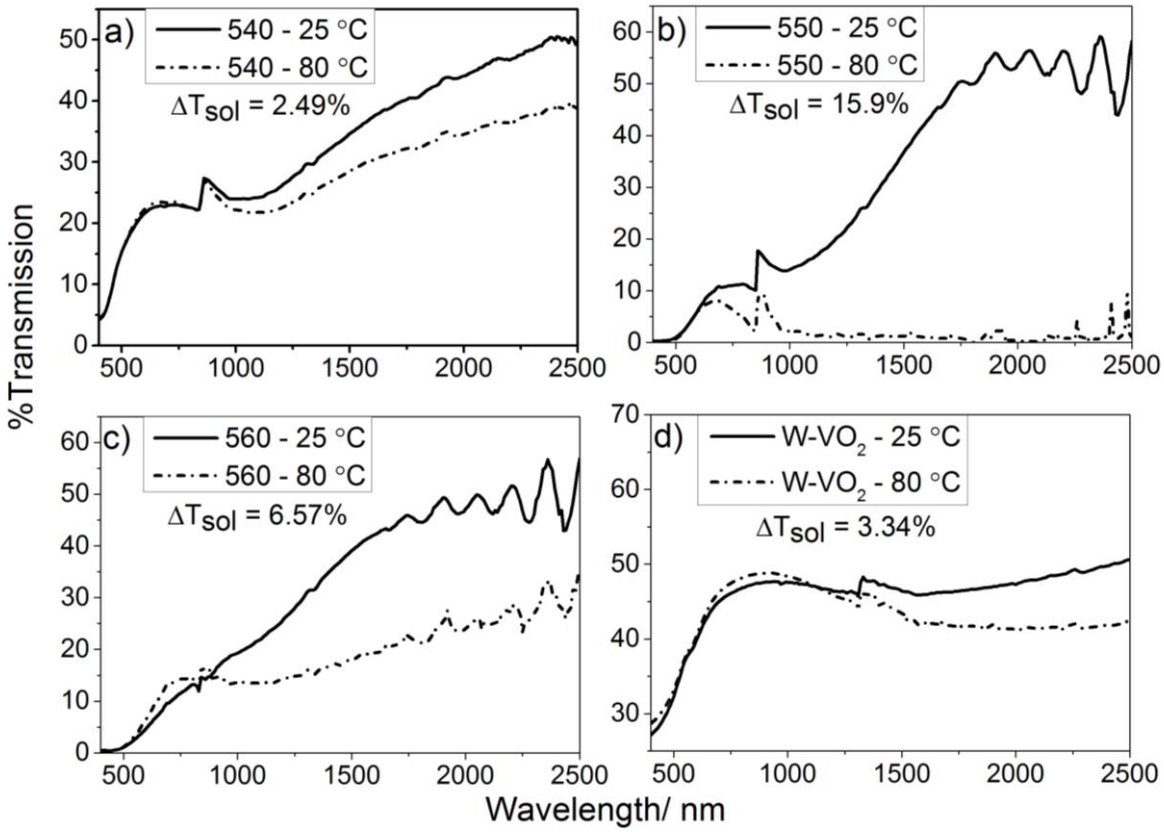

Figure 116: Variable temperature UV/Vis/NIR spectra showing the change in optical properties of thin films of undoped and W-doped VO_2 thin films deposited by AACVD of synthesised vanadium precursor solutions. Solar modulation values (ΔT_{sol}) for each film have been included in the Figure. a) VO_2 (M) film deposited at 540 ˚C, b) 550 ˚C, c) 560 ˚C and d) W-doped VO_2 (M) thin film deposited at 550 ˚C.

Films deposited at 550 ˚C showed by far the highest MST, with the transmittance at 2500 nm falling from 60% to around 2% when the sample was heated from room temperature to 90 ˚C. Films deposited at 560 ˚C demonstrated similar characteristics at room temperature to those deposited at 550 ˚C. However heating the samples reveals that the monoclinic phase of the VO_2

is less pure, roughly halving the transmission to 30%. The VO_2 film deposited at 540 ˚C was the least effective by a considerable margin, seeing a reduction in transmission from 50% to 40% at 2500 nm. These measurements reveal that the optimum temperature for the formation of monoclinic VO_2 from **6** was 550 ˚C.

Solar modulation calculations (ΔT_{sol}) were performed as described by Taylor *et al.*[352] Solar modulation values take into account the effect that gases, such as CO_2 and H_2O, have on the intensity of solar radiation at ground level. This gives a value which can be used to give a better representation of the absolute change in the optical properties of the material. The majority of the energy in the solar spectrum, at ground level, is accounted for by the UV/Visible region (380-780 nm); this leaves a maximum change of *ca.* 20% for the near IR region (780-2500 nm). When comparing the solar modulation values for the VO_2 films, it can be seen that the sample deposited at 550 °C shows a solar modulation of 15.9% which is close to the maximum allowed solar modulation and is comparable to the best results seen for VO_2 thin films by other research groups.[353]

7.2.8. VO_x Nanoparticle Synthesis and Characterisation

$[\{VOCl_2(CH_2(COOEt_2)\}_4]$ **6** was additionally used to produce nanoparticles, *via* thermal decomposition in a high boiling point solvent with structure-directing surfactants under an atmosphere of nitrogen. This follows the standard procedure for many nanoparticle synthesis in which a long chain unsaturated alcohol is coordinated to a metal species, which is then decomposed at high temperatures to form surfactant capped nanoparticles that are easily dispersed in organic solvents.[354–356] Paik *et al.* has used a similar methodology to synthesise VO_x nanocrystals from $VOCl_3$ in the presence of oleylamine and octadecanol, resulting in mixed-phase VO_x nanocrystals.[357] In that case the synthesised particles were flash-annealed at 500 ˚C

for 5 minutes in air at 1 mTorr in order to convert to thermochromic VO_2 (M). The reacton is facilitated by the reaction of $VOCl_3$ with the 1-octadecanol, allowing for the formation of vanadium-oxygen bonds.[358,359] In this synthesis, alcohol is absent, the V-O bonds instead were provided by the diester species.

The decomposition of **6** in the presence of surfactants in a high boiling point solvent was carried out repeatedly, differing the ratios of the two surfactants, as well as the temperature and the inclusion of a fatty alcohol, 1,4-tetradecanediol (Table 20). All reactions were undertaken in 20 ml of dry 1-octadecene (dried over sodium) and after 3 vacuum/re-fill purge cycles with nitrogen. The reaction was heated from room temperature to the target temperature at a rate of 3.3 °C min^{-1} under dynamic nitrogen, during which the reaction mixture was observed to darken in colour gradually from green to black. The addition of oleylamine also induced a colour change of the precursor to blue, presumably due to complexation with the vanadium centre, as a probable result of a d→d transition due to the formation of an octahedral complex. Following subsequent cooling to room temperature, the particles were precipitated with ethanol and separated by centrifugation. All samples gave black precipitates that were readily dispersable in organic solvents, with the exception of sample G.

TEM analysis clearly demonstrates the extent to which the nanoparticle morpholgy is effected by the ratios of surfacant used. Oleylamine was observed to have the most pronounced effect, promoting the growth of spine-like structures as well as nanoparticles which were not seen in its absence (Figure 7a and 7b). Oleic acid purely promoted particle growth only (Figure 7g and 7h). Mixtures of oleic acid and oleylamine were found to be the most effective at generating readily dispersible products, with the optimum blend of equimolar amounts of oleic acid and oleylamine a commonly used in iron oxide nanoparticle syntesis.[360]

Table 20: Compiled reaction conditions for the formation of VO_x nanoparticles using [6] (*No reaction, non-colloidal blue solution formed. ǂAddition of 1,4-tetradecanediol).

Sample	Synthesis temperature °C	Oleylamine mmol	Oleic acid mmol
A	320	6	6
B	320	9	3
C	320	3	9
D	320	0	12
E	320	12	0
F	280	6	6
G*	240	6	6
Hǂ	320	6	6

In samples **A**, **F**, **G** and **H**, the "6:6" blend produced a mixture of mainly spine-like structures of 50-100 nm in length with some round particles also present. These features were preserved on annealing in nitrogen for 8 hours, but were not as pronounced in sample F, in which the synthesis temperature is lower (280 °C), suggesting a degree of temperature dependance on the formation of elongated spines as well as surfactant. However, the features re-emerged with annealing treatment at 550 °C under nitrogen for 10 hours (Figure 117d) and e)). Sample **G**, in which the synthesis temperature was reduced to 240 °C was evidently lower than the nucleation temperature for this system as no nanoparticles were produced.

It proved demanding to gather detailed TEM analysis of the as-synthesised VO_x nanostructures, in particular the lattice plane imaging; due to the presence of high carbon contamination, caused by surfactant layers and decomposition products from the precusor itself. The latter was in evidence through the presence of chlorine by EDS (Figure 117, c) and f).

Sample A and F were both annealed in order to induce the formation of VO_2 (M). However, analysis of lattice planes in both of the the annealed samples (Figure 117e) gave a *d*-spacing of 0.326 nm corresponding to the <111> plane of vanadium oxide (V_4O_9, ICSD 15041), confirming that heat treactment had an identical effect on both samples despite intial differences with synthesis temperatures. It also suggests that the samples were slightly over-oxidised in the annealing process when trying to synthesise VO_2 (M).

The addition of an oxygen source, 1,4-tetradecanediol in sample H with a „6,6“ blend of oleic acid and oleylamine did not induce a phase transformation to VO_2 (M). Instead , the addition of 1,4-tetradecanediol prevented the structure-directing effects of oleylamine from taking effect, giving almost exclusively particulate material (Figure 117i).

EDS spectra showed the persistance of chlorine in the system as a consequence of the precursor. It also showed the reduction in carbon from the heavily carbon contaminated pre-annealed samples versus post annealed samples. Atomic percentages of vanadium and oxygen in the samples are shown in able 3. The at% ratios of V:O for sample A and F pre-anneal was 26.20 : 73.80 and 1.91 : 98.09 respectively, with heat treatment dramatically effecting sample F with the ratio changing to 26.22 : 73.78. The ratio for sample A however, was relatively unchanged (26.40 : 73.60). The very high ratio of oxygen to vanadium in sample G can be attributed to the high levels of carbon contamination obtained from the presence of the surfactants.

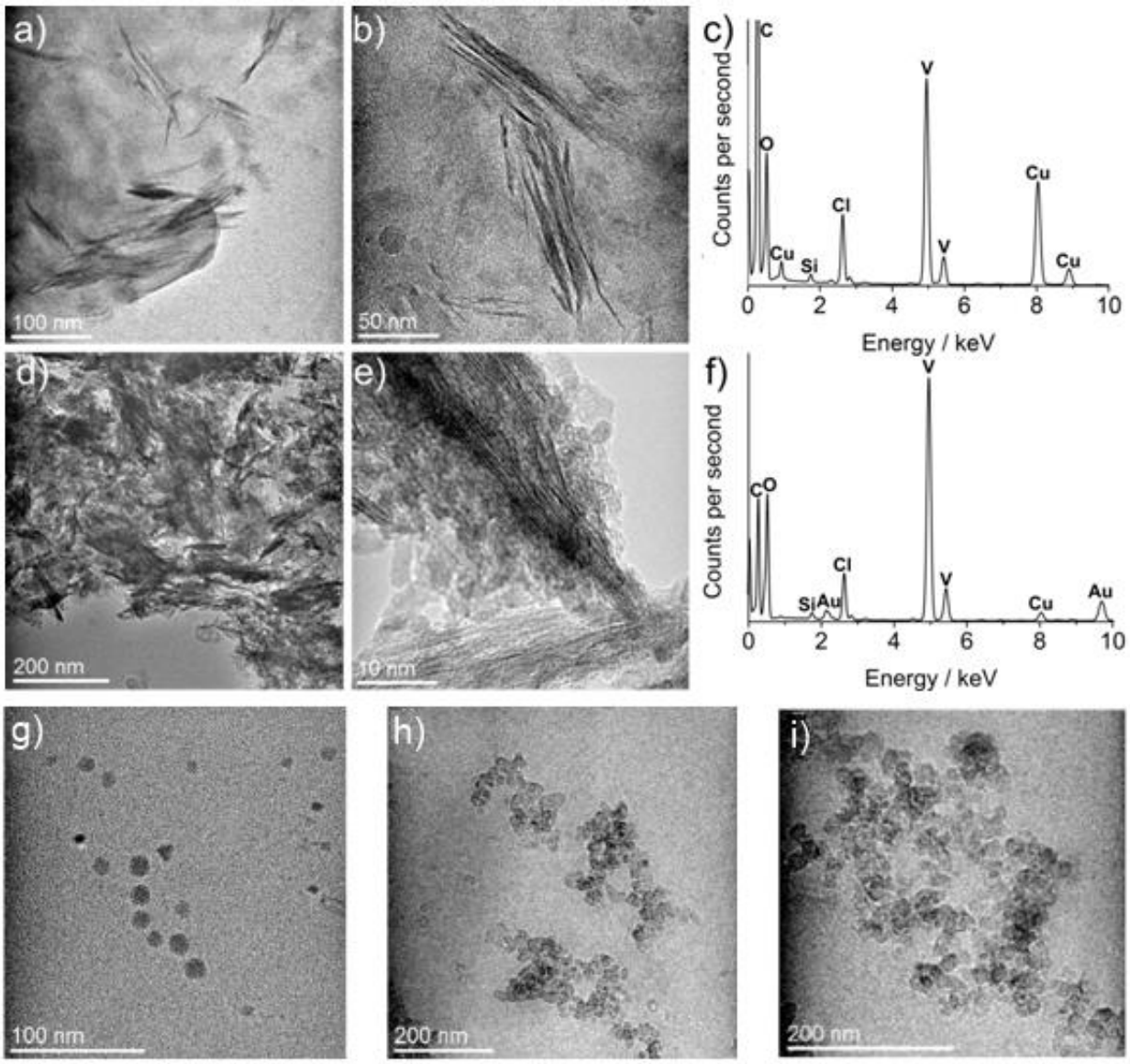

Figure 117: TEM images and EDS spectra of sample **A**, pre-annealing (a and b) and post annealing (d and e). **C** and **G** are the EDS spectra of the pre-annealed and post annealed sample 1 respectively. Also shown are TEM images of samples **B**, **C** and **H** (g, h and i repectively).

The lack of phase transition to VO_2 (M) with thermal treatment at elevated temperatures was confirmed by XRD analysis. The XRD pattern did not match the standard of VO_2 forming a different species. Once again this is likely the result of the high level of carbon contamination from the remnants of the oleic acid/oleylamine ligand system.

Table 21: EDS at% ratios of vanadium to oxygen in nanomaterial samples. Bracketed quantities are those in the annealed spectra.

Sample number	V / at%	O / at%
A	26.2 (26.4)	73.8 (73.6)
B	9.66	90.34
C	1.82	98.18
D	0.18	99.82
E	28.95	71.05
F	1.91 (26.22)	98.09 (73.78)
H	10.21	89.79

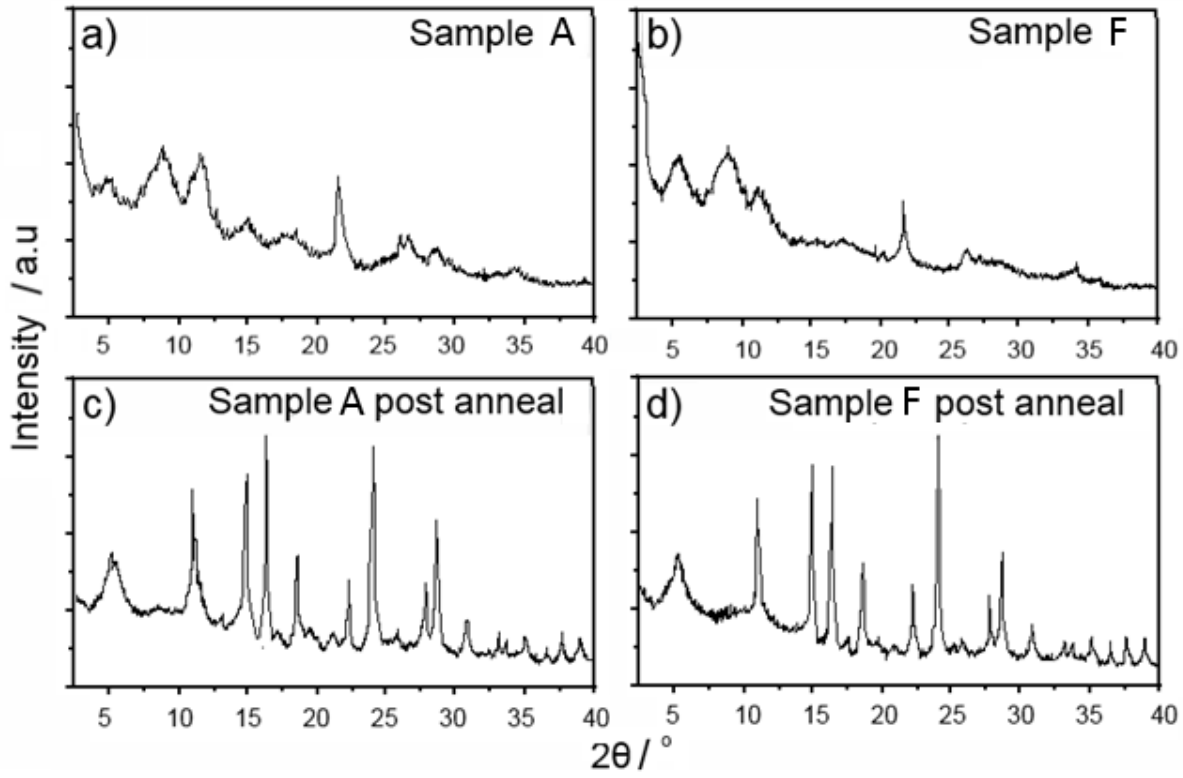

Figure 118: PXRD diffraction patterns for as synthesised powders, a) and b) and following annealing treatment, c) and d). λ= 0.7093 Å.

Powder X-ray Diffraction (PXRD) was performed on the as-synthesised and the post-annealed nanoparticle samples (Figure 118). The as-synthesised nanoparticles, Figure 118 a) and b), have only a few diffraction patterns and it was not possible to confirm the phase of the material from

these. The broad reflections between 5-12° 2θ also suggest that there was a large amorphous component to the samples.

The post-annealed samples, Figure 118c and d), have a greater number of more intense diffraction peaks in the data, with less broadening suggesting that the annealing has resulted in improved crystallinity. Phase analysis of these samples suggested a mix of Magneli phases, with V_3O_7 – 22.2° (0,2,0), V_4O_9 – 11.1° (1,0,2), 16.5° (1,1,3) and V_5O_9 – 5.2° (0,0,1), 24.1° (2,1,1) and 28.8° (2,0,3) lattice planes all being identified in the data. The formation of multiple oxidation states in annealed vanadium samples is relatively commonplace.[360,361]

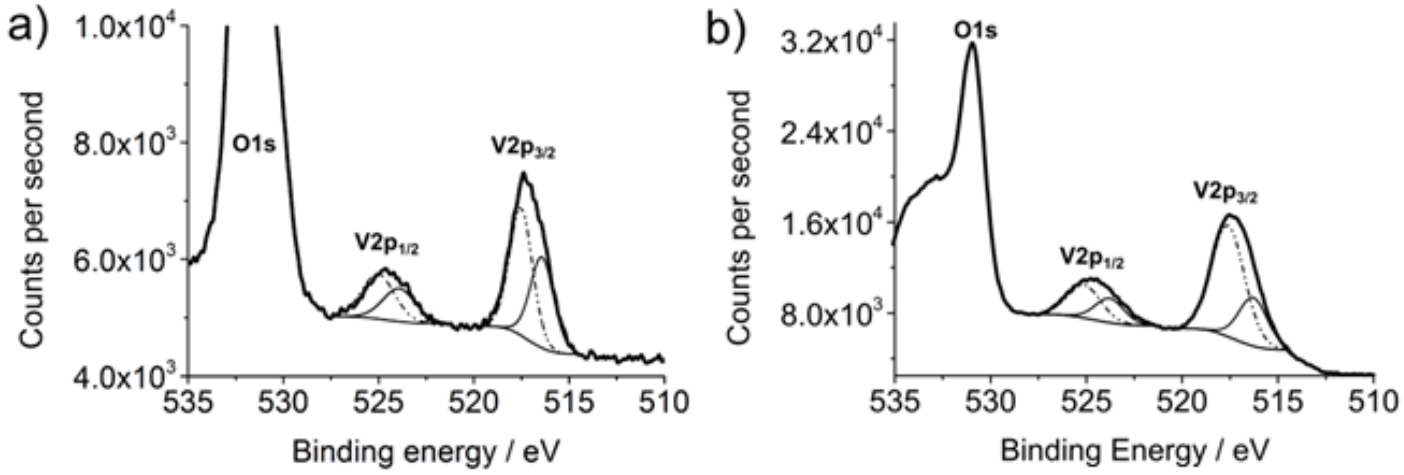

Figure 119: XPS scans of: a) V 2p of Sample 1, VO_2 nanomaterials before annealing and b) after annealing showing V(IV) at lower binding energy (thin solid line) vs. V(V) (dotted line).

X-ray photoelectron spectrcopy was also used to compare the samples before and after annealing. The XPS spectra of the V 2p region in Sample 1 pre (Figure 119a) and post (Figure 119b) anneal show similar profiles to the thin films in Figure 115, with V(IV) peaks reported at 516.5 eV and 516.3 eV for non-annealed and annealed samples respectively (V $2p_{3/2}$) and assigned as VO_2. The V(V) peaks, at 517.7 eV and 517.8 eV respectively were again assigned as V_2O_5.[362]

7.3. Using adducts of $VOCl_3$ and 2,4 pentadione, diethyl malonate and diethyl succinate as precursors for Vanadium Nitride and Carbide

7.3.1. Experimental

All precursors were synthesised as described in Chapter 4. All other starting materials were purchased from Sigma Aldrich and used without further purification. The solvents were dried over activated alumina by the Grubbs method using anhydrous engineering equipment, such that the water concentration was 5 – 10 ppm.[83] All products were synthesised under an atmosphere of nitrogen obtained from BOC in anhydrous solvents using standard Schlenk techniques.

7.3.1.2. Synthesis of vanadium nitride and carbide powders

Vanadium nitride and carbide powders were synthesised by weighing out ~ 0.2 g of compounds **5**, **6** and **7** in a nitrogen filled glove box onto ceramic bricks. The samples were sealed with a layer of laboratory film before removal from the glovebox. The samples were then transferred immediately to a tube furnace. The samples were purged with a flow of nitrogen (for vanadium nitride, BOC, 99.9%) or argon (for vanadium carbide, BOC "pureshield" 99.9%) at room temperature for 30 minutes (flow rate 40 cm min^{-1}) before heating to 1200 °C (heating rate 20 °C min^{-1}) for 24 hours. The samples were then allowed to cool to room temperature under the flow of inert gas.

7.3.2. Results and Discussion

Compounds **5**, **6** and **7**, as synthesised in chapter 4 were heated to temperatures akin to those used in steel tempering under oxygen free flows of inert gases nitrogen and argon in order to obtain VN and VC powders respectively. These powders were analysed by XPS, XRD and TEM in order to deduce their composition and particulate size.

7.3.2.1. Synthesis And Characterisation Of Vanadium Nitride Powders

Vanadium nitride powders were synthesised by annealing compounds **5**, **6** and **7** under nitrogen gas flow at 1200 °C for 24 hours. It is necessary to treat vanadium species at such high temperatures to illicit the formation of vanadium nitride due to the intrinsic stability of various vanadium oxides such as V_2O_5.

It was initially the intention of the experiment to produce VC powder from the decomposition of the precursors, with the ligands acting as the carbon sources, with probable inclusion of some carbon species from the lab film. However compounds **5**, **6** and **7** showed near complete transformation to vanadium nitride at 1200 °C as evidenced by the XRD patterns in Figure 120a. The XRD patterns were compared to a VN standard (ICSD 22321), all samples were shown to be phase pure with only diffraction peaks for VN visible. Annealing at the lower temperature of 1000 °C for 24 hours yielded mixed phases with some VN so it was necessary to perform the reaction at 1200 °C in order for the reaction to reach completion. Yu *et al.*[363] determined the reaction mechanism for the reaction of vanadium(III) oxide (V_2O_3) and carbon in the presence of nitrogen gas at elevated temperatures (up to 1180 °C). Nitridation was simultaneous with carbothermal reduction, from V_2O_3 to V_8C_7 to VN, and was completed at lower temperatures than just V_2O_3 in nitrogen. Compounds **5**, **6** and **7** were able to decompose in a similar way to

this under a nitrogen gas atmosphere due to the presence of oxygen and carbon in the precursor compounds.

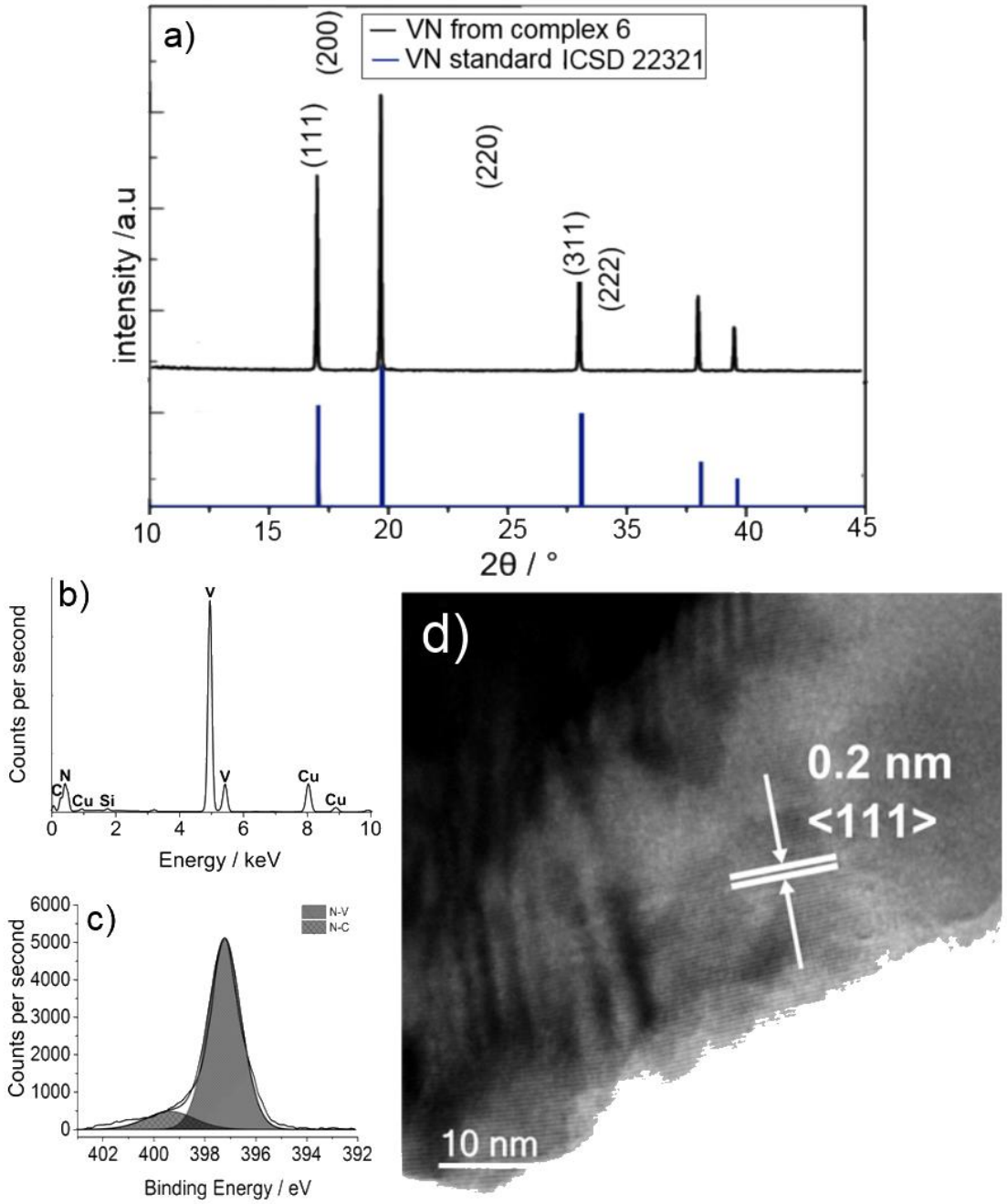

Figure 120: Composite Figure for the VN sample derived from complex **6**. a) shows XRD patterns of VN derived from complex **6** compared to a VN ICSD standard (22321). b)shows an EDS spectrum demonstrating the presence of vanadium and nitrogen with little carbon present. Copper emanated from the copper mesh TEM grid. b) Fitted N1s XPS spectrum showing the regions assigned as VN and VC.) d) is an HRTEM image of a VN crystal with the <111> plane of VN highlighted.

Ortega *et al.*[364] followed the progress of the reaction of by measuring the partial pressures of evolved carbon monoxide, supporting the V_2O_5–V_2O_4-VO_2–V_2O_3–$VO_{0.9}$-VN pathway, despite the difficulty in the detection of $V_{0.9}$.

XPS analysis, Figure 120b) showed the presence of vanadium nitride in both the N 1s and V $2p3_{/2}$ at 397.2 and 513.6 eV respectively. These match with literature values.[365] The XPS also showed evidence for vanadium carbide and oxidised vanadium(V) The carbide was likely due to excess carbon presence in the precursor and the V(V) signal is typical for vanadium, as the vanadium at the surface will readily oxidise when exposed to air.[366]

TEM analysis of all VN samples showed the formation of large, polydisperse crystallites of VN (42.9 ± 17.0 nm (sample derived from **5**), 88.4 ± 47.7 nm (sample derived from **6**) and 72.4 ± 71.4 nm (sample derived from **7**). Small amounts of crystalline carbon was also present around the edges of the VN crystallites, resulting from the film used to seal the samples burning within the furnace. HRTEM analysis of all samples demonstrated the presence of VN, *via* analysis of the *d*-spacings. Several *d*-spacings were indexed (Figure 120 d) with the <111> plane of VN present and identifiable in all samples, with *d*-spacings from the samples derived from compounds **5**,**6** and **7**: 0.24 nm, 0.2 nm and 0.23 nm respectively.

EDS analysis indicated the presence of nitrogen and vanadium with low amounts of carbon (Figure 120 a) and in all samples analysed. Quantitative EDS analysis in all samples showed a *ca.* 50:50 at% ratio, indicative of the formation of VN. The presence of residual carbon species presented difficulties in integrating the nitrogen peak as their EDS fingerprints appear in the same region of the spectrum. The relatively low amount of carbon in the sample and the large VN crystallites allowed for accurate confirmation of a 50:50 at% ratio of V:N, and therefore conformation of the VN empirical formula.

7.3.3. Synthesis and characterisation of vanadium carbide powders

Vanadium carbide powders were synthesised by annealing compounds **5**, **6** and **7** under an argon flow at 1200 °C for 24 hours, yielding a black powder. The VC derived from compound showed excellent conversion as evidenced by XRD analysis in Figure 121a). The samples produced were phase pure, with only diffraction peaks for VC present in the patterns compared to a VC ICSD standard (159870). Powders derived from **5** and **7** show evidence of a partial transformation to VC, however phase purity could not be attained. Figure 121 d shows an HRTEM image of a VC crystal with the <111> plane of VC highlighted.

XPS analysis (Figure 121c) showed the presence of vanadium carbide in both the C1s and V $2p_{3/2}$ at 282.8 and 513.7 eV respectively. These are in agreement with literature values.[367] The C1s showed several other environments, which were matched to C-C, C-O and C-OR- with these environments being more intense than the V-C signal. This was also reflected in the V 2p signal, which was significantly weaker than the C1s, this was attributed to the formation of a carbon 'shell' around the VC particles during annealing.

TEM analysis of all VC samples showed the formation of large, polydisperse crystallites of VC (42.9 ± 17.0 nm , 88.4 ± 47.7 nm and 72.4 ± 71.4 nm from samples derived from **5**, **6** and **7** respectively. These are similar distributions to those obtained for VN. A large amount of crystalline carbon was detected in these particles, moreso than in the VN equivalents.

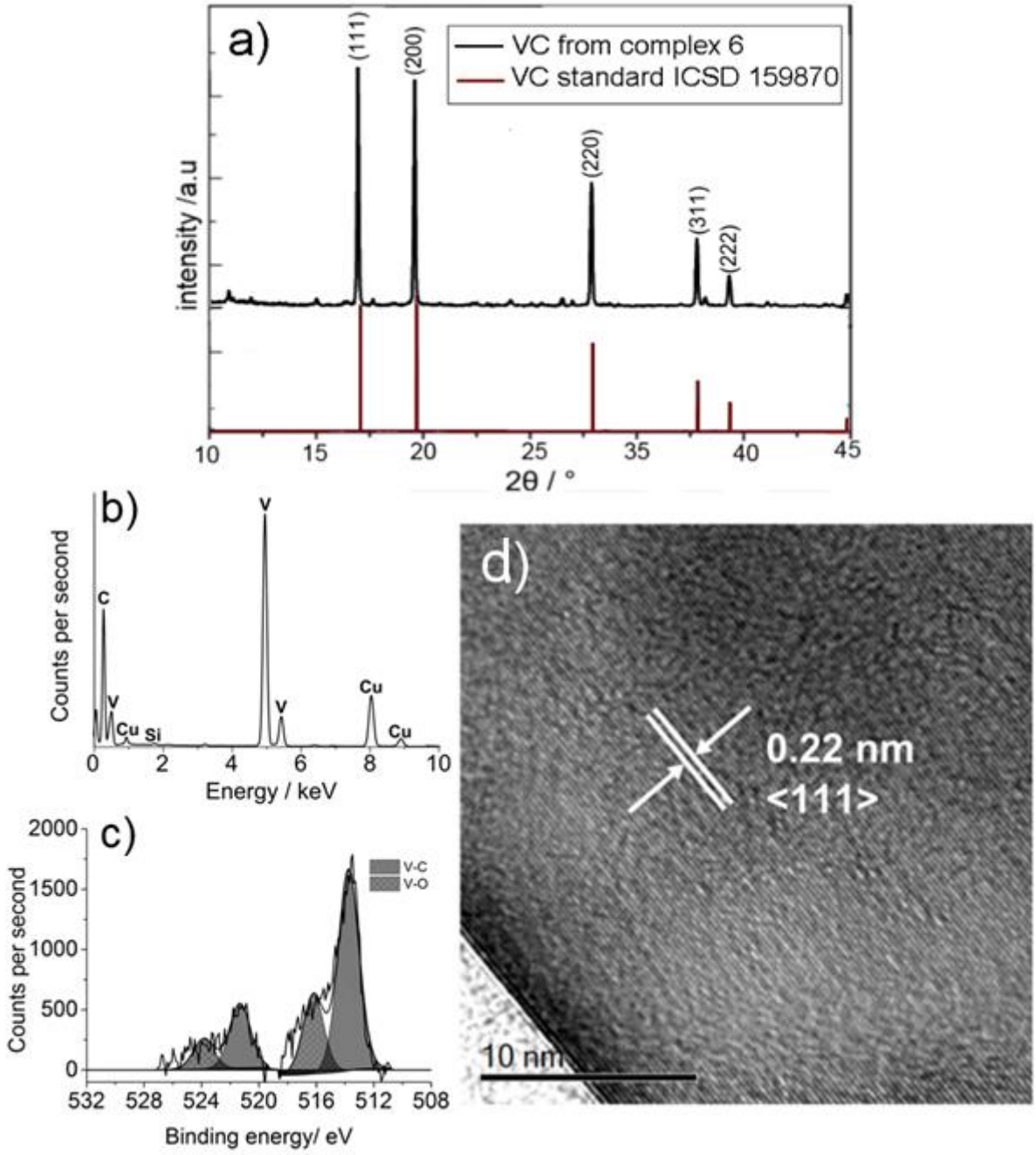

Figure 121: Composite Figure for the VC sample derived from **6**. a) shows XRD patterns of VC derived from **6** b) shows an EDS spectrum demonstrating the presence of vanadium and high levels of carbon. copper emanated from the copper mesh TEM grid. c) shows the fitted V 2p XPS spectrum showing the regions assigned as VC and VO.d) is an HRTEM image of a VC crystal with the <111> plane of VC highlighted.

HRTEM analysis of all samples demonstrated the presence of VN, *via* analysis of the *d*-spacings. Several *d*-spacings were indexed (Figure 121 e) and Figure S2 b) and d)), with the <111> plane of VC identified in all samples, with *d*-spacings from the samples derived from compounds **5**, **6** and **7** : 0.22 nm, 0.22 nm and 0.23 nm respectively.

EDS analysis indicated the presence of carbon and vanadium with high amounts of carbon (Figure 121b) in all samples analysed. Quantitative EDS analysis showed a small difference in each of the samples. The sample derived from **5** showed a *ca.* 95:5 at% ratio of C:V, the sample derived from **6** a *ca.* 90:10 at% ratio, and the sample derived from **7** a *ca.* 85:15 at% ratio. The carbon film on the TEM grid skews the ratio in favour of carbon, but the carbon-rich nature of the structures produced was confirmed by quantitative XPS giving ratios of 94.3 carbon : 5.7 vanadium for the sample derived from **5.**

7.4. Conclusions

$[\{VOCl_2(CH_2(COOEt_2)\}_4]$ **(6)** has shown synthetic verstility as a precursor for the AACVD of vanadium oxide thin films and nanocrystals. Firstly, **6** was shown to be a highly effective precursor for the formation of thermochromic VO_2 (M) thin films onto glass by AACVD. VO_2 (M) films produced at 550 ˚C were shown to have superior solar modulation when compared to films produced at 540 ˚C and 560 ˚C and compare favourably with literature values (15.9%). This suggests that although a very effective precursor for themochromic VO_2(M), the window for such characteristics is very narrow, with the purity of the monoclinic phase being greatly reduced by varying temperature by only 10 ˚C in either direction. The thermochromic switching temperature was reduced through the addition of $W(OEt)_6$ or $W(OPh)_6$ to the precursor solution, reducing the MST to ~30 ˚C. This demonstrates the *via*bility of the AACVD method

when using a designed molecular precursor to form thermochromic materials with tunable properties.

[{$VOCl_2(CH_2(COOEt_2)\}_4$] **(6)** was also decomposed in the presence of alkyl surfactants at elevated temperatures in an inert atmosphere. It was shown that different surfactants affected the shape of the final product, with oleylamine promoting "spine-like" growth, and oleic acid particulate material. Although the heat-induced phase tansformation to VO_2 (M) was ultimately unsuccessful, control over shape and size of the resultant nanomaterials *via* manipulation of surfactant type and concentration in the decomposition of **[6]** was deonstrated.

Complexes **5**, **6** and **7** were also evaluated for their propensity to form VN and VC on annealing at 1200 °C under nitrogen and argon gas respectively. All samples converted to VN at 1200 °C under nitrogen, but complex **6** was the only molecule shown to be a *via*ble precursor for both VC and VN.

Chapter 8

Conclusions

This thesis tackles the industrial problem of metal chlorides separation in a number of ways using laboratory scale chemical techniques, some of which were developed purely for the study, some of which were well established. The reactivity of $TiCl_4$ and $VOCl_3$ with ester groups was analysed in the solid, liquid and gas phases separately. The results of these studies, corroborate on several points, although the techniques involved vary greatly.

Firstly the solid state phase, $TiCl_4$ and $VOCl_3$ were reacted with diesters and triesters. The resulting compounds were characterised using NMR spectroscopy and X-ray crystallography. This lead to the discovery that coordination to a diester species results in the loss of chlorine from the vanadium centre but not the $TiCl_4$ all cases. It was inferred fron this that although the $TiCl_4$ may coordinate in the gas phase to the triglyceride group of the oil, the reaction was so reversible in the gas phase that it would readily able to break away from the molecule, in a way that the $VOCl_3$ could not, explaining the preferential reactivity.

The flow cell experiment was a liquid and gas phase study, focussing not on the separation itself, but on potential side products. The gaseous $TiCl_4$, $VOCl_3$ or mixture was pushed through the chamber with the agitated oil, the gaseous species interacting with the droplets kicked up before distilling into the top of the apparatus. Analysis of the resulting product lead to the discovery that the $TiCl_4$ does react with the glyceride group, chlorinating the species by displacing the two side ester groups, leaving the central intact. This is corroborated by the glycerol tribenzoate $TiCl_4$ complex [**4**], which shows the two side groups coordinated to the same titanium centre, with a second titanium atom coordinating to the central ester groups of

a different molecule. This reaction would be unfavourable in the gas phase and so it is likely that the reaction simply reverses, however in some cases a titanium centre is able to undergo exchange with the glycerol, coordinating resulting in a species that has a low enough boiling point to distil over. This explains the issues that occur later in the plant with furnace fowling, as well as why studies by Huntsman Pigments and Additives found that changing the oil did not alter the problem, as all of the oils tested were triglyceride based.

The final study involved *in situ* gas spectroscopy measurements. The finding of this work appeared to correlate well with the initial experiments. Although the ester used had only one carbonyl group present it was observed that it took coordination of two to a single titanium centre to result in chlorine loss, where as with $VOCl_3$ the relationship between ethyl acetate coordination and chlorine loss is 1:1. It should be noted that the high temperatures and the *in-situ* nature of the study means that the species formed should be considered intermediates.

This work has therefore shown that the gas phase reactions of $TiCl_4$ and $VOCl_3$ in the Chloride Process can be modelled using simpler structures, giving the same conclusions in the solid and gas phases.

Future work in this field would likely involve broadening the scope of the mass spectrometer CVD apparatus to investigate other common inorganic reactions. The most effective precursors in the field would be those with as few atoms present as possible, and also with only one type of ligand, however the results with titanium isopropoxide and butyltin trichloride would suggest that more complex precursors can be studied successfully. Species such as aluminium oxychloride, trimethylindium, trimethylgallium and ferrocene would all be promising candidates.

Another possible study could involve changing the oxidation source. Ethyl acetate worked well in this study due to its similarity to part of the oils used in the Chloride Process but simpler oxygen sources, such as water and oxygen itself, could also be investigated if the amounts entering the system could be monitored and controlled closely. A separate study on the effect of moisture on SiO_2 film growth carried out using the same instrument and reactor proved highly successful.

References

1. Mcnulty, G. S. *Production Of Titanium Dioxide.* in *Proc. Conf. Seville, Spain* 1–16 (2007).
2. Enghag, P. *Encyclopedia of the Elements Technical Data - History - Processing.* 501 (Wiley,2008).
3. Winkler, J. *Titanium Dioxide*: *Production, Properties and Effective Usage*, Vincentz Network GmbH & Co. 11 (2013).
4. Moellmann, J., Ehrlich, S., Tonner, R. & Grimme, S. A DFT-D Study Of Structural And Energetic Properties Of TiO_2 Modifications. *J. Phys. Condens. Matter* **24,** 424206 (2012).
5. Winkler, J. *Titianium Dioxide*, 15 (Vincentz Network GmbH & Co, 2003).
6. Daoud, W. A . *Self-Cleaning Materials and Surfaces: A Nanotechnology Approach*, 45, (John Wiley & Sons, 2013).
7. Ye, L. The Total Amount Of Global TiO_2 Market Value Will Reach USD 31.19 Billion In Year 2022. (*Pulse,* 2016).
8. Hornbostel, C. *Construction Materials: Types, Uses and Applications*, 883, (Wiley, 1991).
9. Benvenuto, M. A. *Industrial Inorganic Chemistry*, 883, (Walter de Gruyter GmbH & Co,2015).
10. Merchant Research And Consulting ltd. *Titanium Dioxide: 2016 World Market Outlook and Forecast up to 2020.* (2016).
11. Wicks, Z. W. J., Jones, F. N., Pappas, S. P. & Wicks, D. A. Organic Coatings - Science And Technology, Vol. 5. *Progress in Organic Coatings* **13,** 38 (2007).
12. Mills, A., Elliott, N., Parkin, I. P., Neill, S. A. O. & Clark, R. J. Novel TiO_2 CVD Films For Semiconductor Photocatalysis. *J. Photochem. Photobiol. A,* **151,** 171–179 (2002).
13. Kumar, C. S. S. R. *Nanocomposites*, 11, (John Wiley & Sons, 2010).
14. Parkin, I. P. & Palgrave, R. G. Self-cleaning coatings. *J. Mater. Chem.* **15,** 1689 (2005).
15. Cai, Y. *Titanium Dioxide Photocatalysis in Biomaterials Applications*. (2013).
16. Dunnill, C. W. H. *et al.* Enhanced photocatalytic activity under visible light in N-doped TiO2 thin films produced by APCVD preparations using t-butylamine as a nitrogen source and their potential for antibacterial film, *J. Photochem. Photobiol. A,* **207,** 244 (2009).
17. O'Regan, B. & Grätzel, M. A Low-Cost, High-Efficiency Solar Cell Based On Dye-Sensitized Colloidal TiO_2 Films. *Nature* **343,** 737–740 (1991).
18. Eric R. Force**,** Geology of Titanium-Mineral Deposits. GSA Special Papers, **259,** (1991).
19. Breen, G. *T Mineral Sands Update Price Revisions - A Turning Point & Time To Gain Exposure To The Sector The Dark Clouds Begin To Lift*. (2013).
20. Sahu, K., Thomas, A., Devabrat, M. & Archana, A. An Overview On The Production Of Pigment Grade Titania From Titania-Rich Slag. *Wate Manag. Res* **24,** 74–79 (2006).
21. Craver, C. & Carrahe, C. Applied Polymer Science: 21st Century. 485 (Elsevier, 2000).
22. Kawaja, S. TiO_2 -2016 Outlook - Are Prices At Rock Bottom? (*Tize,* 2015).
23. Saklatwalla, B., Dunn, H. & Marshall, A., Sulfate Proces Of Making Titianium Dioxide. (1932).
24. Shreve, R. N. & Austin, G. T. Shreve's Chemical Process Industries. 434 (McGraw-Hill, 1984).
25. Ti-Cons Ldt., *Sufate Process Overview*, (2009).
26. Cody, C., Reichert, W., Kemnetz, S. & Magauran, D. Process For Preparing High Quality Titnaium Dioxide, US4505886 A (1966)
27. Goldschmidt, A. & Streitberger, H.J. *BASF Handbook on Basics of Coating Technology*. (William Andrew, 2003).
28. Nosaka, Y. & Nosaka, A. Introduction to Photocatalysis - From Basic Science to Applications. 10–12 (RSC Publishing, 2016).
29. Parker, R. *Greatham Works Process Manual ICON 1 Chlorination Section Contents*, (Huntsman Tioxide, 2001)
30. Boyd, C. . *Purification Of Crude Titanium Tetrachloride With White Mineral Oil*, US3253885 A (1966).
31. Cronin, J. , Elkins, T., Helberg, L. & Merkle, J. Purification Of Titanium Tetrachloride. US2600881

A (2004).
32. Glaeser, H. H. *Removal of $AlCl_3$ from $TiCl_4$ by addition of H_2O and NaCl* US4125586 A (1978).
33. Sutcliffe, S. *Best Operating Practice Guide Titanium Tetrachloride Purification*. 1–23 (Huntsman Tioxide, 2008).
34. Cristal Performance Chemicals. *$TiOCl_2.(H_2O)_x.(HCl)_y$ MSDS*. (2016).
35. Coates, W. *Improvements in or relating to the Purification Of Titainum Tetrachloride by Distillation*, US3156630 A (1954).
36. Haddow, A. Oxidation Of Titanium Tetrachloride to Form Titanium Dioxide. US5599519 A (1995).
37. Tolinski, M. Additives for Polyolefins Getting the Most out of Polypropylene. 141 (Elsevier, 2009).
38. Image Of Rutile Sand as sold by Tianjin Wangda Chemical Co. Ltd. http://www.ecvv.com/product/3831604.html accessed 30/01/2017
39. Image of Purified TiO_2 as sold by SAAQIN ltd. https://www.amazon.com/Titanium-Dioxide-Powder-Lb-SAAQIN/dp/B004W0EQB8 accessed 30/01/2017
40. Gunstone, F. *Fatty Acid and Lipid Chemistry*. (Springer, 1996).
41. Reck, E. & Richards, M. Titanium dioxide — Manufacture, environment and life cycle analysis: The Tioxide experience. *Surf. Coatings Int.* **80,** 568–572 (1997).
42. Müller, U. *Inorganic Structural Chemistry*. (John Wiley & Sons, 1994).
43. Hooper, A. B. & Lipscomb, J. D. Resolution of multiple heme centers of hydroxylamine oxidoreductase from Nitrosomonas. 2. Mössbauer spectroscopy. *J. Am. Chem. Soc.* **42,** 3973–3976 (2002).
44. Sutton, L. *Tables of Interatomic Distances and Configuration in Molecules & Ions (supplement)*. (The Chemical Society, 1956).
45. Webb, S. P. & Gordon, M. S. Intermolecular Self-Interactions of the Titanium Tetrahalides TiX_4 (X = F , Cl , Br). *J. Am. Chem. Soc.* **4,** 2552–2560 (1999).
46. Thomas, T., Pugh, D., Parkin, I. P. & Carmalt, C. J. Syntheses, X-ray structures and CVD of titanium(IV) arsine complexes. *Dalt. Trans.* **39,** 5325–31 (2010).
47. Thomas, T., Pugh, D., Parkin, I. P. & Carmalt, C. J. Novel ion pairs obtained from the reaction of titanium(IV) halides with simple arsane ligands. *Acta Crystallogr. Sect. C Cryst. Struct. Commun.* **67,** 96–99 (2011).
48. Kim, C. S., Nakaso, K., Xia, B., Okuyama, K. & Shimada, M. A new observation on the phase transformation of TiO_2 nanoparticles produced by a CVD method. *Aerosol Sci. Technol.* **39,** 104–112 (2005).
49. Hyett, G., Green, M. A & Parkin, I. P. The use of combinatorial chemical vapor deposition in the synthesis of $Ti(3-\delta)O_4N$ with $0.06 < \delta < 0.25$: a titanium oxynitride phase isostructural to anosovite. *J. Am. Chem. Soc* **129,** 15541–8 (2007).
50. Smith, M. B. *Organic Synthesis*. (Academic Press, 2011).
51. Chadwick, J. C., Duchateau, R., Freixa, Z. & Leeuwen, P. W. N. M. van. *Homogeneous Catalysts*. (John Wiley & Sons, 2011).
52. Malpass, D. B. *Introduction to Industrial Polyethylene: Properties, Catalysts, and Processes.* (John Wiley & Sons, 2010).
53. Natta, G. Stereospecific polymerizations by means of coordinated anionic catalysis. *J. Inorg. Nucl. Chem.* **8,** 589–611 (1958).
54. Cossee, P. Ziegler-Natta catalysis I. Mechanism of polymerization of alpha;-olefins with Ziegler-Natta catalysts. *J. Catal.* **3,** 80–88 (1964).
55. Anslyn, V. A. & Dougherty, D. A. *Modern Physical Organic Chemistry*. (University Science Books, 2006).
56. Prakash, S., Tuli, G., Baku, S. & Banda, R. *Advanced Inorganic Chemistry, Volume 2.* 352 (S. Chand, 2000).
57. Pelletier, E. & Harrod, J. F. Cyclosiloxanes as Frameworks for Multimetallic Compounds. 3. 'H NMR Spectra of Some Substituted Methylcyclosiloxanes'. *Organometallics* **3,** 1070–1075

(1984).
58. Gottlieb, H. E., Kotlyar, V. & Nudelman, A. NMR Chemical Shifts of Common Laboratory Solvents as Trace Impurities In the course of the routine use of NMR as an aid for organic chemistry , a day-to-day problem is the identifica- tion of signals deriving from common contaminants literature , but the. *J. Org. Chem.* **62,** 7512–7515 (1997).
59. Health & Safety & Environmental Deparment. Hexamethylcyclotrisiloxane - Material Safety Data Sheet. (2009).
60. Harrod, J. F., Shaver, A. & Tucka, A. Cyclosiloxanes as Frameworks for Multimetallic Compounds. 3. ^{1}H NMR Spectra of Some Substituted Methylcyclosiloxanes. *J. Chem. Inf. Model.* **53,** 1689–1699 (2013).
61. Sigma Aldrich. Datasheet for 2,4,6,8-Tetramethylcyclotetrasiloxane (CAS Number 2370-88-9). (2016).
62. Sigma Aldrich. Datasheet for Hexamethylcyclotrisiloxane (CAS Number 541-05-9). (2015).
63. Sigma Aldrich. Datasheet forHexamethylcyclotrisiloxane (CAS Number 541-05-9). (2016).
64. Sigma Aldrich Datasheet for Hexamethyldisiloxane (CAS Number 107-46-0). (2016).
65. Sigma Aldrich. Datasheet for (Dichloromethyl)trimethylsilane (CAS no. CAS Number 5926-38-5).
66. Sigma Aldrich. Datasheet for 1-chloro-pentamethyl-disilane (CAS No. 1560-28-7). (2016).
67. Sigma Aldrich. Datasheet for Chloromethyl(dimethyl)silane (CAS Number 3144-74-9). (2016).
68. Sigma Aldrich. Datasheet for Dichloro(chloromethyl)methylsilane (CAS Number 1558-33-4). (2015).
69. B.S. Middleditch. *Artifacts: GC, MS, HPLC, TLC and PC*. (Elsevier, 1989).
70. M. Alger. *Polymer Science Dictionary*. (Springer Science & Business Media, 1996).
71. Wypych, G. *Handbook of Antiblocking, Release, and Slip Additives*. (ChemTec Publishing, 2005).
72. Brandolini, A. & Hills, D. NMR spectra of polymers and polymer additives. 31 (Mobil Chemical Company, 2000).
73. Mishra, B. *Review of Extraction, Processing, Properties, and Applications of Reactive Metals: 1999 TMS Annual Meeting, San Diego, CA, February 28 - March 15, 1999*. (John Wiley & Sons, 2013).
74. Yates, J.G., Lettier, P., *Fluidized-Bed Reactors: Processes and Operating Conditions*, 69, (Springer, 2016).
75. Buxbaum, G. *Industrial Inorganic Pigments*. 55 (Wiley-VCH Verlag GmbH, 1998).
76. Krchma, I. J., *Distillation of Titanium Tetrachloride.* US2463396 A (1946).
77. Xiong, S., Yuan, Z., Yin, Z. & Yan, W. Removal Of The Vanadium Impurities From Crude $TiCl_4$ with High Content Of Vanadium Using A Mixture Of Al Power and White Mineral Oil. *Hydrometallurgy* **119–120,** 16–22 (2012).
78. Cossee, P. Ziegler-Natta Catalysis I. Mechanism of polymerization of α-olefins with Ziegler-Natta catalysts. *J. Catal.* **3,** 80–88 (1964).
79. Maier, G., Ulrich, S. & Boese, R. Isolierung und Kristallstrvkturanalyse Eines Titantetrachlorid-Komplexes Eines 1,3-Dieetons. *Tetrahedron Lett.* **28,** 4515–4516 (1987).
80. Shao, M. Reactions of $TiCl_4$ or $Ti(O^iPr)Cl_3$ with 2,4-Pentanedione . The Molecular Structures of $TiCl_3$(acac)(THF) and $Ti(OiPr)Cl_2$(acac)(THF). *J. Chin. Chem. Soc* **3,** 901–906 (2000).
81. Sobota, P., Szafert, S. & Lis, T. Reactions of $TiCl_4$ with diesters. Crystal structures of $[CH_2(CO_2Et)_2Cl_4Ti]$ and $[C_2H_4(CO_2CH_2CH_2OPh)_2Cl_4Ti]$. *J. Organomet. Chem.* **443,** 85–91 (1992).
82. Kakkonen, H. J. & Pursiainen, J. $TiCl_4$ diester complexes : relationships between the crystal structures and properties of Ziegler-Natta catalysts. *J. Organomet. Chem* **453,** 175–184 (1993).
83. Pangborn, A. B., Giardello, M. A., Grubbs, R. H., Rosen, R. K. & Timmers, F. J. Safe and Convenient Procedure for Solvent Purification. *Organometallics* **15,** 1518–1520 (1996).
84. Japan, R. C. T. *CrystalClear-SM Expert 3..1 b18*. (2013).
85. Farrugia, L. J. WinGX and ORTEP for Windows: an update. *J. Appl. Cryst* **54,** 849–854 (2012).
86. Allen, F. H., Johnson, O., Shields, G. P. & Smith, B. R. CIF applications. XV. enCIFer: a program for viewing, editing and visualizing CIFs. *J. Appl. Cryst* **37,** (2004).
87. Dolomanov, O.V., Bourhis, L.J., Gildea, R.J, Howard, J.A.K. & Puschmann, H. OLEX2: a complete

structure solution, refinement and analysis program. *J. Appl. Cryst* **42,** 339–341 (2009).
88. Palatinus, L. & Chapuis, G. SUPERFLIP - a computer program for the solution of crystal structures by charge flipping in arbitrary dimensions. *J. Appl. Cryst* **40,** 786–790 (2007).
89. Sheldrick, G. M. A short history of SHELX. *Acta Cryst.`` **A64,** 112–122 (2008).
90. Bondi, A. van der Waals Volumes and Radii. *J. Phys. Chem* **3,** 441–451 (27643BC).
91. Pennington, D. A., Hughes, D. L., Bochmann, M. & Lancaster, S. J. The synthesis, structure and catalytic activity of mono(salicylaldiminato) titanium complexes. *Dalt. Trans.* **2,** 3480 (2003).
92. Sobota, P. Reaction between [$MgCl_4$] 2- anion and titanium chlorides. The crystal structure of [NBu_4][trans-$TiCl_4(THF)_2$]·THF. *Polyhedron* **8,** 2013–2016 (2013).
93. Gallucci, J. C., Kozmina, N. & Paquette, L. a. A [{$TiCl_2$(isodiCp)}$_2$(μ-O)] Dimer and a Twinned Cyclic [TiCl(isodiCp)(μ-O)]$_4$ Tetramer. *Acta Crystallogr. Sect. C Cryst. Struct. Commun.* **54,** 1609–1612 (1998).
94. Huang, Y. & Stephan, D. W. Synthesis and structure of titanium diolate complexes derived from CpTiCl ,. *Can. J. Chem* **962,** 956–962 (1995).
95. Schormann, M. [mu]-Oxo-bis[trichlorobis(dimethylsulfane)titanium(IV)]. *Acta Cryst.* **E59,** M674–M675. (2003).
96. Wu, Y., Ho, Y., Lin, C. & Gau, H. Stepwise Reactions of $TiCl_4$ and Ti(OiPr)Cl_3 with 2-Propanol. Variable-Temperature NMR Studies and Crystal Structures of [$TiCl_2$(OiPr)(HOiPr)(μ-Cl)]$_2$ and [TiCl2(OiPr)(HOiPr)(μ-OiPr)]$_2$. *Inorg.Chem.* **2,** 5948–5952 (1996).
97. Sobota, P., Szafert, S. & Lis, T. Reactions of $TiCl_4$ with diesters . Crystal structures of [$CH_2(CO_2Et)_2Cl_2Ti$]. **443,** 85–91 (1993).
98. Sobota, P. *et al.* Synthesis and characterization of new di- and tetra-meric vanadium intermediates of olefin polymerization catalysts. Crystal structures of [V_2(μ-Cl)$_2Cl_4(MeCo_2Et)_4$] and [{$VOCl_2[CH_2(CO_2Et)_2]$}$_4$]·$2CH_2Cl_2$. *J. Chem. Soc. Dalt. Trans.* **424,** 1727–1732 (1995).
99. Crans, D. C., Felty, R. A., Anderson, O. P. & Miller, M. M. Structure and solution properties of a dimeric tetrahedral vanadium(V) chloride alkoxide complex. *Inorg. Chem.* **32,** 247–248 (1993).
100. Rosenthal, E. C. E. From vanadium(V) to vanadium(IV) - and backwards. *Pure Appl. Chem.* **81,** 1197–1204 (2009).
101. Zhang, S. *et al.* Mixed-metal-organic frameworks (M'MOFs) from 1D to 3D based on the 'organic' connectivity and the inorganic connectivity: Syntheses, structures and magnetic properties. *CrystEngComm* **17,** 3312–3324 (2015).
102. Phan, A., Czaja, A. U., G??ndara, F., Knobler, C. B. & Yaghi, O. M. Metal-organic frameworks of vanadium as catalysts for conversion of methane to acetic acid. *Inorg. Chem.* **50,** 7388–7390 (2011).
103. Sun, Q. *et al.* Ideal Spintronics in Molecule-Based Novel Organometallic Nanowires. *Sci. Rep.* **5,** 12772 (2015).
104. Lv, B., Shi, X., Ma, X., Zhang, Z. & Wang, K. Controllable fabrication of multifunctional 1D Ag-based coordination polymer@PVP nanowires. *New J. Chem.* **39,** 349–354 (2015).
105. Zhang, X.-M., Tong, M.-L., Lee, H. K. & Chen, X.-M. The First Noncluster Vanadium(IV) Coordination Polymers: Solvothermal Syntheses, Crystal Structure, and Ion Exchange. *J. Solid State Chem.* **160,** 118–122 (2001).
106. Hosseini-Monfared, H., Asghari-Lalami, N., Pazio, A., Wozniak, K. & Janiak, C. Dinuclear vanadium, copper, manganese and titanium complexes containing O,O,N-dichelating ligands: Synthesis, crystal structure and catalytic activity. *Inorganica Chim. Acta* **406,** 241–250 (2013).
107. Clegg, J. K., Kim, Y. & Lindoy, L. F. Discrete and polymeric supramolecular architectures derived from dinuclear oxovanadium(IV) complexes of aryl-linked bis-diketonato ligands and nitrogen donor co-ligands. *J. Incl. Phenom. Macrocycl. Chem.* **82,** 247–257 (2015).
108. Roy, S. *et al.* Synthesis, characterization and magnetic property of a succinate bridged 1D coordination polymer of cobalt(II) containing benzidine as end-capping ligand. *J. Mol. Struct.* **1061,** 54–60 (2014).
109. Luthria, D. Oil Extraction and Analysis: Critical Issues and Competitive Studies. 104 (2004).
110. Banfi, D.; Patiny, L. www.nmrdb.org: Resurrecting and processing NMR spectra on-line. *Chimia*

(Aarau). **62(4),** 280–281 (2008).
111. Castillo, A. M., Patiny, L. & Wist., J. Fast and Accurate Algorithm for the Simulation of NMR spectra of Large Spin Systems. *J. Magn. Reson.* **209,** 123–130 (2011).
112. Aires-de-Sousa, M. & Hemmer, J. G. Prediction of -^{1}H NMR Chemical Shifts Using Neural Networks. *Anal. Chem.* **74(1),** 80–90. (2002).
113. Darrell Ebbing & Gammon, S. D. *General Chemistry*. (Cengage Learning, 2016).
114. Barrow, H., Brown, D. a., Alcock, N. W., Clase, H. J. & Wallbridge, M. G. H. Reactions of titanium tetrachloride with carboxylic acids. Crystal and molecular structure of the dinuclear titanium oxo compound [{$TiCl_2(O_2CBut)(ButCO_2H)\}_2O$]. *J. Chem. Soc. Dalt. Trans.* **1,** 195 (1994).
115. Dijkgraaf, C. Charge-Transfer Complexes of Titanium Tetrachloride, Titanium Tetrabromide, and Vanadium Oxytrichloride with Aromatic Hydrocarbons. *J. Phys. Chem.* **69,** 660–661 (1965).
116. Jones, Anthony C.; Hitchman, M. L. Chemical Vapour Deposition - Precursors, Processes and Applications. 40 (*Royal Society of Chemistry,* 2009).
117. Ponraj, J. S., Attolini, G. & Bosi, M. Review on Atomic Layer Deposition and Applications of Oxide Thin Films. *Crit. Rev. Solid State Mater. Sci.* **38,** 203–233 (2013).
118. Moravej, M. & Hicks, R. F. Atmospheric plasma deposition of coatings using a capacitive discharge source. *Chem. Vap. Depos.* **11,** 469–476 (2005).
119. Gordon, R. G., Barry, S., Barton, J. T. & Broomhall-Dillard, R. N. R. Atmospheric pressure chemical vapor deposition of electrochromic tungsten oxide films. *Thin Solid Films* **392,** 231–235 (2001).
120. Ha, H. Y., Nam, S. W., Lim, T. H., Oh, I. H. & Hong, S. A. Properties of the TiO_2 membranes prepared by CVD of titanium tetraisopropoxide. *J. Memb. Sci.* **111,** 81–92 (1996).
121. Park, H. S., Waezsada, S. D., Cowley, A. H. & Roesky, H. W. Growth of GaN layer from the single-source precursor (Et_2GaNH_2)(3). *Chem. Mater.* **10,** 2251–2257 (1998).
122. Jones, A. C. & Hitchman, M. L. Overview of Chemical Vapour Deposition. *Chem. Vap. Depos. Precursors, Process. Appl.* 1–36 (2009).
123. Barron, A. in *Chemistry for Electronic Materials* 204–206 (Connexions, 2011).
124. Chua, C. S. *et al.* Effect of annealing temperature on microstructure and UV light photocatalytic activity of TiO2 films grown by atmospheric pressure CVD. *Chem. Vap. Depos.* **20,** 44–50 (2014).
125. Patil, D. R., Patil, L. S., Bange, J. P. & Gautam, D. K. Deposition of oriented nanocrystalline TiO 2 thin films. *J. Optoelectron. Adv. Mater.* **10,** 3251–3256 (2008).
126. Hocine, D. *et al.* Characterization of TiO_2 antireflection coatings elaborated by APCVD for monocrystalline silicon solar cells. *Phys. Status Solidi* **12,** 323–326 (2015).
127. Vernardou, D., Louloudakis, D., Spanakis, E., Katsarakis, N. & Koudoumas, E. Thermochromic amorphous VO2 coatings grown by APCVD using a single-precursor. *Sol. Energy Mater. Sol. Cells* **128,** 36–40 (2014).
128. Kiria, P., Hyett, G. & Binionsa, R. Solid state thermochromic materials. *Adv. Mater. Lett.* **1,** 86–105 (2010).
129. Manning, T., Parkin, I.P., Blackman, C. & Qureshi, U. APCVD of thermochromic vanadium dioxide thin films - solid solutions V_2-xM_xO_2 (M = Mo, Nb) or composites VO_2 : SnO_2. *J. Mater. Chem.* **15,** 4560–4566 (2005).
130. Hatem, D. & Belkaid, M. S. SnO_2 Thin Films Prepared by APCVD for Organic Solar Cells Application. *Adv. Mater. Res.* **685,** 166–173 (2013).
131. Maleki, M. & Rozati, S. M. Investigation of the Effect of the Substrate Position Relative to the Source on the Optoelectrical and Structural Properties of Pure Nanostructured Tin Oxide by APCVD. *Chem. Vap. Depos.* **20,** 352–355 (2014).
132. Morales, C. *et al.* Low temperature SnO_2 films deposited by APCVD. *Microelectronics J.* **39,** 586–588 (2008).
133. Chai, C. C., Peng, J. & Yan, B. P. Preparation and Gas-Sensing Properties of a-Fe_20_3 Thin Films. **24,** (1995).
134. Ashraf, S., Binions, R., Blackman, C. S. & Parkin, I. P. The APCVD of tungsten oxide thin films from reaction of WCl6 with ethanol and results on their gas-sensing properties. *Polyhedron* **26,**

1493–1498 (2007).
135. Riaz, U. Low-temperature atmospheric-pressure chemical vapor deposition of tungsten oxide thin films. *Thin Solid Films* **235,** 15–16 (1993).
136. Pacio, M. *et al.* Study of (100) orientated ZnO films by APCVD system. *Mater. Sci. Eng. B* **174,** 38–41 (2010).
137. Yoo, Y. Z. *et al.* Development of tilted hexagonal platelet ZnO using atmospheric pressure chemical vapor deposition and investigation of its growth mechanism. *Appl. Phys. Lett.* **100,** 1–4 (2012).
138. Maleki, M. & Rozati, S. M. Dependence of ZnO Nanostructured Thin Films Properties on Growth Temperature by APCVD Method. *Acta Phys. Pol. A* **128,** 367–373 (2015).
139. Ruppi, S. Deposition, Microstructure and properties of texture-controlled CVD α-Al_2O_3 coatings. *Int. J. Refract. Met. Hard Mater.* **23,** 306–316 (2005).
140. Blittersdorf, S., Bahlawane, N., Kohse-Hoinghaus, K., Atakan, B. & Muller, J. CVD of Al_2O_3 Thin Films Using Aluminum Tri-isopropoxide. *Chem. Vap. Depos.* **9,** 194–198 (2003).
141. Morosanu, C. E. & Siddall, G. Thin Films by Chemical Vapour Deposition. 138–140 (2013).
142. Bodurov, G., Ivanova, T., Aleksandrova, M. & Gesheva, K. A. Optical characterization of WO_3-VO_x thin films for application in electrochromic devices—'smart windows'. *J. Phys. Conf. Ser.* **356,** 12016 (2012).
143. Powell, M. J. *et al.* Intelligent Multifunctional $VO_2/SiO_2/TiO_2$ Coatings for Self-Cleaning, Energy-Saving Window Panels. *Chem. Mater.* ***28*** **(5)**, 1369–1376 (2016).
144. Tiwari, A., Mishra, A. K., Kobayashi, H. & Turner, A. P. F. *Intelligent Nanomaterials*. (John Wiley & Sons, 2012).
145. Sotelo-Vazquez, C., Quesada-Cabrera, R., Darr, J. A. & Parkin, I. P. Single-step synthesis of doped TiO2 stratified thin-films by atmospheric-pressure chemical vapour deposition. *J. Mater. Chem. A* **2,** 7082 (2014).
146. Manning, T. D., Parkin, I. P., Pemble, M. E., Sheel, D. & Vernardou, D. Intelligent Window Coatings: Atmospheric Pressure Chemical Vapor Deposition of Tungsten-Doped Vanadium Dioxide. *Chem. Mater.* **16,** 744–749 (2004).
147. Ullmann, F., Yamamoto, Y. S., Campbell, F. T., Pfefferkorn, R. & Rounsaville, J. F. *Ullmann's Encyclopedia of Industrial Chemistry*. (VCH, 1991).
148. Shriver, D. A. & Drezden, M. A. The manipulation of air-sensitive compounds. *2nd Ed.,* 95 (*Wiley-Interscience,* 1986).
149. Processes, L. D. *Applications of Metal Amidinate Precursors in CVD / ALD*. 1–9 (Azo Nano, 2013).
150. Moinpour, M., Lubic, K., Nguyen, B. & Moghadam, F. Factors Affecting The Temperature Stability Of APCVD Systems In A Rapidly Changing Semiconductor Manufacturing Environment. (1993).
151. O'Neill, S. A., Clark, R. J. H., Parkin, I. P., Elliott, N. & Mills, A. Anatase Thin Films on Glass from the Chemical Vapor Deposition of Titanium(IV) Chloride and Ethyl Acetate. *Chem. Mater.* **15,** 46–50 (2003).
152. Cross, A. J., Dunnill, C. W. & Parkin, I. P. Production of Predominantly Anatase Thin Films on Various Grades of Steel and Other Metallic Substrates From $TiCl_4$ and Ethyl Acetate by Atmospheric Pressure CVD. *Chem. Vap. Depos.* **18,** 133–139 (2012).
153. Hyett, G., Darr, J. A., Mills, A. & Parkin, I. P. An Investigation into the Optimum Thickness of Titanium Dioxide Thin Films Synthesized by Using Atmospheric Pressure Chemical Vapour Deposition for Use in Photocatalytic Water Oxidation. *Chem. A Eur. J.* **16,** 10546–10552 (2010).
154. Wilkinson, M. *et al.* Combinatorial atmospheric pressure chemical vapor deposition of graded TiO_2-VO_2 mixed-phase composites and their dual functional property as self-cleaning and photochromic window coatings. *ACS Comb. Sci.* **15,** 309–319 (2013).
155. Kotz, J., Treichel, P. & Townsend, J. *Chemistry and Chemical Reactivity* 575 (Brooks Cole, 2008).
156. Smith, J. D. The Chemistry of Metal CVD. *Journal of Organometallic Chemistry* **522,** 161–162 (1996).
157. Drosos, C. & Vernardou, D. Perspectives of energy materials grown by APCVD. *Sol. Energy*

Mater. Sol. Cells **140,** 1–8 (2015).
158. Meyers, L. & P, W. *Atmospheric Pressure Chemical Vapor Deposition of CdTe for High Efficiency Thin Film PV Devices Atmospheric Pressure Chemical Vapor Deposition of CdTe for High Efficiency Thin Film PV Devices Annual Report*. (1999).
159. Downie, N. A. *Industrial Gases*. 394 (Springer, 2007).
160. Hornyak, G. L., Tibbals, H. F., Dutta, J. & Moore, J. J. *Introduction to Nanoscience and Nanotechnology: A Workbook*. 1112 (Notre Dame, 2008).
161. Choy, K. Chemical vapour deposition of coatings. *Prog. Mater. Sci.* **48,** 57–170 (2003).
162. Jones, A. C. & Hitchman, M. L. *Chemical Vapour Deposition: Precursors, Processes and Applications*. (Royal Society of Chemistry, 2009).
163. Turgambaeva, A. E., Prud'homme, N., Krisyuk, V. V. & Vahlas, C. Mass spectrometric monitoring of the gas phase during the CVD of copper from copper cyclopentadienyl triethylphosphine. *Chemical Vapor Deposition* **18,** 209–214 (2012).
164. Schropp, R. E. I. Hot Wire Chemical Vapor Deposition: Recent Progress, Present State of the Art and. *ECS Trans.* **25,** 3–14 (2009).
165. Li, X. M., Eustergerling, B. D. & Shi, Y. J. Mass spectrometric study of gas-phase chemistry in a hot-wire chemical vapor deposition reactor with tetramethylsilane. *Int. J. Mass Spectrom.* **263,** 233–242 (2007).
166. Rego, C. A. *et al.* In-situ mass spectrometric study of the gas-phase species involved in CVD of diamond as a function of filament temperature. *Diamond and Related Materials* **4,** 770–774 (1995).
167. Tsang, R. S., Rego, C. A., May, P. W., Ashfold, M. N. R. & Rosser, K. N. Examination of the effects of nitrogen on the CVD diamond growth mechanism using in situ molecular beam mass spectrometry. *Diamond and Related Materials* **6,** 247–254 (1997).
168. Petherbridge, J. R., May, P. W., Pearce, S. R. J., Rosser, K. N. & Ashfold, M. N. R. Low temperature diamond growth using CO_2/CH_4 plasmas: Molecular beam mass spectrometry and computer simulation investigations. *J. Appl. Phys.* **89,** 1484–1492 (2001).
169. Tsang, R. S., May, P. W., Ashfold, M. N. R. & Rosser, K. N. Influence of phosphine on the diamond growth mechanism: a molecular beam mass spectrometric investigation. *Diam. Relat. Mater.* **7,** 1651–1656 (1998).
170. Rahtu, A., Alaranta, T. & Ritala, M. In situ quartz crystal microbalance and quadrupole mass spectrometry studies of atomic layer deposition of aluminum oxide from trimethylaluminum and water. *Langmuir* **17,** 6506–6509 (2001).
171. Matero, R., Rahtu, A. & Ritala, M. In Situ Quadrupole Mass Spectrometry and Quartz Crystal Microbalance Studies on the Atomic Layer Deposition of Titanium Dioxide from Titanium Tetrachloride and Water. *Chem. Mater* **13,** 4506–4511 (2001).
172. Rahtu, A. & Ritala, M. Integration of a Quadrupole Mass Spectrometer and a Quartz Crytal Microblance For In-Situ Characterization of Atomic Layr Deposition Processes in Flow Rate Typre Reactors. in *CVD XV, proceedings of the fifteenth International Symposium on Chemical Vapor Deposition* 105–110 (2000).
173. Johnstone, R. A. W. *Mass Spectrometry for Organic Chemists*. 21 (Science, 1972).
174. Colombini, M. P. & Modugno, F. *Organic Mass Spectrometry in Art and Archaeology, 56,* (John Wiley & Sons, 2009).
175. Ashcroft, A. E. *Ionization Methods in Organic Mass Spectrometry*. 13 (Royal Society of Chemistry, 1997)
176. de Hoffmann Edmond, S. V. Mass Spectrometry: principles and applications, 3rd Edition . 1–4 (John Wiley and Sons, 2007).
177. Watson, J. T. & O. David Sparkman. *Introduction to Mass Spectrometry - Instrumentation, Applications, and Strategies for Data Interpretation*. *University of Arizona*, 444, (John Wiley & Sons, 2013).
178. Williams, D. H. *Mass Spectrometry*, 89 , (Royal Society of Chemistry, 1973).
179. Walker Johnstone, R. A, Rose, M. E, *Mass Spectrometry For Chemists and Biochemists,* 36,

(Cambridge University Press, 1996).
180. Agnieszka Kraj, Dominic M. Desiderio, N. M. N. Mass Spectrometry: Instrumentation, Interpretation, and Applications. 46 (Wiley, 2008).
181. Herbert, C. G. & Johnstone, R. A. W. Mass spectrometry Basics, 189 (CRC Press, 2002).
182. Ramanathan, R., *Mass Spectrometry in Drug Metabolism and Pharmacokinetics,* 62 (John Wiley & Sons, 2008).
183. Harrison, A. G. *Chemical Ionization Mass Spectrometry, Second Edition*. 59 (CRC Press, 1992).
184. Hiden Analytical. ltd *Mass Spectrometers for Residual Gas Analysis - RGA For Applications in a Vacuum Environment Quadrupole Mass Spectrometers* (2016).
185. Kool, J. & Niessen, W. M. A. *Analyzing Biomolecular Interactions by Mass Spectrometry*. (John Wiley & Sons, 2015).
186. Stein, S. . Titanium Tetrachloride. *NIST Webook* (2016).
187. Howard, C. J., Sabine, T. M. & Dickson, F. Structural and thermal parameters for rutile and anatase. *Acta Crystallographica Section B* **47,** 462–468 (1991).
188. Gurvitch, M. *et al.* VO_2 films with strong semiconductor to metal phase transition prepared by the precursor oxidation process. *J. Appl. Phys.* **102,** 1–13 (2007).
189. Gao, Y., Kang, L., Chen, Z. & Luo, H. Solution Processing of Nanoceramic VO_2 Thin Films for Application to Smart Windows. *Nanofabrication* (2011).
190. Qureshi, U., Manning, T. & Parkin, I. Atmospheric pressure chemical vapour deposition of VO_2 and VO_2/TiO_2 films from the reaction of $VOCl_3$, $TiCl_4$ and water. *J. Mater.* **14,** 1190–1194 (2004).
191. Kam, K. C. & Cheetham, A. K. Thermochromic VO_2 nanorods and other vanadium oxides nanostructures. *Mater. Res. Bull.* **41,** 1015–1021 (2006).
192. Kam, K. C. Investigations of Inorganic and Hybrid Inorganic-organic Nanostructures. (University of California, Santa Barbara, 2007).
193. Cheng, C. *et al.* Self-Assembly and Horizontal Orientation Growth of VO_2 Nanowires. *Sci. Rep.* **4,** 5456 (2014).
194. Shirahata, N., Masuda, Y., Yonezawa, T. & Koumoto, K. Control over film thickness of SnO_2 ultrathin film selectively deposited on a patterned self-assembled monolayer. *Langmuir* **18,** 10379–10385 (2002).
195. Wyckoff, R. W. G. *Crystal Structures Vol. 1 (2nd Ed.)*. (New York : Interscience Publishers, 1964).
196. Chew, C. K. T., Salcianu, C., Bishop, P., Carmalt, C. J. & Parkin, I. P. Functional thin film coatings incorporating gold nanoparticles in a transparent conducting fluorine doped tin oxide matrix. *J. Mater. Chem. C* **3,** 1118–1125 (2015).
197. Wang, J. T. *et al.* Influence of preferred orientation on the electrical conductivity of fluorine-doped tin oxide films. *Sci. Rep.* **4,** 3679 (2014).
198. Evans, P., Pemble, M. E. & Sheel, D. W. Precursor-directed control of crystalline type in atmospheric pressure CVD growth of TiO_2 on stainless steel. *Chem. Mater.* **18,** 5750–5755 (2006).
199. Lee, M. S. *Mass Spectrometry Handbook*. 302, (John Wiley & Sons, 2012).
200. Montaudo, G. & Montaudo, M. S. Mass Spectrometry of Polymers: Polypropylene Glycol. *Z. Naturforsch* **35a,** 1090–1097 (1980).
201. Niederberger, M. & Pinna, N. *Metal Oxide Nanoparticles in Organic Solvents: Synthesis, Formation*. (Springer Science & Business Media, 2009).
202. Knapp, C. E., Kafizas, A., Parkin, I. P. & Carmalt, C. J. The use of combinatorial aerosol-assisted chemical vapour deposition for the formation of gallium-indium-oxide thin films. *J. Mater. Chem.* **21,** 12644 (2011).
203. Marchand, P., Hassan, I. A, Parkin, I. P. & Carmalt, C. J. Aerosol-assisted delivery of precursors for chemical vapour deposition: expanding the scope of CVD for materials fabrication. *Dalton Trans.* **42,** 9406–22 (2013).
204. Special Issue on Aerosol-Assisted Chemical Vapor Deposition - Choy - 2006 - Chemical Vapor Deposition - Wiley Online Library.
205. Lim, S. P., Huang, N. M., Lim, H. N. & Mazhar, M. Aerosol assisted chemical vapour deposited

(AACVD) of TiO_2 thin film as compact layer for dye-sensitised solar cell. *Ceram. Int.* **40,** 8045–8052 (2014).
206. Edusi, C., Hyett, G., Sankar, G. & Parkin, I. P. Aerosol-Assisted CVD of Titanium Dioxide Thin Films from Methanolic Solutions of Titanium Tetraisopropoxide; Substrate and Aerosol-Selective Deposition of Rutile or Anatase. *Chem. Vap. Depos.* **17,** 30–36 (2011).
207. Saeli, M., Piccirillo, C., Warwick, M. E. A. & Binions, R. in *Materials and processes for energy: communicating current research and technological developments* 736–746 (Formatex, 2013).
208. Naik, A. J. T., Bowman, C., Panjwani, N., Warwick, M. E. a. & Binions, R. Electric field assisted aerosol assisted chemical vapour deposition of nanostructured metal oxide thin films. *Thin Solid Films* **544,** 452–456 (2013).
209. Piccirillo, C., Binions, R. & Parkin, I. Synthesis and functional properties of vanadium oxides: V_2O_3, VO_2, and V_2O_5 deposited on glass by aerosol-assisted CVD. *Chemical vapor deposition* **13,** 145–151 (2007).
210. Stoycheva, T. T. *et al.* Aerosol-assisted CVD of SnO_2 thin films for gas-sensor applications. *Chem. Vap. Depos.* **17,** 247–252 (2011).
211. Naeem, R. *et al.* Electric-Field Aerosol-Assisted CVD: Synthesis, Characterization, and Properties of Tin Oxide Microballs Prepared from a Single Source Precursor. *Chem. Vap. Depos.* 360–368 (2015).
212. Pan, J. Chemical Vapor Deposition of One Dimensional Tin Oxide Nanostructures: Structural Studies, Surface Modifications and Device Applications. *Chem. Vap. Depos.* 231 (2010).
213. Chen, S., McLachlan, M., Sapelkin, A. & Binions, R. Aerosol assisted chemical vapour deposition of transparent conductive ZnO thin films with hexagonal microplate surfaces and ultrahigh haze values. *J. Mater. Chem. A* **3,** 22311–22315 (2015).
214. Palgrave, R. & Parkin, I. P. Aerosol assisted chemical vapour deposition of photochromic tungsten oxide and doped tungsten oxide thin films. *J. Mater. Chem.,* **14**, 2864–2867 (2004).
215. Qadri, M. U. *et al.* WO_3 nano-needles by Aerosol Assisted CVD for optical sensing. *Procedia Eng.* **25,** 761–764 (2011).
216. Chew, C., Bishop, P., Salcianu, C., Carmalt, C. J. & Parkin, I. P. Aerosol-assisted deposition of gold nanoparticle-tin dioxide composite films. *RSC Adv.* **4,** 13182 (2014).
217. Chadwick, N. P. *et al.* The use of time resolved aerosol assisted chemical vapour deposition in mapping metal oxide thin film growth and fine tuning functional properties. *J. Mater. Chem. A* **3,** 4811–4819 (2015).
218. Chadwick, N. P. *et al.* Photo-activity and low resistivity in N/Nb Co-doped TiO_2 thin films by combinatorial AACVD. *J. Mater. Chem. A* 407–415 (2016).
219. Noor, N. & Parkin, I. P. Halide doping effects on transparent conducting oxides formed by aerosol assisted chemical vapour deposition. *Thin Solid Films* **532,** 26–30 (2013).
220. Piccirillo, C., Binions, R. & Parkin, I. P. Synthesis and characterisation of W-doped VO2 by Aerosol Assisted Chemical Vapour Deposition. *Thin Solid Films* **516,** 1992–1997 (2008).
221. Bawaked, S. M. *et al.* Aerosol assisted chemical vapor deposition of conductive and photocatalytically active tantalum doped titanium dioxide films. *J. Mater. Chem. A* **2,** 12849–12856 (2014).
222. Bachu, D., Sankar, G. & Parkin, I. P. Aerosol Assisted Chemical Vapour Deposition of Transparent Conductive Zinc Oxide Films. *Chem. Mater.* **24 (24),** 4704-4710, (2012).
223. Ehsan, M. A. *et al.* Cobalt titanate-cobalt oxide composite thin films deposited from heterobimetallic precursor. *Appl. Organomet. Chem.* **26,** 493–498 (2012).
224. Binions, R. & Parkin, Ivan, P. in *Advances in Nanocomposites - Synthesis, Characterization and Industrial Applications* (ed. Boreddy, R.) (2007).
225. Hou, X. & Choy, K.-L. Processing and Applications of Aerosol-Assisted Chemical Vapor Deposition. *Chem. Vap. Depos.* **12,** 583–596 (2006).
226. Jaaniso, R. & Tan, O. K. Semiconductor Gas Sensors. 439 (Elsevier, 2013).
227. Knapp, C. E. & Carmalt, C. J. Solution based CVD of main group materials. *Chem. Soc. Rev.* **45,** 1036–1064 (2016).

228. Vallejos, S., Di Maggio, F., Shujah, T. & Blackman, C. Chemical Vapour Deposition of Gas Sensitive Metal Oxides. *Chemosensors* **4,** 4 (2016).
229. Vallejos, S., Umek, P. & Blackman, C. Aerosol Assisted Chemical Vapour Deposition Control Parameters for Selective Deposition of Tungsten Oxide Nanostructures. *J. Nanosci. Nanotechnol.* **11,** 8214–8220 (2011).
230. Kaye, K., Turner, D., McKenna, D., Cackett, A. & Hyett, G. The Use of Additives to Control the Morphology of Thin Films Synthesized Using Aerosol Assisted Chemical Vapour Deposition. *Phys. Procedia* **46,** 21–26 (2013).
231. Tahir, A. A. *et al.* Photoelectrochemical and photoresponsive properties of Bi2S 3 nanotube and nanoparticle thin films. *Chem. Mater.* **22,** 5084–5092 (2010).
232. Sakka, S. *Handbook of sol-gel science and technology.* (Springer Science & Business Media, 2005).
233. Allendorf, M. D., Bernard, C., Division, E. S. H. T. M., Science, E. S. D. & Division, T. Requirements of Precursors for conventional and Aerosol Assisited CVD. in *Chemical Vapor Deposition: Proceedings of the Fourteenth International Conference and EUROCVD-11* 324–330 (The Electrochemical Society, 1997).
234. Lewis, D. J. & O'Brien, P. Ambient pressure aerosol-assisted chemical vapour deposition of $(CH_3NH_3)PbBr_3$, an inorganic-organic perovskite important in photovoltaics. *Chem. Commun.* **50,** 6319–21 (2014).
235. Fujishima, A. & Honda, K. Electrochemical Photolysis of Water at a Semiconductor Electrode. *Nature* **238,** 37–38 (1972).
236. Schneider, J. *et al.* Understanding TiO_2 Photocatalysis: Mechanisms and Materials. *Chem. Rev.* **114,** 9919–9986 (2014).
237. Linsebigler, A. L., Lu, G. & Yates, J. T. Photocatalysis on TiO2 Surfaces: Principles, Mechanisms, and Selected Results. *Chem. Rev.* **95,** 735–758 (1995).
238. Quesada-Cabrera, R., Sotelo-Vazquez, C., Darr, J. a. & Parkin, I. P. Critical influence of surface nitrogen species on the activity of N-doped TiO_2 thin-films during photodegradation of stearic acid under UV light irradiation. *Appl. Catal. B Environ.* **160–161,** 582–588 (2014).
239. Park, J. S. & Choi, W. Enhanced remote photocatalytic oxidation on surface-fluorinated TiO2. *Langmuir* **20,** 11523–7 (2004).
240. Rampaul, A. *et al.* Titania and tungsten doped titania thin films on glass; active photocatalysts. *Polyhedron* **22,** 35–44 (2003).
241. Lee, D., Omolade, D., Cohen, R. E. & Rubner, M. F. pH-Dependent Structure and Properties of TiO2 /SiO2 Nanoparticle Multilayer Thin Films. *Chem. Mater.* **19,** 1427–1433 (2007).
242. Li, X. & He, J. Synthesis of Raspberry-Like SiO_2–TiO_2 Nanoparticles toward Antireflective and Self-Cleaning Coatings. *ACS Appl. Mater. Interfaces* **5,** 5282–5290 (2013).
243. Kaewtip, C. *et al.* Photocatalytic of TiO_2-SiO_2 Thin Films Co-Doped with Fe3+ and Thio-Urea in the Degradation of Formaldehyde by Indoor and Outdoor Visible Lights. *Adv. Mater. Phys. Chem.* **2,** 40–44 (2012).
244. Machida, M., Norimoto, K. & Watanabe, T. The effect of SiO_2 addition in super-hydrophilic property of TiO 2 photocatalyst. *J. Mater. Sci.* **34,** 2569–2574 (1999).
245. Huang, T., Huang, W., Zhou, C., Situ, Y. & Huang, H. Superhydrophilicity of TiO_2/SiO_2 thin films: Synergistic effect of SiO_2 and phase-separation-induced porous structure. *Surf. Coatings Technol.* **213,** 126–132 (2012).
246. Houmard, M. *et al.* Morphology and natural wettability properties of sol–gel derived TiO_2–SiO_2 composite thin films. *Appl. Surf. Sci.* **254,** 1405–1414 (2007).
247. Permpoon, S. *et al.* Natural and persistent superhydrophilicity of SiO_2/TiO_2 and TiO_2/SiO_2 bi-layer films. *Thin Solid Films* **516,** 957–966 (2008).
248. Zhou, L., Yan, S., Tian, B., Zhang, J. & Anpo, M. Preparation of TiO_2–SiO_2 film with high photocatalytic activity on PET substrate. *Mater. Lett.* **60,** 396–399 (2006).
249. Yu, J., Jimmy, C. & Zhao, X. The effect of SiO_2 addition on the grain size and photocatalytic activity of TiO2 thin films. *J. Sol-Gel Sci. Technol.* **24,** 95–103 (2002).

250. Mills, A., Elliott, N., Parkin, I. P., O'Neill, S. a. & Clark, R. J. Novel TiO2 CVD films for semiconductor photocatalysis. *J. Photochem. Photobiol. A Chem.* **151,** 171–179 (2002).
251. Panjawi, N., Naik, A., Warwick, M. E. A., Hyett, G. & Binions, R. The Preparation of Titanium Dioxide Gas Sensors by the Electric Field Assisted Aerosol CVD Reaction of Titanium Isopropoxide in Toluene. *Chem. Vap. Depos.* **18,** 102–106 (2012).
252. Yamauchi, S. Plasma-Assisted Chemical Vapor Deposition of TiO_2 Thin Films for Highly Hydrophilic Performance. *Cryst. Struct. Theory Appl.* **2,** 1–7 (2013).
253. Klobukowski, E. R., Tenhaeff, W. E., McCamy, J. W., Harris, C. S. & Narula, C. K. Atmospheric pressure chemical vapor deposition of high silica SiO_2–TiO_2 antireflective thin films for glass based solar panels. *J. Mater. Chem. C* **1,** 6188 (2013).
254. Yoon, J., Oh, H. K. & Kwag, Y. J. Structural and Optical Properties of TiO_2 -SiO_2 Composite Films Prepared by Aerosol-Assisted Chemical-Vapor Deposition. *J. Korean Phys. Soc.* **33,** 699–704 (1998).
255. Noor, N. & Parkin, I. P. Enhanced transparent-conducting fluorine-doped tin oxide films formed by Aerosol-Assisted Chemical Vapour Deposition. *J. Mater. Chem. C* **1,** 984–996 (2013).
256. Mills, A. & Wang, J. Simultaneous monitoring of the destruction of stearic acid and generation of carbon dioxide by self-cleaning semiconductor photocatalytic films. *J. Photochem. Photobiol. A Chem.* **182,** 181–186 (2006).
257. Cozzi, P. G., Solari, E., Chiesi-Villa, A. & Rizzoli, C. Interaction Modes of Titanium Tetrachloride with the Carbonyl Functionality, *Euro. J. Inorg. Chem.* **129 (11)** 1361–1368 (1996).
258. Johnson, B. F. . *Inorganic Chemistry of the Transition Elements, Volume 6*. (Royal Society of Chemistry, 1978).
259. Shtelman, A. V. & Becker, J. Y. A convenient method for the synthesis of α-silylacetic acids. *Tetrahedron Lett.* **49,** 3101–3103 (2008).
260. Gaba, R., Bhandari, M. & Kakkar, R. Adsorption studies of acetaldehyde on TiO_2 nanosurface. **4,** 769–778 (2013).
261. Liu, L., Liu, Q., Xiao, W., Pan, C. & Wang, Z. O_2 adsorption and dissociation on an anatase (101) surface with a subsurface Ti interstitial. *Phys. Chem. Chem. Phys.* **18,** 1–8 (2016).
262. Hooper, A. B. & Lipscomb, J. D. Resolution of multiple heme centers of hydroxylamine oxidoreductase from Nitrosomonas. 2. Mössbauer spectroscopy. *J. Am. Chem. Soc.* **42,** 3973–3976 (2002).
263. Clayden, J., Greeves, N. & Warren, S. *Organic Chemistry*. (OUP Oxford, 2012).
264. Harding, C., Janes, R. & Johnson, D. *Elements of the P Block*. (Royal Society of Chemistry, 2002).
265. Diesen, V. *et al.* Visible Light Photocatalytic Activity in AACVD-Prepared N-modified TiO2 Thin Films. *Chem. Vap. Depos.* **20,** 91–97 (2014).
266. Sun, M. *et al.* Thermal formation of silicon-doped TiO2 thin films with enhanced visible light photoelectrochemical response. *Electrochem. commun.* **16,** 26–29 (2012).
267. Jin, R., Wu, Z., Liu, Y., Jiang, B. & Wang, H. Photocatalytic reduction of NO with NH3 using Si-doped TiO2 prepared by hydrothermal method. *J. Hazard. Mater.* **161,** 42–8 (2009).
268. Di Paola, A., Bellardita, M. & Palmisano, L. Brookite, the Least Known TiO2 Photocatalyst. *Catalysts* **3,** 36–73 (2013).
269. Tauc, J. Optical properties and electronic structure of amorphous Ge and Si. *Mater. Res. Bull.* **3,** 37–46 (1968).
270. Noctun, M., Slawomir, K. & Zontek, J. Optical properties of SiO2/TiO2 thin layers prepared by sol-gel method. *Opt. Appl.* **XLI,** 979–987 (2011).
271. Sokrates, T. P. *The Physics of SiO_2 and Its Interfaces Proceedings of the International Proceedings of the International Topical Conference on the Physics of SiO2 and its Interfaces*. (Elsevier, 2013).
272. Long, R., Dai, Y., Meng, G. & Huang, B. Energetic and electronic properties of X- (Si, Ge, Sn, Pb) doped TiO_2 from first-principles. *Phys. Chem. Chem. Phys.* **11,** 8165–72 (2009).
273. Niu, F., Zhai, J., Jiang, L. & Song, W.G. Light induced activity switch in interfacial hydrogen-bond catalysis with photo sensitive metal oxides. *Chem. Commun. (Camb).* 4738–40 (2009).

274. Kim, H., Seo, S. B., Kim, D. Y., Bae, K. & Sohn, S. Y. Enhanced Hydrophilic Property of TiO 2 Thin Film Deposited on Glass Etched with O_2 Plasma. *Trans. Electr. Electron. Mater.* **14,** 152–155 (2013).
275. Warwick, M. E. A. & Binions, R. Advances in thermochromic vanadium dioxide films. *J. Mater. Chem. A* **2,** 3275–3292 (2014).
276. Granqvist, C. G. Oxide-based chromogenic coatings and devices for energy efficient fenestration: Brief survey and update on thermochromics and electrochromics. *J. Vac. Sci. Technol. B, Nanotechnol. Microelectron. Mater. Process. Meas. Phenom.* **32,** 60801 (2014).
277. Kamalisarvestani, M., Saidur, R., Mekhilef, S. & Javadi, F. S. Performance, materials and coating technologies of thermochromic thin films on smart windows. *Renew. Sustain. Energy Rev.* **26,** 353–364 (2013).
278. Granqvist, C. G. Transparent conductors as solar energy materials: A panoramic review. *Sol. Energy Mater. Sol. Cells* **91,** 1529–1598 (2007).
279. Babulanam, S. M., Eriksson, T. S., Niklasson, G. A. & Granqvist, C. G. *Thermochromic VO_2 Films For Energy-Efficient Windows*. in (eds. Holly, S. & Lampert, C. M.) **16,** 8–18 (1987).
280. Goodenough, J. B. *Anomalous Properties of the Vanadium Oxides. Ann. Rev. Mater. Sci.* **1,** 101–138 (1971).
281. Saeli, M., Piccirillo, C., Parkin, I. P., Binions, R. & Ridley, I. Energy modelling studies of thermochromic glazing. *Energy Build.* **42,** 1666–1673 (2010).
282. Batista, C., Ribeiro, R. M. & Teixeira, V. Synthesis and characterization of VO_2-based thermochromic thin films for energy-efficient windows. *Nanoscale Res. Lett.* **6,** 301 (2011).
283. Blackman, C. S., Piccirillo, C., Binions, R. & Parkin, I. P. Atmospheric pressure chemical vapour deposition of thermochromic tungsten doped vanadium dioxide thin films for use in architectural glazing. *Thin Solid Films* **517,** 4565–4570 (2009).
284. Louloudakis, D. *et al.* Atmospheric pressure chemical vapor deposition of amorphous tungsten doped vanadium dioxide for smart window applications. **7,** 10–14 (2016).
285. Jorgenson, G. V. & Lee, J. C. Doped vanadium oxide for optical switching films. *Sol. Energy Mater.* **14,** 205–214 (1986).
286. Burkhardt, W. *et al.* Tungsten and fluorine co-doping of VO_2 films. *Thin Solid Films* **402,** 226–231 (2002).
287. Hu, S. *et al.* Optical properties of Mg-doped VO_2: Absorption measurements and hybrid functional calculations. *Appl. Phys. Lett.* **101,** 10–14 (2012).
288. Hanlon, T. J., Coath, J. A. & Richardson, M. A. Molybdenum-doped vanadium dioxide coatings on glass produced by the aqueous sol-gel method. *Thin Solid Films* **436,** 269–272 (2003).
289. Tan, X. *et al.* Unraveling metal-insulator transition mechanism of VO_2 triggered by tungsten doping. *Sci. Rep.* **2,** 466 (2012).
290. Long, R. *et al.* Identifying structural distortion in doped VO_2 with IR spectroscopy. *Phys. Chem. Chem. Phys.* **14,** 7225–8 (2012).
291. Manning, T. D. & Parkin, I. P. Vanadium(IV) oxide thin films on glass and silicon from the atmospheric pressure chemical vapour deposition reaction of $VOCl_3$ and water. *Polyhedron* **23,** 3087–3095 (2004).
292. Powell, M. J. *et al.* Direct and continuous synthesis of VO_2 nanoparticles. *Nanoscale* **7,** 18686–18693 (2015).
293. Son, J. H., Wei, J., Cobden, D., Cao, G. & Xia, Y. Hydrothermal synthesis of monoclinic VO_2 micro- and nanocrystals in one step and their use in fabricating inverse opals. *Chem. Mater.* **22,** 3043–3050 (2010).
294. Kim, D. H. & Kwok, H. S. Pulsed laser deposition of VO_2 thin films. *Appl. Phys. Lett.* **65,** 3188–3190 (1994).
295. Qureshi, U., Manning, T. D., Parkin, I. P. & Oaj, W. C. H. Atmospheric pressure chemical vapour deposition of VO_2 and VO_2/TiO_2 films from the reaction of $VOCl_3$, $TiCl_4$ and water. 1190–1194 (2004).
296. Fang, B. *et al.* Optical properties of vanadium dioxide thin film in nanoparticle structure. *Opt.*

Mater. (Amst). **47,** 225–230 (2015).
297. Sahana, M. B., Dharmaprakash, M. S. & Shivashankar, S. a. Microstructure and properties of VO_2 thin films deposited by MOCVD from vanadyl acetylacetonate. *J. Mater. Chem.* **12,** 333–338 (2001).
298. Manning, T. D. & Parkin, I. P. Atmospheric pressure chemical vapour deposition of tungsten doped vanadium(IV) oxide from VOCl3, water and WCl6. *J. Mater. Chem.* **14,** 2554–2559 (2004).
299. Piccirillo, C., Binions, R. & Parkin, I. P. Nb-Doped VO_2 Thin Films Prepared by Aerosol-Assisted Chemical Vapour Deposition. *Eur. J. Inorg. Chem.* **2007,** 4050–4055 (2007).
300. Warwick, M., Smith, R., Furlan, N., Crane, J. & Binions, R. Electric Fields and Chemical Vapor Deposition. in *ECS Transactions* **28,** 1–13 (2010).
301. Nguyen, T. D. & Do, T. O. Solvo-hydrothermal approach for the shape-selective synthesis of vanadium oxide nanocrystals and their characterization. *Langmuir* **25,** 5322–5332 (2009).
302. Zhang, H. *et al.* A cost-effective method to fabricate VO2 (M) nanoparticles and films with excellent thermochromic properties. *J. Alloys Compd.* **636,** 106–112 (2015).
303. Nag, J. & Haglund Jr, R. F. Synthesis of vanadium dioxide thin films and nanoparticles. *J. Phys. Condens. Matter* **20,** 264016 (2008).
304. Zhong, L. *et al.* Star-shaped VO_2 (M) nanoparticle films with high thermochromic performance. *CrystEngComm* **17,** 5614–5619 (2015).
305. Billik, P. *et al.* Synthesis and Transport Properties of Nanostructured VO_2 by Mechanochemical Processing. *Meas. Sci. Rev.* **11,** 29–33 (2011).
306. Zhang, Y. *et al.* Influence of different additives on the synthesis of VO2 polymorphs. *Ceram. Int.* **39,** 8363–8376 (2013).
307. Wang, H., Yi, X., Chen, S. & Fu, X. Fabrication of vanadium oxide micro-optical switches. *Sensors Actuators, A Phys.* **122,** 108–112 (2005).
308. Pauli, S. A. *et al.* X-ray diffraction studies of the growth of vanadium dioxide nanoparticles. *J. Appl. Phys.* **102,** (2007).
309. Chae, B.-G. *et al.* Highly Oriented VO_2 Thin Films Prepared by Sol-Gel Deposition. *Electrochem. Solid-State Lett.* **9,** C12–C14 (2006).
310. Krawiec, P.; Kaskel, S. in *Nanoscale Materials in Chemistry* (eds. Klabunde, K. J. & Richards, R. M.) 111–125 (John Wiley & Sons, 2009).
311. Wu, L. *et al.* Understanding the mechanical properties of vanadium carbides: Nano-indentation measurement and first-principles calculations. *J. Alloys Compd.* **548,** 60–64 (2013).
312. Didziulis, S. V. & Butcher, K. D. A perspective on the properties and surface reactivities of carbides and nitrides of titanium and vanadium. *Coord. Chem. Rev.* **257,** 93–109 (2013).
313. Stanciu, V. I., Vitry, V. & Delaunois, F. Tungsten carbide powder obtained by direct carburization of tungsten trioxide using mechanical alloying method. *J. Alloys Compd.* **659,** 302–308 (2016).
314. Hussainova, I. Effect of microstructure on the erosive wear of titanium carbide-based cermets. *Wear* **255,** 121–128 (2003).
315. Liu, K., Li, X. P., Rahman, M. & Liu, X. D. CBN tool wear in ductile cutting of tungsten carbide. *Wear* **255,** 1344–1351 (2003).
316. Hannink, R. H. J. & Murray, M. J. Elastic moduli measurements of some cubic transition metal carbides and alloyed carbides. *Journal of Materials Science* **9,** 223–228 (1974).
317. Kral, C., Lengauer, W., Rafaja, D. & Ettmayer, P. Critical review on the elastic properties of transition metal carbides, nitrides and carbonitrides. *J. Alloys Compd.* **265,** 215–233 (1998).
318. Matrosov, Y. I. & Anashenko, V. N. Vanadium nitride in low-alloy low-carbon steels. *Met. Sci. Heat Treat.* **13,** 893–896 (1971).
319. Muije, P., Horton, R. M. & Duran, S. A. Kinetics of solid vanadium-nitrogen reactions at high temperatures. *Metall. Trans.* **5,** 97–104 (1974).
320. Choi, D., Blomgren, G. E. & Kumta, P. N. Fast and reversible surface redox reaction in nanocrystalline vanadium nitride supercapacitors. *Advanced Materials* **18,** 1178–1182 (2006).

321. Oyama, S. T., Kapoor, R., Oyama, H. T., Hofmann, D. J. & Matijevic, E. Topotactic synthesis of vanadium nitride solid foams. **5814,** 2–6 (1993).
322. Vaidhyanathan, B., Agrawal, D. K. & Roy, R. Novel synthesis of nitride powders of microwave-assisted combustion. *Journal of Materials Research* **15,** 974–981 (2000).
323. Huang, J. W., Peng, H. & Xia, G. B. Microwave synthesis of vanadium nitride for industrial applications. *Ironmak. Steelmak.* **36,** 110–114 (2009).
324. Huang, T. *et al.* Hydrothermal synthesis of vanadium nitride and modulation of its catalytic performance for oxygen reduction reaction. *Nanoscale* **6,** 9608–13 (2014).
325. Hong, Y. C., Shin, D. H. & Uhm, H. S. Production of vanadium nitride nanopowders from gas-phase VOCl3 by making use of microwave plasma torch. *Mater. Chem. Phys.* **101,** 35–40 (2007).
326. Fix, R., Gordon, R. & Hoffman, D. Chemical Vapor Deposition of Vanadium, Niobium, and Tantalum Nitride Thin Films. *Chem. Mater.* **5,** 614–619 (1993).
327. Chen, L. *et al.* A room-temperature synthesis of nanocrystalline vanadium nitride. *Solid State Commun.* **132,** 343–346 (2004).
328. Parkin, I. P. & Elwin, G. S. Atmospheric pressure chemical vapour deposition of vanadium nitride and oxynitride films on glass from reaction of VCl_4 with NH_3. *J. Mater. Chem.* **11,** 3120–3124 (2001).
329. Newport, A., Carmalt, C. J., Parkin, I. P. & O'Neill, S. A. Formation of VN front VCl_4 and NH(SiMe3)2 by APCVD - A potential solar control coating. *Eur. J. Inorg. Chem.* 4286–4290 (2004).
330. Giordano, C., Erpen, C., Yao, W., Milke, B. & Antonietti, M. Metal nitride and metal carbide nanoparticles by a soft urea pathway. *Chem. Mater.* **21,** 5136–5144 (2009).
331. Buha, J., Djerdj, I., Antonietti, M. & Niederberger, M. Thermal transformation of metal oxide nanoparticles into nanocrystalline metal nitrides using cyanamide and urea as nitrogen source. *Chem. Mater.* **19,** 3499–3505 (2007).
332. Ma, J. *et al.* Low temperature synthesis of vanadium carbide (VC). *Mater. Lett.* **63,** 905–907 (2009).
333. Aguzzoli, C., Figueroa, C. A., de Souza, F. S., Spinelli, A. & Baumvol, I. J. R. Corrosion and nanomechanical properties of vanadium carbide thin film coatings of tool steel. *Surf. Coatings Technol.* **206,** 2725–2731 (2012).
334. Yang, G., Sun, X., Li, Z., Li, X. & Yong, Q. Effects of vanadium on the microstructure and mechanical properties of a high strength low alloy martensite steel. *Mater. Des.* **50,** 102–107 (2013).
335. Ollilainen, V., Kasprzak, W. & Holappa, L. The effect of silicon, vanadium and nitrogen on the microstructure and hardness of air cooled medium carbon low alloy steels. *J. Mater. Process. Technol.* **134,** 405–412 (2003).
336. S., G. & Cochrane, R. C. Influence of cooling rate and tempering on precipitation and hardness of vanadium microalloyed steel. *Mater. Des.* **26,** 486–492 (2005).
337. Chicco, B., Borbidge, W. E. & Summerville, E. Experimental study of vanadium carbide and carbonitride coatings. *Mater. Sci. Eng. A* **266,** 62–72 (1999).
338. Aghaie-Khafri, M. & Fazlalipour, F. Kinetics of V(N,C) coating produced by a duplex surface treatment. *Surf. Coatings Technol.* **202,** 4107–4113 (2008).
339. Schmuecker, S. M. & Leonard, B. M. Formation mechanism of nanostructured metal carbides via salt-flux synthesis. *Inorg. Chem.* **54,** 3889–3895 (2015).
340. Claridge, J. B., York, A. P. E., Brungs, A. J. & Green, M. L. H. Study of the temperature-programmed reaction synthesis of early transition metal carbide and nitride catalyst materials from oxide precursors. *Chem. Mater.* **12,** 132–142 (2000).
341. Liu, F. *et al.* Synthesis and characterization of vanadium carbide nanoparticles by thermal refluxing-derived precursors. *J. Mater. Sci.* **46,** 3693–3697 (2011).
342. Chen, Y., Zhang, H., Ye, H. & Ma, J. A simple and novel route to synthesize nano-vanadium carbide using magnesium powders, vanadium pentoxide and different carbon source. *Int. J. Refract. Met. Hard Mater.* **29,** 528–531 (2011).

343. Mahajan, M., Singh, K. & Pandey, O. P. Single step synthesis of nano vanadium carbide - V8C7 phase. *Int. J. Refract. Met. Hard Mater.* **36,** 106–110 (2013).
344. Mahajan, M., Singh, K. & Pandey, O. P. Synthesis of vanadium carbide nanoparticles by thermal decomposition of the precursor. *AIP Conf. Proc.* **1536,** 271–272 (2013).
345. Poirier, L. *et al.* Vanadocene used as a precursor for the chemical vapor deposition of vanadium carbide at atmospheric pressure. *Thin Solid Films* **249,** 62–69 (1994).
346. Brown, G. M. & Maya, L. Cyclopentadienylvanadium carbonyl derivatives as precursors to vanadium carbide. *Inorg. Chem.* **28,** 2007–2010 (1989).
347. Lo, K. H., Shek, C. H. & Lai, J. K. L. Recent developments in stainless steels. *Mater. Sci. Eng. R Reports* **65,** 39–104 (2009).
348. Sourmail, T. Precipitation in creep resistant austenitic stainless steels. *Mater. Sci. Technol.* **17,** 1–14 (2001).
349. Cross, W. B. *et al.* Tungsten oxide coatings from the aerosol-assisted chemical vapor deposition of W(OAr)6 (Ar = C6H5, C6H4F-4, C6H3F2-3,4); photocatalytically active ??-WO3 films. *Chem. Mater.* **15,** 2786–2796 (2003).
350. Buijnsters, J. G. *et al.* CVD diamond deposition on steel using arc-plated chromium nitride interlayers. *Diam. Relat. Mater.* **11,** 536–544 (2002).
351. Halada, G. P. & Clayton, C. R. Comparison of Mo-N and W-N synergism during passivation of stainless steel through x-ray photoelectron spectroscopy and electrochemical analysis. *J. Vac. Sci. Technol. A* **11,** 2342–2347 (1993).
352. Taylor, A. *et al.* A bioinspired solution for spectrally selective thermochromic VO_2 coated intelligent glazing. *Optics express* **21,** A750--A764 (2013).
353. Liu, C., Wang, N. & Long, Y. Multifunctional overcoats on vanadium dioxide thermochromic thin films with enhanced luminous transmission and solar modulation, hydrophobicity and anti-oxidation. *Appl. Surf. Sci.* **283,** 222–226 (2013).
354. Soon, G. K. & Hyeon, T. Colloidal chemical synthesis and formation kinetics of uniformly sized nanocrystals of metals, oxides, and chalcogenides. *Acc. Chem. Res.* **41,** 1696–1709 (2008).
355. Kwon, S. G.; Hyeon, T. Formation mechanisms of uniform nanocrystals via hot-injection and heat-up methods. *Acc Chem Res* **41 (12),** 1696–1709.
356. Bronstein, L. M. *et al.* Nanoparticles by decomposition of long chain iron carboxylates: From spheres to stars and cubes. *Langmuir* **27,** 3044–3050 (2011).
357. Paik, T. *et al.* Solution-Processed Phase-Change Vanadium Oxide (VO x) Nanocrystals. *ACS Nano* 797–806 (2013).
358. Niederberger, M., Bartl, M. H. & Stucky, G. D. Benzyl alcohol and transition metal chlorides as a versatile reaction system for the nonaqueous and low-temperature synthesis of crystalline nano-objects with controlled dimensionality. *J. Am. Chem. Soc.* **124,** 13642–13643 (2002).
359. Niederberger, M. Nonaqueous sol-gel routes to metal oxide nanoparticles. *Acc. Chem. Res.* **40,** 793–800 (2007).
360. Sun, S. & Zeng, H. Size-Controlled Synthesis of Magnetite Nanoparticles Size-Controlled Synthesis of Magnetite Nanoparticles. **124,** 8204–8205 (2002).
361. Demeter, M., Neumann, M. & Reichelt, W. Mixed-valence vanadium oxides studied by XPS. *Surf. Sci.* **454,** 41–44 (2000).
362. Alexander V. Naumkin, Anna Kraut-Vass, Stephen W. Gaarenstroom, and C. J. P. NIST X-ray Photoelectron Spectroscopy Database. *NIST Standard Reference Database 20, Version 4.1* (2012).
363. Yu, S., Fu, N., Gao, F. & Sui, Z. Synthesis of Vanadium Nitride by a One Step Method. *J. Mater. Sci. Technol* **23,** 43–46 (2007).
364. Ortega, A., Roldan, M. A. & Real, C. Carbothermal synthesis of vanadium nitride: Kinetics and mechanism. *Int. J. Chem. Kinet.* **38,** 369–375 (2006).
365. Liu, C.; Wang, N.; Long, Y. Carbon Nitride Deposited Using Energetic Species: A Two-Phase System. *Phys. Rev. Lett.* **73 (1),** 118–121 (1994).
366. Azhan, N. H. *et al.* Large modification in insulator-metal transition of VO_2 films grown on Al_2O_3

(001) by high energy ion irradiation in biased reactive sputtering. *J. Appl. Phys.* **119,** 55308 (2016).
367. Choi, J. G. Ammonia decomposition over vanadium carbide catalysts. *J. Catal.* **182,** 104–116 (1999).
368. Hiden Analytical. *Hiden HPR60 Molecular Beam Mass Spectrometer System vacuum analysis surface science plasma diagnostics gas analysis HPR60 MBMS Overview*. (2015).